TECHNISCHE UNIVERSITÄT MÜNCHEN

Lehrstuhl für Numerische Mechanik

Efficient Uncertainty Quantification for Large-Scale Biomechanical Models Using a Bayesian Multi-Fidelity Approach

Jonas Biehler

Vollständiger Abdruck der von der Fakultät für Maschinenwesen der Technischen Universität München zur Erlangung des akademischen Grades eines

Doktor-Ingenieurs (Dr.-Ing.)

genehmigten Dissertation.

Vorsitzender:	Univ.-Prof. Dr.-Ing. Michael W. Gee
Prüfer der Dissertation:	1. Univ.-Prof. Dr.-Ing. Wolfgang A. Wall
	2. Univ.-Prof. Phaedon-Stelios Koutsourelakis, Ph.D.

Die Dissertation wurde am 23.03.2016 bei der Technischen Universität München eingereicht und durch die Fakultät für Maschinenwesen am 18.11.2016 angenommen.

Abstract

Computational models are ubiquitous in science and engineering and are often the only means by which systems and processes can be studied. The more researchers and engineers rely on numerical simulation techniques, the more important truly predictive simulations become. Predictive simulations, which account for incomplete and inaccurate information about the problems of interest and provide distributions or error bars rather than deterministic results, are desirable in virtually all application scenarios for numerical models. However, one field of application which is in particular need of predictive techniques is biomedical engineering.

In many biomedical applications information about model input parameters is scarce and patient-specific model parameters, such as constitutive properties, are usually not easy to obtain. Furthermore, it is often difficult or impossible to validate simulation results with experimental tests *in vivo* and, in addition, the consequences of faulty predictions can be fatal. Thus, uncertainties and imprecise information have to be considered in the computational model. However, due to limited computational resources and several shortcomings of traditional uncertainty quantification approaches, parametric uncertainties, modeled as random fields, have not yet been considered in patient-specific, nonlinear, large-scale, and complex biomechanical models.

The main focus of this work lies in the development of a comprehensive uncertainty quantification framework based on efficient multi-fidelity sampling and Bayesian formulations. Thereby, the emphasis is on biomedical applications. Specifically, the developed framework is applied to computational models of abdominal aortic aneurysms and reduced order models of the human lung as prototype applications. The goal of this work is the development and application of a novel approach to quantify the impact of uncertain model input parameters and to enable predictive simulations by providing probability distributions, error bars, or worst case estimates for the respective quantity of interest.

As a first step, uncertainty quantification requires an accurate probabilistic description of the uncertain model input parameters as random variables or multi-dimensional random fields. Therefore, innovative approaches to infer suitable parameters for these probabilistic models from available experimental data are devised, allowing patient-specific, probabilistic predictions of uncertain model input parameters with unprecedented accuracy. For the propagation of the uncertainties, a multi-fidelity framework is developed. The key feature of the presented method is the ability to rigorously exploit and incorporate information from cheap low-fidelity models. Thereby, the approach merely requires that the low-fidelity model and the corresponding high-fidelity model share a similar stochastic structure, i.e., dependence on the random input variables. The result is a tremendous flexibility in choice of the low-fidelity model.

The flexibility and capabilities of the framework are demonstrated by performing uncertainty quantification in large-scale, nonlinear, patient-specific finite element models of abdominal aortic aneurysms and the human lung as showcase examples. However, the approach is readily transferable to many other application scenarios. The employed approach results in a tremendous reduction of computational costs, rendering uncertainty quantification in combination with complex patient-specific nonlinear biomechanical models practical for the first time. Regarding abdominal aortic aneurysms, the impact of the uncertainty in the input parameters on mechanical quantities typically related to aneurysm rupture potential is analyzed, and estimates on the distribution and variability of these mechanical quantities due to uncertain constitutive parameters or wall thickness are provided for the first time.

Zusammenfassung

Numerische Modelle sind heutzutage allgegenwärtig in Ingenieurwesen und Wissenschaft und stellen häufig die einzige Möglichkeit dar, Systeme und Prozesse zu analysieren. Je mehr sich Wissenschaftler und Ingenieure auf numerische Simulationsmethoden verlassen, desto wichtiger werden vorhersagefähige Simulationen. Vorhersagefähige Simulationen, die unvollständige und ungenaue Informationen über das zu untersuchende System berücksichtigen und Wahrscheinlichkeitsverteilungen oder Fehlerbalken darstellen sind in praktisch allen Anwendungsgebieten numerischer Modelle deterministischen Methoden überlegen und diesen vorzuziehen.

Für viele biomedizinische Simulationsanwendugen trifft dies im besonderen Maße zu. Einer der Gründe hierfür ist, dass bei vielen biomedizinischen Fragestellungen patientenspezifische Modellparameter überhaupt nicht beziehungsweise. nicht in ausreichender Genauigkeit bestimmbar sind. Des Weiteren ist es häufig schwierig beziehungsweise unmöglich, Simulationsergebnisse mittels experimenteller Untersuchungen *in vivo* zu validieren. Es kommt erschwerend hinzu, dass fehlerhafte Vorhersagen fatale Konsequenzen haben können. Aus diesen Gründen müssen unscharfe Informationen sowie Unsicherheiten im numerischen Modell berücksichtigt werden. Aufgrund beschränkter Rechenkapazität sowie bestehender Defizite traditioneller Verfahren zur Quantifizierung von Unsicherheiten wurden parametrische Unsicherheiten in Form von Zufallsfeldern bis dato nicht in komplexen, patientenspezifischen, nichtlinearen biomechanischen Modellen berücksichtigt.

Den Schwerpunkt der vorliegenden Arbeit bildet die Entwicklung eines umfassenden Werkzeugs zur Quantifizierung von Unsicherheiten basierend auf effizientem multi-fidelity Sampling in Kombination mit Bayesschen Ansätzen. Das Hauptaugenmerk liegt dabei auf biomedizinischen Anwendungen. Als exemplarische biomedizinische Fragestellungen, die mit dem entwickelten Ansätzen untersucht werden können, werden numerische Modelle von abdominalen Aortenaneurysmen sowie der menschlichen Lunge betrachtet. Das Ziel dieser Arbeit ist die Entwicklung und Anwendung neuartiger Ansätze, die den Einfluss von Modelleingangsparameterunsicherheiten quantifizieren und vorhersagefähiger Simulationen durch die Berechnung von Wahrscheinlichkeitsverteilungen, Fehlerbalken, oder Worst-Case-Szenarien für die betrachtete Modellausgangsgröße ermöglichen.

Als ersten Schritt bedarf es einer präzisen probabilistischen Beschreibung der unsicheren Modelleingangsparameter als Zufallsvariablen oder mehrdimensionale Zufallsfelder. Hierfür werden innovative Ansätze entwickelt, um die Parameter dieser stochastischen Modelle aus verfügbaren experimentellen Daten abzuleiten und somit eine probabilistische, patientenspezifische Vorhersage unsichererer Modelleingangsgrößen zu ermöglichen. Zur Berechnung der Fortpflanzung von Unsicherheiten im numerischen Modell wird ein neuartiger multi-fidelity Ansatz verwendet. Die Schlüsseleigenschaft der dargestellten Methode ist, dass Informationen aus vereinfachten Modellen konsequent genutzt werden können und so der Berechnungsaufwand drastisch gesenkt werden kann. Dabei setzt der verwendete Ansatz lediglich eine ähnliche stochastische Struktur der Modelle voraus, was zu einer großen Flexibilität bezüglich der Wahl des vereinfachten Modells führt.

Die Leistungsfähigkeit und Vielseitigkeit des Ansatzes und der Implementierung werden anhand ausgewählter Anwendungen in Form von großen, nichtlinearen, patientenspezifischen Finite-Element-Modellen abdominaler Aortenaneurysmen sowie der menschlichen Lunge aufgezeigt. Der entwickelte Ansatz ist ebenfalls direkt auf andere Anwendungsszenarien übertragbar.

Die dabei erzielte Reduktion des Rechenaufwands ermöglicht erstmals die Betrachtung derart komplexer, patientenspezifischer Probleme in einem sinnvollen, zeitlichen Rahmen. Bei den Modellen der abdominalen Aortenaneurysmen wird der Einfluss unsicherer Modelleingangsparameter auf mechanische Kenngrößen, die mit dem Rupturrisiko des Aneurysmas assoziiert sind, bestimmt. Außerdem können erstmals Verteilungen und Abschätzungen über die Schwankungen dieser mechanischer Größen aufgrund unsicherer Modelleingangsparametern wie Wanddicke oder Konstitutivparameter berechnet werden.

Contents

Nomenclature

Notation of scalars, vectors, and matrices

c, C	Deterministic scalar variable
$\boldsymbol{v}$	Deterministic vector
$\boldsymbol{M}$	Deterministic matrix
$\mathsf{x}, \mathsf{x}(\omega), \theta(\omega)$	Random variable
$\mathbf{x}, \mathbf{x}(\omega), \boldsymbol{\theta}(\omega)$	Random vector
$\mathsf{f}(\boldsymbol{x}), \mathsf{f}(\boldsymbol{x}, \omega)$	Random process/field

Operators and symbols

$(\cdot)^T$	Transpose of a matrix or vector
$(\cdot)^{-1}$	Inverse of a matrix
$\dot{(\cdot)}$	Time derivative
$\cup$	Union
$\cap$	Intersection
$\subset$	Subset
$\mathbb{E}[\cdot]$	Expectation
$\mathbb{M}[\cdot]$	Median
$\mathbb{V}[\cdot]$	Variance
$\|\cdot\|$	L2-norm
$\|\cdot\|$	Determinant of a matrix
$\log(\cdot)$	Natural logarithm
Div	Material divergence operator
Grad	Material gradient operator

Computational solid mechanics

Φ_t	Nonlinear deformation map
Ω_0, Ω_t	Reference and spatial configuration
$\boldsymbol{X}, \boldsymbol{x}$	Position in reference and deformed configuration
$\boldsymbol{u}$	Displacement field
$\boldsymbol{F}, \boldsymbol{F}_{\text{vol}}\bar{\boldsymbol{F}}$	Deformation gradient, volumetric part, isochoric part
$\boldsymbol{I}$	Identity tensor
J	Determinant of deformation gradient
V_0, V	Volume in reference and deformed configuration
A_0, A	Area in reference and deformed configuration
$\boldsymbol{C}, \boldsymbol{C}_{\text{vol}}, \bar{\boldsymbol{C}}$	Right Cauchy-Green tensor, volumetric part, isochoric part
$\boldsymbol{E}$	Green-Lagrange strain tensor
$\boldsymbol{b}$	Left Cauchy-Green tensor
$\boldsymbol{e}$	Euler-Almansi strain tensor
$I_i, \bar{I}_i$	i-th principal invariant, i-th modified invariant
$\boldsymbol{t}$	Traction vector
$\boldsymbol{f}$	Resulting force
$\boldsymbol{n}$	Outward normal
$\boldsymbol{\sigma}$	Cauchy stress tensor
$\boldsymbol{P}$	First Piola-Kirchhoff stress tensor
$\boldsymbol{S}$	Second Piola-Kirchhoff stress tensor
$\Psi, \Psi_{\text{vol}}, \Psi_{\text{iso}},$	Strain-energy function, volumetric part, isochoric part
$\mathbb{C}$	Elasticity tensor
Γ_u, Γ_σ	Neumann and dirichlet boundary
$\hat{\boldsymbol{b}}_0$	Body forces
ρ_0	Density in reference configuration
$\hat{\boldsymbol{u}}$	Prescribed displacements
$\boldsymbol{w}$	Weight functions
$\delta\mathscr{W}$	Virtual work
$\mathfrak{H}^1$	Sobolev space
$\boldsymbol{d}$	Discrete nodal displacements
$\boldsymbol{N}$	Matrix of element shape functions
$\boldsymbol{\xi}$	Position in finite element parameter space
$\overline{\boldsymbol{X}}, \bar{\boldsymbol{x}}$	Nodal positions in reference and current configuration
$\boldsymbol{J}^{(e)}$	Element Jacobian matrix
$\boldsymbol{M}$	Mass matrix
$\boldsymbol{f}^{\text{int}}$	Vector of internal forces
$\boldsymbol{f}^{\text{ext}}$	Vector of external forces
$\boldsymbol{K}_T$	Effective tangential stiffness matrix

Probability theory and statistics

A, B, A^c, B^c	Event and complementary event
$P(A)$	Probability of event A
$P(A\|B)$	Conditional probability
Ω	Sample space
$\mathcal{F}$	$\sigma-$algebra
$p_{\mathsf{x}}(x)$	Probability density or mass function
$p_{\mathsf{x},\mathsf{y}}(x\|y)$	Conditional probability density or mass function
$F_{\mathsf{x}}(x)$	Cumulative distribution function
$\mathrm{cov}(\mathsf{x}, \mathsf{y})$	Covariance of two random variables x and y
$\rho(\mathsf{x}, \mathsf{y})$	Correlation coefficient of x and y
$\boldsymbol{\Sigma}(\mathbf{x}, \mathbf{y})$	Covariance matrix of two random vectors $\mathbf{x}$ and $\mathbf{y}$
$\mathrm{erf}(\cdot)$	Error function
d	Dimension of stochastic process
$\sigma^2_{\mathsf{g}}(\boldsymbol{x})$	Variance function of stochastic process
$m^2_{\mathsf{g}}(\boldsymbol{x})$	Mean function of stochastic process
$r^2_{\mathsf{g}}(\boldsymbol{x}, \boldsymbol{x}')$	Auto-correlation function of stochastic process
$k^2_{\mathsf{g}}(\boldsymbol{x}, \boldsymbol{x}')$	Auto-covariance function of stochastic process
$\rho^2_{\mathsf{g}}(\boldsymbol{x}, \boldsymbol{x}')$	Normalized auto-covariance function of stochastic process
$\boldsymbol{\tau}$	Lag vector
ℓ	Correlation length
$\boldsymbol{K}, \boldsymbol{\Sigma}$	Covariance matrix
$\mathcal{GP}(m_{\mathsf{g}}(\boldsymbol{x}), k_{\mathsf{g}}(\boldsymbol{x}, \boldsymbol{x}'))$	Gaussian process with mean $m_{\mathsf{g}}(\boldsymbol{x})$ and auto-covariance $k_{\mathsf{g}}(\boldsymbol{x}, \boldsymbol{x}')$
$\boldsymbol{P}$	Matrix containing the charateristic length scales
$B_\nu(\cdot)$	Modified Bessel function
$\Phi(\cdot)$	Standard Gaussian cumulative distribution function
$\phi(\cdot)$	Standard Gaussian probability density function
λ_k	Eigenvalues of a covariance kernel
$v_k(\boldsymbol{x})$	Eigenfunctions of a covariance kernel
ω_{k_i}	Phase angles of Fourier expansion
$\tilde{L}$	Length of generated field
$\tilde{L}_{x_i}$	Length of generated field in x_i-direction
n_k	Truncation threshold of Fourier expansion
$c_{\boldsymbol{k}}$	Coefficients of Fourier expansion
$\mathcal{K}$	Indexing set for truncation
γ	Retained fraction of variability
$s_{\mathsf{g}}(\cdot)$	Power spectral density
$s_{\mathsf{h},t}(\cdot)$	Target power spectral density of non-Gaussian process h
$\boldsymbol{\tau}$	Frequency vector
κ_{iu}	Cut-off wave numbers

Bayesian regression

d	Dimension of the problem
n	Number of training cases
n^*	Number of test cases
m	Number of basis functions
$\mathcal{D}$	Dataset
$\boldsymbol{X}$	Design matrix
$\boldsymbol{x}$	Vector of explanatory variables, input variables
$\boldsymbol{x}^*$	Test input
y	Response variable, target variable
y^*	Prediction of response variable for test input
$\bar{y}$	Average of all target variable in the training set
$\bar{y}^*$	Mean prediction of target variable for test input
$\tilde{y}^*$	Measured target variable corresponding to test input
f	Latent function
f^*	Prediction of latent function for test input
$\bar{f}^*$	Mean prediction of latent function
ϵ	Noise or error
$\boldsymbol{\theta}$	Vector of (hyper-)parameters
$\boldsymbol{\theta}_m, \boldsymbol{\theta}_k, \boldsymbol{\theta}_l$	Parameters of mean, covariance, and likelihood function
$\hat{\boldsymbol{\theta}}$	Point estimate of $\boldsymbol{\theta}$ based on maximum marginal likelihood
$\bar{\boldsymbol{\theta}}$	Posterior mean value of $\boldsymbol{\theta}$
$\boldsymbol{\theta}_{\text{MAP}}$	Maximum posterior value of $\boldsymbol{\theta}$
$\boldsymbol{w}$	Vector of weights
$\boldsymbol{w}_{\text{LS}}$	Least square estimate of weights
SS_{ess}	Error sum of squares
σ_ϵ^2	Variance of the noise/error
$\boldsymbol{\phi}$	Set of basis functions
$\boldsymbol{\Phi}$	Design matrix when basis functions are used
$\boldsymbol{I}$	Identity matrix
L	Likelihood function
$\mathcal{L}$	Negative logarithm of marginal likelihood
Γ	Gamma function
$\sigma_{\text{s}}^{*\,2}$	Standardized mean predictive variance
$\sigma_{\text{P,s}}^{*\,2}$	Patient standardized mean predictive variance

UQ Methods

$f(\cdot)$	Computational model
$f_{\mathrm{GP}}(\cdot)$	Gaussian process based surrogate model
$f_{\mathrm{PCE}}(\cdot)$	Polynomial chaos based surrogate model
$\boldsymbol{x}$	Vector of (uncertain) input parameters
y	Model output of interest
$\mathcal{A}$	Failure domain
y_{fail}	Failure threshold
P_{fail}	Failure probability
$\hat{P}_{\mathrm{fail}}$	Monte Carlo estimate of P_{fail}
$\mathbf{1}_{\mathcal{A}}(y)$	Indicator function
N_{SAM}	Number of samples
μ_{y}	Mean of y
$\hat{\mu}_{\mathsf{y}}$	Monte Carlo estimate of μ_{y}
σ^2_{y}	Variance of y
$\hat{\sigma}^2_{\mathsf{y}}$	Monte Carlo estimate of σ^2_{y}
N_{fail}	Number of samples that lie in the failure domain
$\delta_{y^{(i)}}$	Delta-Dirac mass
W	Normalized importance weight
w	Unnormalized importance weight
$\check{w}_n$	Unnormalized incremental weigth
$q_{\mathsf{x}}(\boldsymbol{x})$	Importance distribution
$\pi_t(\boldsymbol{x})$	Target density
Z_t	Normalizing constant
$\gamma_t(\boldsymbol{x})$	Normalized $\pi_t(\boldsymbol{x})$
λ_n	Transition parameter
$\iota(\boldsymbol{x})$	Initial tractable distribution
$\tilde{\gamma}_n(\boldsymbol{x}_{1:n})$	Auxiliary distribution defined on extended space
$L_k(\boldsymbol{x}_{k+1}, \boldsymbol{x}_k)$	Backward Markov kernel
$K_k(\boldsymbol{x}_{k-1}, \boldsymbol{x}_k)$	Forward Markov kernel
$\eta(\boldsymbol{x}^*\|\boldsymbol{x}_n^{(i)})$	Proposal distribution
$\alpha(\boldsymbol{x}^*, \boldsymbol{x}_{n-1})$	Acceptance ratio
$\phi_j(\boldsymbol{x})$	Multivariate orthogonal polynomials
w_j	Weight of polynomial j
δ_{ij}	Kronecker delta
$\boldsymbol{x}^{(s)}$	Quadrature or sampling points
$q^{(s)}$	Quadrature weights
N_s	Number of quadrature points
$\boldsymbol{Q}$	Weight matrix
$\boldsymbol{x}^{(i)'}$	i-th simulation design point
$\tilde{m}(\boldsymbol{x}; \hat{\boldsymbol{\theta}}_m)$	Posterior mean function of GP surrogate
$\tilde{k}(\boldsymbol{x}, \boldsymbol{x}'; \hat{\boldsymbol{\theta}}_k)$	Posterior covariance function of GP surrogate
$\hat{\boldsymbol{\theta}} = [\hat{\boldsymbol{\theta}}_m, \hat{\boldsymbol{\theta}}_k]$	Hyper-parameters of GP surrogate

$\tilde{m}^{(\mathrm{j})'}(\boldsymbol{x})$	Posterior mean of GP using simulation design points
$\tilde{k}^{(\mathrm{j})'}(\boldsymbol{x}, \boldsymbol{x}')$	Posterior covariance of GP using simulation design points
M	Mean of y
$\hat{M}$	Estimate of mean of y based on GP surrogate
$\hat{\sigma}^2_{\hat{M}}$	Variance of mean of y due to code uncertainty in GP
$M_{f^{(\mathrm{j})}_{\mathrm{GP}}}$	Mean of y based on $j-$th realization of posterior GP
q	Quantile of y
$q_{f^{(\mathrm{j})}_{\mathrm{GP}}}$	Quantile of y based on $j-$th realization of posterior GP
V	Variance of y
$V_{f^{(\mathrm{j})}_{\mathrm{GP}}}$	Variance of y based on $j-$th realization of posterior GP
$\mathsf{F}_{\mathsf{y}}(y)$	CDF of y
$F^{(\mathrm{j})}_{\mathsf{y}}(y)$	CDF of y based on $j-$th realization of posterior GP
$\hat{F}_{\mathsf{y}}(y)$	Mean of $\hat{F}_{\mathsf{y}}$ based on GP surrogate

Bayesian Multi Fidelity Monte Carlo

$y_{\mathrm{hi-fi}}$	Quantity of interest computed with high-fidelity model
$y_{\mathrm{lo-fi}}$	Quantity of interest computed with low-fidelity model
z	Vector of uncertain model input parameters
$\boldsymbol{\theta}(\omega)$	Vector of parameters of regression function
$p_{\boldsymbol{\theta}}(\boldsymbol{\theta})$	Prior density of regression model parameters
$\pi_{\boldsymbol{\theta}}(\boldsymbol{\theta})$	Posterior density of regression model parameters
${\sigma_\epsilon}^2(\omega)$	Variance of the noise term
$\hat{\pi}(y_{\mathrm{hi-fi}})$	Posterior mean estimate of probability density of $y_{\mathrm{hi-fi}}$
$\pi(\boldsymbol{\theta}, \sigma^2_\epsilon)$	Joint posterior density of $\boldsymbol{\theta}(\omega)$ and ${\sigma_\epsilon}^2(\omega)$
N_{SAM}	Number of samples
$N_{\mathrm{particles}}$	Number of particles
N_{real}	Number of GP realizations
$W^{(i)}$	Importance weight
$\Phi(\cdot)$	Standard normal CDF
y_0	Failure threshold
$H(\cdot)$	Heavyside function
$q_{\mathcal{A}}(y_{\mathrm{lo-fi}}, \boldsymbol{\theta}, \sigma_\epsilon)$	Probability of $y_{\mathrm{hi-fi}} \in \mathcal{A}$, given $y_{\mathrm{lo-fi}}, \boldsymbol{\theta}$, and σ_ϵ
$\hat{q}_{\mathcal{A}}(y_{\mathrm{lo-fi}})$	Expected value of $q_{\mathcal{A}}(y_{\mathrm{lo-fi}}, \boldsymbol{\theta}, \sigma_\epsilon)$ with respect to $\boldsymbol{\theta}$ and σ_ϵ
$q_{\mathcal{A},0.01}$, $q_{\mathcal{A},0.99}$	1% and 99% quantile of $q_{\mathcal{A}}$
γ	Continuation parameter
λ	Load factor
$\boldsymbol{p}$	Vector containing element wise constitutive parametres
$\boldsymbol{d}^{(1)}$	Nodal displacements corresponding to $\boldsymbol{p}^{(1)}$

Experimental measured quantities of aneurysm wall

σ_{max}	Failure strength
T_{max}	Failure tension
F_{max}	Maximum recorded force
A_0	Initial cross-sectional area of tensile test specimen
b_0	Tensile test specimen width
t	Wall thickness
t_{ILT}	ILT thickness
d_{bif}	Distance to bifurcation
$\tilde{\rho}$	Correlation coefficient between adjacent tensile test specimens
$\tilde{\boldsymbol{\tau}}$	Distance between tensile test specimens

Models of abdominal aortic aneurysms

c	Stiffness parameter of ILT
c_{lum}	ILT stiffness luminal layer
c_{med}	ILT stiffness medial layer
c_{ablum}	ILT stiffness abluminal layer
η	Empirical coefficient
κ	Bulk modulus
ν	Poisson ratio
α, β	Stiffness parameters of arterial wall
μ_β	Location parameter of the probability distribution of β
σ_β	Scale parameter of the probability distribution of β
t	Wall thickness
μ_t	Location parameter of the probability distribution of t
σ_t	Scale parameter of the probability distribution of t
$t_{\text{stoch}}(\boldsymbol{x}, \mathbf{z})$	Stochastic wall thickness
t_{const}	Deterministic, constant wall thickness
$\boldsymbol{\sigma}^{(i)}_{t_{\text{stoch}}}(\boldsymbol{x})$	Stresses based on stochastic wall thickness
σ_{max}	Maximum wall stress
σ_{fail}	Failure threshold

Models of the human lung

C,I,R	Capacitive, inductive, and resistive component
$N_{\mathrm{adj},i}$	Number of adjacent acini or pleural spaces for acinus i
P_{in},P_{out}	Pressure at airway in- and outlet
P_{a}	Acinar pressure
P_{pl}	Pleural pressure
P_{t}	Pressure at tracheal inlet
P_{intr}	Inter-acinar pressure
Q_{in},Q_{out}	Flow rate at airway in- and outlet
$V_{\mathrm{a,0}}$	Initial acinus volume
V_{a}	Current acinus volume
$V_{\mathrm{CP_p}}$	Percentile vital capacitance
V	Lung volume
V_{R}	Residual volume of the lung
V_{TLC}	Total lung capacitance
V_{tidal}	Tidal volume
κ	Acinar stiffness parameter
κ_0	Baseline acinar stiffness
μ_κ	Location parameter of the probability distribution of κ
σ_κ	Scale parameter of the probability distribution of κ
$\varepsilon_{\mathrm{vol}}$	Volumetric acinar strain
$\varepsilon_{\mathrm{vol,max}}$	Maximum volumetric acinar strain

Abbreviations

AAA	Abdominal aortic aneurysm
ADP	Adenosine diphosphate
ALI	Acute lung injury
ARDS	Acute respiratory distress syndrome
BMFMC	Bayesian multi-fidelity Monte Carlo
CHD	Coronary heart disease
DM	Diabetes mellitus
CDF	Cumulative distribution function
CKD	Chronic kidney disease
COV	Coefficient of variation
CT	Computed tomography
EELV	End-expiratory lung volume
EGFR	Estimated glomerular filtration rate
ESS	Effective sample size
EVAR	Endovascular aneurysm repair
FFT	Fast Fourier transform
FORM	First order reliability method
GP	Gaussian Process
IBVP	Initial boundary value problem
ILT	Intra Luminal Thrombus
IS	Importance sampling
LHS	Latin hypercube sampling
LOOCV	Leave-one-out cross-validation
MAP	Maximum a Posterior
MC	Monte Carlo
MCH	Mean corpuscular hemoglobin
MCHC	Mean corpuscular hemoglobin concentration
MCMC	Markov Chain Monte Carlo
MCV	Mean corpuscular volume
MLMC	Multi-Level Monte Carlo
MULF	Modified updated lagrangian formulation
NORD	Local normalized diameter
OR	Open surgical repair
PCE	Polynomial chaos expansion
PDE	Partial differential equation
PDF	Probability density function
PEEP	Positive end-expiratory pressure
PMF	Probability mass function
PSD	Power spectral density
PSMSE	Patient standardized mean square error
PVD	Peripheral vascular disease

RMSE	Root mean square error
RPI	Rupture Potential Index
R&V	Raghavan & Vorp material model
SD	Standard deviation
SEF	Strain energy function
SMC	Sequential Monte Carlo
SMSE	Standardized mean square error
SORM	Second order reliability method
UQ	Uncertainty Quantification
VDG	Vande Geest Model
VILI	Ventilatory Associated Lung Injury

1 Introduction

1.1 Motivation and background

Methodological advances in computational biomechanics in combination with the advent of relatively cheap high-performance computing platforms have led to a tremendous improvement of computational models for various biomechanical systems, biophysiological processes, and diseases. These computational models have in turn led to an improved understanding of the systems and processes under investigation. Many challenging biomechanical problems have been addressed by researchers in recent decades such as establishing models for the full cardiovascular system or specific parts thereof [11, 42, 104, 247, 335]. Many aspects of cardiovascular diseases, e.g., coronary artery stenosis [324] or aneurysms both aortic [102, 103, 109, 203] and cerebral [168, 276, 293], can be nowadays assessed using computational tools. Another prominent example are computational models of the human respiratory system [163]. Of course, many other applications of computational tools in medicine exist. Aside from diagnosis and assessment of diseases, computational models are of course also used for the development and design of medical devices and surgical procedures.

As these computational models mature to the verge of clinical application [91], the predictive capabilities of the computational models becomes increasingly important. The term predictive is used here in the sense that incomplete and often inaccurate information about the problems of interest is accounted for, and that, moreover, error bars or probability distributions are provided as simulation results rather than deterministic values. In addition, as pointed out previously by Chen et al. [61] and Kennedy and O'Hagan [174], uncertainty is introduced also by the often ambiguous choice of mathematical models and applied boundary conditions, which will affect the simulation results as well.

Although the need for predictive models applies also in many, if not all, other engineering disciplines, predictive computational models are particularly important in many biomedical applications for several reasons. First of all, faulty or wrong predictions made by computational models can have dire consequences for patients. Second, many of the model input parameters cannot be precisely measured or assessed with the accuracy that is standard in many of the more classical engineering problems. In addition, many of these parameters intrinsically vary within and between patients and are also significantly affected by lifestyle, age, and diseases, which lead to further substantial variations. Third, computational simulation models have surpassed experimental capabilities and meaningful experimental tests to validate or calibrate complex computational models are often difficult or impossible to perform.

However, often when truly patient-specific data are inaccessible assumptions about these parameters are made, or population-averaged values are used. The difference between the actual patient-specific values and any assumed or averaged values in the input parameters in a deterministic model of course translates to uncertainty or potential error in the computed quantities.

Therefore, in absence of truly patient-specific parameters, it is extremely important to be aware of the uncertainty in population averaged or assumed patient-specific model parameters. In lack of true patient-specific values, these uncertainties should be incorporated into the computational model to quantify the impact of the uncertainty on the computed results and to obtain more reliable predictions or worst-case scenarios. The identification and quantification of the uncertainties in the computational results will help to assess the margin of error of simulation results due to uncertain model parameters, thus enabling estimates on the accuracy of deterministic models. This is particularly important if computational models are, ultimately, to be incorporated in the clinical decision process, e.g, for diagnostic purposes of cardiovascular diseases, or to obtain recommendations for prevention and treatment of individual patients. In any of these scenarios it is crucial to take the aforementioned uncertainties and incomplete information into account.

The predictive capabilities of computational models can be significantly improved if a probabilistic point of view is adopted and the uncertainties in the input parameters are accounted for in the model. Identification and quantification of these uncertainties will inevitably lead to more accurate simulations but also to a deeper understanding of the investigated systems, physiological processes, or diseases, and also bring to light limitations of existing models. Therefore, the development and application of efficient computational approaches for uncertainty quantification (UQ) is crucial for the advance of numerical models of biomechanical systems to clinical research and, ultimately, to clinical application.

The predictive error or uncertainty in todays computational models can be attributed to various causes. In order to recognize and analyze the different components a taxonomy of uncertainties in computational models according to [174, 240] is introduced here.

- **Parametric uncertainty** The first major source of uncertainty is referred to as *parametric uncertainty*. Often there is uncertainty about the values of certain model input parameters such as physical input parameters like stiffness, porosity, permeability, diffusivity, etc.. Frequently, the boundary conditions are also subject to uncertainty. In the context of biomechanical models this includes, e.g., the blood pressure or in- and outflow conditions in the form of velocity profiles. Another source of uncertainty are uncertain (computational) geometries. In biomedical application model geometries are often reconstructed from medical image data, the resolution of which is often not sufficient to extract all relevant geometric features of the model.

- **Model inadequacy** In the sense that "all models are wrong, but some are useful" (George E. P. Box) simulating a real world system or process by means of computational models will likely yield a difference between model prediction and truth, even if all input parameters were known exactly and no parametric uncertainty existed. This discrepancy is referred to as model inadequacy.

- **Residual variability** Suppose a model predicts a specific system response for a given set of parameters and conditions. However, in reality the system response might not always be the same although the same parameters and conditions hold. This might be due to an inherent randomness of the system or due to model inadequacy because the chosen set of parameters and conditions do not fully capture or describe the system. This variability is referred to as residual variability in [174].

- **Code uncertainty** This uncertainty results from the fact that a computational model usually cannot be evaluated at all possible combination of input parameters that are of interest. Examples for this kind of uncertainty are sampling errors or interpolation errors if the model output for some input configuration is interpolated from the model output of other input configurations.

The identification and propagation of these uncertainties is difficult and no unified mathematical approach exists to address all types of uncertainty described above in a consistent and efficient manner. The focus of this work are parametric uncertainties as described above and their efficient propagation through complex computational models. The quantification of this kind of uncertainty has received a lot of attention amongst researchers, scientists, and engineers in the last two decades, which has lead to marked progress. However, even though the importance of reliable, predictive simulations is generally acknowledged in the biomechanics community, the amount of research regarding UQ and sensitivity analysis in combination with biomedical problems is very limited, so far. In the context of cardiovascular models, only few scientist have started to address the issue of uncertain model input parameters by means of UQ.

When speaking of parametric uncertainties, literature often distinguishes between *aleatory*, i.e., truly random irreducible uncertainty, and *epistemic* uncertainty, which describes uncertainty due to lack of knowledge or data. Epistemic uncertainty is also often referred to as reducible uncertainty. However, an exact discrimination and definition of these two types is often difficult and the border between aleatory and epistemic is blurred [82, 240]. When trying to distinguish between aleatory and epistemic uncertainty one quickly winds up in a philosophical debate whether such a thing as true randomness exists.

Anyway, the uncertainties considered in this work are essentially epistemic since the predominant problem in biomechanical models is rather a lack of knowledge, i.e., the values for a parameter of a specific patient are not known, than parameters being truly random. Mostly, the problem is rooted in not being able to determine model input parameters in a non-invasive fashion. Thus, roughly speaking, the systems and models considered in this work are not truly random but treated as random because the exact values of the parameters of the model for a specific patient are not known. To this end, a Bayesian view of probability is adopted in this work, i.e., probability is used as a vehicle to formulate statements about degrees of belief or to represent a state of knowledge rather than a frequency of some phenomenon or parameter.

The main goal of this work is the development of a comprehensive UQ framework, which allows the treatment of complex, large-scale, non-linear models. In addition, the approach should be able to cope with high-stochastic dimension, i.e, many random input parameters. The example problems that the developed framework is predominantly applied to in this work are patient-specific models of abdominal aortic aneurysms (AAAs). Hence, before the aim, objectives, and outline of this work are explained, the reader is provided with the necessary background information about AAAs and engineering approaches regarding the assessment of the disease.

Abdominal aortic aneurysm are permanent balloon like dilatations of the aorta between the renal arteries and the aortic bifurcation. An example of an AAA is shown in Figure 1.1. In the majority of the cases, this enlargement of the aorta is accompanied by the formation of *intraluminal trombus* (ILT) as a product of blood coagulation [143]. Due to the relatively high prevalence (4% - 8% in men and 0.5%-1.5% in women [190, 191, 195, 231, 343]) in the population and the high-mortality rate in case an AAA ruptures, AAA are amongst the leading causes

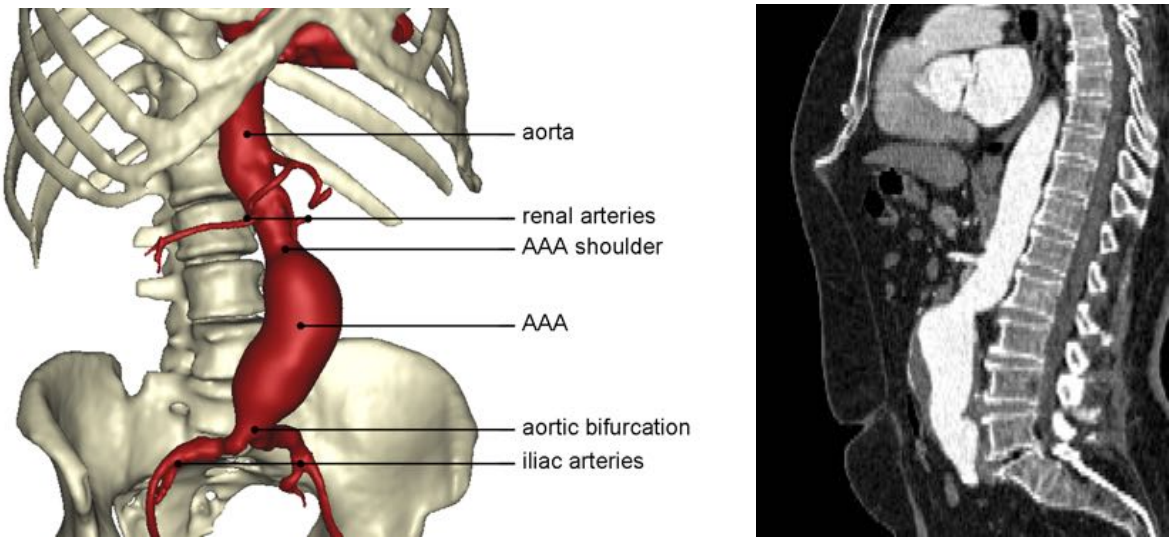

(a) Three-dimensional reconstruction of an AAA.

(b) Computed tomography image (sagittal view) of an AAA.

Figure 1.1 Infrarenal abdominal aortic aneurysm. Figure taken from [202].

of death in the elder population. Clinically, AAAs can be categorized into asymptomatic, symptomatic, and ruptured AAAs. The vast majority of all AAAs are asymptomatic and their discovery is often coincidental, although many countries have introduced screening programs to detect AAAs at an early stage. Symptomatic AAAs, characterized by sudden pain in the abdomen or back, are a clear indication for surgical intervention, because 90% of all symptomatic AAAs rupture within 2 years if left untreated [222]. Ruptured AAAs present a severe cardiovascular emergency, which requires immediate surgical treatment. The prognosis of ruptured AAAs is grim with roughly 90% of the patients dying before reaching the hospital [285, 372]. Even if the patient is in the hospital at the time of rupture and can be treated right away, mortality rates are still 48% on average [47].

For asymptomatic AAAs the indication for surgical intervention is not so clear. Amongst other risk factors discussed in literature such as female gender [52, 84], hyper tension [51], smoking [256], family history of AAA [187], geometry of the AAA [349], or large amounts of ILT [143], the size of the aneurysm, usually in form of the maximum diameter serves as major indicator of rupture risk. Epidemiological studies, such as the UK small aneurysm trial [51] relate the diameter of an aneurysm to the annual rupture risk. According to [51] AAAs have a 0.3 % annual risk of rupture if the diameter is smaller than 4.0 cm. As the aneurysm gets larger, the risk of rupture increases. Aneurysms with a diameter between 4.0 to 4.9 cm are reported to have 1.5% annual risk of rupture, whereas aneurysms between 5.0 to 5.9 cm have a 6.5% annual risk of rupture. For larger aneurysms the annual risk of rupture rises markedly.

There are two treatment options for AAA open surgical repair (OR) and endovascular repair (EVAR). OR is a highly invasive technique where a prosthesis is used to replace the bulged and weakened section of the aorta in an open surgical intervention. In contrast, EVAR entails the minimal invasive deployment of a stent-graft across the aneurysm through the iliac arteries by means of a catheter. Each of the methods has its indication and distinctive advantages and

disadvantages but both techniques are associated with significant mortal risk for the patient. In the short term, 30-day mortality rates are clearly in favor of the EVAR treatment, with mortality rates between 1.6 % and 1.2 % for endovascular repair and a mortality rate of 4.6% for OR [129, 258], respectively. However, studies investigating long term effects question these benefits [39, 130], as endovascular repairs require more secondary intervention due to endoleakage, migration, or other graft-related complications. In any case, surgical intervention can not be considered risk free and the risk associated with surgical intervention has to be balanced with the risk of rupture.

To date clinicians mainly rely on statistical rupture risk indicators such as the diameter of the AAA. Guidelines indicate 5.5 cm as threshold for surgical intervention [49]. From a mechanical point of view, the diameter criterion can be interpreted as very crude mechanical model for the wall stress within an AAA. Based on the law of Laplace, the wall stress in a cylindrical tube is proportional to the radius, given constant wall thickness and pressure. Thus, the diameter can be used as a proxy for the wall stress. Obviously, this very simple model does not provide good estimates for the wall stress in complex patient-specific AAA geometries, nor can it account for ILT.

Based on the notion that rupture of an aneurysm is a mechanical phenomenon that occurs if local wall load exceeds the local wall strength, researchers have started to conceive more elaborate models to predict wall loading in AAA. Specifically, computational finite element models have been used to assess mechanical quantities such as wall stress. In several retrospective studies AAA wall stress and other biomechanical factors, e.g., rupture risk indices [109, 340] have been related to AAA rupture potential. Moreover, it has been shown that these biomechanical factors are able to discriminate better than the diameter criterion between ruptured and non-ruptured AAAs for diameter matched groups of ruptured and non-ruptured AAAs [100, 109, 203].

Most of the finite element models used to assess AAA rupture potential are based on a solid mechanics approach. It is refrained from the term rupture risk in this context because the computational models typically do not provide a rupture risk in the stochastic sense, i.e., a probability of rupture, but only a mechanical quantity which shows a statistical correlation to the risk of rupture. Thereby, models have been gradually refined to include nonlinear materials, calcifications, and anisotropic wall materials. Many of the models used to determine AAA rupture potential are based on a stress measure or on stress divided by a wall strength. This quotient is frequently referred to as rupture potential index or rupture risk index [109, 340]. However, there is still a debate about the most suitable failure criterion for aneurysmatic arterial wall in literature. Strain and strain-energy based failure models have been proposed in addition to stress based measures [206, 345–347]. Other researchers strive to include growth and remodelling phenomena into their models. Moving away from ”snap-shots” trying to capture the current mechanical state of the aneurysm, computational growth and remodelling approaches aim at modelling the dynamic mechanobiological process governing aneurysm formation, enlargement and eventually rupture [10, 161, 185, 347].

In any case, all of the models mentioned above require a multitude of patient-specific parameters, not all of which are directly or non-invasively measurable. If computational simulation models for AAAs are ever to be used in a clinical setting, these models obviously need to provide reliable predictions without requiring any additional invasive examinations to determine patient-specific model parameters. Unfortunately, many of the patient-specific parameters, e.g., the arterial wall thickness, constitutive parameters, wall strength, and boundary conditions, vary

significantly within and between patients. Thus, these parameters, although not truly random, are not exactly known when the simulation has to be performed. This essentially raises two questions, which this work attempts to answer, how to construct mathematical models for the uncertainties present in the various model parameters, and second how to efficiently propagate the uncertainties through the respective computational model.

1.2 Objectives and achievements

The goal of this work is the development of an efficient UQ framework which enables the propagation of uncertainties through nonlinear, large-scale, and patient-specific models. An additional challenge is the often very high stochastic dimension of the problems at hand in these circumstances. Although a major requirement to the developed framework is its general applicability, it is chiefly applied in this work to computational models of AAA as example application of complex patient-specific biomechanical models. The computational assessment of the mechanical state of AAAs is a particular suitable application because, the consequences of faulty predictions can have fatal ramifications. Hence, the provision of confidence intervals of all computed quantities or worst case estimates in face of parametric uncertainty is of paramount importance.

On the most abstract level, two major objectives can be formulated for this work: The first is the development of a methodological framework which allows the mathematical description of uncertainties in various model input parameters and their efficient propagation through complex, nonlinear models. The second is the application of this framework to exemplary model problems. Here, first and foremost computational models of AAAs are considered and the impact of uncertain input parameters on the relevant output quantities is investigated. However, models of the human lung are studied as well to demonstrate the general applicability of the framework.

Development of methods The challenge this work embarks on is the development of an UQ framework which allows efficient UQ in combination with complex, nonlinear and large-scale computational model and uncertainties which are best described by three-dimensional non-Gaussian random fields. The term large-scale computational model is used here to imply that the evaluation of these models requires a significant amount of computational resources, i.e., the solution takes hours our days on multiple processors.

In order to obtain meaningful results in an UQ analysis, an accurate mathematical description of the input uncertainties is needed. Because the first envisaged application of the developed framework are finite element models of AAAs, an accurate mathematical model for the input uncertainties in AAA models is needed. Therefore, a worldwide unique experimental dataset is used to construct probabilistic models with varying degrees of sophistication capable of capturing inter- as well as intra-patient variations of several parameters. Several probabilistic models are constructed using, amongst others, Bayesian regression techniques harnessing non-invasively assessable parameters from the dataset to obtain probabilistic, patient-specific predictions for model input parameters such as wall thickness, constitutive parameters, and failure measures with unprecedented accuracy.

The second step in an UQ analysis is the propagation of the uncertainties through the computational model. The development of an efficient framework for this task is one of the major

objectives of this work. The typically high stochastic dimension resulting from a random field description of the uncertain parameters render current non-sampling based UQ approaches infeasible. Moreover, the large nonlinear patient-specific finite element models prevent the use of sampling based schemes as these often require an exuberant amount of model evaluations. Thus, a framework based on a novel multi-fidelity UQ approach proposed by Koutsourelakis [183], which is referred to as Bayesian multi-fidelity Monte Carlo (BMFMC), is developed. More specifically, the approach incorporates information from approximate, low-fidelity models and, in combination with Bayesian formulations, is able to alleviate the computational burden that is posed even by advanced sampling based UQ methods. The use of a non-parametric Bayesian regression model allows to not only establish a quantitative connection between an approximate model and an accurate and expensive high-fidelity model, but also provides confidence intervals. Using this approach the cost of UQ for models with high-stochastic dimension can be significantly reduced, rendering UQ on a patient-specific basis possible also in clinical scenarios. Thereby, it is important to note that the proposed approach provides not only the first moments of the response, but also an estimate of the full probability distribution. In addition to the use of low-fidelity models, parameter continuation approaches are developed to exploit the problem structure of repeated forward model evaluations in order to further improve the overall efficiency of the UQ scheme.

Biomedical applications To demonstrate the capabilities and flexibility of the developed UQ framework, the multi-fidelity approach is applied to a range of challenging problems including patient-specific nonlinear finite element models of AAAs and reduced order models of the human lung. It is shown that the computational cost for UQ in patient-specific models can be reduced to the equivalent of only a moderate number of runs of the high-fidelity model. Furthermore, the developed framework speeds up the computation such that results can be obtained within one day even for large forward models. However, the purpose and variety of the considered example goes beyond mere demonstrative purposes. To the knowledge of the author, this is the first time that patient-specific AAA models are investigated while accounting for uncertainty in the parameters through three-dimensional random fields. The impact of several different parameters on mechanical quantities typically related to AAA rupture risk is investigated. Moreover, different probabilistic models are compared, e.g, in case of the wall thickness, where wall thickness models based on random fields are compared with a wall thickness model based on random variable.

1.3 Organization of this thesis

This thesis begins with a short summary of computational mechanics in Chapter 2. All aspects of relevance for the setup of computational solid mechanics models of AAAs are covered. Specifically, the basics of nonlinear continuum mechanics including hyper-elastic constitutive laws, finite element discretization schemes, and solution schemes for linear and nonlinear systems of equations are discussed. In addition, a method to account for prestressed cardiovascular structures is introduced.

The rather brief introduction to the fundamentals of the computational mechanics is followed by a more detailed introduction to probability theory and Bayesian statistics in Chapter 3. Since

the present thesis is the first work at the Institute for Computational Mechanics that deals with UQ, which requires a fair amount of probability theory, this Chapter provides an explanation of the relevant concepts of probability theory and Bayesian inference. First, the concepts of random variables and random processes are elaborated. Thereby, a special focus lies on the concept of Gaussian processes (GPs) and their unique properties, because extensive use of GPs is made throughout this work for various tasks. Most importantly, they from the underlying basis for many of the probabilistic models used for uncertain model input parameters in this work. Secondly, GPs are extensively used in this work for the purpose of regression. The description of the regression techniques used in this work comprise the second part of this Chapter. Here, the Bayesian interpretation of linear regression is provided before two more elaborate, non-parametric Bayesian techniques are explained.

Aside from providing the reader with a brief problem description and introduction to model based UQ, Chapter 4 is essentially a mixture between a literature review of existing, well known UQ methods and their limitations regarding applicability to large-scale nonlinear problems with high stochastic dimension, and a description of UQ techniques that are also used in this work. Sampling based UQ approaches like Monte Carlo (MC) and more advanced sampling based schemes are introduced, before some classic reliability and second order methods are briefly reviewed. Next, two particularly popular examples from the class of surrogate based UQ techniques are explained. Since GP based models are used in this work for low-dimensional UQ problems, greater emphasis is put on this methodology. Polynomial Chaos expansion (PCE) based approaches, being the second covered class of surrogate techniques, are also mentioned here because they are very popular in the engineering community and are frequently used to construct surrogate models for the purpose of UQ. The differences to the GP approach used in this work are discussed and PCE based surrogates are contemplated from a more statistical viewpoint.

After some general remarks on using models with different levels of fidelity, Chapter 5 contains a description of the developed BMFMC UQ framework, which allows the incorporation of information from low-fidelity model versions of the system under investigation to speed up the computation of the relevant statistical summaries. The details on how to compute high-fidelity solution statistics are followed by some remarks on the efficient implementation of the approach using nested parallelism and a parameter continuation scheme. Moreover, the relation to other multi-fidelity approaches, which have been recently proposed in literature, is discussed to provide some perspective.

Chapter 6, which is largely based on [33], deals with the construction of suitable probabilistic models for several mechanical parameters of the AAA wall. A brief review of mechanical modelling of aneurysmatic arterial wall is given before the implications of random variable and random field models are discussed. This is followed by a description of the developed techniques for the probabilistic prediction of mechanical wall parameters. These predictions can be either based on direct study population measurements of these parameters or on probabilistic predictions using additional non-invasively assessable explanatory variables in combination with Bayesian regression approaches. Furthermore, the extraction of suitable probabilistic models for several mechanical wall parameters from a large experimental dataset is described and the predictive capabilities of several techniques are compared.

In Chapter 7 the results from the previous Chapter are used to set up realistic stochastic models of AAAs. The uncertainties in the model input parameters are propagated through the

finite element models and the impact on mechanical output quantities such as wall stress, strain, or strain-energy is studied for several patient-specific AAA geometries. Thereby, Chapter 7 documents the application and performance of the developed BMFMC approach. As a first step towards fully probabilistic models of AAAs, models with uncertainties in wall thickness or one constitutive parameter are studied. However, as these parameters are modelled by random fields, the stochastic dimension of the considered problems is very high. In addition, it is demonstrated that the BMFMC approach can also handle problems with more than one random field in a proof of concept fashion. This chapter is based, in parts, on [32].

To show that the proposed framework is indeed very general and not limited to models of AAAs or only applicable to solid mechanics problems, the framework is used to perform UQ in combination with a reduced order model of the human lung in Chapter 8.

Chapter 9 provides the conclusion of this thesis and summarizes the most important results of the present work, ongoing work, and open questions. Also, some directions for future research are provided.

2 Computational solid mechanics

This chapter contains a brief summary of the fundamentals of nonlinear continuum mechanics, a description of the initial boundary value problem of nonlinear solid mechanics, and a short section about the corresponding finite element formulations and solution approaches for nonlinear systems of equations. In addition, a technique to account for prestress in structures such as AAAs is briefly explained. The chapter is by no means meant to be a thorough introduction to these topics, but merely presents the necessary armamentarium for the problems and examples considered in the following chapters of this thesis.

The number of different approaches one can take to briefly summarize the fundamental principles and to introduce all necessary quantities is limited, as the material itself dictates a more or less strict path. In the opinion of the author the approach taken by Popp [255] is well structured and sufficiently comprehensive, and hence the outline of this chapter follows the corresponding one in [255]. An abundant amount of literature exists, offering a more in depth treatment of both subjects. The reader is referred to, e.g., [43, 155, 207, 237] for an introduction to nonlinear solid mechanics and to, e.g., [159, 186, 363, 374] for a more detailed description of finite element solution schemes, respectively.

2.1 Nonlinear solid mechanics

2.1.1 Kinematics

The structures investigated in this work exhibit geometric as well as constitutive nonlinearities and thus have to be described using nonlinear continuum mechanics. Throughout this work it is assumed that the structure under consideration undergoes only elastic deformation. The following description is thus restricted to elastic deformations. In addition, a restriction to cartesian coordinates is made. The starting point is the definition of an bijective nonlinear deformation map Φ_t which describes the deformation and motion of the body from an undeformed reference configurations $\Omega_0 \subset \mathbb{R}^3$ to a deformed spatial configuration $\Omega_t \subset \mathbb{R}^3$

$$\Phi_t(\boldsymbol{X}) = \begin{cases} \Omega_0 & \rightarrow \Omega_t \\ \boldsymbol{X} & \rightarrow \boldsymbol{x} = \Phi_t(\boldsymbol{X}, t). \end{cases} \tag{2.1}$$

Therein, the coordinates of all points in the reference configuration at $t = 0$ are denoted by $\boldsymbol{X}$ and the changed positions at a generic time t are denoted by $\boldsymbol{x}$. The two tensors are connected via the displacement field $\boldsymbol{u}$, defined by

$$\boldsymbol{x}(\boldsymbol{X}, t) = \boldsymbol{X} + \boldsymbol{u}(\boldsymbol{X}, t). \tag{2.2}$$

The partial derivative of the current position vector field with respect to the reference coordinates is defined as *deformation gradient* $\boldsymbol{F}$, which serves as a fundamental measure for deformation

and strain

$$\boldsymbol{F} = \frac{\partial \boldsymbol{x}(\boldsymbol{X}, t)}{\partial \boldsymbol{X}} = \boldsymbol{I} + \frac{\partial \boldsymbol{u}(\boldsymbol{X}, t)}{\partial \boldsymbol{X}}. \tag{2.3}$$

Here, $\boldsymbol{I}$ denotes the second-order identity tensor. The definition of a mapping between an infinitesimal line element $\mathrm{d}\boldsymbol{X}$ in the reference configuration to the corresponding line element $\mathrm{d}\boldsymbol{x}$ in the current configuration, is the geometric interpretation of the deformation gradient $\boldsymbol{F}$

$$\mathrm{d}\boldsymbol{x} = \boldsymbol{F}\mathrm{d}\boldsymbol{X}. \tag{2.4}$$

Based on the assumption that the deformation is bijective and smooth, the inverse mapping of this so called *push-forward* operation can be obtained

$$\mathrm{d}\boldsymbol{X} = \boldsymbol{F}^{-1}\mathrm{d}\boldsymbol{x}, \tag{2.5}$$

where $\boldsymbol{F}^{-1}$ is the inverse of the deformation gradient $\boldsymbol{F}^{-1} = \frac{\partial \boldsymbol{X}}{\partial \boldsymbol{x}}$. The reverse mapping is generally referred to as *pull-back* operation. Moreover, the Jacobian determinant of the deformation is defined as:

$$J = \det(\boldsymbol{F}) > 0. \tag{2.6}$$

Due to the bijectivity and smoothness of the deformation, the determinant of the deformation gradient is always positive. The Jacobian can be used to define push-forward and pull-back operations for infinitesimal volume elements

$$\mathrm{d}V = \det \boldsymbol{F}\mathrm{d}V_0 = J\mathrm{d}V_0, \tag{2.7}$$

where $\mathrm{d}V_0$ and $\mathrm{d}V$ denote the volumes of an infinitesimal volume element in the reference configuration and current configuration, respectively. The push-forward operation for an infinitesimal area element is given by the following equation

$$\mathrm{d}A = J\boldsymbol{F}^{-T}\mathrm{d}A_0, \tag{2.8}$$

which is typically referred to as Nanson's formula. These relations can easily be obtained from the definition of deformation gradient.

Based on the deformation gradient, several objective measures of deformation and strain can be derived. Thereby, objective means that the measure is invariant under any superimposed rigid body motion. First, the *right Cauchy-Green tensor* is defined as

$$\boldsymbol{C} = \boldsymbol{F}^T\boldsymbol{F}. \tag{2.9}$$

On the basis of $\boldsymbol{C}$, the so-called *Green-Lagrange strain tensor* can be computed using

$$\boldsymbol{E} = \frac{1}{2}(\boldsymbol{C} - \boldsymbol{1}). \tag{2.10}$$

The symmetric Green-Lagrange strain tensor is a widely used strain measure in nonlinear continuum mechanics. Both, the right Cauchy-Green and the Green-Lagrange tensor are defined in the reference configuration. Deformation measures which are related to the spatial configuration can also be derived based the deformation gradient $\boldsymbol{F}$. Using the *left Cauchy-Green deformation tensor* $\boldsymbol{b}$, which is defined as

$$\boldsymbol{b} = \boldsymbol{F}\boldsymbol{F}^T, \tag{2.11}$$

the *Euler-Almansi strain tensor* can be calculated by

$$\boldsymbol{e} = \frac{1}{2}\left(\mathbf{1} - \boldsymbol{b}^{-1}\right). \tag{2.12}$$

Similar to the Green-Lagrange strain tensor, the Euler-Almansi strains tensor is an objective measure for finite strains. In contrast to the Green-Lagrange strains, the Euler-Almansi strain tensor is defined with respect to the spatial configuration. Both tensors share the same so-called *principal invariants*, which are often used for the formulation of nonlinear constitutive laws. The three invariants I_1, I_2, and I_3 are defined as follows:

$$I_1 = I_1(\boldsymbol{C}) = I_1(\boldsymbol{b}) = \text{tr}\boldsymbol{C}, \tag{2.13}$$

$$I_2 = I_2(\boldsymbol{C}) = I_2(\boldsymbol{b}) = \frac{1}{2}\left[(\text{tr}\boldsymbol{C})^2 - \text{tr}(\boldsymbol{C}^2)\right], \tag{2.14}$$

$$I_3 = I_3(\boldsymbol{C}) = I_3(\boldsymbol{b}) = \det \boldsymbol{C} = J^2. \tag{2.15}$$

For the formulation of nonlinear constitutive laws it is sometimes helpful to split the deformation into a *volumetric* (volume-changing) part and an *isochoric* (volume-preserving) part [155, 237]. To achieve this separation of volumetric and isochoric deformation, a multiplicative split of the deformation gradient is performed

$$\boldsymbol{F} = \boldsymbol{F}_{\text{vol}}\bar{\boldsymbol{F}}, \tag{2.16}$$

therein $\boldsymbol{F}_{\text{vol}} = J^{\frac{1}{3}}\boldsymbol{I}$ denotes the volumetric part and $\bar{\boldsymbol{F}} = J^{-\frac{1}{3}}\boldsymbol{F}$ the isochoric part of the deformation gradient, respectively. Since the isochoric part is volume preserving:

$$\bar{J} = \det \bar{\boldsymbol{F}} = 1. \tag{2.17}$$

Naturally, isochoric and volumetric parts of other deformation measures can be computed as well. For instance, the right Cauchy-Green tensor can be decomposed into

$$\boldsymbol{C} = \boldsymbol{C}_{\text{vol}}\bar{\boldsymbol{C}}, \tag{2.18}$$

with volumetric ($\boldsymbol{C}_{\text{vol}}$) and isochoric ($\bar{\boldsymbol{C}}$) part defined as

$$\boldsymbol{C}_{\text{vol}} = J^{\frac{2}{3}}\boldsymbol{I} \quad \text{and} \quad \bar{\boldsymbol{C}} = J^{-\frac{2}{3}}\boldsymbol{C}. \tag{2.19}$$

Based on $\bar{\boldsymbol{C}}$ the so-called *modified invariants* can be computed

$$\bar{I}_1 = J^{-\frac{2}{3}}I_1, \quad \bar{I}_2 = J^{-\frac{4}{3}}I_2, \quad \bar{I}_3 = \det \bar{\boldsymbol{C}} = 1. \tag{2.20}$$

Note that by definition, $\bar{I}_3$ is always equal to one since the isochoric part of the deformation is volume preserving.

2.1.2 Stress measures

Deformation of an elastic body results in internal stresses, which are a measured in the physical unit of force per unit area. Several stress measures exist since the acting force as well as the area can be defined in either the current or the reference configuration. The starting point in the current configuration is the definition of a traction vector $\boldsymbol{t}(\boldsymbol{x}, \boldsymbol{n}, t)$, which is defined as the limit of a resulting force $\boldsymbol{f}$ acting on a surface element ΔA with unit outward normal vector $\boldsymbol{n}$

$$\boldsymbol{t}(\boldsymbol{x}, \boldsymbol{n}, t) = \lim_{\Delta a \to 0} \frac{\Delta \boldsymbol{f}}{\Delta A} = \frac{d\boldsymbol{f}}{da}. \tag{2.21}$$

Then, Cauchy's stress theorem postulates the existence of a unique second order tensor field, the so-called *Cauchy stress tensor* as follows

$$\boldsymbol{t} = \boldsymbol{\sigma} \cdot \boldsymbol{n}. \tag{2.22}$$

The Cauchy stress tensor $\boldsymbol{\sigma}$ is defined in the a priori unknown deformed, current configuration and can be interpreted as true internal stress, in the sense of a spatial acting force $\boldsymbol{f}$ per unit surface area in the current configuration. The Cauchy stress tensor is symmetric and admits the interpretation of its diagonal terms as normal stresses and of its off-diagonal terms as shear stresses. Using the previously defined pull-pack operations for line and surface elements, one can derive two other common stress measures, namely the *first* and *second Piola-Kirchhoff stress tensor*. In contrast to the Cauchy stress, which relates spatial acting force to unit surface area in the current configuration, the unsymmetric first Piola-Kirchhoff stress tensor $\boldsymbol{P}$ relates the spatial acting force to a surface element in the reference configuration. It is obtained from the Cauchy stress tensor by applying Nanson's formula, i.e., (2.8), yielding

$$\boldsymbol{P} = J\boldsymbol{\sigma}\boldsymbol{F}^{-T}. \tag{2.23}$$

If, in addition, the force $\boldsymbol{f}$ is pulled back into the reference configuration using (2.4), the second Piola-Kirchhoff stress tensor $\boldsymbol{S}$ is obtained

$$\boldsymbol{S} = J\boldsymbol{F}^{-1}\boldsymbol{\sigma}\boldsymbol{F}^{-T}. \tag{2.24}$$

Like the Cauchy stress tensor, the second Piola-Kirchhoff tensor is symmetric. In contrast, it lacks the clear engineering interpretation of $\boldsymbol{\sigma}$ due to the performed pull-back operations. However, it is often very useful in computational mechanics and frequently used for the formulation of constitutive laws for solids. Various strain and stress measures exist; however, they cannot be combined in an arbitrary fashion, but so-called *energy-conjugate pairs* of strain and stress measures have to be used [43], meaning that they deliver identical strain-energies and virtual works. For the stress and strain measures introduced so far, the following pairs arise: $\{\boldsymbol{S}, \boldsymbol{E}\}$, $\{\boldsymbol{P}, \boldsymbol{F}\}$, and $\{\boldsymbol{\sigma}, \boldsymbol{e}\}$.

2.1.3 Constitutive laws for nonlinear elasticity

Having introduced strain as a measure for deformation and stress, the constitutive law provides the missing link between the two. For purely elastic deformation, the constitutive law allows the calculation of the stress tensor solely based on the current deformation state of the

solid body. Restricting considerations to hyper-elastic materials, the stress tensor can be derived from a scalar potential function Ψ, which is called *strain-energy function* (SEF). Using Green-Lagrange strains and the energy-conjugate second Piola-Kirchhoff stresses, the typically nonlinear relationship between strain and stress is defined by

$$\boldsymbol{S} = \frac{\partial \Psi}{\partial \boldsymbol{E}} = 2\frac{\partial \Psi}{\partial \boldsymbol{C}}. \tag{2.25}$$

Of course, this relationship can be formulated for other energy-conjugate pairs of strains and stresses as well [155].

During the course of a computational solution of the initial boundary value problem, which will be defined in Section 2.1.4, a linearized constitutive equation is required. For this, one needs the fourth oder elasticity tensor $\mathbb{C}$, which can be computed using

$$\mathbb{C} = \frac{\partial^2 \Psi}{\partial \boldsymbol{E} \partial \boldsymbol{E}} = 4\frac{\partial^2 \Psi}{\partial \boldsymbol{C} \partial \boldsymbol{C}}. \tag{2.26}$$

For isotropic materials the strain energy function can equivalently be expressed in terms of the first three invariants of $\boldsymbol{C}$, as defined in (2.14)

$$\Psi = \Psi(I_1(\boldsymbol{C}), I_2(\boldsymbol{C}), I_3(\boldsymbol{C})). \tag{2.27}$$

In case of anisotropic materials, additional invariants have to be considered. Based on the split of the deformation into an isochoric and a volumetric part, it is also possible to formulate constitutive laws where isochoric and volumetric contributions are decoupled [43, 237, 304]. This split of the constitutive laws allows for a separate treatment of bulk and shear stiffness of the solid. Moreover, this split is often employed to model *nearly incompressible* solids. The term nearly incompressible is used here for materials which are, in fact, incompressible; however, their numerical treatment is facilitated if the incompressibility condition is slightly relaxed and small volumetric deformations are admissible [43]. In this work, nearly incompressible formulations are used to model the constitutive behaviour of soft biological tissue, which is generally considered to be incompressible. Using the modified invariants computed from $\bar{\boldsymbol{C}}$, the strain-energy is split in two parts

$$\Psi(\bar{I}_1, \bar{I}_2, J) = \Psi_{\text{iso}}(\bar{I}_1, \bar{I}_2) + \Psi_{\text{vol}}(J). \tag{2.28}$$

Dependence on $\bar{I}_3$ is omitted, since it is always equal to one by definition and thus does not contribute to the strain-energy. In case of heterogenous materials, the strain energy function may, in addition to $\boldsymbol{C}$ or the invariants, also depend on the location in the solid, i.e., $\Psi(\boldsymbol{C}, \boldsymbol{X})$. In order to constitute a valid strain-energy function and thus constitutive law, Ψ must fulfill several conditions. Firstly, the stored strain-energy must be positive for any deformation state. Under the assumption that there are no residual stresses, i.e., that the reference configuration is stress free, the strain-energy function at $\boldsymbol{C} = \boldsymbol{I}$ has to fulfill $\Psi(\boldsymbol{C} = \boldsymbol{I}) = 0$. Moreover, the SEF has to be objective, meaning that the SEF must be independent from any superimposed rigid body translations or rotations. Lastly, the functional form of the SEF has to be such that it fulfills what is generally referred to as *polyconvexity*. See, e.g., [24, 207] for an in depth discussion of this subject.

2.1.4 Initial boundary value problem

Having introduced the basic notation for kinematics, stresses, and constitutive laws in the previous section, this section introduces the *initial boundary value problem* (IBVP) for solid mechanics, which arises as a consequence of the balance equations for linear and angular momentum, mechanical energy, and conservation of mass. Since growth and remodeling processes or material degradation are not considered in this work, conservation of mass is always fulfilled and hence will not be further dwelled upon. Moreover, the balance of mechanical energy reduces to a consequence of the balance of linear momentum for purely mechanical systems, in other words, no other kind of energy such as thermal or electrical energy is taken into consideration. Thus, the balance of mechanical energy does not provide extra information in addition to the balance of linear momentum. The balance of linear momentum requires that the time derivative of linear momentum equals the sum of all external forces which act on the body. Similarly, the balance of angular momentum requires that the time derivative of the angular momentum with respect to a fixed point is equal to the sum of all external moments. Together with a set of initial and boundary conditions, the consequence of the balance of linear momentum comprises the IBVP, i.e., a set of coupled second-order partial differential equations (PDEs). These are given in the following with respect to the reference configuration; a formulation in spatial description can be derived as well. Note that the balance of angular momentum is automatically fulfilled by demanding symmetry of the stress tensor. The boundary $\partial\Omega_0$ of the domain Ω_0 is divided into two disjoint sets, Γ_u and Γ_σ. Thereby Γ_σ denotes the Neumann boundary on which tractions $\hat{\boldsymbol{t}}_0$ are prescribed. The other part represents the Dirichlet boundary where the displacements $\hat{\boldsymbol{u}}$ are prescribed

$$\Gamma_u \cup \Gamma_\sigma = \partial\Omega_0 \text{ and } \Gamma_u \cap \Gamma_\sigma = \emptyset. \tag{2.29}$$

The IBVP for nonlinear solid mechanic then reads:

$$\mathrm{Div}(\boldsymbol{F}\cdot\boldsymbol{S}) + \hat{\boldsymbol{b}}_0 = \rho_0\ddot{\boldsymbol{u}} \text{ in } \quad \Omega_0 \times [0,T], \tag{2.30}$$

$$\boldsymbol{u} = \hat{\boldsymbol{u}} \quad \text{on} \quad \Gamma_u \times [0,T], \tag{2.31}$$

$$\boldsymbol{P}\cdot\boldsymbol{N} = \hat{\boldsymbol{t}}_0 \quad \text{on} \quad \Gamma_\sigma \times [0,T]. \tag{2.32}$$

Where Div is the material divergence operator, the vector $\hat{\boldsymbol{b}}_0$ defines the body force, and ρ_0 denotes the density in the reference configuration. Moreover, T denotes the endpoint of the considered time interval. In addition to the boundary conditions defined in (2.31) and (2.32), initial conditions have to be specified as well

$$\boldsymbol{u}(\boldsymbol{X},0) = \hat{\boldsymbol{u}}_0 \text{ in } \Omega_0, \tag{2.33}$$

$$\dot{\boldsymbol{u}}(\boldsymbol{X},0) = \hat{\dot{\boldsymbol{u}}}_0 \text{ in } \Omega_0. \tag{2.34}$$

In the equations above $\dot{\boldsymbol{u}}(\boldsymbol{X},t)$ and $\ddot{\boldsymbol{u}}(\boldsymbol{X},t)$ denote the first and second material time derivates of the displacements $\boldsymbol{u}(\boldsymbol{X},t)$, respectively. After choosing an appropriate constitutive law for the problem at hand, the definition of the IBVP is complete. The solution of this IBVP requires numerical approaches since a general analytic solution to this problem cannot be obtained. Only very few special cases admit an analytic solution; typically elementary geometries under additional restrictions regarding boundary conditions and constitutive law. The IBVP as given above is referred to as the *strong form* of the IBVP, since a point wise fulfillment of the balance of linear momentum is required. Using the method of weighted residuals, an alternative formulation

of the IBVP, the so-called *weak form*, can be derived. This weak form defines the starting point for the finite element methods, which allow a numerical treatment and solution of the problem.

2.2 Finite element formulations and solution schemes

While the strong form requires fulfillment of (2.30) to (2.32), an equivalent demand is that the weighted residual of these equations are zero. Choosing arbitrary weighting functions $\boldsymbol{w}$ and integrating the residuals over the respective domains yields

$$\int_{\Omega_0} (\mathrm{Div}(\boldsymbol{F}\cdot\boldsymbol{S}) + \hat{\boldsymbol{b}}_0 - \rho_0\ddot{\boldsymbol{u}})\cdot\boldsymbol{w}\,\mathrm{d}V_0 + \int_{\Gamma_\sigma} \hat{\boldsymbol{t}}_0 - (\boldsymbol{P}\cdot\boldsymbol{N})\cdot\boldsymbol{w}\,\mathrm{d}A_0 = 0. \tag{2.35}$$

Moreover, in order to fulfill the Dirichlet boundary conditions one has to ask for

$$\boldsymbol{w} = \boldsymbol{0} \text{ on } \Gamma_u \ \times [0,T]. \tag{2.36}$$

Applying the Gauss divergence theorem yields

$$\int_{\Omega_0} (\mathrm{Grad}\boldsymbol{w})^T \colon (\boldsymbol{F}\cdot\boldsymbol{S})\,\mathrm{d}V_0 - \int_{\Omega_0} \hat{\boldsymbol{b}}_0\cdot\boldsymbol{w}\,\mathrm{d}V_0 - \int_{\Omega_0} \rho_0\ddot{\boldsymbol{u}}\cdot\boldsymbol{w}\,\mathrm{d}V_0 - \int_{\Gamma_\sigma} \hat{\boldsymbol{t}}_0\cdot\boldsymbol{w}\,\mathrm{d}A_0 = 0, \tag{2.37}$$

which denotes the weak form of the IBVP. Therein, Grad is the material gradient operator.

It is important to note that the restatement of the IBVP above is completely equivalent to the strong form given in (2.30) and (2.32) if arbitrary weighting functions are admissible [159]. It is referred to as weak form because it poses weaker differentiability requirements to the solution functions $\boldsymbol{u}$, since only the first derivative of $\boldsymbol{u}$ with respect to $\boldsymbol{X}$ appears in (2.37), instead of the second as in (2.30). The weak form can be identified as the Principle of Virtual Work (PVW) if the weight functions are interpreted as virtual displacements. Replacing $\boldsymbol{w}$ with $\delta\boldsymbol{u}$ in (2.37) yields

$$\begin{aligned}\delta\mathscr{W} = &\int_{\Omega_0} (\mathrm{Grad}\delta\boldsymbol{u})^T \colon (\boldsymbol{F}\cdot\boldsymbol{S})\,\mathrm{d}V_0 \\ &- \int_{\Omega_0} \hat{\boldsymbol{b}}_0\cdot\delta\boldsymbol{u}\mathrm{d}V_0 - \int_{\Omega_0} \rho_0\ddot{\boldsymbol{u}}\cdot\delta\boldsymbol{u}\mathrm{d}V_0 - \int_{\Gamma_\sigma} \hat{\boldsymbol{t}}_0\cdot\delta\boldsymbol{u}\mathrm{d}A_0 = 0.\end{aligned} \tag{2.38}$$

Algebraic rearrangement allows the clear identification of three work contributions comprising the virtual work

$$\delta\mathscr{W} = \underbrace{\int_{\Omega_o} \rho_0\ddot{\boldsymbol{u}}\cdot\delta\boldsymbol{u}\,\mathrm{d}V_0}_{-\delta\mathscr{W}_{\text{kin}}} + \underbrace{\int_{\Omega_0} \boldsymbol{S}\colon\delta\boldsymbol{E}\,\mathrm{d}V_0}_{-\delta\mathscr{W}_{\text{int}}} \underbrace{- \int_{\Omega} \hat{\boldsymbol{b}}_0\cdot\delta\boldsymbol{u}\,\mathrm{d}V_0 - \int_{\Gamma_\sigma} \hat{\boldsymbol{t}}\cdot\delta\boldsymbol{u}\,\mathrm{d}A_0}_{-\delta\mathscr{W}_{\text{ext}}} = 0, \tag{2.39}$$

namely the kinetic virtual work contribution $\delta\mathscr{W}_{\text{kin}}$, the internal virtual work contribution $\delta\mathscr{W}_{\text{int}}$, and the virtual work contribution of the external loads $\delta\mathscr{W}_{\text{ext}}$. While the problems in this work exhibit hyper-elastic behavior and only conservative external loads are considered, it is important to stress that at no point in the derivation of the weak form an assumption regarding constitutive law or external loads was made. Thus, the PVW is a very general principle and can be applied

even in the context of non-conservative external loads and non-elastic deformations. Based on the highest appearing derivative in the weak form, the function spaces for the solution functions $\boldsymbol{u}$ and the weight functions $\delta\boldsymbol{u}$ are chosen to be:

$$\mathfrak{U} = \{\boldsymbol{u} \in \mathfrak{H}^1(\Omega) |\ \boldsymbol{u}(\boldsymbol{X}, t) = \hat{\boldsymbol{u}}(\boldsymbol{X}, t) \text{ on } \Gamma_u\}, \tag{2.40}$$

$$\mathfrak{V} = \{\delta\boldsymbol{u} \in \mathfrak{H}^1(\Omega) |\ \delta\boldsymbol{u}(\boldsymbol{X}) = 0 \text{ on } \Gamma_u\}. \tag{2.41}$$

Here $\mathfrak{H}^1$ denotes the first order Sobolev space of square-integrable functions and square-integrable first derivatives. Based on the definitions above, the IBVP can be restated in an abstract fashion as

$$\text{Find } \boldsymbol{u} \in \mathfrak{U} \text{ such that } \delta\mathscr{W} = 0 \,\forall\, \delta\boldsymbol{u} \in \mathfrak{V}. \tag{2.42}$$

As mentioned above, as long as the admissible functions of $\boldsymbol{u}$ and $\delta\boldsymbol{u}$ are not further restricted, the weak form is equivalent to the strong form and still does not admit a general solution. It is the restriction of admissible functions to finite dimensional subspaces $\mathfrak{U}^h$ for $\boldsymbol{u}$ and $\mathfrak{V}^h$ for $\delta\boldsymbol{u}$ which defines the approximative step in the derivation of the finite element method. At the same time it is this step that enables a numerical solution of the IBVP at hand.

2.2.1 Discretization in space and time

In practice, the abstract notion of restricting the function space translates to a finite element discretization of the spatial domain Ω_0, the solution $\boldsymbol{u}$, and the weight functions $\delta\boldsymbol{u}$. Simply speaking, it entails an approximate partition of the domain into geometrical primitives called *elements*, which are connected to each other at discrete points, referred to as *nodes*. Then, instead of seeking a continuos solution of the IBVP on the continuous domain Ω_0, one tries to find an approximate solution at these nodes and uses a local interpolation scheme between those nodes to obtain a solution throughout the domain. Therefore, the domain Ω_0 is subdivided into N_{ele} non-overlapping subdomains

$$\Omega_0 \approx \bigcup_{e=1}^{N_{\text{nele}}} \Omega_0^{(e)}. \tag{2.43}$$

Based on these elements, which are connected at the nodes, a local interpolation scheme for the solution is devised, often on the basis of low order Lagrange polynomials. In the context of finite elements, the used polynomials are generally referred to as shape-functions. The displacement within an element can then be written as

$$\boldsymbol{u}^{(e)}(\boldsymbol{X}, t) \approx \boldsymbol{u}_h^{(e)}(\boldsymbol{X}, t) = \sum_{k=1}^{N_{\text{nodes}}^{(e)}} N_k(\boldsymbol{X}) \boldsymbol{d}_k(t). \tag{2.44}$$

Where the vector $\boldsymbol{d}_k(t)$ contains the nodal displacements, which are still continuous in time. Alternatively, all shape functions of an element can be arranged in matrix form and (2.44) can be rewritten as matrix vector product

$$\boldsymbol{u}_h^{(e)}(\boldsymbol{X}, t) = \sum_{k=1}^{N_{\text{nodes}}^{(e)}} N_k(\boldsymbol{X}) \boldsymbol{d}_k(t) = \boldsymbol{N}(\boldsymbol{X}) \boldsymbol{d}^{(e)}(t), \tag{2.45}$$

where the vector $\boldsymbol{d}^{(e)}(t)$ contains the nodal displacements of all nodes belonging to a particular element e. Analogous, the same ansatz can be made for the virtual displacements

$$\delta\boldsymbol{u}^{(e)}(\boldsymbol{X},t) \approx \boldsymbol{u}_h^{(e)}(\boldsymbol{X},t) = \sum_{k=1}^{N_{\text{nodes}}^{(e)}} N_k(\boldsymbol{X})\delta\boldsymbol{d}_k(t) = \boldsymbol{N}(\boldsymbol{X})\delta\boldsymbol{d}^{(e)}(t), \tag{2.46}$$

where $\delta\boldsymbol{d}_k(t)$ denotes the vector of virtual nodal displacements. Using the same ansatz for both the displacements and the virtual displacements (or more generally weighting functions), is referred to as *Bubnov-Galerkin* method, which is the predominant choice for finite elements in solid mechanics. If different shape functions are used for the displacements and their virtual counterparts, the discretization scheme is referred to as *Petrov-Galerkin* method. While other approaches are also conceivable, the so-called *isoparametric concept* is employed in this work, meaning that the ansatz functions used for the displacements are also used to approximate the geometry in reference $\boldsymbol{X}$ and current configuration $\boldsymbol{x}$.

The main purpose is to map an element to a simple undistorted reference geometry or parameter space described by $\boldsymbol{\xi} = (\xi, \eta, \zeta)$, which facilitates, e.g., numerical integration of the weak form. Of course, the change of coordinate system must be accounted for by using the determinant of the element's Jacobian matrix

$$\boldsymbol{J}^{(e)} = \frac{\partial \boldsymbol{X}^{(e)}}{\partial \boldsymbol{\xi}}. \tag{2.47}$$

Following the isoparametric concept, displacements, current geometry, and reference geometry can be written as

$$\boldsymbol{u}_h^{(e)}(\boldsymbol{\xi},t) = \boldsymbol{N}(\boldsymbol{\xi})\boldsymbol{d}^{(e)}(t), \tag{2.48}$$

$$\boldsymbol{x}_h^{(e)}(\boldsymbol{\xi},t) = \boldsymbol{N}(\boldsymbol{\xi})\overline{\boldsymbol{x}}^{(e)}(t), \tag{2.49}$$

$$\boldsymbol{X}_h^{(e)}(\boldsymbol{\xi}) = \boldsymbol{N}(\boldsymbol{\xi})\overline{\boldsymbol{X}}^{(e)}. \tag{2.50}$$

Here, $\overline{\boldsymbol{X}}^{(e)}$ and $\bar{\boldsymbol{x}}^{(e)}(t)$ are the nodal position in reference and current configuration, respectively. Moreover, based on geometrical shape, number of nodes, and chosen interpolation functions a wide range of different elements can be formulated. The finite element models considered in this work are typically discretized with 3D elements based on low order Lagrange polynomials. Examples include 8-noded hexahedral elements (hex8), 6-noded wedge-shaped elements (wedge6), and 4-noded tetrahedral elements (tet4). Depending on the complexity of the model geometry, it can be advantageous to use multiple types of elements within one model. Further description of the construction of shape-functions and different element types is given in the respective literature, e.g., [159, 374]. Due to the non-overlapping partition and the local interpolation scheme, the integral over the domain Ω_0 in the weak form can be subdivided into a sum

of integrals over the individual element domains.

$$\delta\mathscr{W} = \sum_{e=1}^{N_{\text{ele}}} \Bigg[\delta \boldsymbol{d}_h^{(e)\,T} \Bigg\{ \underbrace{\int_{\Omega^{\text{e}}} \boldsymbol{N}^T \rho_0 \boldsymbol{N} \mathrm{d}V_0}_{\text{elem. mass matrix } \boldsymbol{M}^{(e)}} \ddot{\boldsymbol{d}}^{(e)} + \underbrace{\int_{\Omega_e} \left(\frac{\partial \boldsymbol{E}(\boldsymbol{d}^{(e)})}{\partial \boldsymbol{d}^{(e)}} \right)^T \boldsymbol{S}(\boldsymbol{d}^{(e)}) \mathrm{d}V_0}_{\text{elem. int. force vector } \boldsymbol{f}^{\text{int},(e)}} - \underbrace{\int_{\Omega_e} \boldsymbol{N}^T \hat{\boldsymbol{b}}_0 \mathrm{d}V_0 - \int_{\Gamma_\sigma} \boldsymbol{N}^T \hat{\boldsymbol{t}}_0 \mathrm{d}A_0}_{\text{elem. ext. force vector } \boldsymbol{f}^{\text{ext},(e)}} \Bigg\} \Bigg]^{(e)} = 0 \tag{2.51}$$

Based on the above definition of element mass matrix $\boldsymbol{m}^{(e)}$, element internal force vector $\boldsymbol{f}^{\text{int},(e)}$, and element external force vector $\boldsymbol{f}^{\text{ext},(e)}$, the discretized version of the weak form can be written as

$$\delta\mathscr{W} = \sum_{e=1}^{N_{\text{numele}}} \left[\delta \boldsymbol{d}^{(e),\,T} \left\{ \boldsymbol{M}^{(\text{e})} \ddot{\boldsymbol{d}}^{(e)} + \boldsymbol{f}^{\text{int},(\text{e})}(\boldsymbol{d}^{(e)}) - \boldsymbol{f}^{\text{ext},(\text{e})}(\boldsymbol{d}^{(e)}) \right\} \right] = 0. \tag{2.52}$$

Since the displacements are required to be C^0 continuous through (2.41) and the elements are connected at the nodes, adjacent elements can contribute to the same nodal displacement. The process of sorting the contribution of the elements into a single global system of equations is referred to as assembly which is denoted by the operator $\mathop{\mathsf{A}}_{e=1}^{N_{\text{ele}}}$. The assembly of the discretized weak form

$$\mathop{\mathsf{A}}_{e=1}^{\text{numele}} \left[\delta \boldsymbol{d}^{(e)\,T} \left\{ \boldsymbol{M}^{(\text{e})} \ddot{\boldsymbol{d}}^{(e)} + \boldsymbol{f}^{\text{int},(\text{e})}(\boldsymbol{d}^{(e)}) - \boldsymbol{f}^{\text{ext},(\text{e})}(\boldsymbol{d}^{(e)}) \right\} \right] = 0, \tag{2.53}$$

leads to a global, semi-discrete system of nonlinear equations

$$\delta \boldsymbol{d}^T \{ \boldsymbol{M}\, \ddot{\boldsymbol{d}} + \boldsymbol{f}^{\text{int}}(\boldsymbol{d}) - \boldsymbol{f}^{\text{ext}}(\boldsymbol{d}) \} = 0. \tag{2.54}$$

Here, the vector $\boldsymbol{d}$ denotes the global vector of nodal displacements and $\ddot{\boldsymbol{d}}$ denotes its second time derivative. Since (2.54) must hold for arbitrary virtual nodal displacements, the term in the braces, i.e., the residuum, has to vanish

$$\boldsymbol{r}(\boldsymbol{d}) = \boldsymbol{M}\, \ddot{\boldsymbol{d}} + \boldsymbol{f}^{\text{int}}(\boldsymbol{d}) - \boldsymbol{f}^{\text{ext}}(\boldsymbol{d}, t) = \boldsymbol{0}. \tag{2.55}$$

For the sake of completeness, it is noted that (2.55) can be extended to consider damping as well. While the system of equations is discrete in space, it is still continuous in time. Usually this is the point where a time-discretization based on a finite difference scheme is introduced. Many different approaches for this task have been proposed in the literature, see, e.g., Belytschko et al. [29] for an overview. However, since all solid mechanics problems considered in this work are quasi-static, time dependence and inertia terms are neglected from this point forward. Without dependence on time, the discrete system of nonlinear equations simplifies to

$$\boldsymbol{r}(\boldsymbol{d}) = \boldsymbol{f}^{\text{int}}(\boldsymbol{d}) - \boldsymbol{f}^{\text{ext}}(\boldsymbol{d}) = \boldsymbol{0}. \tag{2.56}$$

In the vast majority of cases, this system of nonlinear equations cannot be directly solved with an iterative solution method, like the Newton-Raphson method. The Newton-Raphson method

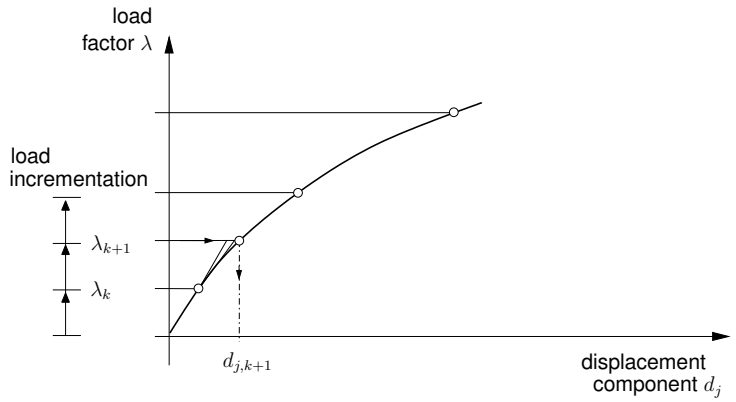

Figure 2.1 Load-displacement diagram

requires an "good" initial iterate in order to converge. Therefore, the nonlinear equations are usually solved for a certain number of incremental load levels, where the solution of one load level provides a reasonable initial iterate for the next one, thus allowing for an efficient iterative solution using a Newton-Raphson scheme. Before a more detailed explanation of the Newton-Raphson solution scheme is given, the employed load incrementation procedure will be explained briefly. Instead of applying the full external load at once, a load factor λ is introduced, which enables an incremental increase of the external load

$$\boldsymbol{f}_{\lambda}^{\mathrm{ext}} = \lambda \boldsymbol{f}^{\mathrm{ext}}. \tag{2.57}$$

A visualization of the described incrementation procedure is given in Figure 2.1. As mentioned before, each incremental step requires an iterative solution to achieve equilibrium at the current load level. In certain circumstances other incrementation procedures, such as displacement controlled or so-called arc-length controlled schemes might be better choices, see [70, 270] for details. However, for the problems considered in this work, the simple load controlled scheme is sufficient. For a given load step k the system of algebraic equations for static equilibrium has to be solved for $\boldsymbol{f}_{\lambda_{k+1}}^{\mathrm{ext}}$ to obtain the displacements $\boldsymbol{d}_{k+1}$, i.e., the root of the residual in (2.56) has to be found. This is done using the Newton-Raphson method. Based on the directional derivative of the residual function at a certain starting point, the root of the function is approximated by computing the root of the linearized function, which entails solving a linear system of equations. The obtained approximation is then the starting point for the next step. The procedure is repeated until a convergence criterion is met, e.g., the L2-norm of the residual is smaller then a certain threshold $\left\|\boldsymbol{r}(\boldsymbol{d}_{k+1}^{i})\right\| < \mathrm{tol}$. Based on a first order Taylor expansion around $\boldsymbol{d}_{k+1}^{i}$, the linearization of (2.56) is

$$\tilde{\boldsymbol{r}} = \boldsymbol{r}(\boldsymbol{d}_{k+1}^{i}) + \underbrace{\left.\frac{\partial \boldsymbol{r}(\boldsymbol{d})}{\partial \boldsymbol{d}}\right|_{\boldsymbol{d}_{k+1}^{i}}}_{\boldsymbol{K}_T} \Delta\boldsymbol{d}_{k+1}^{i+1} = \boldsymbol{r}(\boldsymbol{d}_{k+1}^{i}) + \boldsymbol{K}_{\mathrm{T}} \Delta\boldsymbol{d}_{k+1}^{i+1}. \tag{2.58}$$

The so-called *effective tangential stiffness matrix* $\boldsymbol{K}_T$ contains contributions from the linearization of internal and external forces. The root of the linearized residual can be computed by solving a linear system of equations

$$\boldsymbol{K}_{\mathrm{T}} \Delta\boldsymbol{d}_{k+1}^{i+1} = -\boldsymbol{r}(\boldsymbol{d}_{k+1}^{i}), \tag{2.59}$$

and updating the displacements according to:

$$\boldsymbol{d}_{k+1}^{i+1} = \boldsymbol{d}_{k+1}^{i} + \Delta\boldsymbol{d}_{k+1}^{i+1}. \tag{2.60}$$

After the convergence criterion is met, the procedure is repeated for the following load steps.

During the course of a nonlinear finite element solution scheme, linear systems, as the one given above, have to be solved repeatedly. Moreover, for large finite element models the repeated solution of these linear systems account for the bulk of the overall computational costs. Thus, efficient solution techniques for linear systems are of pivotal importance. Depending on system size and the matrix' properties, many different direct or iterative approaches for the solution of large linear systems are available [263, 283]. For all large models and resulting large linear systems considered in this work, iterative solution techniques based on the generalized minimal residual (GMRES) [283] method are employed. The method is used in combination with the multilevel preconditioner ML [110], which is integrated in the AztecOO iterative package [152]. ML and AztecOO are part of the collection of open source software libraries called Trilinos, which are developed and maintained by the Sandia National Laboratories [153]. Another Trilinos package, AMESOS, also provides an interface to direct solvers, such as UMFPACK [72], which is used for the treatment of the smaller numerical models in this work. All finite element simulations in this work were conducted using the parallel in-house research code BACI, which is jointly developed at the Institute for Computational Mechanics and the Mechanics and High-Performance Computing Group at Technische Universität München [350]. The C++ code BACI heavily relies on many of the open-source libraries of the Trilinos Project, including the linear solver packages.

2.2.2 Treatment of prestressed structures

When creating patient-specific finite element models of cardiovascular structures such as AAAs from segmented CT image data, it is important to account for the prestressed imaged state. The vessel walls are subject to intraluminal pressure, exerted by the blood within the lumen of the vessels. Hence, the imaged geometry is in equilibrium with the intraluminal pressure load and is not stress free. Several approaches have been proposed in to either identify the stress free geometry, or to imprint a so-called *prestress* or *prestrain* in the current, imaged configuration [74, 111, 112, 197, 355]. In this work an approach based on a *modified updated Lagrangian formulation* (MULF) proposed by Gee et al. [111, 112] is used to imprint stresses. If the loads corresponding to the prestressed state are known, the MULF scheme can be used to imprint a deformation gradient which accounts for the prestress without changing the geometry. Based on the works of Gee et al. [111, 112], the basic steps of the MULF scheme are briefly summarized below.

Starting point is a known spatial configuration Ω_t with a known coordinate vector field $\boldsymbol{x}_t$. The configuration Ω_t is not stress free and the reference geometry is not known. The goal is to compute an approximation to the stress state of the configuration Ω_t, given some known external loads $\hat{\boldsymbol{t}}_t$. In this work, the spatial configuration is obtained from CT scans of AAAs and the blood is assumed to act on the arterial wall as pressure load.

The MULF scheme is based on a multiplicative split of the deformation gradient $\boldsymbol{F}_{\mathrm{tot}}$ into two parts

$$\boldsymbol{F}_{\mathrm{tot}} = \boldsymbol{F}_u \boldsymbol{F}_{\mathrm{pre}}, \tag{2.61}$$

corresponding to a share $\boldsymbol{F}_u$ resulting from deformation and a part $\boldsymbol{F}_{\mathrm{pre}}$ accounting for prestress, respectively. The increase of $\boldsymbol{S}(\boldsymbol{F}_{\mathrm{tot}})$ caused by $\boldsymbol{F}_{\mathrm{pre}}$ is called prestress. The MULF scheme is used to approximate $\boldsymbol{F}_{\mathrm{pre}}$ attributed to the applied loads $\hat{\boldsymbol{t}}_t$, using an incremental update of the loads while keeping $\boldsymbol{x}_t$ fixed.

Consider two neighboring configurations Ω_n with $\boldsymbol{x}_n^h$ and Ω_{n+1} where $\boldsymbol{x}_{n+1}^h = \boldsymbol{x}_n^h + \Delta\boldsymbol{x}_{n+1}^h$ and the corresponding deformation gradients are $\boldsymbol{F}_n$ and $\boldsymbol{F}_{n+1}$. Moreover, let $\Delta\boldsymbol{F}_{n+1}$ describe the mapping between the configuration Ω_n and the following configuration Ω_{n+1} which can be computed using

$$\Delta\boldsymbol{F}_{n+1} = \boldsymbol{I} + \boldsymbol{N}_{,\boldsymbol{\xi}}\boldsymbol{J}_t^{-1}\Delta\boldsymbol{x}_{n+1}^h, \tag{2.62}$$

with the identity tensor $\boldsymbol{I}$, the derivatives of the shape functions with respect to the element coordinates $\boldsymbol{N}_{,\boldsymbol{\xi}}$, and the inverse of the Jacobian $\boldsymbol{J}_n^{-1}$. By setting the residual in (2.58) to zero, $\Delta\boldsymbol{x}_{n+1}^h$ can be calculated. In addition, all other quantities that are required for the calculation of $\Delta\boldsymbol{F}_{n+1}$, i.e., $\boldsymbol{N}_{,\boldsymbol{\xi}}$ and $\boldsymbol{J}_t^{-1}$, can be determined without knowledge of $\boldsymbol{x}_n$. Using $\Delta\boldsymbol{F}_{n+1}$, $\boldsymbol{J}_{n+1}^{-1}$ can be computed as well

$$\boldsymbol{J}_{n+1}^{-1} = \boldsymbol{J}_n^{-1}\Delta\boldsymbol{F}_{n+1}^{-1} \tag{2.63}$$

The total deformation gradient can then be computed using

$$\boldsymbol{F}_{n+1} = \Delta\boldsymbol{F}_{n+1}\boldsymbol{F}_n, \tag{2.64}$$

without knowledge of the reference configuration, or $\boldsymbol{x}_n$. During the course of a standard simulation scheme starting from Ω_0, the current configuration would be updated by setting $\boldsymbol{x}_{n+1}^h = \boldsymbol{x}_n^h + \Delta\boldsymbol{x}_{n+1}^h$ before repeating the steps (2.62) to (2.64). In the MULF scheme this update step is omitted, $\Delta\boldsymbol{x}_{n+1}^h$ is simply set to zero, and Ω_{n+1} is set to Ω_n. This way, raising the external load incrementally, $\boldsymbol{F}_{\mathrm{pre}}$ can be successively build up repeating the updates in (2.62) to (2.64) until the desired external load $\hat{\boldsymbol{t}}_t$ is reached. Now, $\boldsymbol{S}(\boldsymbol{F}_{\mathrm{pre}})$ provides an approximation to the desired prestressed state [112]. If further calculations from this point on are necessary, the prestressed state of the model can be considered in standard nonlinear finite element solution schemes simply by setting

$$\boldsymbol{F}_{\mathrm{tot}} = \boldsymbol{F}_u\boldsymbol{F}_{\mathrm{pre}}, \tag{2.65}$$

where $\boldsymbol{F}_u$ is determined as usual, using (2.3).

3 Probability theory and Bayesian statistics

The understanding of the methods described and developed in this work require a fair amount probability theory and hence, this chapter aims at introducing the aspects of probability theory that are relevant to this work. For a more extensive introduction to probability theory the reader is referred to the textbooks [30, 48, 280], or for a more mathematical treatment of the subject, e.g, [133, 246].

The chapter is comprised of two main parts. In the first part, the basic rules of probability, random variables, and the concept of stochastic processes and fields are covered. Both random variables and random processes are extensively used in the following chapters to describe uncertain input parameters of computational models. In addition to the fundamental concepts, an important aspect in the context of UQ is the efficient generation of realizations, i.e., sample functions, of stochastic processes. Therefore, the present chapter also addresses and explains the techniques used in this work for the efficient generation of realizations of stochastic processes.

The second part of this chapter introduces the concept of Bayesian inference, with a particular focus on Bayesian regression techniques. Throughout this work, extensive use is made of Bayesian regression techniques, e.g., for the prediction of patient-specific input parameters or to construct surrogate models for computationally expensive finite element models. Moreover, Bayesian regression is a centerpiece to the developed Bayesian multi-fidelity Monte Carlo scheme which warrants a somewhat more detailed introduction of the concept of Bayesian regression. Thus, after briefly describing linear regression from a Bayesian point of view, two more elaborate, non-parametric regression approach are described

3.1 Fundamentals of probability theory

We start our discussion about probability theory, which provides the necessary tools to quantify and modify uncertainty, by defining the two main components of a general probabilistic model. The first ingredient is the so-called sample space Ω, which defines the set of all possible outcomes of an experiment. The second is a probability law which assigns a nonnegative number $P(A)$ to a set A of possible outcomes, referred to as event. This number $P(A)$ is called the probability of A. A very general definition as to what constitutes a probability is given by Kolmogorov [180] is based on the following three axioms. The probability of any event A is nonnegative

$$P(A) \geq 0. \tag{3.1}$$

The probability of the complete sample space Ω is equal to 1, i.e.,

$$P(\Omega) = 1. \tag{3.2}$$

The probability of the union of two events A and B, written as $A \cup B$ in the following, can be computed using the addition rule of probability. If A and B are two mutually exclusive events, it reads

$$P(A \cup B) = P(A) + P(B). \tag{3.3}$$

The two events A and B are called mutually exclusive or disjoint if the occurrence of A excludes the occurrence of B and vice versa. In addition, the following concepts from set theory are introduced. The intersection $A \cap B$ of the two events A and B is defined as the event that occurs if both A and B occur. For every event A, a corresponding complementary event can be defined which be denoted by A^c in the following.

Technically, in order to define a valid probability measure P, a collection $\mathcal{F}$ of events to which probabilities can be assigned needs to be defined. However, because the mathematical intricacies of the requirements for $\mathcal{F}$ are well beyond the scope of this work, it is only mentioned that this collection is a so-called $\sigma-$algebra. For further details, the reader is referred to [37]. To conclude, a so-called probability space, the formal definition of a probabilistic model, is defined by the triple $(\Omega, \mathcal{F}, P)$.

On the basis of the three axioms of probability, additional laws or rules, which of course have to comply with the axioms above, can be defined. A fundamental concept in probability theory is that of conditional probabilities. The resulting law or rule allows reasoning about the outcome of an experiment if only partial information is available. Assuming that the outcome of an experiment is B, what is the probability that the outcome of the experiment also belongs to an event A? The formal definition of conditional probability $P(A|B)$, which is read as probability of A given B, is

$$P(A|B) = \frac{P(A \cap B)}{P(B)}. \tag{3.4}$$

Rearrangement yields the multiplication or product rule of probability

$$P(A \cap B) = P(A|B)P(B). \tag{3.5}$$

If the occurrence of event B does not provide any information about the occurrence of event A, the two events are called *independent*. Hence, the occurrence of B does not alter the probability of A

$$P(A|B) = P(A). \tag{3.6}$$

Inserted into (3.4) above equation can be restated in the more general form which also holds for $P(B) = 0$

$$P(A \cap B) = P(A)P(B). \tag{3.7}$$

Independence is a symmetric property, i.e, if A is independent of B, then B is also independent of A. Conditional probabilities are very useful for computing probabilities of an event A that can be decomposed into several distinct events for which only the conditional probability and the probability of the conditioning event is known. Let $\{B_1, B_2, ...B_l\}$ be a set of pairwise disjoint events with $P(B_n) > 0$. which form a partition of the entire sample space Ω, that is $\cup_{n=1}^{\infty} B_n = \Omega$, then the law of total probability states that

$$P(A) = \sum_{n=1}^{\infty} P(A|B_n)P(B_n). \tag{3.8}$$

The famous Bayes' rule relates the two conditional probabilities $P(A|B)$ and $P(B|A)$

$$P(A|B) = \frac{P(A)P(B|A)}{P(B)} \tag{3.9}$$

and can be derived as direct consequence of the definition of conditional probability and the multiplication rule. In the given original form, it was first published in 1763, shortly after the death of Thomas Bayes, by Richard Price [26]. The importance of this deceptively simple formula can hardly be overstated as it is the basis for countless innovations in the last decades. It is also pivotal for the understanding of the concepts presented in this work. An important interpretation of the Bayes theorem is that it provides a coherent way to update one's belief in the light of new, additional information. It is, in essence, the mathematical formula for learning by experience.

3.2 Random variables

In the previous section, a probabilistic model has been defined using the abstract concepts of sample spaces and events, i.e., the outcome of an experiment to which probabilities can be assigned. Often, the outcome of an experiment is a numerical value or can be associated with a numerical value. The notion of a random variable formalizes the assignment of a particular number to each possible outcome of an experiment. Mathematically, a random variable defines a real-valued function of the experimental outcome $\mathsf{x}(\omega) : \Omega \to \mathbb{R}$, where ω is used here to denote the outcome of the experiment. Note that in this work, random quantities are denoted using a font without serifs and the dependence on ω is usually omitted for the sake of an uncluttered notation. An exception are random variables denoted by greek letters where the random nature is signified through retaining the dependence on ω.

Two types of random variables are distinguished. A discrete random variable is defined as real-valued function that can take at most countably infinite number of values. In contrast a continuous random variable can take an uncountably infinite number of values, e.g, any value from the interval $[-1, 1]$. The most common way to characterize a random variable is through its probability mass function if the variable is discrete, or its probability density function if the variable is continuous.

3.2.0.1 Probability mass function

For discrete random variables the probability mass function (PMF), denoted by $p_{\mathsf{x}}(x)$, assigns a probability to any possible value x that the random variable x can take

$$p_{\mathsf{x}}(x) = P(x = \mathsf{x}) \tag{3.10}$$

From the additivity and normalization axioms defined in (3.3) and (3.2) it follows that the sum of p_{x} over all possible values of x is

$$\sum_x p_{\mathsf{x}}(x) = 1. \tag{3.11}$$

3.2.0.2 Probability density function

The analogue of the probability mass function for a continuous random variable is the probability density function (PDF) of x. The PDF, also denoted by $p_{\mathsf{x}}(\mathsf{x})$, is a nonnegative function which gives the probability that x lies in the interval $[a, b]$ by

$$P(\mathsf{x} \in (a, b)) = \int_a^b p_{\mathsf{x}}(x)\mathrm{d}x. \tag{3.12}$$

In order to constitute a valid PDF, the function $p_{\mathsf{x}}(x)$ must be nonnegative, that is $p_{\mathsf{x}} \geq 0, \forall x$. In addition, the normalization axiom has to be fulfilled by continuous random variables as well. Hence, its required that

$$\int_{-\infty}^{\infty} p_{\mathsf{x}}(x)\mathrm{d}x = 1. \tag{3.13}$$

3.2.1 Cumulative distribution functions

The probability distributions of both discrete as well as continuous random variables can be characterized with a single mathematical concept: the cumulative distribution function (CDF). The CDF of a random variable x is denoted by $F_{\mathsf{x}}(x)$ and completely determines the probability distribution. It provides the probability that a random variable x falls within the interval $(-\infty, x)$

$$F_{\mathsf{x}}(x) = P(\mathsf{x}(\omega) \leq x) = P(\mathsf{y} \leq x) \begin{cases} \sum_{k \leq x} p_{\mathsf{x}}(k) & \text{if x is discrete,} \\ \int_{-\infty}^{x} p_{\mathsf{x}}(t)\mathrm{d}t & \text{if x is continuous.} \end{cases} \tag{3.14}$$

Of course, one can also obtain the PMF and PDF from the CDF through differencing and differentiation, respectively. In addition to (3.14), Bertsekas and Tsitsiklis [30] list the following general properties that $F_{\mathsf{x}}(x)$ must fulfill:

- $0 \leq F_{\mathsf{x}}(x) \leq 1, \forall\, x$
- F_{x} is monotonically nondecreasing, if $x < y$, then $F_{\mathsf{x}}(x) < F_{\mathsf{x}}(y)$
- If x is discrete, then $F_{\mathsf{x}}(x)$ is a piecewise constant function of x
- If x is continuous, then $F_{\mathsf{x}}(x)$ is a continuos function of x

3.2.2 Functions of random variables

Based on a random variable x, another random variable can be defined by applying a transformation to x. For instance, consider a general nonlinear function $f(\cdot)$, then a random variable y can be defined through transformation of the random variable x:

$$\mathsf{y} = f(\mathsf{x}) \tag{3.15}$$

If x is a discrete random variable, y is also a discrete random variable and its PMF can be computed by summing the probabilities of all values of x such that $f(x) = y$:

$$p_{\mathsf{y}}(y) = \sum_{\{x|f(x)=y\}} p_{\mathsf{x}}(x). \tag{3.16}$$

For the consideration of the continuous case, the following two restrictions for the transformation $f(x)$ are made. First, it is assumed that the function f is differentiable. Second, $f(\cdot)$ is required to be strictly monotonic on some interval I which contains the range of the random variable x, such that $f(x) = 0, x \notin I$. Thus, $f(\cdot)$ is invertible and its derivative is either nonnegative or nonpositive, depending on whether the function is monotonically increasing or decreasing, respectively. If aforementioned requirements hold, the PDF of y is given by

$$p_{\mathsf{y}}(y) = p_{\mathsf{x}}(f^{-1}(y)) \left| \frac{\mathrm{d}}{\mathrm{d}y}(f^{-1}(y)) \right|. \tag{3.17}$$

3.2.3 Extension to multivariate random variables

Since many applications require the consideration of multiple random variables simultaneously and investigation of their mutual interactions, the notions of PMF and PDF are extended to multiple random variables. Furthermore, the concepts of conditional and marginal probability distributions are introduced. Based on a collection of either discrete or continuous random variables $\mathsf{x}_1, \mathsf{x}_2, \mathsf{x}_3, ...\mathsf{x}_n$, denoted by the vector $\mathbf{x}$, the so-called joint probability mass function or joint probability density $p_{\mathbf{x}}(\boldsymbol{x})$ can be defined. This collection of random variables is generally referred to as multivariate random variable or random vector.

For the remainder of the section, a restriction to two random variables is made to facilitate the discussion; however, the extension to more than two variables is straightforward. First, consider two discrete random variables x and y, denoted by $\mathbf{x} = [\mathsf{x}, \mathsf{y}]^T$ in the following. The probability of the event $\{\mathsf{x} = x, \mathsf{y} = y\}$ is given by the joint PMF, of the two random variables $p_{\mathsf{x},\mathsf{y}}$,

$$p_{\mathsf{x},\mathsf{y}}(x, y) = p_{\mathbf{x}}(\boldsymbol{x}) = P(\mathsf{x} = x, \mathsf{y} = y) \tag{3.18}$$

Based on the joint PMF, one can compute the PMFs of x and y using

$$p_{\mathsf{x}}(x) = \sum_y p_{\mathsf{x},\mathsf{y}}(x, y), \quad p_{\mathsf{y}}(y) = \sum_x p_{\mathsf{x},\mathsf{y}}(x, y). \tag{3.19}$$

In this context, $p_{\mathsf{x}}(x)$ and $p_{\mathsf{y}}(y)$ are referred to as marginal probability mass functions and provide a probability distribution of one variable if the other one is not known. Similarly, one can describe the distribution of two continuous variables associated with the same experiment with their joint probability density function. The joint PDF is a nonnegative function which allows the computation of the probability that x and y lie within $\mathcal{A}$, a subset of $\mathbb{R}^2$

$$P((\mathsf{x}, \mathsf{y}) \in \mathcal{A}) = \int\int_{(x,y)\in\mathcal{A}} p_{\mathsf{x},\mathsf{y}}(x, y)\,\mathrm{d}x\mathrm{d}y. \tag{3.20}$$

The joint PDF is sufficient to compute the probability of any event that can be defined regarding the two random variables because the joint PDF contains all probabilistic information about x

and y including mutual dependencies. If the event of interest involves only one of the two, e.g, the event $\{\mathsf{x} \in \mathcal{B}\}$ where $\mathcal{B}$ is a subset of the real line, (3.20) becomes

$$\int_{x \in \mathcal{B}} \int_{-\infty}^{\infty} p_{\mathsf{x},\mathsf{y}}(x, y)\, \mathrm{d}x\mathrm{d}y, \tag{3.21}$$

which yields the following definition for the marginal PDF $p_{\mathsf{x}}(x)$

$$p_{\mathsf{x}}(x) = \int_{-\infty}^{\infty} p_{\mathsf{x},\mathsf{y}}(x, y)\mathrm{d}y. \tag{3.22}$$

The marginal distribution of y can be obtained in the same fashion. The joint distribution of two random variables can be obtained by the applying the sum and the product rule of probability

$$p_{\mathsf{x}}(x) = \int p_{\mathsf{x},\mathsf{y}}(x, y)\mathrm{d}y, \tag{3.23}$$

$$p_{\mathsf{x},\mathsf{y}}(x, y) = p_{\mathsf{y}|\mathsf{x}}(y|x)p_{\mathsf{x}}(x). \tag{3.24}$$

Note that (3.23) and (3.24) represent extensions of the sum and the product rule defined in (3.3) and (3.5) for discrete events to continuous random variables. The formal justification of this extension requires extensive use of measure theory and hence only the result is stated here. Similarly to the PDF and PMF, the CDF can also be extended to include multiple random variables.

3.2.4 Expectation and moments of random variables

While PMF, PDF, and CDF completely define all probabilistic properties of one or more random variables, it is often helpful to characterize a probability distribution based on its so-called moments, which provide a summary of the distribution in terms of a few representative numbers. The most important summary associated with a random variable is the expected value, here also referred to as expectation, first moment, or mean value, which defines its probabilistic average. The expected value of a random variable x is denoted by $\mathbb{E}_{\mathsf{x}}[\mathsf{x}]$. For a discrete random variable it is defined as

$$\mathbb{E}_{\mathsf{x}}[\mathsf{x}] = \sum_{x} x p_{\mathsf{x}}(x) \tag{3.25}$$

such that each possible value x of x is weighted by the relative probability $p_{\mathsf{x}}(x)$. For continuous variables, the sum in (3.25) becomes an integral with respect to the corresponding probability density function

$$\mathbb{E}_{\mathsf{x}}[\mathsf{x}] = \mu = \int x p_{\mathsf{x}}(x)\mathrm{d}x. \tag{3.26}$$

Often, one has only a finite number of N samples from the PMF or the PDF. If this is the case, then for both, discrete and continuous variables, the expected value can be approximated by the sum

$$\mathbb{E}_{\mathsf{x}}[\mathsf{x}] \approx \frac{1}{N} \sum_{n=1}^{N} x_n, \tag{3.27}$$

which becomes exact in the limit $N \to \infty$. Apart from the mean, another important summary is the 2nd central moment of the random variable x, which is defined as expected value of $(\mathsf{x}-\mathbb{E}_{\mathsf{x}}[\mathsf{x}])^2$. The 2nd central moment, also referred to as the variance of x, provides an important measure for the variability of the random variable x around its mean and is defined as

$$\mathbb{V}_{\mathsf{x}}[\mathsf{x}] = \mathbb{E}_{\mathsf{x}}\big[(\mathsf{x} - \mathbb{E}_{\mathsf{x}}[\mathsf{x}])^2\big] = \int (x-\mu)^2 p_{\mathsf{x}}(x)\mathrm{d}x. \tag{3.28}$$

The square root of the variance, the so-called standard deviation σ_{x}

$$\sigma_{\mathsf{x}} = \sqrt{\mathbb{V}_{\mathsf{x}}[\mathsf{x}]}, \tag{3.29}$$

provides another measure of dispersion of x around its mean value. In addition to the first moment, the mean, the nth moment of a random variable is defined as the expectation of the random variable x^n. Moreover, the nth central moment about the mean is defined by $\mathbb{E}_{\mathsf{x}}\big[(\mathsf{x} - \mathbb{E}_{\mathsf{x}}[\mathsf{x}])^n\big]$. The standardized third and fourth central moment, i.e., divided by the standard deviation, are called skewness and kurtosis and provide a measure for asymmetry and "peakedness", respectively.

3.2.5 Expectation of functions of random variables

The concept of expectation can be used to find weighted averages of a function $f(x)$ under a probability distribution $p_{\mathsf{x}}(x)$ and not just of the variable itself. This is an extremely important operation for instance in the context of UQ where the function $f(x)$ represents the output of a complex numerical model. If a full probabilistic description in the form of a PDF is not available, the expected value of $f(\mathsf{x})$ and the variance of $f(\mathsf{x})$ provide very useful characteristics of the distribution. For continuous variables, the expectation is expressed as the integral with respect to the corresponding probability distribution

$$\mathbb{E}_{\mathsf{x}}[f(\mathsf{x})] = \int f(x) p_{\mathsf{x}}(x)\mathrm{d}x, \tag{3.30}$$

which can be approximated by the following sum if only a finite number of samples are available

$$\mathbb{E}_{\mathsf{x}}[f(\mathsf{x})] \approx \frac{1}{N}\sum_{n=1}^{N} f(x_n). \tag{3.31}$$

3.2.6 Percentiles

Like the mean, the so-called median of a distribution provides another measure of location. The median $\mathbb{M}_{\mathsf{x}}[\mathsf{x}]$ is defined as any number which fulfills the following set of inequalities

$$P(\mathsf{x} \le \mathbb{M}_{\mathsf{x}}[\mathsf{x}]) \ge \frac{1}{2} \quad \text{and} \quad P(\mathsf{x} \ge \mathbb{M}_{\mathsf{x}}[\mathsf{x}]) \ge \frac{1}{2}. \tag{3.32}$$

The median is the 50th percentile, which, roughly speaking, means that of an uneven number of samples from a distribution, 50% of the samples will be smaller than the median.

In general, percentiles or quantiles define the value below which a given percentage of the distribution falls. Hence, the 95th or 99th percentile can be used to compute a worst case estimate for a random variable, in the sense that it is not very likely that the random variable will have a value greater than the 95th or even 99th percentile.

3.2.7 Covariance and correlation

The covariance is a measure for the extent to which two random variables change together

$$\mathrm{cov}(\mathsf{x},\mathsf{y}) = \mathbb{E}_{\mathsf{x},\mathsf{y}}\big[(\mathsf{x}-\mathbb{E}_{\mathsf{x}}[\mathsf{x}])(\mathsf{y}-\mathbb{E}_{\mathsf{y}}[\mathsf{y}])\big] = \mathbb{E}_{\mathsf{x},\mathsf{y}}[\mathsf{x},\mathsf{y}] - \mathbb{E}_{\mathsf{x}}[\mathsf{x}]\mathbb{E}_{\mathsf{y}}[\mathsf{y}]. \tag{3.33}$$

If the covariance has a positive sign, then, on average, large values of one variable tend to correspond to large values of the other. In the opposite case, if the covariance has a negative sign, large values of one variable tend to correspond to small values of the other. When $\mathrm{cov}(\mathsf{x},\mathsf{y}) = 0$, one speaks of uncorrelated random variables. If two variables are independent, they are also uncorrelated, but not vice versa. The interpretation of the magnitude of the covariance is difficult and hence one often encounters the normalized variant of the covariance, the correlation coefficient which is defined as

$$\rho(\mathsf{x},\mathsf{y}) = \frac{\mathrm{cov}(\mathsf{x},\mathsf{y})}{\sqrt{\mathbb{V}(\mathsf{x})\mathbb{V}(\mathsf{y})}}, \tag{3.34}$$

and satisfies

$$-1 \leq \rho(\mathsf{x},\mathsf{y}) \leq 1. \tag{3.35}$$

If a direct increasing or decreasing linear relation exists between the two variables x and y, the correlation coefficient is 1, or -1, respectively. The concept of covariance can be extended to the multivariate case. For two random vectors $\mathbf{x}$ and $\mathbf{y}$, the covariance matrix can be computed using

$$\boldsymbol{\Sigma}(\mathbf{x},\mathbf{y}) = \mathbb{E}_{\mathbf{x},\mathbf{y}}\big[(\mathbf{x}-\mathbb{E}_{\mathbf{x}}[\mathbf{x}])(\mathbf{y}-\mathbb{E}_{\mathbf{y}}[\mathbf{y}])\big], \tag{3.36}$$

therein the (i,j)-th element of the covariance matrix $\boldsymbol{\Sigma}$ is $\mathrm{cov}(\mathsf{x}_i,\mathsf{y}_j)$.

3.2.8 The Gaussian probability distribution

Throughout this work, extensive use of the uni- and multivariate Gaussian distribution as well as its extension to Gaussian processes is made. Because the Gaussian or normal distribution is central to the understanding of the concepts in this work, this section is devoted to the description of the Gaussian distribution and the discussion of some of its important properties. Moreover, the Gaussian distribution is used to exemplify some of the abstract concepts introduced in the previous sections. Other important probability distributions that are used on this work can be found in Appendix A.

For a single real-valued random variable, the univariate Gaussian distribution is defined by its probability density function

$$p_{\mathsf{x}}(x|\mu,\sigma) = \mathcal{N}(x|\mu,\sigma) = \frac{1}{(2\pi\sigma^2)^{1/2}}\exp\Big\{-\frac{1}{2\sigma^2}(x-\mu)^2\Big\}, \tag{3.37}$$

where μ denotes the mean and σ^2 the variance parameter. Alternatively, the Gaussian PDF can be formulated in terms of the inverse of the variance, the so-called precision $\tau = 1/\sigma$. Often, the shorthand notation $\mathsf{x} \sim \mathcal{N}(\mu,\sigma)$ will be used if a random variable obeys a Gaussian distribution. Integration of (3.37) yields the well-known CDF of the Gaussian distribution

$$F_{\mathsf{x}}(x) = \frac{1}{2}\big[1+\mathrm{erf}\big(\frac{x-\mu}{\sigma\sqrt{2}}\big)\big], \tag{3.38}$$

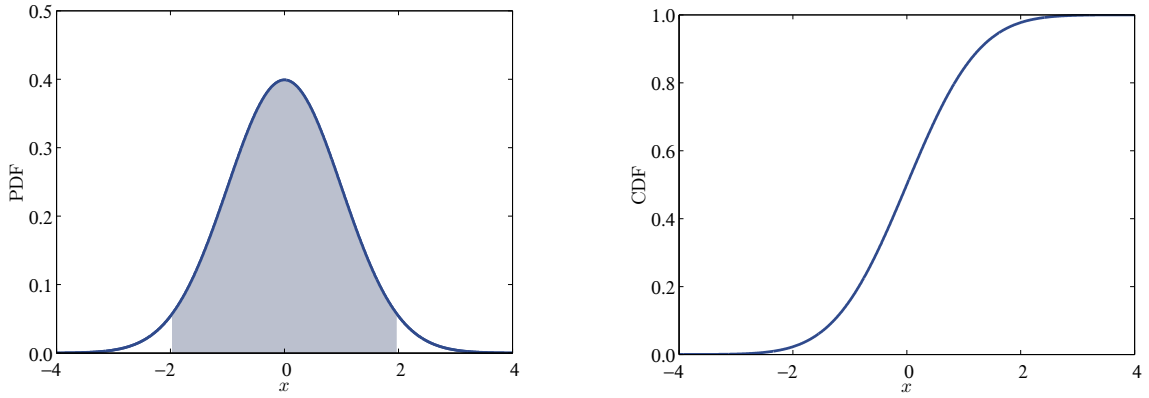

(a) **(b)**

Figure 3.1 Standard univariate Gaussian distribution. (a) Probability density function with 95% confidence region shown in light blue. (b) Cumulative distribution function.

where erf denotes the error function. Figure 3.1 shows the PDF and CDF for the standard Gaussian distribution, i.e., $\mu = 0$, $\sigma = 1$. In addition, Figure 3.1a shows also what will be referred to as the 95% confidence interval or confidence region in the remainder of this work. Of all observations, 95% will fall in the domain which is shown in light blue. The 95% or 99% confidence interval can be computed from the CDF of a random variable. For a Gaussian random variable, however, confidence intervals can be computed directly using μ and σ, e.g., the 95% confidence interval is approximately given by $\mu \pm 1.96\sigma$.

The Gaussian distribution can be extended to the multivariate case for which the PDF is defined by

$$\mathcal{N}(\boldsymbol{x}|\boldsymbol{\mu}, \boldsymbol{\Sigma}) = \frac{1}{(2\pi)^{d/2}} \frac{1}{|\boldsymbol{\Sigma}|^{1/2}} \exp\Big\{-\frac{1}{2}(\boldsymbol{x}-\boldsymbol{\mu})^T \boldsymbol{\Sigma}^{-1}(\boldsymbol{x}-\boldsymbol{\mu})\Big\}. \tag{3.39}$$

Here $\boldsymbol{\mu}$ is the d-dimensional mean vector, $\boldsymbol{\Sigma}$ is the symmetric, positive definite, $d \times d$ covariance matrix, and $|\boldsymbol{\Sigma}|$ denotes its determinant. Multivariate Gaussian distributions have two very important properties, namely that both marginal and conditional distributions of multivariate Gaussian distributions are again Gaussian distributions. These properties are crucial to the study and conditioning of so-called Gaussian processes, which will be introduced in one of the following sections. For the sake of brevity, the proof of these properties is omitted and only the result is given. If two multivariate random variables $\mathbf{x}$ and $\mathbf{y}$ are considered, which are jointly Gaussian random vectors

$$\begin{bmatrix}\mathbf{x}\\ \mathbf{y}\end{bmatrix} \sim \mathcal{N}\left(\begin{bmatrix}\boldsymbol{\mu}_\mathrm{x}\\ \boldsymbol{\mu}_\mathrm{y}\end{bmatrix}, \begin{bmatrix}\boldsymbol{\Sigma}_\mathrm{xx} & \boldsymbol{\Sigma}_\mathrm{xy}\\ \boldsymbol{\Sigma}_\mathrm{xy}^T & \boldsymbol{\Sigma}_\mathrm{yy}\end{bmatrix}\right), \tag{3.40}$$

then the marginal distribution $p_\mathbf{x}(\boldsymbol{x})$ is a Gaussian distribution as well and can be computed by

$$p_\mathbf{x}(\boldsymbol{x}) = \int p(\boldsymbol{x}, \boldsymbol{y}) \mathrm{d}\boldsymbol{y} = \mathcal{N}(\boldsymbol{\mu}_\mathbf{x}, \boldsymbol{\Sigma}_\mathbf{xx}). \tag{3.41}$$

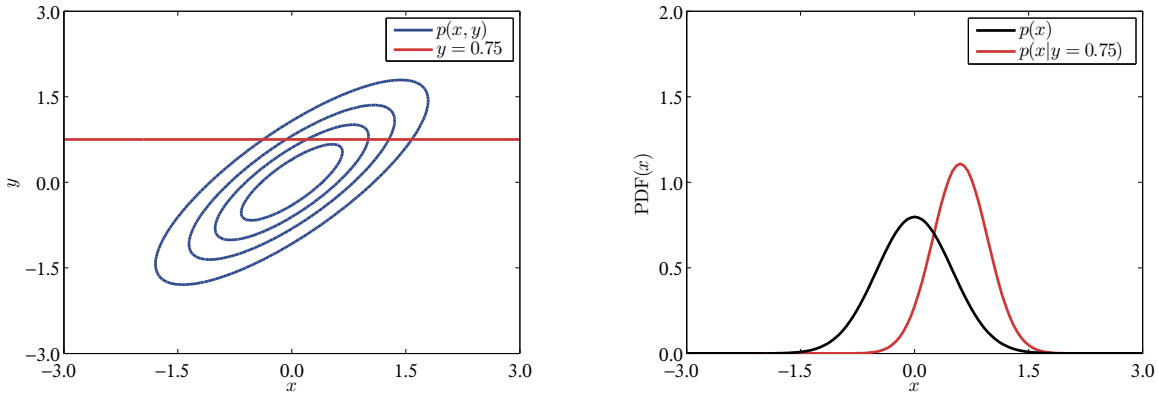

(a) **(b)**

Figure 3.2 Partitioned Gaussian distributions. (a) Contours of a bivariate Gaussian distribution $p(x, y)$. (b) Marginal distribution $p(x)$, shown in black and the conditional distribution $p(x|y)$ for $y = 0.75$, shown in red

The conditional distribution of x given y is also Gaussian

$$p_{\mathsf{x}}(\boldsymbol{x}|\boldsymbol{y}) = \mathcal{N}(\boldsymbol{\mu}_{\mathsf{x}|\mathsf{y}}, \boldsymbol{\Sigma}_{\mathsf{x}|\mathsf{y}}) \tag{3.42}$$

with

$$\boldsymbol{\mu}_{\mathsf{x}|\mathsf{y}} = \boldsymbol{\mu}_{\mathsf{x}} + \boldsymbol{\Sigma}_{\mathsf{xy}}\boldsymbol{\Sigma}_{\mathsf{yy}}^{-1}(\boldsymbol{y} - \boldsymbol{\mu}_{\mathsf{y}}), \tag{3.43}$$

$$\boldsymbol{\Sigma}_{\mathsf{x}|\mathsf{y}} = \boldsymbol{\Sigma}_{\mathsf{xx}} - \boldsymbol{\Sigma}_{\mathsf{xy}}\boldsymbol{\Sigma}_{\mathsf{yy}}^{-1}\boldsymbol{\Sigma}_{\mathsf{xy}}. \tag{3.44}$$

To illustrate these properties, Figure 3.2 depicts an example of a bivariate Gaussian distribution with the associated marginal and conditional distributions. Furthermore, Figure 3.2 shows the effect of a positive covariance between x and y, i.e., on average, large values of x tend to correspond to large values of y.

3.3 Random processes and fields

A *random* or *stochastic process* $\mathsf{g}(t, \omega), t \in T$ is essentially the extension of a multivariate random variable to an infinite number of dimensions. It is a mathematical construct to model a process whose dependence on a parameter t can be captured by probabilistic laws. For historic reasons, the index parameter t is often associated with time but it can also denote a spatial coordinate or, more generally, a scalar- or vector-valued parameter from an index set T. This index set can either be continuous or discrete or a combination from both. In the literature and in this work, the term *random field* is used instead of random process if the index parameter denotes spatial coordinates. Moreover, in case of a multi-dimensional index parameter, the symbol $\boldsymbol{x}$ will be used. The values that $\mathsf{g}(\boldsymbol{x})$ can assume are referred to as state-space which can also be either continuous or discrete. In addition, one can distinguish between scalar-valued stochastic

processes and vector-valued, i.e., multivariate processes. In the following discussion the focus lies on univariate processes with a general multi-dimensional index parameter $\boldsymbol{x} \in T = \mathbb{R}^d$.

A stochastic process can be interpreted as a function of two variables, the index parameter $\boldsymbol{x}$ and the probability parameter ω which can take values from the sample space Ω based on the outcome of a random experiment. For a fixed value $\boldsymbol{x}$, $\mathrm{g}(\boldsymbol{x}, \omega)$ becomes a random variable. If ω is held fixed, $\mathrm{g}(\boldsymbol{x}, \omega)$ defines a function in, e.g., time or space and is referred to as realization or sample function of the stochastic process. The collection of all possible realizations is called ensemble of the stochastic process. The distribution of the random variable for a particular $\boldsymbol{x}$ is given by the so-called *first-order distribution* $F_{\mathrm{g}}(g, \boldsymbol{x})$

$$F_{\mathrm{g}}(g, \boldsymbol{x}) = P(\mathrm{g}(\boldsymbol{x}) \leq g), \tag{3.45}$$

or the *first-order density* resulting from

$$p_{\mathrm{g}}(g(\boldsymbol{x})) = \frac{\partial F_{\mathrm{g}}(g, \boldsymbol{x})}{\partial g} \tag{3.46}$$

If the first-order density does not depend on the parameter $\boldsymbol{x}$, then the density is referred to as first-order density of $\mathrm{g}(\boldsymbol{x}, \omega)$. Otherwise, the process has a family of first-order densities. Based on the first-order density, the mean function and the variance function of the stochastic process can be derived. Similar to the expected value of a random variable, the mean function $m_{\mathrm{g}}(\boldsymbol{x})$ is defined by

$$m_{\mathrm{g}}(\boldsymbol{x}) = \mathbb{E}_{\mathrm{g}}[\mathrm{g}(\boldsymbol{x})] = \int_{-\infty}^{\infty} g p_{\mathrm{g}}(g, \boldsymbol{x}) \mathrm{d}g. \tag{3.47}$$

The variance function of the random process is defined as

$$\sigma_{\mathrm{g}}^2(\boldsymbol{x}) = \mathbb{E}_{\mathrm{g}}\big[\mathrm{g}(\boldsymbol{x}) - m_{\mathrm{g}}(\boldsymbol{x})\big]^2 = \mathbb{E}_{\mathrm{g}}\big[\mathrm{g}(\boldsymbol{x})^2\big] - \mathbb{E}_{\mathrm{g}}\big[m_{\mathrm{g}}(\boldsymbol{x})\big]^2. \tag{3.48}$$

The *second-order distribution* of the process is defined as the joint distribution of the two random variables $\mathrm{g}(\boldsymbol{x}_1)$ and $\mathrm{g}(\boldsymbol{x}_2)$

$$F(g_1, g_2, \boldsymbol{x}_1, \boldsymbol{x}_2) = P(\mathrm{g}(\boldsymbol{x}_1) \leq g_1, \mathrm{g}(\boldsymbol{x}_2) \leq g_2). \tag{3.49}$$

The corresponding second-order density can be computed using

$$p(g_1, g_2, \boldsymbol{x}_1, \boldsymbol{x}_2) = \frac{\partial^2 F_{\mathrm{g}}(g_1, g_2, \boldsymbol{x}_1, \boldsymbol{x}_2)}{\partial g_1, \partial g_2}. \tag{3.50}$$

Based on the second-order distribution, another important characteristic of the stochastic process, the expectation of the joint moment, the so-called *auto-correlation function*

$$\begin{aligned} r_{\mathrm{g}}(\boldsymbol{x}_1, \boldsymbol{x}_2) &= \int_{-\infty}^{\infty} \int_{-\infty}^{\infty} g_1 g_2 p_{\mathrm{g}}(g_1, g_2, \boldsymbol{x}_1, \boldsymbol{x}_2) \mathrm{d}g_1 \mathrm{d}g_2 \\ &= \mathbb{E}\Big[g_1 g_2\Big] \end{aligned} \tag{3.51}$$

can be computed. The so-called *auto-covariance function* is closely related to auto-correlation function and can be computed by

$$\begin{aligned} k_{\mathrm{g}}(\boldsymbol{x}_1, \boldsymbol{x}_2) &= \int_{-\infty}^{\infty} \int_{-\infty}^{\infty} [g_1 - m_{\mathrm{g}}(\boldsymbol{x}_1)][g_2 - m_{\mathrm{g}}(\boldsymbol{x}_2)] p_{\mathrm{g}}(g_1, g_2, \boldsymbol{x}_1, \boldsymbol{x}_2) \mathrm{d}g_1 \mathrm{d}g_2 \\ &= \mathbb{E}\Big[[g_1 - m_{\mathrm{g}}(\boldsymbol{x}_1)][g_2 - m_{\mathrm{g}}(\boldsymbol{x}_2)]\Big] \end{aligned} \tag{3.52}$$

The variance function $\sigma_{\mathrm{g}}^2(\boldsymbol{x})$ can be obtained from the covariance function by setting $\boldsymbol{x}_1 = \boldsymbol{x}_2 = \boldsymbol{x}$. Through division by the variance, the normalized auto-covariance function, or correlation coefficient function can be obtained.

$$\rho_{\mathrm{g}}(\boldsymbol{x}_1, \boldsymbol{x}_2) = \frac{k_{\mathrm{g}}(\boldsymbol{x}_1, \boldsymbol{x}_2)}{\sqrt{k_{\mathrm{g}}(\boldsymbol{x}_1, \boldsymbol{x}_1), k_{\mathrm{g}}(\boldsymbol{x}_2, \boldsymbol{x}_2)}} = \frac{k_{\mathrm{g}}(\boldsymbol{x}_1, \boldsymbol{x}_2)}{\sqrt{\sigma_{\mathrm{g}}^2(\boldsymbol{x}_1)\sigma_{\mathrm{g}}^2(\boldsymbol{x}_2)}} \tag{3.53}$$

The correlation coefficient functions provides a measure of linear dependence, analogous to the correlation coefficient for two random variables. Note, that the above definition of the auto-correlation function is not the one which is commonly used in the statistics literature, in which the auto-correlation function is typically defined as the normalized version of the auto-covariance function given by (3.53).

If a mean and covariance or correlation function are used to characterize a stochastic process, one speaks of a second-order or second moment characterization of the stochastic process. While this characterization is frequently used and mean and covariance function provide a lot of information, it is only an incomplete characterization of a general stochastic process since two processes with the same second-order description can exhibit very different sample properties. An exception to this rule are *Gaussian processes* (GPs), which are completely determined by mean and covariance function, and no additional information is required. GPs will be covered in more detail in the following section.

For the sake of completeness, it is mentioned that for a general stochastic process, a full specification of all n-th order densities is required [246]. The joint n-th order density is defined by

$$p_n(g_1, g_2, g_3, ..., g_n, \boldsymbol{x}_1, \boldsymbol{x}_2, \boldsymbol{x}_3, ..., \boldsymbol{x}_n). \tag{3.54}$$

A stochastic process is then defined by a system of n-th order probability density functions for all n and for every finite subset $\boldsymbol{x}_1, \boldsymbol{x}_2, \boldsymbol{x}_3, ..., \boldsymbol{x}_n$ of T.

There is rarely, if ever, sufficient data to determine the full joint probability distribution of a stochastic process. If the stochastic processes is *homogeneous* or *ergodic*, the analysis and synthesis of the stochastic process is significantly facilitated. While ergodicity entails homogeneity, the converse is not always true. Homogeneity in the strict sense means that the joint probability density p_n is invariant to translations of the parameters $\boldsymbol{x}_1, \boldsymbol{x}_2, \boldsymbol{x}_3.., \boldsymbol{x}_n$. If the parameter $\boldsymbol{x}$ is one-dimensional and especially if it is associated with time, the term stationarity is used instead of homogeneity. The strict sense definition is of limited practical value. Hence, in this work a stochastic process is referred to as homogeneous if it is homogenous in the weak sense, that is, homogeneous in mean and covariance. To be stationary in a weak sense, the following two conditions must hold. The mean function has to be constant and not dependent on the parameter $\boldsymbol{x}$, i.e.,

$$\mathbb{E}_{\mathrm{g}}[\mathrm{g}(\boldsymbol{x})] = m_{\mathrm{g}} = const < \infty, \; \forall \, \boldsymbol{x} \in T. \tag{3.55}$$

Furthermore, the covariance function has to depend only on the difference or lag between $\boldsymbol{x}_1$ and $\boldsymbol{x}_2$ and not on their absolute position

$$k_{\mathrm{g}}(\boldsymbol{x}_1, \boldsymbol{x}_2) = k_{\mathrm{g}}(\boldsymbol{x}_1 - \boldsymbol{x}_2) = k_{\mathrm{g}}(\boldsymbol{\tau}). \tag{3.56}$$

A stochastic process characterized by mean and covariance function which fulfill these conditions is homogeneous in the weak sense. Note, that in (3.56) $\boldsymbol{\tau}$, is the so-called *lag-vector* or simply lag.

Another property regarding the regularity of multi-dimensional processes is the isotropy of the covariance function. A covariance function of a multi-dimensional process is referred to as isotropic if its properties are invariant under rotation of the coordinate system which is equivalent to the covariance function only depending on the distance between two points, i.e.,

$$k_{\mathrm{g}}(\boldsymbol{x}_1, \boldsymbol{x}_2) = k_{\mathrm{g}}(\|\boldsymbol{x}_1 - \boldsymbol{x}_2\|) = k_{\mathrm{g}}(\|\boldsymbol{\tau}\|). \tag{3.57}$$

A stochastic process is ergodic in the strict sense if the joint probability distribution can be completely determined from one realization of the process alone. As with homogeneity, weaker criteria for ergodicity are often used. Roughly speaking, if a stochastic process is ergodic in the mean or correlation function, then the mean or the correlation function of the process can be computed from an average over the parameter space T. The formal requirements and conditions for ergodicity are omitted for the sake of brevity and the reader is referred to, e.g., [260, 308] for a more thorough definition.

Like random variables, stochastic processes can also be extended to the multivariate case. These types of processes are also referred to as *vector processes* in literature. If the individual components of the vector-process are coupled, the cross-correlation between the components is described with a cross-covariance function

$$k_{\mathrm{g_1 g_2}}(\boldsymbol{x}_1, \boldsymbol{x}_2) = \mathrm{cov}[\mathrm{g}_1(\boldsymbol{x}_1)\mathrm{g}_2(\boldsymbol{x}_2)]. \tag{3.58}$$

3.3.1 Gaussian processes

Having introduced the general concept of stochastic processes, this section deals with a special subclass of stochastic processes, so-called *Gaussian processes*. Moreover, this section intends to illustrate some of the introduced abstract concepts on the basis of GPs. A stochastic process is referred to as Gaussian if all joint probability distributions are Gaussian, i.e., it is an infinite collection of random variables, any finite subset of which has a multivariate Gaussian distribution. Also, the second-order probability distribution is Gaussian and thus for a fixed location parameter, a Gaussian random variable is obtained. A key feature of Gaussian processes is that they are fully specified by the definition of a mean $m_{\mathrm{g}}(\boldsymbol{x})$ and covariance function $k_{\mathrm{g}}(\boldsymbol{x}, \boldsymbol{x}')$. Throughout this work, the following notation to define a Gaussian process will be used:

$$\mathrm{g}(\boldsymbol{x}) \sim \mathcal{GP}(m_{\mathrm{g}}(\boldsymbol{x}), k_{\mathrm{g}}(\boldsymbol{x}, \boldsymbol{x}')). \tag{3.59}$$

Note that from here on, the common notation $\boldsymbol{x}$ and $\boldsymbol{x}'$ instead of $\boldsymbol{x}_1$ and $\boldsymbol{x}_2$ for the arguments of the covariance function will be used. Like other stochastic processes, Gaussian processes can be interpreted as a distribution over functions, in the sense that a Gaussian process defines an ensemble of functions which share some common properties. The mean function defines an overall trend whereas the covariance function defines the smoothness, the scale of fluctuations, and the amount of fluctuation of the realizations or sample functions. For a visualization, consider the realizations of a one-dimensional, stationary Gaussian process depicted in Figure 3.3. The figure shows four realizations of two zero mean Gaussian processes with different covariance functions, resulting in, roughly speaking, different degrees of smoothness. This illustrates the usage of a stochastic process as a tool to specify a collection of functions with certain properties that are characterized statistically. In addition, Figure 3.3 shows the 95% confidence area

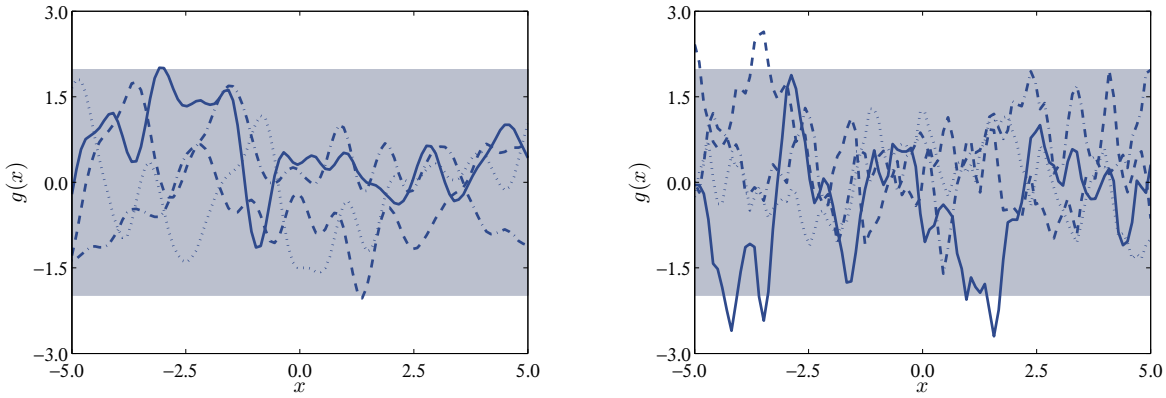

Figure 3.3 Realisations of Gaussian processes and 95% confidence interval. (a) Squared exponential covariance function, (b) Matérn covariance function.

which is based on the variance of the Gaussian random variables at each of the input points. In the following, the covariance functions that are employed in this work will be introduced to discuss their parameters and overall properties.

3.3.1.1 Covariance functions

Not every conceivable function of $\boldsymbol{x}$ and $\boldsymbol{x}'$ constitutes a valid covariance function. In order to be an admissible covariance function, the function must be positive semidefinite. In this context, this means that any $n \times n$ matrix $\boldsymbol{K}$ which is computed based on the points $\{\boldsymbol{x}^{(i)}\}_{i=1}^{n}$ and has the entries $K_{ij} = k(\boldsymbol{x}^{(i)}, \boldsymbol{x}^{(j)})$, is positive semidefinite. In the following, the covariance functions that are used in this work are introduced. For a comprehensive overview of covariance functions, the reader is referred to, e.g., [2, 361].

Squared exponential covariance function One of the most common covariance function is the so-called squared exponential or Gaussian covariance function. In its simplest form, the covariance only depends on the absolute distance between two points $\boldsymbol{x}$ and $\boldsymbol{x}'$,

$$k(\boldsymbol{x}, \boldsymbol{x}') = \sigma_{\mathrm{g}}^2 \exp\{-\frac{\|\boldsymbol{x} - \boldsymbol{x}'\|^2}{\ell^2}\}. \tag{3.60}$$

Therein, σ_{g}^2 denotes the variance of the process, i.e., the variance of the Gaussian random variable for fixed $\boldsymbol{x}$. Often, a slightly different definition of this covariance function is used where ℓ^2 is multiplied by a factor two. The parameter ℓ defines the characteristic length-scale of the process, which determines how fast the correlation between the value of the process at two points decays with their distance. For a one-dimensional process, this is illustrated in Figure 3.4. Figure 3.4a depicts the covariance function for two different characteristics length scales and Figure 3.4b shows three realizations for each of the corresponding processes.

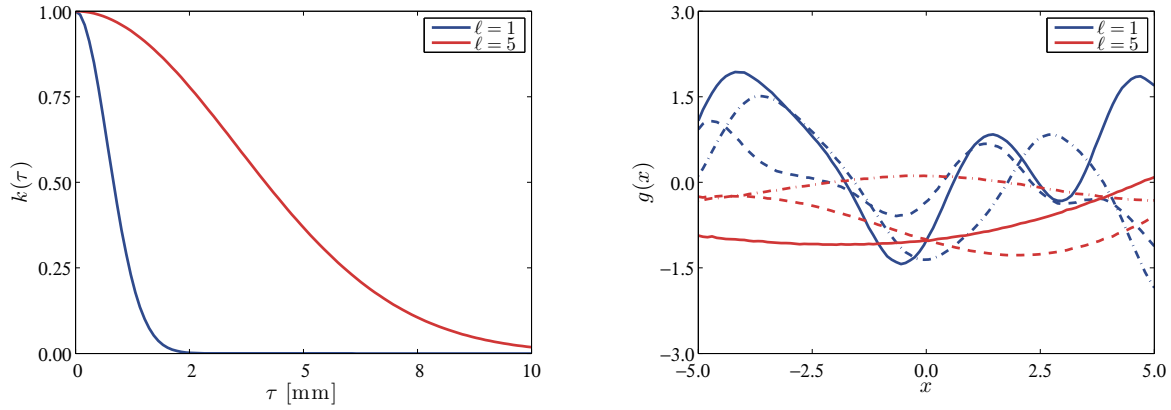

(a) **(b)**

Figure 3.4 Influence of characteristic length scale. (a) Squared exponential covariance function with unit variance and different characteristic length scales. (b) Realizations drawn from Gaussian processes with a squared exponential covariance function.

If the process shows a different behavior for each dimension, this can be accounted for by separately prescribing a characteristic length scale for each dimension. (3.60) then becomes

$$k(\boldsymbol{x}, \boldsymbol{x}') = \sigma_{\mathrm{g}}^2 \exp\{-(\boldsymbol{x} - \boldsymbol{x}')^T \boldsymbol{P}^{-1} (\boldsymbol{x} - \boldsymbol{x}')\} \tag{3.61}$$

with the diagonal $\boldsymbol{P}$ matrix that contains the squares of the characteristic length scales $\ell_i^2 > 0$ for the different dimensions

$$\boldsymbol{P} = \begin{pmatrix} \ell_1^2 & & & \\ & \ell_2^2 & & \\ & & \ddots & \\ & & & \ell_d^2 \end{pmatrix}. \tag{3.62}$$

Example realizations of one isotropic and one anisotropic process are shown in Figure 3.5.

Matérn Class of covariance functions In its general form the Matérn class of covariance functions [209] is given by

$$k(r) = \sigma_{\mathrm{g}}^2 \frac{2^{1-\nu}}{\Gamma(\nu)} \left(\sqrt{2\nu} r\right)^{\nu} B_\nu \left(\sqrt{2\nu} r\right) \tag{3.63}$$

where r is definded as

$$r = \sqrt{(\boldsymbol{x} - \boldsymbol{x}')^T \boldsymbol{P}^{-1} (\boldsymbol{x} - \boldsymbol{x}')}, \tag{3.64}$$

and $B_\nu(\cdot)$ is a modified Bessel function [3]. In addition to the characteristic length scales ℓ_i, the Matérn class has another positive parameter ν which controls the smoothness of the process. In the limit $\nu \to \infty$, the squared exponential covariance function is retained. For small ν, the corresponding stochastic process is rougher. After some algebraic rearrangement, setting $\nu = 3/2$ yields

$$k(\boldsymbol{x}, \boldsymbol{x}') = \sigma_{\mathrm{g}}^2 \left(1 + \sqrt{3} r\right) \exp\left(-\sqrt{3} r\right). \tag{3.65}$$

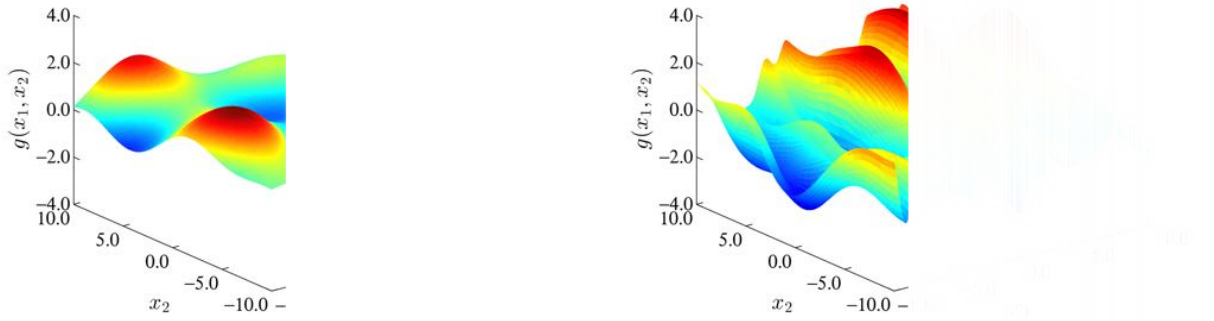

(a) **(b)**

Figure 3.5 Realizations of two-dimensional Gaussian processes (a) Realization of isotropic process (b) Realization of anisotropic process, i.e., different characteristic length scales in x_1 and x_2.

3.3.2 Non-Gaussian processes

There are many natural phenomena that cannot be accurately described, or are incompatible with a Gaussian distribution. For instance, the random parameters considered in this work exhibit a distinct non-Gaussian distribution. Characterization of a non-Gaussian process through its family of finite-dimensional distribution functions is difficult. In this work, a restriction to a special class of non-Gaussian processes, namely so-called translation processes, is made and the reader is referred to [131] for a more detailed discussion of this subject. The non-Gaussian translation processes considered in this work can be obtained via memoryless transformation from a Gaussian process. Based on a Gaussian process $\mathsf{g}(\boldsymbol{x})$ with zero mean unit variance and homogeneous covariance function, a non-Gaussian translation process can be obtained via the following nonlinear transformation [131]

$$\mathsf{h}(\boldsymbol{x}) = F_{\mathsf{h}}^{-1} \circ \Phi\big(\mathsf{g}(\boldsymbol{x})\big) = F_{\mathsf{h}}^{-1}\{\Phi\big(\mathsf{g}(\boldsymbol{x})\big)\} \tag{3.66}$$

where $\Phi(\cdot)$ denotes the standard Gaussian CDF as in (3.38) of the underlying Gaussian process, F_{h} denotes an arbitrary non-Gaussian target CDF, and F_{h}^{-1} the corresponding inverse function. The transformation is called memoryless because the value of $\mathsf{g}(\boldsymbol{x})$ at an arbitrary location $\boldsymbol{x}$ depends solely on the value of $\mathsf{g}(\boldsymbol{x})$ at $\boldsymbol{x}$.

If the distribution $F_{\mathsf{h}}(h)$ is continuous, then the resulting process $\mathsf{h}(\boldsymbol{x})$ has the first-order probability distribution

$$P\big(\mathsf{h}(\boldsymbol{x}) \leq h\big) = P\big(F_{\mathsf{h}}^{-1} \circ \Phi\big(\mathsf{g}(\boldsymbol{x})\big)\big) \leq h) = F_{\mathsf{h}}(h), \tag{3.67}$$

and thus $\mathsf{h}(\boldsymbol{x})$ can have arbitrary first-order probability distributions. The q-th order moment is obtained via

$$\mathbb{E}[\mathsf{h}(\boldsymbol{x})]^q = \mathbb{E}[F_{\mathsf{g}}^{-1} \circ \Phi\big(\mathsf{g}(\boldsymbol{x})\big)]^q = \int_{-\infty}^{\infty} \big(F_{\mathsf{h}}^{-1}\{\Phi(g)\}\big)^q \phi(g)\mathrm{d}g \tag{3.68}$$

The transformation also affects the auto-covariance function of the process. According to Grigoriu [131], the auto-correlation function of the translation process can be computed based on the normalized auto-covariance function $\rho(\tau)$ of the underlying Gaussian process by

$$k_{\mathsf{h}}(\boldsymbol{\tau}) = \int_{-\infty}^{\infty}\int_{-\infty}^{\infty} F_{\mathsf{h}}^{-1}\{\Phi(g_1)\}F_{\mathsf{h}}^{-1}\{\Phi(g_2)\}\phi\big(g_1, g_2; \rho_{\mathsf{g}}(\boldsymbol{\tau})\big)\mathrm{d}g_1\mathrm{d}g_2 \tag{3.69}$$

where ϕ denotes the standard joint Gaussian density of the two correlated random variables $\mathsf{g}_1 = \mathsf{g}(\boldsymbol{x})$ and $\mathsf{g}_2 = \mathsf{g}(\boldsymbol{x}+\boldsymbol{\tau})$. In analogy to (3.69), higher-order densities of $\mathsf{h}(\boldsymbol{x})$ can also be computed, see, e.g., [131].

3.3.3 Sample generation techniques for Gaussian processes

In the context of UQ, one needs to generate sample functions of stochastic processes, or rather evaluate sample functions at discrete points in space or time. The procedure of generating discrete realizations of stochastic processes is often referred to as simulation of stochastic processes in the corresponding literature. In order to avoid misunderstandings, the term simulation is avoided in the context of generating realizations of stochastic processes and is used only in the context of finite element simulations.

The most important aspect of generating sample functions is accuracy, in the sense that an ensemble of generated sample functions shows the desired properties in terms of first-order distribution function and auto-covariance function. The second requirement is the efficiency of the generating algorithm, i.e., the computational effort to compute one realization of the stochastic process with a given spatial or temporal resolution. Another issue, which arises mainly in the context of UQ with certain methods, regards the dimensionality of the representation. Essentially, all approaches to generate sample functions aim at achieving this based on a vector of independent random variables from which samples can be drawn using standard pseudorandom number generators. Depending on the employed approach to generate the sample functions, the number of random variables needed to represent a stochastic process can differ significantly. As the efficiency of some UQ approaches depend on the number of random variables, this can be an important criterion and maybe explains the popularity of some approaches, particularly, in the stochastic mechanics community.

The generation of sample functions of stochastic processes is a field of ongoing investigation and active research, in particular for non-Gaussian processes. Many approaches have been proposed in the past, an in depth introduction and discussion of which is well beyond the scope of this work. In the following sections, the methods to generate sample functions of stochastic processes, which are used in this work, are introduced and the difficulties that can arise in the non-Gaussian case will be discussed. For a more in depth and complete overview of techniques to generate sample functions of stochastic processes, the reader is referred to, e.g., [41, 309, 314].

3.3.3.1 Direct decomposition of the covariance matrix

If one is interested in a realization of a Gaussian process evaluated at a moderate number of locations $\{\boldsymbol{x}^{(i)}\}_{i=1}^{N}$, all that is needed is a draw from a finite-dimensional multivariate Gaussian

distribution. The mean vector $\boldsymbol{\mu}$ and the covariance matrix $\boldsymbol{\Sigma}$ are readily obtained from the mean and covariance function of the process

$$\mu_i = m(\boldsymbol{x}^{(i)}) \quad \Sigma_{ij} = \mathrm{cov}(\boldsymbol{x}^{(i)}, \boldsymbol{x}^{(j)}) \quad i, j = 1, ..., N. \tag{3.70}$$

A sample from a multivariate Gaussian distribution $\mathcal{N}(\boldsymbol{\mu}, \boldsymbol{\Sigma})$ is obtained using a sample of uncorrelated Gaussian variables with zero mean and unit variance and the following relationship

$$\mathbf{g} = \boldsymbol{\mu} + \boldsymbol{L}\mathbf{z} \tag{3.71}$$

where $\boldsymbol{L}$ is defined as $\boldsymbol{L}\boldsymbol{L}^T = \boldsymbol{\Sigma}$. Independent samples from the standard normal distribution are readily available through standard pseudorandom number generators. The decomposition of the covariance matrix can be performed with, e.g., the Cholesky factorization. If the required spatial or temporal resolution is high, i.e., the number of points N is large, the Cholesky factorization, which has a computational complexity of approximately $N^3/3$, becomes impractical. In addition, UQ approaches, whose computational complexity depends on the number of random input variables, can in general not be used in combination with this approach since the stochastic dimension is to high even for moderate spatial resolutions.

3.3.3.2 Karhunen-Loève expansion

Another alternative for the generation of sample functions, that is popular especially in the stochastic mechanics community, is based on the Karhunen-Loève expansion of the stochastic process. The Karhunen-Loève expansion has been proposed by several authors in the late 1940's [169, 170, 196] and is also known in other fields of study as principal component analysis or proper orthogonal decomposition. Consider the stochastic process $\mathsf{g}(\boldsymbol{x}, \omega)$ where $\boldsymbol{x}$ is the location vector defined on a domain $\boldsymbol{D}$ and ω denotes an event from the sample space Ω. Dependence on ω is omitted in the following for the sake of an uncluttered notation. The Karhunen-Loève expansion decomposes the sample functions of a centered, i.e., zero mean stochastic process into the following series

$$\mathsf{g}(\boldsymbol{x}) = \sum_{k=0}^{\infty} \sqrt{\lambda_k} v_k(\boldsymbol{x}) \mathsf{z}_k, \tag{3.72}$$

where $\{\mathsf{z}_k\}$ is a set of uncorrelated random variables and λ_k and $v_k(\boldsymbol{x})$ are the eigenvalues and eigenfunctions of the covariance kernel of the stochastic process, respectively. The eigenvalues and eigenfunctions can be determined by solving the following integral equation

$$\int_{\boldsymbol{D}} k_{\mathsf{g}}(\boldsymbol{x}, \boldsymbol{x}') v_k(\boldsymbol{x}) \mathrm{d}\boldsymbol{x} = \lambda_k v_k(\boldsymbol{x}'). \tag{3.73}$$

The series is optimal in the Fourier sense, that is, it minimizes mean squared error when truncated after a finite number of terms and it can be shown that the expansion is unique [117]. If the expanded process is Gaussian, the set of random variables $\{\mathsf{z}_k\}$ becomes Gaussian, too, and as a consequence of the Gaussian property, they are also independent. Thus, realizations of a Gaussian process can be generated using the truncated version of (3.72)

$$\mathsf{g}(\boldsymbol{x}) = \sum_{k=0}^{N} \sqrt{\lambda_k} v_k(\boldsymbol{x}) \mathsf{z}_k, \tag{3.74}$$

in combination with a vector of independent Gaussian random variables with zero mean and unit variance. These are available through standard random number generators. Of course, non-centered Gaussian processes with mean $\mathbb{E}_{\mathsf{g}}[\mathsf{g}(\boldsymbol{x})]$ can also be considered using

$$\mathsf{g}(\boldsymbol{x}) = \mathbb{E}_{\mathsf{g}}[\mathsf{g}(\boldsymbol{x})] + \sum_{k=0}^{\infty} \sqrt{\lambda_k} v_k(\boldsymbol{x}) \mathsf{z}_k = m_{\mathsf{g}}(\boldsymbol{x}) + \sum_{k=0}^{\infty} \sqrt{\lambda_k} v_k(\boldsymbol{x}) \mathsf{z}_k. \tag{3.75}$$

The number of terms that have to be considered in the expansion depends on the regularity and smoothness of the covariance function. Furthermore, the characteristic length scale of the covariance functions plays an important role. The shorter the characteristic length, the more terms have to be considered in the Karhunen-Loève expansion to keep the error of the approximation constant.

In order to generate realizations using (3.72), the functions $v_k(\boldsymbol{x})$ must be determined by solving the generalized eigenvalue problem (3.73). Analytic solutions are available only for very few covariance functions, e.g., the exponential covariance function [117], and hence a numerical approach to solve (3.73) is often required. One option to obtain a numerical solution is to use a Galerkin projection based on a finite element discretization [117]. Recently, it has been shown that the Karhunen-Loève expansion is independent from the domain on which the eigenvalue problem is solved [257].

3.3.3.3 Direct Fourier series expansion of the covariance function

Similar to the frequently employed Karhunen-Love expansion Nobile et al. [230] and Tamellini [322] proposed a Fourier expansion of the covariance function in order to facilitate the generation of sample functions of homogeneous Gaussian processes with a squared exponential covariance structure. It allows for an efficient truncation of the series and enables a fast computation. Extended to the three-dimensional case, the formula from [230] reads

$$\begin{aligned}
\mathsf{g}(\boldsymbol{x}) = \mathbb{E}_{\mathsf{g}}[\mathsf{g}(\boldsymbol{x})] + \sigma_{\mathsf{g}} \sum_{\boldsymbol{k}=(k_1,k_2,k_3)\in\mathbb{N}_0^3} \sqrt{c_{\boldsymbol{k}}}[& \\
& \mathsf{z}_{\boldsymbol{k}}^1 \cos(\omega_{k_1} x_1) \cos(\omega_{k_2} x_2) \cos(\omega_{k_3} x_3) \\
& + \mathsf{z}_{\boldsymbol{k}}^2 \sin(\omega_{k_1} x_1) \sin(\omega_{k_2} x_2) \cos(\omega_{k_3} x_3) \\
& + \mathsf{z}_{\boldsymbol{k}}^3 \cos(\omega_{k_1} x_1) \sin(\omega_{k_2} x_2) \cos(\omega_{k_3} x_3) \\
& + \mathsf{z}_{\boldsymbol{k}}^4 \sin(\omega_{k_1} x_1) \cos(\omega_{k_2} x_2) \cos(\omega_{k_3} x_3) \\
& + \mathsf{z}_{\boldsymbol{k}}^5 \cos(\omega_{k_1} x_1) \cos(\omega_{k_2} x_2) \sin(\omega_{k_3} x_3) \\
& + \mathsf{z}_{\boldsymbol{k}}^6 \sin(\omega_{k_1} x_1) \sin(\omega_{k_2} x_2) \sin(\omega_{k_3} x_3) \\
& + \mathsf{z}_{\boldsymbol{k}}^7 \cos(\omega_{k_1} x_1) \sin(\omega_{k_2} x_2) \sin(\omega_{k_3} x_3) \\
& + \mathsf{z}_{\boldsymbol{k}}^8 \sin(\omega_{k_1} x_1) \cos(\omega_{k_2} x_2) \sin(\omega_{k_3} x_3)],
\end{aligned} \tag{3.76}$$

where $\omega_{k_1} = \frac{k_1\pi}{\tilde{L}}, \omega_{k_2} = \frac{k_2\pi}{\tilde{L}}, \omega_{k_3} = \frac{k_3\pi}{\tilde{L}}$. Here $\tilde{L}$ denotes the length of the generated field in all three dimensions. Moreover, $\mathsf{z}_{\boldsymbol{k}}^i$ denotes random amplitudes that are independent identically distributed (i.i.d) standard normal random variables. The normalized coefficients $c_{\boldsymbol{k}}$ fulfill the following condition

$$\sum_{\boldsymbol{k}=(k_1,k_2,k_3)\in\mathbb{N}_0^3} c_{\boldsymbol{k}} = 1, \tag{3.77}$$

and can be computed using

$$c_{\boldsymbol{k}} \approx \lambda_{k_1}\lambda_{k_2}\lambda_{k_3}, \quad \lambda_{k_i} = \begin{cases} \frac{\ell\sqrt{\pi}}{2\tilde{L}} & \text{if } k = 0 \\ \frac{\ell\sqrt{\pi}}{\tilde{L}} \exp\left(-\frac{k\pi\ell^2}{4\tilde{L}^2}\right) & \text{if } k > 0 \end{cases} \tag{3.78}$$

To be computable, the series in (3.79) has to be truncated

$$\begin{aligned} \mathsf{g}(\boldsymbol{x}) = \mathbb{E}_{\mathsf{g}}[\mathsf{g}(\boldsymbol{x})] + \sigma \sum_{\boldsymbol{k}=(k_1,k_2,k_3)\in\mathcal{K}} \sqrt{c_{\boldsymbol{k}}}[\\ \mathsf{z}^1_{\boldsymbol{k}} \cos(\omega_{k_1}x_1)\cos(\omega_{k_2}x_2)\cos(\omega_{k_3}x_3) \\ + \mathsf{z}^2_{\boldsymbol{k}} \sin(\omega_{k_1}x_1)\sin(\omega_{k_2}x_2)\cos(\omega_{k_3}x_3) \\ + \mathsf{z}^3_{\boldsymbol{k}} \cos(\omega_{k_1}x_1)\sin(\omega_{k_2}x_2)\cos(\omega_{k_3}x_3) \\ + \mathsf{z}^4_{\boldsymbol{k}} \sin(\omega_{k_1}x_1)\cos(\omega_{k_2}x_2)\cos(\omega_{k_3}x_3) \\ + \mathsf{z}^5_{\boldsymbol{k}} \cos(\omega_{k_1}x_1)\cos(\omega_{k_2}x_2)\sin(\omega_{k_3}x_3) \\ + \mathsf{z}^6_{\boldsymbol{k}} \sin(\omega_{k_1}x_1)\sin(\omega_{k_2}x_2)\sin(\omega_{k_3}x_3) \\ + \mathsf{z}^7_{\boldsymbol{k}} \cos(\omega_{k_1}x_1)\sin(\omega_{k_2}x_2)\sin(\omega_{k_3}x_3) \\ + \mathsf{z}^8_{\boldsymbol{k}} \sin(\omega_{k_1}x_1)\cos(\omega_{k_2}x_2)\sin(\omega_{k_3}x_3)], \end{aligned} \tag{3.79}$$

where $\mathcal{K}$ is an indexing set that is large enough to take a sufficient portion of the total variability of the the process g into account. The amount of variability γ retained by the truncation in (3.79) can be computed by $\sum_{\boldsymbol{k}\in\mathcal{K}_0^3} c_{\boldsymbol{k}} = \gamma$ Moreover, since the magnitude of the coefficients $c_{\boldsymbol{k}}$ is proportional to $k_1^2 + k_2^2 + k_3^2$, the following truncation is used

$$\mathcal{K} = \{\boldsymbol{k} : k_1^2 + k_2^2 + k_3^2 < n_k, n_k \in \mathbb{N}\}. \tag{3.80}$$

The amount of variability that is retained by the expansion can be adjusted by changing the truncation threshold n_k. Note that the expansion given above produces accurate results for $\ell < 0.35\tilde{L}$ [322].

3.3.3.4 Spectral representation method

Another method to generate sample functions of stochastic processes is based on the so-called spectral representation method which was pioneered in [299–301]. The so-called power spectral density (PSD), which describes the distribution of variance over generalized frequency, can be computed from the auto-covariance function of a process, and vice versa, by the Wiener-Khintchine relationships [176, 357]

$$s_{\mathsf{g}}(\boldsymbol{\kappa}) = \frac{1}{(2\pi)^d} \int_{-\infty}^{\infty} e^{-i\boldsymbol{\kappa}\boldsymbol{\tau}} k_{\mathsf{g}}(\boldsymbol{\tau}) \mathrm{d}\boldsymbol{\tau} \tag{3.81}$$

and

$$k_{\mathsf{g}}(\boldsymbol{\tau}) = \int_{-\infty}^{\infty} e^{i\boldsymbol{\kappa}\boldsymbol{\tau}} s_{\mathsf{g}}(\boldsymbol{\kappa}) \mathrm{d}\boldsymbol{\kappa}. \tag{3.82}$$

Therein, d denotes the dimension of the index set $\boldsymbol{x}$, $\boldsymbol{\tau}$ the lag-vector, and $\boldsymbol{\kappa}$ the generalised frequency vector. For some auto-covariance functions, an analytic solution of (3.81) exists [6,

264, 341]. For the sake of completeness, because the squared exponential covariance function is used frequently in this work, the corresponding PSD is stated explicitly in the following. For a d-dimensional process, the squared exponential covariance function

$$k_{\mathrm{g}}(\boldsymbol{\tau}) = \sigma_{\mathrm{g}}^2 \exp\Big[-\big(\frac{\|\boldsymbol{\tau}\|}{\ell}\big)^2\Big], \tag{3.83}$$

corresponds to the power-spectral density [368]

$$s_{\mathrm{g}}(\boldsymbol{\kappa}) = \sigma_{\mathrm{g}}^2\big(\frac{\ell}{2\sqrt{\pi}}\big)^d \exp\big[-\big(\frac{\ell\,\|\boldsymbol{\kappa}\|}{2}\big)^2\big]. \tag{3.84}$$

Based on a PSD, realizations of a multi-dimensional, homogeneous, Gaussian stochastic processes can be generated using the spectral representation method [299]. Thereby, the realizations of the process are represented by a series of cosine functions with random phase angles. The spectral representation can be applied to create sample functions of one or multi-dimensional stochastic processes. In the following, the methodology is introduced for the three-dimensional case, i.e., $\boldsymbol{x} = (x_1, x_2, x_3)$ since it is the formulation used in this work. According to Shinozuka and Deodatis [299], a three-dimensional stochastic process can be represented by the following series for $N_1, N_2, N_3 \to \infty$,

$$\begin{aligned}\mathsf{g}(\boldsymbol{x}) = \mathsf{g}(x_1, x_2, x_3) =& \sqrt{2}\sum_{n_1=0}^{N_1-1}\sum_{n_2=0}^{N_2-1}\sum_{n_3=0}^{N_3-1}\sqrt{2 s_{\mathrm{g}}(\kappa_{1n_1}, \kappa_{2n_2}, \kappa_{3n_3})\Delta\kappa_1\Delta\kappa_2\Delta\kappa_3}\\ &\Big[\cos\big(\kappa_{1n_1}x_1 + \kappa_{2n_2}x_2 + \kappa_{3n_3}x_3 + \mathsf{u}^1_{n_1n_2n_3}\big)\\ &+ \cos\big(\kappa_{1n_1}x_1 - \kappa_{2n_2}x_2 + \kappa_{3n_3}x_3 + \mathsf{u}^2_{n_1n_2n_3}\big)\\ &+ \cos\big(\kappa_{1n_1}x_1 + \kappa_{2n_2}x_2 - \kappa_{3n_3}x_3 + \mathsf{u}^3_{n_1n_2n_3}\big)\\ &+ \cos\big(\kappa_{1n_1}x_1 - \kappa_{2n_2}x_2 - \kappa_{3n_3}x_3 + \mathsf{u}^4_{n_1n_2n_3}\big)\Big].\end{aligned}$$

Here the $\mathsf{u}^i_{n_1n_2n_3}, i = 1, ..., 4$, denote four different sets of independent random phase angles which are uniformly distributed (cf. Table A.1) in the range $[0, 2\pi]$. Furthermore,

$$\kappa_{1n_1} = n_1\Delta\kappa_1; \quad \kappa_{2n_2} = n_2\Delta\kappa_2; \quad \kappa_{3n_3} = n_3\Delta\kappa_3; \tag{3.85}$$

$$\Delta\kappa_1 = \frac{\kappa_{1u}}{N_1}; \quad \Delta\kappa_2 = \frac{\kappa_{2u}}{N_2}; \quad \Delta\kappa_3 = \frac{\kappa_{3u}}{N_3} \tag{3.86}$$

where κ_{1u} , κ_{2u}, and κ_{3u} are the upper cut-off wave numbers above which the PSD is assumed to be zero or at least of insignificant magnitude. Sample functions generated with (3.85) are asymptotically Gaussian for $N \to \infty$ by virtue of the central limit theorem. However, a value of $N_i = 64$ yielded accurate results and hence was used throughout this work for the generation of sample functions.

It is important to note that (3.85) is valid only for so-called quadrant symmetric processes [341] where the PSD and the auto-covariance function fulfill the symmetry conditions

$$\begin{aligned}&k_{\mathrm{g}}(x_1, x_2, x_3) = k_{\mathrm{g}}(x_1, x_2, -x_3) = k_{\mathrm{g}}(x_1, -x_2, x_3) = k_{\mathrm{g}}(-x_1, x_2, x_3) =\\ &k_{\mathrm{g}}(x_1, -x_2, -x_3) = k_{\mathrm{g}}(-x_1, -x_2, x_3) = k_{\mathrm{g}}(-x_1, x_2, -x_3) = k_{\mathrm{g}}(-x_1, -x_2, -x_3),\end{aligned} \tag{3.87}$$

$$
\begin{aligned}
&s_{\mathrm{g}}(\kappa_1,\kappa_2,\kappa_3) = s_{\mathrm{g}}(\kappa_1,\kappa_2,-\kappa_3) = s_{\mathrm{g}}(\kappa_1,-\kappa_2,\kappa_3) = s_{\mathrm{g}}(-\kappa_1,\kappa_2,\kappa_3) = \\
&s_{\mathrm{g}}(\kappa_1,-\kappa_2,-\kappa_3) = s_{\mathrm{g}}(-\kappa_1,-\kappa_2,\kappa_3) = s_{\mathrm{g}}(-\kappa_1,\kappa_2,-\kappa_3) = s_{\mathrm{g}}(-\kappa_1,-\kappa_2,-\kappa_3).
\end{aligned} \tag{3.88}
$$

While the conditions for quadrant symmetry are always fulfilled in the examples considered in this work and hence (3.85) can be used to generate sample functions of Gaussian processes, the formula for the general case can be found in [299], which also contains the formulas for lower dimensional processes.

It can be shown that the samples generated using (3.85) are periodic along all axes with the periods

$$
\tilde{L}_{x_1} = \frac{2\pi}{\Delta\kappa_1}; \quad \tilde{L}_{x_2} = \frac{2\pi}{\Delta\kappa_2}; \quad \tilde{L}_{x_3} = \frac{2\pi}{\Delta\kappa_3}; \tag{3.89}
$$

As a consequence, if the cut-off wave numbers are fixed, the periods become longer as smaller $\Delta\kappa_i$ or larger N_i are chosen, respectively. While (3.85) is easy to implement, especially if the PSD is available in closed form, the formulation is not particularly efficient because of the three-fold sum and the large number of necessary cosine function evaluation. However, (3.85) can be restated in a form that admits treatment and sample function generation using the Fast Fourier Transform (FFT), which significantly speeds up the computation [299, 369]. Using the FFT technique to generate realization based on the spectral representation works very well for one- and two-dimensional processes. However, for three-dimensional processes memory limitation often hampers the effective application of the FFT. Processes with longer characteristic length scales require smaller $\Delta\kappa_i$ to properly resolve the frequency content. In combination with spatial resolution requirements, this can result in very large three-dimensional arrays impeding the use of standard FFT techniques and libraries even on current hardware. Hence, one has to resort to the direct but slower computation using (3.85).

It is mentioned that the approaches described above are, in fact, related, e.g., it can be shown that the Karhunen-Loève expansion is equivalent to the spectral representation method in some circumstances [134, 310].

3.3.4 Sample generation techniques for non-Gaussian processes

In this work, non-Gaussian processes are used as probabilistic model for random media and geometries. The Gaussian model cannot be used because of physical constraints such as positivity. While Gaussian processes are fully described by their mean and covariance function, this is not the case for non-Gaussian processes. Nevertheless, a second-order description is frequently used for non-Gaussian processes as well. Hence, when generating sample functions of non-Gaussian processes, the goal is to generate an ensemble of functions which match a prescribed first-order probability distribution and a prescribed covariance function.

Using translation process theory it is possible to generate an ensemble of sample functions which match the prescribed first-order probability distribution. Therefore, sample functions $g^{(i)}(\boldsymbol{x})$ from a Gaussian process with zero mean and unit variance are generated first. These sample function are then transformed by

$$
h^{(i)}(\boldsymbol{x}) = F_{\mathrm{h}}^{-1}\{\Phi\big(g^{(i)}(\boldsymbol{x})\big)\}, \tag{3.90}
$$

and samples from a non-Gaussian process which exhibits the desired first-order distribution are obtained. Matching a prescribed covariance function in addition to the first-order distribution can be significantly more challenging, in some cases even impossible. The normalized covariance function $\rho_{\mathrm{g}}(\boldsymbol{\tau})$ of the underlying Gaussian process is affected by the nonlinear transformation in (3.90) and the resulting translation process will exhibit a different normalized covariance function $\rho_{\mathrm{h}}(\boldsymbol{\tau})$, which can be computed using (3.69). Thus, in order for the normalized covariance of the non-Gaussian process to match a prescribed target normalized covariance $\rho_{\mathrm{h},t}(\boldsymbol{\tau})$, (3.69) has to be inverted to compute a covariance function of the underlying Gaussian process, which, if translated, will yield the desired target function. However, this approach is not always feasible as covariance function and first-order distribution have to be compatible and cannot be prescribed arbitrarily. Grigoriu [131] distinguishes two cases of incompatibility where the inversion of (3.69) cannot be used to compute a valid normalized covariance function for the underlying Gaussian process. Briefly, the transformation (3.69) maps the normalized covariance function of the Gaussian process, which can take values in the range $[-1, 1]$, to the normalized covariance function of the non-Gaussian image, which takes values in the range $[\xi^*, 1]$. This behavior is called correlation distortion. The lower bound ξ^* depends on the nonlinear transform and thus on the desired first-order distribution and is not necessarily equal to -1 [131]. The desired $\rho_{\mathrm{h},t}(\boldsymbol{\tau})$ can only take values in this range. If it takes values outside the admissible range, one speaks of type one incompatibility. Type two incompatibility arises when the inverse transformation of $\rho_{\mathrm{h},t}$ results in a function which is not positive semi-definite and hence not admissible as a normalized covariance function of the underlying Gaussian process.

However, even if one of the aforementioned incompatibilities between covariance function and first-order distribution arises, it is often desirable to employ translation process theory to generate samples which match the prescribed characteristics as closely as possible. Depending on the application, the focus might shift between the accurate representation of the first-order distribution or the covariance function. In reliability problems where random media are modeled using non-Gaussian processes, it is considered more important to match the first-order probability distribution including an accurate representation of its tails [132].

Nevertheless, additionally matching the prescribed covariance function as close as possible is desirable for some applications as well and hence the efficient and generation of sample functions of non-Gaussian stochastic processes has been and still is an area of active and ongoing research. An in-depth discussion of the various possibilities and approaches is well beyond the scope of this work. However, for the sake of completeness some reference to important publications in this area of research are given here in chronological order: Yamazaki and Shinozuka [369], Grigoriu [131, 132], Gurley et al. [139], Popescu et al. [254], Gurley and Kareem [138], Deodatis and Micaletti [80], Puig et al. [261], Sakamoto and Ghanem [286, 287], Graham et al. [124], Shi and Deodatis [295], Bocchini and Deodatis [41], Shields et al. [297].

The approach proposed by Shields et al. [297] is very appealing because of its simplicity and efficiency and has been implemented in this work to be able to modify the normalized auto-covariance function of the underlying Gaussian process such that the covariance function of the non-Gaussian process matches a prescribed target. The approach is used here since it works for for the compatible case as well and it is based on an iterative scheme which relies on the repeated evaluation of (3.69) and then (3.81), followed by an update of the PSD of the

underlying Gaussian process s_{g} using

$$s_{\mathrm{g}}^{i+1}(\boldsymbol{\kappa}) = \left[\frac{s_{\mathrm{h},t}(\boldsymbol{\kappa})}{s_{\mathrm{h}}^{i}(\boldsymbol{\kappa})}\right]^{\lambda} s_{\mathrm{g}}^{i}(\boldsymbol{\kappa}). \tag{3.91}$$

Therein, $s_{\mathrm{h},t}$ denotes the desired target PSD, which corresponds to the desired target covariance function, and s_{g} denotes the PSD of the underlying Gaussian process in iteration i and $i+1$, respectively. The parameter is set to 1.4, in accordance with Shields et al. [297] to optimize convergence speed. In the first iteration, $s_{\mathrm{h}}^{1}(\boldsymbol{\kappa})$ is set to $s_{\mathrm{h},t}(\boldsymbol{\kappa})$ as start value. The iterative scheme is terminated once a the relative difference between $s_{\mathrm{h},t}(\boldsymbol{\kappa})$ and $s_{\mathrm{h}}^{i}(\boldsymbol{\kappa})$ reaches a predefined threshold.

For a simple covariance function such as the isotropic, radially symmetric squared exponential covariance function, which has only one length scale parameter, another option to estimate this parameter exists. One can apply the inverse of the transform in (3.90) to the quantity that is to be modeled as stochastic process and estimate the correlation length in the transformed space. This approach is particularly advantageous if the KLE expansion or the direct Fourier series expansion is employed because an analytic decomposition of the covariance function, which exists only for certain cases, can still be used and a comparatively expensive numerical solution can be avoided.

Some approaches to generate sample functions of non-Gaussian processes accurately matching some desired characteristics in an ensemble average sense have been elaborated. Now, it is important to discuss some difficulties in obtaining or choosing these characteristics for uncertain model input parameters in the context of UQ.

If an uncertain quantity is to be modeled as a stochastic process using a second-order description, first the type of first-order probability distribution and covariance function have to be specified and then their respective parameters need to be determined. Especially, the covariance function can have multitude of parameters. Given sufficient data, i.e., measurements at multiple locations from multiple realizations of the process, these parameters can be estimated. If the process is ergodic, measurements from a single realization can be sufficient as well. Alas, data is usually scarce and rarely sufficient to reliably and uniquely determine the probability distribution, covariance function, and all the hyper-parameters which determine the particular shape of these two functions. Hence, although it is important to accurately match the desired characteristics of a stochastic process describing uncertainties in some model input parameters, it is also crucial to acknowledge that these prescribed characteristics and the corresponding hyper-parameters are often an educated guess. It is common practice in the field of stochastic mechanics to make extensive assumptions about covariance functions and probability distributions for stochastic processes used as probabilistic model for random and uncertain quantities [58]. Chapter 6 addresses these problems and describes the procedure used in this work to estimate random field parameters for several mechanical quantities of AAA wall based on available data.

With regard to the generation of sample functions of non-Gaussian processes using translation process theory, it is worth mentioning that the change or distortion of the covariance function due to the nonlinear transform in (3.90) is often comparable or smaller than the variation due to a lack of knowledge about hyper-parameters such as the correlation length. For illustration, consider the normalized covariance functions that are depicted in Figure 3.6. Each plot in Figure 3.6 shows normalized covariance functions of a Gaussian process with squared

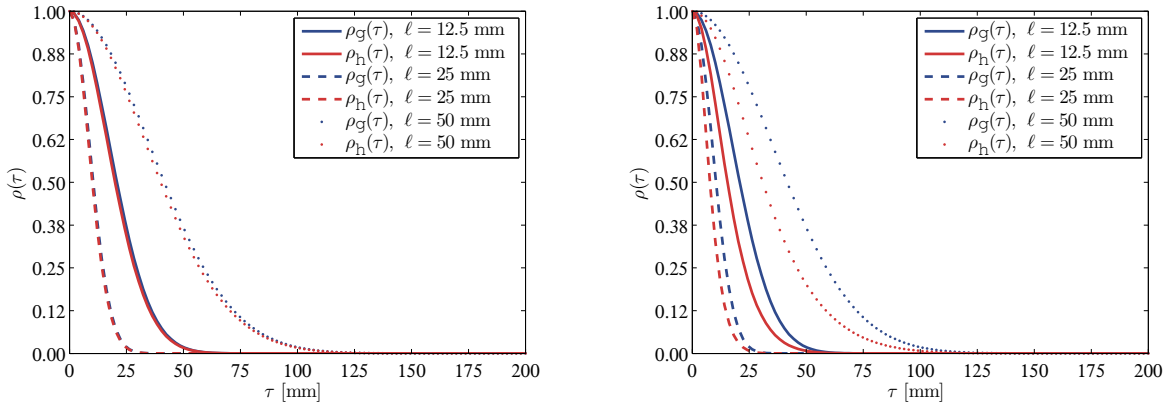

(a) **(b)**

Figure 3.6 Normalized correlation functions of Gaussian and corresponding non-Gaussian translation process. (a) COV $= 0.5$, (b) COV $= 2$.

exponential covariance function for three different correlation lengths, 12.5 mm, 25 mm, and 50 mm in blue. The red curves in the two plots in Figure 3.6 show the corresponding normalized covariance function of a log-normal translation process obtained using an analytic solution for (3.69) from Grigoriu [131] for log-normal translation processes. Depending on the coefficient of variation (COV) of the log-normal distribution, the distortion of the normalized covariance function is more or less pronounced. If the coefficient of variation is 0.5, the difference in the covariance function is barely visible, as shown in Figure 3.6a. If the coefficient of variation of the log-normal distribution is larger, Figure 3.6b depicts the case where the coefficient of variation is 2, the difference increases as well. However, as also can be seen in Figure 3.6b, if the correlation length cannot be accurately determined, the effect of the non-linear transformation can still be considered secondary. Similar results are reported for other non-Gaussian probability distributions with moderate coefficients of variation; Der Kiureghian and Liu [83] state that $\rho_{\mathrm{g}}(\tau) \approx \rho_{\mathrm{h}}(\tau)$ without any additional measure to counter distortion of the normalized covariance function.

3.3.5 Cross-correlated random processes and fields

Although cross-correlated random processes or fields are beyond the scope of this work, references to approaches suitable for the generation of realizations of cross-correlated non-Gaussian vector random fields are provided for the sake of completeness and future reference [63, 101, 296, 348, 370].

3.4 Bayesian inference and prediction

Having introduced the basics of probability theory and corresponding nomenclature, the following sections introduce the concept of Bayesian inference and prediction in particular for

regression problems and the closely related interpolation problems. From here on, the term regression will be used to describe both problems, regression , i.e., fitting a function to noisy data and approximate interpolation, i.e, fitting a function which passes (almost) exactly through the data points. Bayesian inference is a method of statistical inference to draw conclusions from data about quantities which cannot be directly measured or observed. Within the Bayesian paradigm, which is adopted throughout this work, probability is used as a yardstick for uncertainty. Consequently, each uncertain quantity or parameter is assigned a probability distribution to reflect this uncertainty. The distribution describing the uncertainty can be rationally updated and modified in light of new information using Bayes' theorem. This updated probability statement is the statistical conclusion obtained by Bayesian inference.

In this work, Bayesian regression techniques are used to a) obtain predictions for patient-specific parameters which are otherwise obtainable only through invasive measurements, b) to make inference about functions in terms of computational models with uncertain input parameters, and c) to infer a probabilistic relationship between computational models of different fidelity. Since these techniques are applied in such a variety of contexts, the presentation of the material in this section is rather abstract and self-contained. However, the similarities will become clear in later chapters of this work. The focus of the present chapter is to convey the concepts that are needed for probabilistic inference and predictions based on available data. Moreover, the theory presented in this section will facilitate the discussion of different uncertainty UQ in Chapter 4.

The vantage point for all considered inference problems is a dataset $\mathcal{D} = \{\boldsymbol{x}^{(i)}, y^{(i)}\}_{i=1}^{n}$ where the vector $\boldsymbol{x} \in \mathbb{R}^d$ contains d predictor measurements also referred to as *explanatory variables or input variables*. The outcome measurement is denoted by y and is also referred to as *response variable, target variable*, or simply *target*. Note that, if not stated otherwise, the input vector $\boldsymbol{x}$ is considered to be augmented with an additional entry which is always one in order to account for a bias or offset. Using matrix-vector notation, the dataset can be also written as: $\mathcal{D} = (\boldsymbol{X}, \boldsymbol{y})$ where

$$\boldsymbol{X} = \left[\boldsymbol{x}^{(1)}|\boldsymbol{x}^{(2)}|\cdots|\boldsymbol{x}^{(n)}\right] = \begin{bmatrix} x_1^{(1)} & x_1^{(2)} & \cdots & x_1^{(n)} \\ x_2^{(1)} & x_2^{(2)} & & \vdots \\ x_3^{(1)} & x_3^{(2)} & & \\ \vdots & \vdots & & \\ x_d^{(1)} & & & x_d^{(n)} \end{bmatrix}; \in \mathbb{R}^{d\times n}, \quad \boldsymbol{y} = \begin{bmatrix} y^{(1)} \\ y^{(2)} \\ y^{(3)} \\ \vdots \\ y^{(n)} \end{bmatrix}; \in \mathbb{R}^{n\times 1}. \tag{3.92}$$

In addition, a latent function f linking input variables to the target is introduced. This function could, e.g., be a functional relationship but also stand for a complex finite finite element model. Often, measurements are contaminated with noise such that the following additive error model is usually assumed

$$y^{(i)} = f(\boldsymbol{x}^{(i)}) + \epsilon^{(i)}. \tag{3.93}$$

However, under certain circumstances, the measurements can be considered noise-free, e.g., when the $y^{(i)}$ are generated by computer simulations. The function f typically depends on a number of unobservable parameters $\boldsymbol{\theta}$. Based on the observed dataset $\mathcal{D} = \{\boldsymbol{x}^{(i)}, y^{(i)}\}_{i=1}^{n}$, one of the goals is the inference of these parameters in terms of a probability distribution.

The way Bayesian inference works is that all available prior knowledge about the parameters $\boldsymbol{\theta}$ before looking at the data is captured by the so-called *prior distribution*, or short *prior* $p(\boldsymbol{\theta})$.

If little or no information is available, vague or non-informative priors such as Jeffreys' priors [166] can be used. However, it is noted that the design of truly uninformative priors can be tricky and the necessity of prior distributions is considered one of the most controversial aspects of Bayesian statistics.

Once the prior distribution is set, it is modified in light of observed data, i.e., $\mathcal{D} = \{\boldsymbol{x}^{(i)}, y^{(i)}\}_{i=1}^{n}$ through a conditional probability distribution referred to as likelihood function $p(\mathcal{D}|\boldsymbol{\theta})$ using Bayes theorem, resulting in the *posterior* distribution of the parameters. Bayes' theorem adjusts the distribution of the model parameters such that they are both probable under the prior and compatible with the observed evidence or data. Note that for the sake of an uncluttered notation, the previously used subscript to indicate which random variable a probability density $p(\cdot)$ describes is omitted from here on if the attribution is clear from the argument of the density alone.

Similar to the formulation for the probabilities of discrete events in (3.9), Bayes' theorem can be stated for continuos random variables

$$\text{posterior} = \frac{\text{likelihood} \times \text{prior}}{\text{marginal likelihood}}, \quad p(\boldsymbol{\theta}|\mathcal{D}) = \frac{p(\mathcal{D}|\boldsymbol{\theta})p(\boldsymbol{\theta})}{p(\mathcal{D})}. \tag{3.94}$$

The marginal likelihood, often referred to as evidence, serves as normalizing factor and ensures that the posterior is a valid probability distribution which integrates to one. The marginal likelihood can be expressed as integral of likelihood and prior

$$p(\mathcal{D}) = \int p(\mathcal{D}|\boldsymbol{\theta})p(\boldsymbol{\theta})\mathrm{d}\boldsymbol{\theta}. \tag{3.95}$$

For the computation of the posterior, this term is frequently omitted since a distribution that is proportional to the likelihood times prior is often sufficient. Bayes' theorem then reads

$$p(\boldsymbol{\theta}|\mathcal{D}) \propto p(\mathcal{D}|\boldsymbol{\theta})p(\boldsymbol{\theta}). \tag{3.96}$$

However, while the marginal likelihood it often neglected for the computation of the posterior, it commonly used for model comparison.

Once the posterior distribution $p(\boldsymbol{\theta}|\mathcal{D})$ has been obtained, it can be used to make predictions about the value of the response variable y^* corresponding to a new test input $\boldsymbol{x}^*$. The Bayesian approach offers multiple choices to obtain estimates for y^*. The most consistent way is to compute the weighted average over all possible values of $\boldsymbol{\theta}$, i.e., integrate over the posterior distribution $p(\boldsymbol{\theta}|\mathcal{D})$ to obtain the *posterior predictive distribution* for y^*. Assuming, for the time being that y is noise free. Then, $y^* = f^* = f(\boldsymbol{x}^*; \boldsymbol{\theta})$ and the posterior predictive distribution for f can be computed by

$$p(f^*|\mathcal{D}) = \int f(\boldsymbol{x}^*; \boldsymbol{\theta})p(\boldsymbol{\theta}|\mathcal{D})\mathrm{d}\boldsymbol{\theta}. \tag{3.97}$$

In contrast to deterministic inference approaches, a probabilistic prediction for f^* is obtained, taking into account the remaining uncertainty about $\boldsymbol{\theta}$ after seeing the data. This probability statement is often very helpful as it enables the computation of confidence intervals. Moreover, point estimates for f^*, e.g., mean or median, are readily computed based on (3.97).

Another way to obtain point estimates for f^* is to use the maximum posterior (MAP) value $\boldsymbol{\theta}_{\text{MAP}}$ or mean posterior value $\bar{\boldsymbol{\theta}}$ estimate and compute the corresponding value for f^* based on these point estimates of $\boldsymbol{\theta}$. This approach is often chosen in situations where the MAP or mean posterior value of $\boldsymbol{\theta}$ is significantly easier to obtain than the full distribution.

Bayes' formula (3.94) looks deceptively simple. The difficulty, and the reason why Bayesian methods have only relatively recently gained considerable attention, lies not so much in writing down an analytic formula for the posterior, but rather in the actual computation of the multi-dimensional integrals like (3.97) or the posterior mean. Although it is possible to evaluate the posterior density at any given location, the aforementioned integrals can often not be performed analytically, in which case, the posterior is referred to as analytically intractable.

Only relatively simple models and some combinations of likelihood and prior yield an analytically tractable posterior. Complex models in combination with elaborate prior models require the use of advanced numerical sampling procedures such as Markov Chain Monte Carlo or sequential Monte Carlo samplers [89, 275], which will be briefly introduced in Section 4.3.2. The computational costs of these sampling procedures can reach from significant to prohibitive, depending on the model. Aside from sampling based approaches, approximate inference schemes based on, e.g., expectation propagation [217] or variational Bayesian inference [38] can also be used.

3.5 Bayesian regression

While the previous section introduced the concept of Bayesian inference in a rather abstract fashion, the current section is concerned with the application of these concepts to regression problems. There is a vast amount of literature about different regression approaches and methodologies and it is well beyond the scope of this work to provide an overview of all available techniques. Hence, the following sections merely contain a description of the regression approaches employed in this work and the reader is referred to the respective literature on the topic. Good overviews of available techniques with a slight bias towards Bayesian approaches is provided, e.g., by Bishop [38], Gelman and Hill [114], Hastie et al. [145], MacKay [201], Murphy [223].

Below, three different regression models are described: linear regression, Gaussian process regression, and another non-parametric approach proposed by Koutsourelakis [183] which will be referred to as Koutsourelakis model or approach from here on. Before the Bayesian interpretation of the standard linear regression model is explained, a brief recap of linear regression from a least squares perspective is provided. This is meant to aid the reader unfamiliar with the Bayesian way of thinking to understand the Bayesian approach of regression and inference by comparing the two points of view. In addition the comparison illustrates the similarities and differences between the Bayesian and the least squares approach. The least squares perspective is also helpful for the understanding of polynomial chaos based UQ approaches discussed later on.

The starting point for all regression problems considered in this work is the assumption of an additive noise or error as in (3.93). Based on the available dataset $\mathcal{D} = \{\boldsymbol{x}^{(i)}, y^{(i)}\}_{i=1}^{n}$, the model parameters, or rather the distribution of these parameters, have to be estimated, which in turn can then be used to make predictions about y^* for a new test input $\boldsymbol{x}^*$. Based on this data, the goal of a regression analysis is either information, in the sense that the objective is to uncover

one or more relationships between one or more explanatory variables, or prediction, in the sense that the goal is to predict the value of y^* for a set of new yet unseen explanatory variables $\boldsymbol{x}^*$. Throughout this work, the focus will be more on the prediction side. The dataset which is used to train the model, i.e., to infer the model parameters, will be referred to as training set. As opposed to the test set which is used afterwards to evaluate the predictive performance of the model.

3.5.1 Linear regression from a least squares perspective

In ordinary linear regression one usually starts with the assumption that the function f has the following functional form:

$$f(\boldsymbol{x}) = \boldsymbol{x}^T \boldsymbol{w}, \tag{3.98}$$

where the vector $\boldsymbol{w}$ denotes the weights or parameters of the regression model which need to be determined. At this point, it is important to mention that linearity of f is only needed with respect to $\boldsymbol{w}$, not with respect to $\boldsymbol{x}$, and hence, the methodology can be readily extended using basis functions which are nonlinear in $\boldsymbol{x}$, see Section 3.5.1.3. The weights can be obtained by solving a simple least squares problem. Inserting (3.98) into (3.93) yields the squared error

$$\sum_{i=1}^{n} \big(\epsilon^{(i)}\big)^2 = \sum_{i=1}^{n} \big(y^{(i)} - f(\boldsymbol{x}^{(i)})\big)^2 = \sum_{i=1}^{n} \big(y^{(i)} - \boldsymbol{x}^{(i)^T} \boldsymbol{w}\big)^2. \tag{3.99}$$

The matrix $\boldsymbol{X}$ as defined in (3.92) is usually referred to as design matrix in many statistics textbooks. Please note that a slightly different definition is used here and the design matrix is often defined as the transpose of the definition used in this work. Using the definition above, (3.99) can be rewritten as

$$\|\boldsymbol{\epsilon}\|^2 = \big(\boldsymbol{y} - \boldsymbol{X}^T \boldsymbol{w}\big)^T \big(\boldsymbol{y} - \boldsymbol{X}^T \boldsymbol{w}\big). \tag{3.100}$$

The squared error has to be minimal:

$$\min_{\boldsymbol{w} \in \mathbb{R}^N} \|\boldsymbol{\epsilon}\|^2 = \min_{\boldsymbol{w} \in \mathbb{R}^N} \big(\boldsymbol{y} - \boldsymbol{X}^T \boldsymbol{w}\big)^T \big(\boldsymbol{y} - \boldsymbol{X}^T \boldsymbol{w}\big). \tag{3.101}$$

Hence, taking the derivative and setting it to zero yields the least squares estimate for the weights

$$\boldsymbol{w}_{\mathrm{LS}} = [\boldsymbol{X}\boldsymbol{X}^T]^{-1} \boldsymbol{X}\boldsymbol{y}. \tag{3.102}$$

Having determined the weights of the model, it can be used to make predictions for a yet unseen data point $\boldsymbol{x}^*$. Based on the weights, the predicted value for $\bar{y}^*$ corresponding to a new data point $\boldsymbol{x}^*$ is simply

$$\bar{y}^* = \boldsymbol{x}^{*T} \boldsymbol{w}_{\mathrm{LS}}. \tag{3.103}$$

Obviously, this prediction is not perfect and it would be desirable to assess the accuracy of this prediction.

In addition to the weights, an estimate for the average error between the predicted values $f(\boldsymbol{x}^{(i)})$ and the true values $\boldsymbol{y}$ can be computed, e.g, by computing the error sum of squares SS_{ess}

$$SS_{ess} = \left\| (\boldsymbol{y} - \boldsymbol{X}^T \boldsymbol{w})^T (\boldsymbol{y} - \boldsymbol{X}^T \boldsymbol{w}) \right\|^2. \tag{3.104}$$

Dividing by the number of samples in the training set, the root mean squared error (RMSE), which can be used to assess the accuracy, is obtained using

$$\text{RMSE} = \sqrt{\frac{SS_{ess}}{n}}. \tag{3.105}$$

3.5.1.1 Linear regression as Bayesian inference problem

Having described the linear regression problem from a least squares perspective, the current section introduces the Bayesian point of view. The starting point is again the assumption of a linear model with additive noise

$$y^{(i)} = f(\boldsymbol{x}^{(i)}) + \epsilon^{(i)} = \boldsymbol{x}^{(i)^T}\boldsymbol{w} + \epsilon^{(i)}, \tag{3.106}$$

followed by the assumption that the error abides by a Gaussian distribution, in other words, the $\epsilon^{(i)}$ are independent identically distributed samples from a Gaussian distribution

$$\epsilon(\omega) \sim \mathcal{N}(0, \sigma_\epsilon^2) \tag{3.107}$$

with zero mean and yet unknown variance σ_ϵ^2.

This gives rise to a Gaussian likelihood for the parameters of the model, which are in this case the weights $\boldsymbol{w}$.

$$p(\boldsymbol{y}|\boldsymbol{X}, \boldsymbol{w}, \sigma_\epsilon^2) = \prod_{i=1}^{n} \frac{1}{\sqrt{2\pi}\sigma_\epsilon} \exp\Big(-\frac{1}{2\sigma_\epsilon^2}\big(y^{(i)} - f(\boldsymbol{x}^{(i)})\big)^2\Big) \tag{3.108}$$

The likelihood is a conditional probability distribution for the observations $\boldsymbol{y}$, viewed as a function of the parameters, here $\boldsymbol{w} and \sigma_\epsilon^2$. Interpreted as a function of the parameters, it is also often written in the following form:

$$p(\boldsymbol{y}|\boldsymbol{X}, \boldsymbol{w}, \sigma_\epsilon^2) = L(\boldsymbol{w}, \sigma_\epsilon^2|\mathcal{D}). \tag{3.109}$$

The likelihood is not necessarily a valid probability distribution with respect to the parameters and hence must not integrate to one. Insertion of the linear model yields

$$p(\boldsymbol{y}|\boldsymbol{X}, \boldsymbol{w}, \sigma_\epsilon^2) = \prod_{i=1}^{n} \frac{1}{\sqrt{2\pi}\sigma_\epsilon} \exp\Big(-\frac{1}{2\sigma_\epsilon^2}\big(y^{(i)} - \boldsymbol{x}^{(i)^T}\boldsymbol{w}\big)^2\Big). \tag{3.110}$$

Algebraic rearrangement leads to

$$p(\boldsymbol{y}|\boldsymbol{X}, \boldsymbol{w}, \sigma_\epsilon^2) = \frac{1}{(2\pi)^{n/2}\sigma_\epsilon^n} \exp\Big(\sum_{i=1}^{n} -\frac{1}{2\sigma_\epsilon^2}\big(y^{(i)} - \boldsymbol{x}^{(i)^T}\boldsymbol{w}\big)^2\Big), \tag{3.111}$$

which can be rewritten using the design matrix as

$$p(\boldsymbol{y}|\boldsymbol{X}, \boldsymbol{w}, \sigma_\epsilon^2) = \frac{1}{\sqrt{(2\pi)^n(\sigma_\epsilon^2)^n}} \exp\left(-\frac{1}{2\sigma_\epsilon^2}(\boldsymbol{y} - \boldsymbol{X}^T\boldsymbol{w})^T(\boldsymbol{y} - \boldsymbol{X}^T\boldsymbol{w})\right) \tag{3.112}$$

or

$$p(\boldsymbol{y}|\boldsymbol{X}, \boldsymbol{w}, \sigma_\epsilon^2) = \frac{1}{\sqrt{(2\pi)^n (\sigma_\epsilon^2)^n}} \exp\left(-\frac{1}{2\sigma_\epsilon^2} \left\|(\boldsymbol{y} - \boldsymbol{X}^T\boldsymbol{w})\right\|^2\right), \tag{3.113}$$

or in short

$$p(\boldsymbol{y}|\boldsymbol{X}, \boldsymbol{w}, \sigma_\epsilon^2) = \mathcal{N}(\boldsymbol{X}^T\boldsymbol{w}, \sigma_\epsilon^2\boldsymbol{I}). \tag{3.114}$$

The second choice that needs to be made is that of prior distributions for the variance of the noise and the weights. Without any additional information, it makes sense to choose a non-informative Jeffreys' prior. For linear regression, a common choice is a uniform prior for the weights $p(\boldsymbol{w}) = \mathcal{U}(-\infty, \infty)$, which technically is not a proper probability distribution as it does not integrate to one. Hence, it is often referred to as improper prior. Improper priors can lead to problems as the posterior can become improper, too. However, in the case of the considered regression problem, this is not the case [115]. For the variance, the prior is chosen as $p(\sigma^2) \propto \sigma_\epsilon^{-2}$, which can be interpreted as a flat, uniform prior on the log scale, i.e., $p(\log\sigma) = \mathcal{U}(-\infty, \infty)$ [113, 167]. As a result, the full prior model is $p(\boldsymbol{w}, \sigma_\epsilon^2) \propto \sigma_\epsilon^{-2}$. Likelihood and prior are combined to compute the posterior distribution for the weights using Bayes' theorem,

$$p(\boldsymbol{w}, \sigma_\epsilon^2|\mathcal{D}) = \frac{p(\boldsymbol{y}|\boldsymbol{X}, \boldsymbol{w}, \sigma_\epsilon^2)p(\boldsymbol{w})p(\sigma_\epsilon^2)}{p(\boldsymbol{y}|\boldsymbol{X})}, \tag{3.115}$$

which can be rewritten as

$$p(\boldsymbol{w}|\sigma_\epsilon^2, \boldsymbol{X}, \boldsymbol{y})p(\sigma_\epsilon^2|\boldsymbol{X}, \boldsymbol{y}) = \frac{p(\boldsymbol{y}|\boldsymbol{X}, \boldsymbol{w}, \sigma_\epsilon^2)p(\boldsymbol{w})p(\sigma_\epsilon^2)}{p(\boldsymbol{y}|\boldsymbol{X})}. \tag{3.116}$$

In this particular case, the posterior distributions can be computed analytically. As the likelihood is Gaussian and a flat prior was used, the conditional posterior distribution can be shown to be Gaussian as well,

$$p(\boldsymbol{w}|\sigma_\epsilon^2, \boldsymbol{X}, \boldsymbol{y}) = \mathcal{N}\Big((\boldsymbol{X}\boldsymbol{X}^T)^{-1}\boldsymbol{X}\boldsymbol{y}, (\boldsymbol{X}\boldsymbol{X}^T)^{-1}\sigma_\epsilon^2\Big). \tag{3.117}$$

It is obvious that the posterior mean estimate of the weights is equivalent to the estimate of the weights $\boldsymbol{w}_{\text{LS}}$ obtained with the least squares approach in in (3.117). However, the Bayesian approach provides information beyond the posterior mean estimate of the weights, e.g., credible intervals for the weights can be readily computed using the computed posterior distribution. The marginal posterior distribution of σ_ϵ^2 can be shown to follow a scaled inverse-χ^2 distribution (cf. Table A.1)

$$p(\sigma_\epsilon^2|\boldsymbol{X}, \boldsymbol{y}) = \text{Inv-}\chi^2(n - d, s^2), \tag{3.118}$$

with s^2 being

$$s^2 = \frac{1}{n - d}(\boldsymbol{y} - \boldsymbol{X}^T\boldsymbol{w}_{\text{LS}})^T(\boldsymbol{y} - \boldsymbol{X}^T\boldsymbol{w}_{\text{LS}}), \tag{3.119}$$

where $\boldsymbol{w}_{\text{LS}}$ is the estimated mean value of the weights.

3.5.1.2 Making predictions

The obtained posterior distributions for $\boldsymbol{w}$ and σ_ϵ^2 can be used to obtain probabilistic predictions for a new test input $\boldsymbol{x}^*$ in terms of a conditional probability distribution $p(y^*|\boldsymbol{x}^*, \boldsymbol{X}, \boldsymbol{y})$. As the regression model is based on the assumption of Gaussian noise, the conditional predictive posterior distribution of y^* given $\boldsymbol{w}, \sigma_\epsilon^2$, $\boldsymbol{y}$, and $\boldsymbol{X}$ is Gaussian. In combination with the probabilistic estimates for both $\boldsymbol{w}$ and σ_ϵ^2, the probabilistic estimate for y^* is computed by averaging over all possible values of $\boldsymbol{w}$ and σ_ϵ^2, i.e., integrate over the distributions of $\boldsymbol{w}$ and σ_ϵ^2, which gives

$$p(y^*|\boldsymbol{x}^*, \boldsymbol{X}, \boldsymbol{y}) = \int p(y^*|\boldsymbol{w}, \sigma_\epsilon^2 \boldsymbol{X}, \boldsymbol{y}) p(\boldsymbol{w}|\sigma_\epsilon^2, \boldsymbol{X}, \boldsymbol{y}) p(\sigma_\epsilon^2|\boldsymbol{X}, \boldsymbol{y}) d\sigma_\epsilon^2 d\boldsymbol{w}. \tag{3.120}$$

The integrals above can be solved analytically and the resulting predictive distribution for y^* is a non standardized t-distribution (cf. Table A.1) with center

$$\bar{y} = \boldsymbol{x}^{*T} \boldsymbol{w}_{\text{LS}}, \tag{3.121}$$

a squared scale parameter

$$\hat{\sigma}_n^2 = s^2(1 + \boldsymbol{x}^{*T}(\boldsymbol{X}\boldsymbol{X}^T)^{-1}\boldsymbol{x}), \tag{3.122}$$

and $n - d$ degrees of freedom [115]

$$p(y^*|n-d, \hat{y}, \hat{\sigma}_n^2) = \frac{\Gamma(\frac{(n-d)+1}{2})}{\Gamma(\frac{(n-d)}{2})\sqrt{\pi(n-d)\hat{\sigma}_n^2}} \left(1 + \frac{1}{(n-d)} \frac{(y-\hat{y})^2}{\hat{\sigma}_n^2}\right)^{-\frac{(n-d)+1}{2}}. \tag{3.123}$$

For notational convenience, the dependance on the data is omitted here. Using the predictive distribution, the expected value of y^* as well as confidence intervals can be readily computed. The expected values is simply $\bar{y}^*$, which is equal to the estimate one would have obtained with the least squares procedure. The 95% confidence intervals are computed using

$$y_{\text{ci}}^* = \bar{y}^* \pm t_{(0.025, n-d)} \sqrt{\sigma^{*\,2}} \tag{3.124}$$

where $t_{(0.025,n-d)}$ denotes the 2.5 percentile of the t-distribution with $n - d$ degrees of freedom. If the number of data points is large and the dimension d comparably small, the t-distribution approaches the Gaussian distribution with negligible error and the 95% confidence intervals are readily computed based on the confidence interval of a Gaussian distribution

$$y_{\text{ci}}^* = \bar{y}^* \pm 1.96\sqrt{\sigma^{*\,2}}. \tag{3.125}$$

As alternative to using the full posterior distribution of $\boldsymbol{w}$ and σ_ϵ^2 to estimate $p(y^*)$, point estimates for $\boldsymbol{w}$ and σ_ϵ^2 can be used to compute point estimates for y^*, e.g., the MAP or the posterior mean. For certain symmetric distributions, e.g., the Gaussian distribution, the MAP is equal to the posterior mean and for the linear regression example considered here, the MAP for the weights also coincides with the least squares estimate. The MAP estimate can be computed by maximizing the posterior with respect to the weights and the variance of the noise, respectively. In order to close the gap to the least squares procedure, the steps to obtain the MAP for weights are given here for the sake of completeness. Multiplication of likelihood and prior yields

$$p(\boldsymbol{y}|\boldsymbol{X}, \boldsymbol{w}, \sigma_\epsilon^2) = \frac{1}{\sqrt{(2\pi)^n (\sigma_\epsilon^2)^n}} \exp\left(-\frac{1}{2\sigma_\epsilon^2} \left\|(\boldsymbol{y} - \boldsymbol{X}^T\boldsymbol{w})\right\|^2\right) \frac{1}{\sigma_\epsilon^2}. \tag{3.126}$$

This expression needs to be maximized with respect to $\boldsymbol{w}$ in order to obtain the MAP. Because it is computationally more convenient, the negative logarithm of (3.126) is minimized instead:

$$\max_{\boldsymbol{w}\in\mathbb{R}^N}\Big(p(\boldsymbol{w},\sigma_\epsilon^2|\boldsymbol{X},\boldsymbol{y})\Big) = \min_{\boldsymbol{w}\in\mathbb{R}^N}\Big(C_1 + \frac{1}{2\sigma_\epsilon^2}(\boldsymbol{y}-\boldsymbol{X}^T\boldsymbol{w})^T(\boldsymbol{y}-\boldsymbol{X}^T\boldsymbol{w})\Big). \tag{3.127}$$

Taking the derivative of the equation above and setting it to zero yields

$$0 = \frac{1}{2\sigma_\epsilon^2}[\boldsymbol{X}\boldsymbol{y} + \boldsymbol{X}\boldsymbol{X}^T\boldsymbol{w}]. \tag{3.128}$$

Thus,

$$\boldsymbol{w}_{\text{LS}} = [\boldsymbol{X}\boldsymbol{X}^T]^{-1}\boldsymbol{X}\boldsymbol{y}, \tag{3.129}$$

which is equal to the result obtained in (3.102) with the least squares approach.

At this point, it is important to mention that the same predictions including confidence intervals can also be obtained from a frequentist point of view for linear regression [356]. For more complex models, however, this is usually not the case.

3.5.1.3 Extension using nonlinear basis functions

Of course, the assumption that f varies linearly with $\boldsymbol{x}$ is very restrictive. However, this problem can be circumvented, at least in principle, by a choosing a higher-dimensional input space by using a set of m nonlinear basis functions $\boldsymbol{\phi}(\boldsymbol{x})$, which map the d-dimensional input space onto a higher m-dimensional feature space, and then use the linear model in this space, i.e.,

$$f(\boldsymbol{x}) = \boldsymbol{\phi}(\boldsymbol{x})^T\boldsymbol{w}. \tag{3.130}$$

Analogous to the definition of $\boldsymbol{X}$, the design matrix then becomes

$$\boldsymbol{\Phi} = \begin{bmatrix}\boldsymbol{\phi}(\boldsymbol{x}^{(1)}) & \boldsymbol{\phi}(\boldsymbol{x}^{(2)}) \cdots \boldsymbol{\phi}(\boldsymbol{x}^{(n)})\end{bmatrix}; \in \mathbb{R}^{m\times n}, \tag{3.131}$$

containing the columns $\boldsymbol{\phi}(\boldsymbol{x})$ for all $\boldsymbol{x}^{(i)}$. Analysis of the model in (3.130) is carried out like for the standard linear model but $\boldsymbol{X}$ is replaced with $\boldsymbol{\Phi}$ in all formulas. Although using nonlinear basis functions can remedy the restriction of linearity with respect to $\boldsymbol{x}$, the appropriate choice of basis functions can be difficult. While nonlinear basis functions add flexibility, choosing a high-dimensional basis can lead to severe overfitting of the model and poor predictive performance when used on new test inputs $\boldsymbol{x}^*$. The problem can be alleviated by using appropriate priors or, if argued from a least squares perspective, regularization. Gaussian process regression, which is presented in the following section is a popular, and very flexible regression approach, which can, in fact, be interpreted as linear regression using an infinite number of basis function in combination with a Gaussian prior on the weights [200, 361].

3.5.2 Gaussian process regression

The derivation of GP regression from the perspective of linear regression using kernel basis functions is beyond the scope of this work and the reader is referred to [200, 361] for further details. However, an alternative interpretation, which is referred to as *function space-view* by

Williams and Rasmussen [361], provides another way to reach the same result. This approach is followed here in the subsequent paragraphs. The approach hinges on the interpretation that a Gaussian process is a distribution over functions and that inference can be made directly in this function space. As already mentioned above, a Gaussian process is completely defined by a mean $m(\boldsymbol{x};\boldsymbol{\theta}_m)$ and a covariance function $k(\boldsymbol{x},\boldsymbol{x}';\boldsymbol{\theta}_k)$. The latter provides the covariance of values of the Gaussian process at the two locations $\boldsymbol{x}$ and $\boldsymbol{x}'$ in the input space. The vectors $\boldsymbol{\theta}_m$ and $\boldsymbol{\theta}_k$ contain the a-priori unknown hyper-parameters of the mean and the covariance function such as, e.g., the characteristic length scales. Any prior knowledge about the smoothness of the process can readily be incorporated by choosing a particular covariance function, e.g., one of the covariance functions presented in Section 3.3.1.1.

Starting point for GP regression is the definition of a GP prior over $f(\boldsymbol{x})$

$$\mathsf{f}(\boldsymbol{x})|\boldsymbol{\theta}_m,\boldsymbol{\theta}_k \sim \mathcal{GP}\big(m_{\mathsf{f}}(\boldsymbol{x};\boldsymbol{\theta}_m), k_{\mathsf{f}}(\boldsymbol{x},\boldsymbol{x}';\boldsymbol{\theta}_k)\big). \tag{3.132}$$

The assumption of an additive, independent, and identically distributed Gaussian error gives rise to a Gaussian likelihood defining the relative plausibility of $f(\boldsymbol{x})$ given the data

$$p(\boldsymbol{y}|\boldsymbol{f},\boldsymbol{X}) = \mathcal{N}(\boldsymbol{f},\boldsymbol{I}\sigma_\epsilon^2). \tag{3.133}$$

Therein, $\boldsymbol{I}$ is the identity matrix and the vector $\boldsymbol{f}$ denotes the finite-dimensional subset of f evaluated at all training points $\boldsymbol{x}^{(i)}$. Likelihood and prior can be combined to compute the posterior of f which is also a GP and consequently the posterior distribution $p(f^*|\boldsymbol{x}^*,\mathcal{D})$ for a new point in the input space $\boldsymbol{x}^*$ is Gaussian

$$p(f^*|\boldsymbol{x}^*,\mathcal{D}) = \mathcal{N}(\bar{f}^*,\sigma_f^{*2}) \tag{3.134}$$

with mean

$$\begin{aligned}\bar{f}^* =& m(\boldsymbol{x}^*;\hat{\boldsymbol{\theta}}_m) + \boldsymbol{k}(\boldsymbol{x}^*,\boldsymbol{X};\hat{\boldsymbol{\theta}}_k)^T \\ & (\boldsymbol{K}+\hat{\sigma_\epsilon}^2\boldsymbol{I})^{-1}\big(\boldsymbol{y}-\boldsymbol{m}(\boldsymbol{X};\hat{\boldsymbol{\theta}}_m)\big)\end{aligned} \tag{3.135}$$

and variance

$$\begin{aligned}\sigma_f^{*2} =& k(\boldsymbol{x}^*,\boldsymbol{x}^*;\hat{\boldsymbol{\theta}}_k) - \boldsymbol{k}(\boldsymbol{x}^*,\boldsymbol{X};\hat{\boldsymbol{\theta}}_k)^T \\ & (\boldsymbol{K}+\hat{\sigma_\epsilon}^2\boldsymbol{I})^{-1}\boldsymbol{k}(\boldsymbol{x}^*,\boldsymbol{X};\hat{\boldsymbol{\theta}}_k).\end{aligned} \tag{3.136}$$

In the formula above, $\boldsymbol{K}$ denotes the covariance matrix $\boldsymbol{K}$ with the entries $K_{ij} = k(\boldsymbol{x}_i,\boldsymbol{x}_j;\hat{\boldsymbol{\theta}}_k)$ and $\boldsymbol{k}(\boldsymbol{x}^*,\boldsymbol{X};\hat{\boldsymbol{\theta}}_k)$ denotes the covariance vector between the test point $\boldsymbol{x}^*$ and the n training points aggregated in $\boldsymbol{X}$. The posterior variance in (3.136) captures the uncertainty about the function f after seeing the data. Areas with fewer data point will exhibit larger variance as compared to regions in the input space where data is more dense. Often, also the predictive distribution $p(y^*)$ is of interest rather than the distribution $p(f^*)$, and hence, (3.134) is used in combination with the previous assumption that, conditional on f^*, y^* is normally distributed, i.e.,

$$p(y^*|f^*) = \mathcal{N}(f^*,\hat{\sigma_\epsilon}^2). \tag{3.137}$$

Thus, the predictive distribution of y^* is computed by averaging over all possible values of f^*

$$p(y^*|\boldsymbol{x}^*,\mathcal{D}) = \int p(y^*|f^*)p(f^*|\boldsymbol{x}^*,\mathcal{D})df^*, \tag{3.138}$$

which results in the predictive distribution for y^*, which is also Gaussian,

$$p(y^*|\boldsymbol{x}^*, \mathcal{D}) = \mathcal{N}(\bar{f}^*, \sigma^{*2}) \tag{3.139}$$

with mean

$$\begin{aligned} \bar{y}^* = \bar{f}^* =& m(\boldsymbol{x}^*; \hat{\boldsymbol{\theta}}_m) + \boldsymbol{k}(\boldsymbol{x}^*, \boldsymbol{X}; \hat{\boldsymbol{\theta}}_k)^T \\ & (\boldsymbol{K} + \hat{\sigma_\epsilon}^2 \boldsymbol{I})^{-1} \big(\boldsymbol{y} - \boldsymbol{m}(\boldsymbol{X}; \hat{\boldsymbol{\theta}}_m)\big), \end{aligned} \tag{3.140}$$

and variance

$$\begin{aligned} \sigma^{*2} =& k(\boldsymbol{x}^*, \boldsymbol{x}^*; \hat{\boldsymbol{\theta}}_k) - \boldsymbol{k}(\boldsymbol{x}^*, \boldsymbol{X}; \hat{\boldsymbol{\theta}}_k)^T \\ & (\boldsymbol{K} + \hat{\sigma_\epsilon}^2 \boldsymbol{I})^{-1} \boldsymbol{k}(\boldsymbol{x}^*, \boldsymbol{X}; \hat{\boldsymbol{\theta}}_k) + \hat{\sigma_\epsilon}^2. \end{aligned} \tag{3.141}$$

Since the predictive distribution is Gaussian, the 95% confidence region is readily computed using

$$y^*_{ci} = \bar{f}^* \pm 1.96\sqrt{\sigma^{*2}}. \tag{3.142}$$

3.5.2.1 Determination of hyper-parameters

So far, the issue of determining the value of the hyper-parameters of mean and covariance function has been neglected. In typically scenarios, the value of the hyper-parameters is not known a-priori and estimates for the hyper-parameter have to be inferred from the data as well. For notational convenience, the collection of all hyper-parameters and the variance of the noise $[\boldsymbol{\theta}_m; \boldsymbol{\theta}_k; \sigma_\epsilon^2]$ will be denoted as $\boldsymbol{\theta}$ in the following. In a fully Bayesian approach, a hyper-prior distribution $p(\boldsymbol{\theta})$ is assigned to all unknown hyper-parameters. These hyper-parameters would then be marginalized out from the joint posterior distribution in order to obtain the predictive distribution for y^*. However, as a result the joint posterior would no longer be analytically tractable.

Hence, a different approach is followed here and the marginal likelihood is maximized instead to obtain reasonable point estimates for the hyper-parameters [361, Chap. 5]. This procedure is often referred to as training of the GP. Its result is the tractable Gaussian posterior given above in (3.139).

The marginal likelihood (*evidence*) can be computed by

$$p(\boldsymbol{y}|\boldsymbol{X}, \boldsymbol{\theta}) = \int p(\boldsymbol{y}|f, \boldsymbol{X}, \boldsymbol{\theta}_l) p(f|\boldsymbol{\theta}_p) df. \tag{3.143}$$

Instead of maximizing the marginal likelihood directly, it is more convenient to minimize the negative logarithm of the marginal likelihood $\mathcal{L}(\boldsymbol{\theta})$ instead. The negative logarithm of the marginal likelihood is given by

$$\begin{aligned} \mathcal{L}(\boldsymbol{\theta}) =& \frac{1}{2}(\boldsymbol{y} - \boldsymbol{m}(\boldsymbol{X}; \boldsymbol{\theta}_m))^T (\boldsymbol{K} + \sigma_\epsilon^2 \boldsymbol{I})^{-1} \\ & (\boldsymbol{y} - \boldsymbol{m}(\boldsymbol{X}; \boldsymbol{\theta}_m)) + \frac{1}{2} \log \left| \boldsymbol{K} + \sigma_\epsilon^2 \boldsymbol{I} \right| \\ & + \frac{n}{2} \log 2\pi. \end{aligned} \tag{3.144}$$

A suitable point estimate for the hyper-parameters $\boldsymbol{\theta}$ can then be obtained by

$$\hat{\boldsymbol{\theta}} = \arg\min_{\boldsymbol{\theta} \in \boldsymbol{\Theta}} \big(\mathcal{L}(\boldsymbol{\theta})\big). \tag{3.145}$$

Some of the hyper-parameters are subject to a positivity constraint. A simple way to ensure that these parameters remain positive is to perform the minimization of $\mathcal{L}$ with respect to the logarithm of these hyper-parameters. The negative log of the marginal likelihood can, of course, feature multiple local minima and the usual gradient based optimization schemes might not always converge to the global minimum. However, it was found that an educated initial guess for the hyper-parameters in combination with conjugate gradient schemes provides good results for the problems considered here. Note that the GPML toolbox [271] was employed for the construction of the GP based regression models used in this work.

3.5.3 Koutsourelakis regression approach

The third kind of regression model, which is used in this work, was proposed by Koutsourelakis [183]. Hence, this particular variant will be referred to as Koutsourelakis model, or Koutsourelakis approach. Although this model bears some resemblance to the GP regression approach, the Koutsourelakis approach differs from the GP approach regarding flexibility of the model and consistency with the Bayesian paradigm. More specifically, the regression approach proposed by Koutsourelakis is more flexible and can cope with varying scales of fluctuation, i.e., changing characteristic length scales. In addition, in can be considered a more consistent approach because it is based on a hierarchical, fully Bayesian formulation with priors and hyper-priors assigned to all a-priori unknown parameters and hyper-parameters. As a consequence, the posterior is no longer analytically tractable and advanced sampling schemes are needed to draw samples from it. While the loss of analytic tractability can be considered a drawback of this approach, the fully Bayesian approach adds flexibility to the model and the overall approach is considered to be more consistent with the Bayesian paradigm.

The main concepts of the Bayesian regression model proposed by Koutsourelakis [183] will be briefly outlined here for the sake of completeness. Because it is convenient for the specification of the prior for this model, it is assumed that the input has been rescaled to the interval $[0, 1]$. Moreover, in contrast to the models discussed in the two previous sections, the input vector $\boldsymbol{x}$ is not augmented with a constant term in the following. Starting from the same assumption as before, i.e., that the error can be modeled as additive Gaussian noise, the model proposed by Koutsourelakis [183] assumes the following functional form based on isotropic Gaussian kernel functions

$$f(\boldsymbol{x}, \boldsymbol{\theta}) = a_0 + \sum_{j=1}^{k} a_j \exp\left(-\tau_j \left\|\boldsymbol{\nu}_j - \boldsymbol{x}\right\|^2\right), \tag{3.146}$$

therein, the vector $\boldsymbol{\theta}$ contains all parameters of the model, including the number of kernel functions used in this expansion which defines the cardinality k of the model, and which will be also inferred from the data.

$$\boldsymbol{\theta} = \{k, \{a_j\}_{j=0}^{k}, \{\tau_j\}_{j=1}^{k}, \{\boldsymbol{\nu}_j\}_{j=1}^{k}\}. \tag{3.147}$$

The coefficients $\{a_j\}_{j=0}^{k}$ determine the weight of each kernel and a constant term, respectively. The effect of the precision parameters of the kernels $\{\tau_j\}_{j=1}^{k}$ is analogue to the inverse of the characteristic length scale of a covariance function. Small values of τ correspond to a larger scale of variability and vice versa. The set $\{\boldsymbol{\nu}_j\}_{j=1}^{k}$ contains the locations of the kernel centers.

With likelihood and functional form defined, the prior distribution for all parameters has to be specified. Note that by following a fully Bayesian approach with a hierarchical non-parametric

prior, non-Gaussian posterior distributions can be obtained for y if all model parameters are integrated out. This property is considered to be an advantage of this approach. The Koutsourelakis model shares some similarities with another Bayesian regression approach called the relevance vector machine [326, 327]. However, in contrast to [326], the number of kernel functions is not a priori fixed, and, in addition, a more elaborate hierarchical prior model is adopted here.

3.5.3.1 Prior model

As proposed by Koutsourelakis [183], a hierarchical prior model with the following from is employed:

$$\begin{aligned} p(k, \{a_j\}_{j=0}^k, \{\tau_j\}_{j=0}^k, \{\boldsymbol{\nu}_j\}_{j=0}^k) \propto p(k) \times p(\{a_j\}_{j=0}^k|k) \\ \times p(\{\tau_j\}_{j=0}^k|k) \times p(\{\boldsymbol{\nu}_j\}_{j=0}^k)|k). \end{aligned} \tag{3.148}$$

The prior on the number of kernel functions in (3.146) is chosen to be a Poisson prior (cf. Table A.1), which favors sparse representations, avoids over-fitting, and ensures that the simplest regression model explaining the data is chosen [183].

$$p(k|\lambda_k) = \exp(-\lambda_k)\frac{\lambda_k^k}{k!}, \quad k = 0, 1..., \infty. \tag{3.149}$$

As result of the chosen prior, the total number of kernel functions and the dimension of the parameter space is a priori not fixed, but due to computational limitations the distribution is truncated at $k_{\max}$. To increase robustness and flexibility, an exponential hyper-prior $p(\lambda_k|s) = s\exp(-\lambda_k s)$ (cf. Table A.1) is put on the hyper-parameter λ_k. The resulting distribution can be integrated with respect to λ and the following result is obtained

$$p(k|s) \propto \frac{1}{(s+1)^{k+1}}, \quad k = 0, 1, ..., k_{\max}. \tag{3.150}$$

A Gamma(a_τ, b_τ) prior (cf. Table A.1), which favors smoother functions with a longer scale of variability, is put on the each of the τ_j. Assuming that the τ_j are independent, this yields

$$p(\{\tau_j\}_{j=1}^k|k, a_\tau, b_\tau) = \prod_{j=1}^k \frac{{b_\tau}^{a_\tau}}{\Gamma(a_\tau)}\tau_j^{a_\tau - 1}\exp(-b_\tau\tau_j). \tag{3.151}$$

Here, $\Gamma(\cdot)$ denotes the Gamma function. Setting $b_\tau = \mu_j a_\tau$ defines a location parameter μ_j, on which an exponential hyper-prior $p(\mu_j|a_\mu) = 1/a_\mu \exp(-\mu_j/a_\mu)$ with hyper-parameter a_μ is used. Integrating over the μ_j yields the prior model for the scale parameters:

$$p(\{\tau_j\}_{j=1}^k|k, a_\tau, b_\tau) = \prod_{j=1}^k \frac{\Gamma(a_\tau + 1)}{\Gamma(a_\tau)}\frac{{a_\tau}^{a_\tau}}{{\tau_j}^{a_\tau - 1}}\frac{1}{a_\mu}\frac{1}{(a_\tau\tau_j + {a_\mu}^{-1})^{a_\tau+1}} \tag{3.152}$$

For the weights, a multivariate normal prior was chosen,

$$p(\{a_j\}_{j=1}^k|k, \sigma_a) = \mathcal{N}(\mathbf{0}, \sigma_a^2\boldsymbol{I}_{k+1}), \tag{3.153}$$

where $\boldsymbol{I}_{k+1}$ denotes the $k+1$-dimensional identity matrix. A Gamma(a_0, b_0) distribution is placed as a prior on $1/\sigma_a^2$. Integrating out $1/\sigma_a^2$ then yields

$$p(\{a_j\}_{j=1}^k | k, \sigma_a) = \frac{1}{(2\pi)^{(k+1)/2}} \frac{\Gamma(a_0 + \frac{k+1}{2})}{\left(b_0 + \frac{1}{2}\sum_{j=0}^k a_j^2\right)^{a_0+(k+1)/2}} \tag{3.154}$$

Lastly, a prior distribution for the location of the kernel functions is needed. As before, the prior is chosen in accordance with Koutsourelakis [183], who proposed a uniform prior

$$p(\boldsymbol{\nu}_{j=1}^k | k) = \frac{1}{\mathcal{V}^k} \tag{3.155}$$

where $\mathcal{V}$ denotes the volume of the hypercube of the input space. By combining (3.148) with (3.150) to (3.155), one arrives at the complete prior model for the parameters $\boldsymbol{\theta}$:

$$\begin{aligned} p(\boldsymbol{\theta}|s, a_\tau, a_\mu, a_0, b_0) &= \frac{1}{(s+k)^{k+1}} \\ &\times \prod_{j=1}^k \frac{\Gamma(a_\tau + 1)}{\Gamma(a_\tau)} \frac{a_\tau^{a_\tau}}{\tau_j^{(a_\tau-1)}} \frac{1}{a_\mu} \frac{1}{(a_\tau \tau_j + a_\mu^{-1})^{(a_\tau+1)}} \\ &\times \frac{b_0^{a_0}}{\Gamma(a_0)} \frac{1}{(2\pi)^{(k+1)/2}} \frac{\Gamma(a_0 + \frac{k+1}{2})}{\left(b_0 + \frac{1}{2}\sum_{j=0}^k a_j^2\right)^{a_0+(k+1)/2}}. \end{aligned} \tag{3.156}$$

The remaining hyper-parameters $s = 1.0, a_\tau = 1.0, a_\mu = 0.01, a_0 = 1.0, b_0 = 1.0$ were set according to Koutsourelakis [183] and are used throughout this work. In addition to the prior on $\boldsymbol{\theta}$, an Inv-Gamma(a, b) prior (cf. Table A.1) was chosen for the variance σ_ϵ^2 of the Gaussian noise with hyper-parameters $a = 2$ and $b = 10^{-6}$ used throughout this work.

3.5.3.2 Obtaining the posterior distribution

Combining likelihood and prior using Bayes' theorem yields the following equation for the posterior distribution

$$p(\boldsymbol{\theta}, \sigma_\epsilon^2 | \boldsymbol{X}, \boldsymbol{y}) \propto p(\boldsymbol{y}|\boldsymbol{X}, \boldsymbol{\theta}, \sigma_\epsilon^2) p(\boldsymbol{\theta}) p(\sigma_\epsilon^2). \tag{3.157}$$

It is convenient to integrate out the variance of the noise σ_ϵ^2 analytically first. The expression for the likelihood where the variance of the noise has been integrated out is easy to obtain because the prior $p(\sigma_\epsilon^2)$ is conjugate to the likelihood above. Inserting the Inv-Gamma(a, b) prior and integrating with respect to σ_ϵ^2 yields

$$\begin{aligned} L(\boldsymbol{\theta}) = p(\boldsymbol{y}|\boldsymbol{X}, \boldsymbol{\theta}) &= \int p(\boldsymbol{y}|\boldsymbol{X}, \boldsymbol{\theta}, \sigma_\epsilon^2) p(\sigma_\epsilon^2) \mathrm{d}\sigma_\epsilon^2 \\ &= \frac{\Gamma(a + \frac{n}{2})}{\left(b + \frac{1}{2}\sum_{i=1}^n (y^{(i)} - f(\boldsymbol{x}^{(i)}, \boldsymbol{\theta}))^2\right)^{a+n/2}}, \end{aligned} \tag{3.158}$$

which can be used to obtain the marginal posterior distribution $p(\boldsymbol{\theta}|\boldsymbol{X}, \boldsymbol{y})$ through combination with the prior $p(\boldsymbol{\theta})$

$$p(\boldsymbol{\theta}|\boldsymbol{X}, \boldsymbol{y}) \propto L(\boldsymbol{\theta}) p(\boldsymbol{\theta}). \tag{3.159}$$

The expression above is analytically intractable and advanced Monte Carlo procedures such as Markov Chain Monte Carlo (MCMC) or sequential Monte Carlo (SMC) are required to draw samples from the posterior. While the discussion of MCMC is beyond the scope of this work and the reader is referred to, e.g., [14, 106, 275] for an introduction to MCMC methods, a brief description of the SMC approach used in this work will follow in Section 4.3.2. In order to use SMC to obtain samples from the posterior, a sequence of auxiliary distributions is required, bridging the gap between the prior, which can be easily sampled from, and the posterior. To that end Koutsourelakis [183] introduced the following sequence of $\{\pi_{n,\lambda}\}$ based on a modified Likelihood $L_\lambda(\boldsymbol{\theta})$ and the number of training samples n

$$\pi_{n,\lambda}(\boldsymbol{\theta}) \propto L_{n,\lambda}(\boldsymbol{\theta})p(\boldsymbol{\theta}), \tag{3.160}$$

with $L_{n,\lambda}(\boldsymbol{\theta})$ being defined as

$$L_{n,\lambda}(\boldsymbol{\theta}) = \frac{\Gamma(a+\frac{n+\lambda}{2})}{\left(b+\frac{1}{2}\sum_{i=1}^{n}(y^{(i)}-f(\boldsymbol{x}^{(i)},\boldsymbol{\theta}))^2+\lambda(y^{(i+1)}-f(\boldsymbol{x}^{(i)},\boldsymbol{\theta}))^2\right)^{a+(n+\lambda)/2}} \tag{3.161}$$

As with the other regression techniques presented in this work, the goal is to make probabilistic predictions about the value of y for a new test input $\boldsymbol{x}^*$. Hence, in addition to the posterior $p(\boldsymbol{\theta}|\boldsymbol{X},\boldsymbol{y})$, information about the variance of the noise term is needed as well. It can be shown that the conditional posterior $p(\sigma_\epsilon^2|\boldsymbol{\theta},\boldsymbol{X},\boldsymbol{y})$ has the following form

$$p(\sigma_\epsilon^2|\boldsymbol{\theta},\boldsymbol{X},\boldsymbol{y}) = \text{Inv-Gamma}\Big(a+\frac{n}{2}, b+\frac{\sum_{i=1}^{n}(y^{(i)}-f(\boldsymbol{x}^{(i)},\boldsymbol{\theta}))^2}{2}\Big) \tag{3.162}$$

Hence, if a set of samples from the posterior $p(\boldsymbol{\theta}|\boldsymbol{X},\boldsymbol{y})$ is available, samples of σ_ϵ^2 are easily computed by sampling from (3.162).

In the present work, the regression model proposed by Koutsourelakis [183] was used for regression with one-dimensional input only. Moreover, the functional relationship was slightly modified through the addition of a linear term in (3.146), which enhanced the performance of the model and reads

$$f(x,\boldsymbol{\theta}) = a_0 + a_1 x + \sum_{j=2}^{k} a_j \exp(-\tau_j \left\|\nu_j - x\right\|^2). \tag{3.163}$$

To accommodate the linear term, the prior had to be adjusted accordingly. For one-dimensional input, the adjusted full prior model then reads

$$\begin{aligned} p(\boldsymbol{\theta}|s,a_\tau,a_\mu,a_0,b_0) &= \frac{1}{(s+k)^{k+1}} \\ &\times \prod_{j=1}^{k} \frac{\Gamma(a_\tau+1)}{\Gamma(a_\tau)} \frac{a_\tau^{a_\tau}}{\tau_j^{(a_\tau-1)}} \frac{1}{a_\mu} \frac{1}{(a_\tau\tau_j + a_\mu^{-1})^{(a_\tau+1)}} \\ &\times \frac{b_0^{a_0}}{\Gamma(a_0)} \frac{1}{(2\pi)^{(k+2)/2}} \frac{\Gamma(a_0+\frac{k}{2}+1)}{\left(b_0+\frac{1}{2}\sum_{j=0}^{k} a_j^2\right)^{a_0+k/2+1}}. \end{aligned} \tag{3.164}$$

4 Existing approaches for uncertainty quantification and limitations regarding complex models

Model-based UQ is arguably now one of the fastest growing methodological paradigms in the field of computational simulation of engineering systems and has received a lot of attention amongst researchers from different scientific fields in recent years. Both the engineering community and the field of applied mathematics have contributed tremendously to this area of research. This has led to marked progress and the development of many different approaches for the propagation of uncertainties through computational models. In this work, the focus lies on probabilistic approaches, i.e., approaches where uncertainty is described using random variables or processes. Non-probabilistic approaches, such as approaches based on fuzzy set theory, interval analysis, Dempster-Shafer theory, or polymorphic uncertainty are not considered in this work and the reader is referred to the corresponding literature on the subject [77, 165, 220, 294].

The present chapter begins with an abstract description of the UQ problem at hand and a brief discussion of the challenges associated with model based UQ. Then, a short review and introduction to state-of-the-art methods for UQ is given. Because some of these approaches are employed in this work a more detailed explanation than necessary in a pure literature review, is given. The emphasis is placed on two major categories which apply to the majority of the existing approaches. The first broad class of algorithms is based on sampling approaches like Monte Carlo (MC) and all its variants. These methods can be applied regardless of forward model complexity or stochastic dimension, but often require an impractical or infeasible amount of forward model evaluations for accurate results. First, standard the Monte Carlo approach is discussed as it is extensively used for validation purposes in this work, before some of the more advanced techniques are briefly reviewed. Sequential Monte Carlo (SMC) algorithms are introduced, because SMC is used in this work to sample from high-dimensional distributions arising in the context of Bayesian inference. As SMC can also be used for the purpose of UQ, especially for estimating small failure probabilities, and because it fits better together with a discussion of Monte Carlo and importance sampling, it is also discussed in this chapter instead of the previous one.

Then, some classic approaches such as second order methods and reliability methods based on first and second order reliability analysis (FORM/SORM) will be briefly touched for the sake of completeness, before discussing the second major category of UQ methods, which are methods based on some kind of surrogate model or metamodel. More specifically, surrogate models that are either based on some form of the Polynomial Chaos Expansion (PCE) or on Gaussian process models are introduced in this chapter. For low dimensional stochastic problems, i.e., systems which are governed by relatively few random variables, surrogate models are often the method of choice and provide results of comparable accuracy to Monte Carlo solutions at a

fraction of the computational cost. However, surrogate based UQ approaches are not suitable for problems with high stochastic dimension.

4.1 Problem description

In the context of UQ it is often helpful to think of a model, e.g., a finite element model of an AAA, as an abstract function $f : \mathbb{R}^d \to \mathbb{R}$ which maps a vector of input parameters $\boldsymbol{x} \in \mathbb{R}^d$ to the response y

$$y = f(\boldsymbol{x}). \tag{4.1}$$

Thereby, model input parameter is to be understood in a very broad sense, meaning that $\boldsymbol{x}$ can describe, e.g., constitutive parameters, boundary conditions, the geometry of the model, or any combination of these, either explicitly or via an appropriate parametrization. The model $f(\cdot)$ is often referred to as *forward model*, *solver* or *simulator*. It is also often spoken of a *code* which can be evaluated at certain locations in the input space. In principle, it is thereby irrelevant whether $f(\cdot)$ is a complex computational model which requires the run of an elaborate finite element solver to compute y or an analytic function. For the sake of simplicity scalar quantities of interests, i.e., model outputs y, are considered here to facilitate the discussion. However, vector valued output could be considered as well and the extension to multi-dimensional output is straightforward for many UQ methods. As with the input, the model output is to be interpreted in a very general sense and can also be a function of direct model output quantities.

Throughout this work, uncertainty is described using probability theory. Hence, if the input parameters are uncertain, they can be described by a random vector x. As a consequence, the response becomes random too

$$\mathsf{y} = f(\mathsf{x}). \tag{4.2}$$

The goal of UQ is inference about the random variable y. Depending on the application different summaries or statistics are relevant. Frequently, one is interested in expectations of the form

$$\int h(y) p_{\mathsf{y}}(y) \mathrm{d}y = \mathbb{E}[h(\mathsf{y})] = \mathbb{E}[h(f(\mathsf{x}))] = \int h(f(\boldsymbol{x})) p_{\mathsf{x}}(\boldsymbol{x}) \mathrm{d}\boldsymbol{x}. \tag{4.3}$$

For $h(\mathsf{y}) = \mathsf{y}$ and $h(\mathsf{y}) = (\mathsf{y} - \mathbb{E}[\mathsf{y}])^2$ one obtains the first moments $\mathbb{E}[\mathsf{y}]$ and $\mathbb{V}[\mathsf{y}]$, respectively. Often the mean and variance are not sufficient and also an estimate of the PDF or CDF of y is desired. These can be used to compute quantiles or prediction intervals. For instance, in this work the 95% quantile, i.e., the value of y below which 95% of the observations/realizations fall, is used as worst case estimate for y.

Aside from mean, variance, or the full probability distribution the computation of a so-called failure probability is of interest in many UQ applications. Based on the assumption that a system fails if the output falls into the domain $\mathcal{A}$, it is desired to compute the probability of failure, i.e., $P(y \in \mathcal{A})$. The failure domain could for instance be defined by a failure threshold, i.e., $\mathcal{A} : y > y_{\text{fail}}$. The probability of failure can then be computed by evaluation of the following integral

$$P(y \in \mathcal{A}) = P_{\text{fail}} = \int \mathbf{1}_{\mathcal{A}}(y(\boldsymbol{x})) p_{\mathsf{x}}(\boldsymbol{x}) \mathrm{d}\boldsymbol{x} \tag{4.4}$$

The estimation of the above mentioned quantities is often a challenging problem because $f(\cdot)$ is usually not known explicitly, since it represents a complex computational model. And even if it were known in closed form, an analytic solution to (4.3) or (4.4) is not available in all but the simplest cases. Moreover, the dimension of the problem, often referred to as the *stochastic dimension* of the problem, can be very high. This can have two reasons. First, only one or few physical input parameters of the computational model are uncertain, but each of them has to be modelled by a stochastic process or field. These processes have to be discretized using, e.g., one of the methods described in Section 3.3.3, which typically results in a description based on many, often thousands, random variables. Second, many of the physical input parameters are, in fact, uncertain, but admit a description with random variables instead of random processes or fields. To be able to distinguish the two cases the notion of physical and mathematical stochastic dimension is introduced here. The physical stochastic dimension denotes the number of uncertain physical parameters in the model, whereas the mathematical stochastic dimension denotes the total number of random input variables which might also originate from a stochastic field model for a single uncertain physical input parameter.

The type of summary or statistic, that a UQ method provides, is obviously an important criterion for choosing a method, as not all UQ approaches can provide estimates for all summaries or statistics of the quantity of interest y. For instance, multiple so-called *reliability methods* have been designed in the past specifically to tackle the computation of small failure probabilities. While some of these methods are very efficient for the computation of small failure probabilities, these methods typically cannot be used to obtain information beyond this failure probability.

Another important aspect is the ability to cope with forward model complexity. UQ methods drastically differ in their ability to cope with the complexity of the forward model. Some UQ approaches are for instance limited to linear forward models. In the context of computational solid mechanics many forward models exhibit nonlinear behaviour due to, e.g., geometric nonlinearities, constitutive nonlinearities, or boundary condition nonlinearities. Regarding other applications, many models also show distinct nonlinearities or even discontinuities in the map from model input to model output.

Similarly, UQ approaches differ in their ability to deal with stochastic model complexity. Some methods are limited to a certain type of probability distribution for the random model inputs, such as the standard normal distribution. Moreover, not all methods can cope with correlated input parameters or a high stochastic dimension of the problem. Many UQ methods suffer from the so-called *curse of dimensionality*, meaning that the computational complexity is drastically influenced by the stochastic dimension of the model.

Often it is distinguished between so-called intrusive and non-intrusive UQ approaches. Intrusive approaches are essentially based on modifications of the governing equations by including parametrized input uncertainty into the model and deriving a new set of equations to be solved with a tailored numerical solution scheme. This implies that access to the source code is needed and that elaborate legacy codes can, in general, not be used. Thus, the implementation of these methods can be cumbersome and time consuming. Moreover, intrusive implementations are often tailored to a specific problem, i.e., a specific partial differential equation, which hampers reuse. In contrast, non-intrusive approaches use the forward model as a black-box and do not necessarily require access and/or modification of the source code of the forward solver, but merely require a series of evaluations of the forward model. Having said that, it is often useful

to be able to modify the source code of the forward solver even if non-intrusive approaches are used. For instance, implementation of a parameter continuation scheme, which requires modification of the code, can dramatically speed up forward model evaluations. Because non-intrusive approaches treat the forward model as black-box it is often straightforward to adapt non-intrusive approaches to another type of forward problem, which is considered a major advantage.

While the aim of UQ is essentially the inference and description of the unknown distribution of the stochastic model output y due to uncertain input parameters $\mathbf{x}$, the aim of sensitivity analysis is the identification of the contributions of particular subsets or individual uncertain input parameters x_i to the overall uncertainty in y. Identification of the components which contribute the most and the least to the overall output uncertainty is important. First of all because the components of $\mathbf{x}$ which do not contribute much to the overall output uncertainty could be fixed at some average value. Secondly, a more accurate assessment of the parameters which contribute the most to the output uncertainty would yield the biggest improvement and hence resources should be focused primarily on the more accurate assessment of these parameters. However, the primary focus of this work is UQ and hence methods for sensitivity analysis are not discussed in detail here but the inclined reader is referred to, e.g., [156, 288, 306] for a more detailed discussion of the subject.

4.2 Monte Carlo

Standard Monte Carlo is by far the most versatile and easy to implement UQ method. A relatively recent review on UQ methods for engineering problems describes the Monte Carlo method as "*perhaps the only universal tool for treating complex stochastic finite element applications*" [314]. It can be applied regardless of system complexity and stochastic dimension. Moreover, it enables the computation of any desired response statistic and also provides an estimate for the PDF of the quantity of interest. In addition, all desired quantities can, at least in principle, be computed to arbitrary precision. That, however, comes at significant and sometimes prohibitive computational cost, which is essentially the "only" drawback of the Monte Carlo method. Because the Monte Carlo method is extensively used in this work, the basics of the standard Monte Carlo methods are discussed here in more detail.

In order to use Monte Carlo one requirement is the ability to draw a number of samples from the vector of random input quantities, i.e., $\{\boldsymbol{x}^{(i)}\}_i^{N_{\mathrm{SAM}}} \sim p_{\mathbf{x}}(\boldsymbol{x})$ and then evaluate the model f for these samples. Additionally, some very mild assumptions about the random output y have to be made, namely that the integrals (3.27) and (3.28) exist, i.e., that y has a mean $\mathbb{E}[\mathsf{y}] = \mu_{\mathsf{y}}$ and finite variance. If this is the case the following estimators can be used, resulting in approximations for mean and variance of y:

$$\mu_{\mathsf{y}} \approx \hat{\mu}_{\mathsf{y}} = \frac{1}{N_{\mathrm{SAM}}} \sum_{i=1}^{N_{\mathrm{SAM}}} f(\boldsymbol{x}^{(i)}) = \frac{1}{N_{\mathrm{SAM}}} \sum_{i=1}^{N_{\mathrm{SAM}}} y^{(i)}, \tag{4.5}$$

$$\sigma_{\mathsf{y}}^2 \approx \hat{\sigma}_{\mathsf{y}}^2 = \frac{1}{1 - N_{\mathrm{SAM}}} \sum_{i=1}^{N_{\mathrm{SAM}}} \Big(f(\boldsymbol{x}^{(i)}) - \hat{\mu}_{\mathsf{y}} \Big)^2. \tag{4.6}$$

The estimate for the mean $\hat{\mu}_{\mathsf{y}}$ is also a random variable. The variance of $\hat{\mu}_{\mathsf{y}}$ can computed by

$$\mathbb{V}[\hat{\mu}_{\mathsf{y}}] = \mathbb{E}[(\hat{\mu}_{\mathsf{y}} - \mu_{\mathsf{y}})^2] = \frac{\sigma_{\mathsf{y}}^2}{N_{\text{SAM}}} \tag{4.7}$$

and be used to assess the accuracy of the Monte Carlo estimate, e.g., by computing the RMSE:

$$\text{RMSE}(\hat{\mu}) = \frac{\sigma_{\mathsf{y}}}{\sqrt{N_{\text{SAM}}}} \approx \frac{\hat{\sigma}_{\mathsf{y}}}{\sqrt{N_{\text{SAM}}}}. \tag{4.8}$$

Since the variance of y is generally not known, it has to be estimated from the samples as well. The estimate $\hat{\sigma}_{\mathsf{y}}^2$ is asymptotically correct; however, for small sample sizes the estimate might be very poor, which might lead to a false sense of convergence.

In addition, Monte Carlo can also be used to estimate failure probabilities. To estimate the failure probability, the integral in (4.4) is approximated by the empirical mean

$$\hat{P}_{\text{fail}} = \frac{1}{N_{\text{SAM}}} \sum_{i=1}^{N_{\text{SAM}}} 1_{\mathcal{A}}(\boldsymbol{x}^{(i)}) = \frac{N_{\text{fail}}}{N_{\text{SAM}}}. \tag{4.9}$$

The variance of that estimate can also be computed as

$$\mathbb{V}[\mathsf{P}_{\text{fail}}] = P_{\text{fail}}(1 - P_{\text{fail}}), \tag{4.10}$$

which in turn can be used to compute confidence intervals for P_{fail}. However, it is more common to express the accuracy of the estimate in terms of the COV, which in this case can be calculated as

$$\text{COV}_{P_{\text{fail}}} = \sqrt{\text{Var}[P_{\text{fail}}]}/P_{\text{fail}} \approx 1/\sqrt{N_{\text{SAM}} P_{\text{fail}}}. \tag{4.11}$$

In practical applications though one generally does not know P_{fail} and hence the estimated $\hat{P}_{\text{fail}}$ has to be used to assess the accuracy, which can be low if P_{fail} is very small.

Aside from expectation, variance, and failure probabilities, Monte Carlo provides empirical estimates for PDF, CDF, or confidence intervals for y as well. The Monte Carlo estimate for $p_{\mathsf{y}}(y)$ for instance is obtained by

$$p_{\mathsf{y}}(y) \approx \frac{1}{N_{\text{SAM}}} \sum_{i=1}^{N_{\text{SAM}}} \delta_{y^{(i)}}(y(\boldsymbol{x}^{(i)})), \tag{4.12}$$

where $\delta_{y^{(i)}}$ is the delta-Dirac mass. From a more general point of view, the Monte Carlo method provides a particulate approximation to the distribution of interest which also can be written more general as

$$p_{\mathsf{y}}(y) \approx \sum_{i=1}^{N_{\text{SAM}}} W^{(i)} \delta_{y^{(i)}}(y(\boldsymbol{x}^{(i)})), \tag{4.13}$$

where the $W^{(i)}$ denote the so-called *normalized weights*. In case of standard Monte Carlo all samples have the same weight $W^{(i)} = 1/N_{\text{SAM}}$. However, this does not need to be the case. In many sampling based schemes so-called *weighted particles* $\{y^{(i)}, W^{(i)}\}_{i=1}^{N_{\text{SAM}}}$ are used to approximate a distribution. Thereby, the particles usually do not have the same weight.

Confidence intervals for y are readily computed by reordering the samples in ascending order, e.g., through re-indexing the samples $y^{(i)}$ as $y^{(i)'}$ such that $y^{(1)'} \leq y^{(1)'} \leq \cdots y^{(N_{\text{SAM}})'}$. Then, a $(1-\alpha)\%$ confidence interval containing $(1-\alpha)\%$ of all samples is readily obtained through

$$[y_{\text{cf,low}}, y_{\text{cf,up}}] = [y_j, y_k] \quad \text{with} \quad j = (N_{\text{SAM}}+1)\alpha/2 \quad \text{and} \quad k = (N_{\text{SAM}}+1)(\alpha/2-1). \tag{4.14}$$

Arbitrary quantiles can be computed in a similar fashion as well. Having discussed the general Monte Carlo procedure as well as the requirements, it is apparent that the Monte Carlo method is a very general approach and easy to implement, since the computational model is treated as a black-box. Moreover, because the samples are independent from each other, the algorithm can be easily executed in parallel harnessing massively parallel computer architectures. The ability to estimate any desired response statistics is also considered very beneficial. In addition, as can be seen in (4.8) and (4.11) the accuracy of the estimates do not depend on the dimension of $\mathbf{x}$ per se. This feature sets Monte Carlo apart from many other UQ approaches whose accuracy deteriorates dramatically with increasing dimension of the problem, given that the number of forward model evaluations is fixed. While the dimension by itself does not affect the accuracy if additional random dimensions are considered, it is likely that the variance of the response σ_{y}^2 increases, which in turn effects the error in (4.8). An exception are models where one or more physical parameters are modelled as stochastic processes, which results in a high stochastic dimension of the problem. If the accuracy of the representation of the process is increased, say by considering a larger number of terms in the representation of the process, the additional random input variables will not have a dramatic effect on σ_{y}^2.

Although Monte Carlo is conceptually simple, easy to implement, and can provide all desired statistical quantities, its application is hampered by the computational effort that is needed to achieve accurate results. The convergence rate of Monte Carlo is $\mathcal{O}(1/\sqrt{N_{\text{SAM}}})$ and an accurate estimation of the aforementioned quantities requires a large number of model evaluations. Especially, for the estimations regarding the tail of the distribution, e.g., small failure probabilities or 99% quantiles, (4.11) indicates that the number of necessary samples becomes extremely high. Moreover, the error estimates for the computed quantities hold only in the limit $N_{\text{SAM}} \to \infty$, and might not be accurate for smaller sample sizes. Anyway, for current state of the art model in computational mechanics the solution time to for a single forward model evaluation is typically in the order of hours or even days using multiple processors. Hence, direct Monte Carlo with several thousands or tens of thousands samples is prohibitively expensive or at least impractical.

4.3 Advanced sampling techniques

Since its introduction in 1949 by Metropolis and Ulam [214], researchers have made considerable progress in improving the overall efficiency of standard Monte Carlo sampling. Most of the conducted research aimed at reducing the computational cost by reducing the variance of the estimators through selecting samples that fill the sample space more effectively than purely random sampling. A popular class of techniques to improve on the accuracy of standard Monte Carlo is stratified sampling, which includes the popular *Latin hypercube sampling* (LHS) method [211]. The basic idea of these techniques is the subdivision of the sample space into smaller regions which are then sampled separately. In the most basic version of LHS the range

of each random dimension is divided into a number of j disjoint subsets which have equal probability. Then, for each dimension separately, j sample components are drawn, one from each subset. Subsequently, a sample can be assembled by randomly drawing without replacement from each of the generated sample components. This process is then repeated j times. Since the assembly process is random, LHS is not unique and several algorithms have been proposed to determine optimal pairings to produce samples which fill the sample space more effectively. The design of optimal space filling sampling is an active area of research and many variants to LHS as well as many alternatives have been proposed, see, e.g., [298, 344] and the references therein. LHS has been successfully applied to UQ problems and it has been demonstrated that it can improve the accuracy compared to standard Monte Carlo [150, 243]. Alas, it is in general hard to predict the gain in computational efficiency since it depends on the specific application as well as the structure and dimensionality of the investigated system [315]. Another option are so-called *Quasi-Monte Carlo* methods, where the sampling is no longer random but based on deterministic sequences, see, e.g., [55, 123] for further information.

4.3.1 Importance sampling based schemes

Importance sampling (IS) is another well known sampling approach, which forms the basis of many advanced sampling schemes, including sequential Monte Carlo techniques, which will be discussed shortly. It is essentially a variance reduction technique to increase the accuracy of Monte Carlo. However, another equally important aspect is that the IS also provides a way to compute estimates of properties of a distribution when only samples from a different distribution than the distribution of interest are available.

Consider for instance the expectation of a general function $\varphi(\boldsymbol{x})$ under a probability distribution $p_{\mathbf{x}}(\boldsymbol{x})$ in the form of

$$\mathbb{E}[\varphi(\mathbf{x})] = \int \varphi(\boldsymbol{x}) p_{\mathbf{x}}(\boldsymbol{x}) \mathrm{d}\boldsymbol{x}. \tag{4.15}$$

The underlying concept is to draw samples $\boldsymbol{x}^{(i)}$ from a so called importance distribution $q_{\mathbf{x}}(\boldsymbol{x})$ instead of $p_{\mathbf{x}}(\boldsymbol{x})$. Ideally, the distribution $q_{\mathbf{x}}(\boldsymbol{x})$ is concentrated in the important regions of the parameter space. First, the usual integral (4.15) is simply extended with the importance distribution $q_{\mathbf{x}}(\boldsymbol{x})$, yielding

$$\mathbb{E}[\varphi(\mathbf{x})] = \int \varphi(\boldsymbol{x}) p_{\mathbf{x}}(\boldsymbol{x}) \mathrm{d}\boldsymbol{x} = \int \frac{\varphi(\boldsymbol{x}) p_{\mathbf{x}}(\boldsymbol{x}) q_{\mathbf{x}}(\boldsymbol{x})}{q_{\mathbf{x}}(\boldsymbol{x})} \mathrm{d}\boldsymbol{x}. \tag{4.16}$$

Then, instead of drawing samples from $p_{\mathbf{x}}(\boldsymbol{x})$ samples are drawn from $q_{\mathbf{x}}(\boldsymbol{x})$, $\{\boldsymbol{x}^{(i)}\}_i^{N_{\mathrm{SAM}}} \sim q_{\mathbf{x}}(\boldsymbol{x})$ and $\mathbb{E}[\varphi(\mathbf{x})]$ can be computed by

$$\mathbb{E}[\varphi(\mathbf{x})] \approx \frac{1}{N_{\mathrm{SAM}}} \sum_{i=1}^{N_{\mathrm{SAM}}} \frac{\varphi(\boldsymbol{x}^{(i)}) p_{\mathbf{x}}(\boldsymbol{x}^{(i)})}{q_{\mathbf{x}}(\boldsymbol{x}^{(i)})} = \frac{1}{N_{\mathrm{SAM}}} \sum_{i=1}^{N_{\mathrm{SAM}}} \varphi(\boldsymbol{x}^{(i)}) w(\boldsymbol{x}^{(i)}), \tag{4.17}$$

with the unnormalized importance weight $w(\boldsymbol{x})$ defined as

$$w(\boldsymbol{x}) = \frac{p_{\mathbf{x}}(\boldsymbol{x})}{q_{\mathbf{x}}(\boldsymbol{x})}. \tag{4.18}$$

Using a more general notation and the concept of weighted particles $\{\boldsymbol{x}^{(i)}, W^{(i)}\}_{i=1}^{N_\mathrm{p}}$ introduced above, (4.17) can be written as

$$\mathbb{E}[\varphi(\mathbf{x})] \approx \sum_{i=1}^{N_\mathrm{p}} \varphi(\boldsymbol{x}^{(i)}) W^{(i)}, \tag{4.19}$$

with the normalized importance weights $W^{(i)}$, which can be computed from the unnormalized importance weights $w^{(i)}$ of each particle by

$$W^{(i)} = \frac{w(\boldsymbol{x}^{(i)})}{\sum_{i=1}^{N_\mathrm{p}} w(\boldsymbol{x}^{(i)})} = \frac{w^{(i)}}{\sum_{i=1}^{N_\mathrm{p}} w^{(i)}}. \tag{4.20}$$

Moreover, the particles provide an approximation to the distribution $p_{\mathbf{x}}(\boldsymbol{x})$

$$p_{\mathbf{x}}(\boldsymbol{x}) \approx \sum_{i=1}^{N_\mathrm{p}} W^{(i)} \delta_{\boldsymbol{x}^{(i)}}(\boldsymbol{x}). \tag{4.21}$$

There are many scenarios in which importance sampling can be useful, one of which is the more efficient estimation of failure probabilities, i.e., when $\varphi(\boldsymbol{x}) = \mathbf{1}(f(\boldsymbol{x}) > y_\mathrm{fail}) = \mathbf{1}_{\mathcal{A}}(\boldsymbol{x})$. For the efficient estimation of P_fail the importance distribution has to be concentrated in the region of the failure domain. If a suitable importance distribution can be found, it can be shown that importance sampling yields a more accurate estimator [275]. However, finding a suitable importance distribution is non-trivial in practice, especially for high-dimensional problems. Several approaches have been proposed to construct importance distributions for the estimation of small failure probabilities. Using design points obtained with, e.g., FORM analysis (cf. Section 4.4) or performing an initial sampling step to identify import regions has been proposed by Bourgund and Bucher [45] and Bucher [53]. Other approaches are based on kernel density estimation using samples in the failure domain obtained with Markov Chain Monte Carlo (MCMC) [15, 17]. Overall, it was found that the effort required to construct suitable importance distribution can be very significant and that the extension to high dimensional problems is not straightforward [18, 171]. To overcome the limitations of IS for reliability problems, other sampling methods to estimate small failure probabilities have been proposed, e.g., line sampling [184], asymptotic sampling [54], and subset simulation [17, 21]. Especially the latter was particularly successful and has been applied to a variety of reliability problems [19, 20, 27, 245, 250]. Subset simulation is also known as annealed importance sampling [228]. It is worth mentioning that the aforementioned sampling schemes can be augmented by surrogate models (cf. Section 4.6) to further improve the performance by reducing the number of model evaluations through incorporation of cheap to evaluate surrogate models [46, 71, 94]. However, it is important to keep in mind that surrogate models tend to perform worse with increasing stochastic dimension of the problem.

4.3.2 Sequential Monte Carlo

Another, scenario in which the importance sampling principle can be applied is when one cannot sample directly from the distribution of interest. Consider for instance a Bayesian regression

model $f(\boldsymbol{x}, \boldsymbol{\theta})$ as given in (3.146), where $\boldsymbol{\theta}$ contains the parameters of the model which are to be inferred from data. Making predictions for a new test input $\boldsymbol{x}^*$,i.e., compute $p(f^*|\boldsymbol{x}^*, \mathcal{D})$ or obtain point estimates such as $\mathbb{E}[\mathsf{f}^*]$ requires sampling from the posterior distribution $p(\boldsymbol{\theta})$, which usually cannot be done using the usual pseudorandom generators or other standard methods such as rejection sampling. Since designing a suitable importance sampling distribution from scratch is extremely difficult or even impossible for moderate to high dimensional distributions, MCMC techniques are usually used to obtain samples from the posterior distribution [13, 361]. As pointed out in, e.g., [183], some of the disadvantages of MCMC techniques can be improved upon by using sequential Monte Carlo (SMC) techniques. Sequential Monte Carlo algorithms are, to some extend, an extension of importance sampling, which present a remedy to this problem by, roughly speaking, building up the importance distribution sequentially [57, 76]. Furthermore, the aforementioned subset simulation can also be understood as a particular version of SMC.

Sequential Monte Carlo provides a very general framework to sample from complex high dimensional distributions based on a number of intermediate distributions as bridging steps. SMC is used in this work to obtain samples from the posterior distribution of the Bayesian regression model described in Section 3.5.3 and not to estimate failure probabilities. However, the brief description of the approach is kept very general such that the application of the method in the context of estimating small failure probabilities becomes clear as well.

Assuming that $\pi_t(\boldsymbol{x})$ is the target density, one wishes to sample from or integrate over, and that, moreover, this density is known up to a normalizing constant Z_t, i.e.,

$$\pi_t(\boldsymbol{x}) = \frac{\gamma_t(\boldsymbol{x})}{Z_t}. \tag{4.22}$$

Instead of considering the target distribution directly, a sequence of intermediate distributions is designed to break down the problem into a series of easier ones. The goal is a series of distributions $\{\pi_n\}_{n=1}^t$ which transition gradually from a simple, and hence easy to sample from, distribution to the distribution of interest. Such series often arise naturally in Bayesian inference schemes. Consider, e.g., the following sequence

$$\pi_n(\boldsymbol{x}) \propto p(\boldsymbol{x}|y_1, ..., y_n), \tag{4.23}$$

where t data points are available. Or a sequence of bridging distributions to move smoothly from a tractable $\pi_1 = \eta$ distribution to the target distribution π_t

$$\pi_n(\boldsymbol{x}) \propto \pi(\boldsymbol{x})^{\lambda_n} \eta(\boldsymbol{x})^{1-\lambda_n}, \tag{4.24}$$

where $0 \leq \lambda_n \leq \lambda_t = 1$. Another option is the sequence defined in (3.160).

For estimating small failure probabilities, i.e., $P(f(\boldsymbol{x}) > y_{\text{fail}}) \approx 0$, the following definition of $\{\pi_n\}_{n=1}^t$ based on an increasing sequence of thresholds $f_1 \leq f_2 \leq f_3 \leq f_t = y_{\text{fail}}$ can be used:

$$\pi_n(\boldsymbol{x}) \propto \pi(\boldsymbol{x}) \mathbf{1}_{\mathcal{A},n}(\boldsymbol{x}), \tag{4.25}$$

where $\mathbf{1}_{\mathcal{A},n}(\boldsymbol{x})$ is the indicator function of the events $f(\boldsymbol{x}) > f_n$. Without going into the details, which are provided in [76], as to why this is necessary in order to build up an importance

distribution sequentially, a second, auxiliary sequence of distributions is defined on an extended space

$$\tilde{\gamma}_n(\boldsymbol{x}_{1:n}) = \gamma_n(\boldsymbol{x}_n) \prod_{k=1}^{n-1} L_k(\boldsymbol{x}_{k+1}, \boldsymbol{x}_k). \tag{4.26}$$

Therein, $\tilde{\gamma}_n(\boldsymbol{x}_{1:n})$ is defined on $\Omega^n = \Omega \times \Omega \times \Omega \times \cdots \times \Omega$. In addition, the notation $\boldsymbol{x}_{1:n} = [\boldsymbol{x}_1, \boldsymbol{x}_2, \cdots, \boldsymbol{x}_n]$ is used. The construction of this sequence is such that $\{\tilde{\gamma}_n(\boldsymbol{x}_{1:n})\}_{n=1}^{t}$ admits $\gamma_n(\boldsymbol{x}_n)$ as marginal distribution in every step. Based on the notion that the index n is associated with time, the auxiliary distributions are defined using so-called *backward* Markov kernels $L_k(\boldsymbol{x}_{k+1}, \boldsymbol{x}_k)$, which denote the probability density of moving from $\boldsymbol{x}_{k+1}$ to $\boldsymbol{x}_k$. Similarly, the importance sampling distribution is build up sequentially as well

$$q_n(\boldsymbol{x}_{1:n}) = q_1(\boldsymbol{x}_1) \prod_{k=2}^{n} K_k(\boldsymbol{x}_{k-1}, \boldsymbol{x}_k) \tag{4.27}$$

using a series of so-called *forward* Markov kernels $K_k(\boldsymbol{x}_{k-1}, \boldsymbol{x}_k)$ describing a probability density of moving from $\boldsymbol{x}_{k-1}$ to $\boldsymbol{x}_k$

With the definition of these two sequences of distributions, sequential importance sampling can be performed as follows: The starting point is a set of weighted particles $\{\boldsymbol{x}_1^{(i)}, W_1^{(i)}\}_{i=1}^{N_\mathrm{p}}$ drawn from $q_1(\boldsymbol{x})$ which is easy to sample from; a popular choice is, e.g., $q_1(\boldsymbol{x}) = \pi_1(\boldsymbol{x})$. In the following steps, the particles are perturbed in the sense that samples are drawn from $q_n(\boldsymbol{x}_{1:n})$. Since the goal is to sample from $\{\tilde{\gamma}_n(\boldsymbol{x}_{1:n})\}$, the weights have to be corrected. For the unnormalized importance weights, the new weight in step n can be computed using the update formula:

$$w_n^{(i)} = \frac{\tilde{\gamma}_n(\boldsymbol{x}_{1:n}^{(i)})}{q_n(\boldsymbol{x}_{1:n}^{(i)})} = \frac{\gamma_n(\boldsymbol{x}_n^{(i)}) \prod_{s=1}^{n-1} L_s(\boldsymbol{x}_{s+1}^{(i)}, \boldsymbol{x}_s^{(i)})}{q_n(\boldsymbol{x}_{1:n}^{(i)}) \prod_{k=2}^{n} K_k(\boldsymbol{x}_{k-1}^{(i)}, \boldsymbol{x}_k^{(i)})} = w_{n-1}^{(i)} \breve{w}_n(\boldsymbol{x}_{n-1}^{(i)}, \boldsymbol{x}_n^{(i)}) \tag{4.28}$$

with the unnormalized incremental weigths $\breve{w}_n$ being

$$\breve{w}_n(\boldsymbol{x}_{n-1}^{(i)}), \boldsymbol{x}_n^{(i)})) = \frac{\gamma_n(\boldsymbol{x}_n^{(i)}))L_{n-1}(\boldsymbol{x}_n^{(i)}), \boldsymbol{x}_{n-1}^{(i)}))}{\gamma_{n-1}(\boldsymbol{x}_n^{(i)}))K_n(\boldsymbol{x}_{n-1}^{(i)}), \boldsymbol{x}_n^{(i)}))}. \tag{4.29}$$

It can be shown [76] that a good choice for $L_{n-1}(\boldsymbol{x}_n, \boldsymbol{x}_{n-1})$ is

$$L_{n-1}(\boldsymbol{x}_n, \boldsymbol{x}_{n-1}) = \frac{\pi_n(\boldsymbol{x}_{n-1}) K_n(\boldsymbol{x}_{n-1}, \boldsymbol{x}_n)}{\pi_n(\boldsymbol{x}_n)} \tag{4.30}$$

if π_n and π_{n-1} are close, and under the condition that K_n is a MCMC kernel that is π_{n-1} invariant. The MCMC kernel is referred to as π_{n-1} invariant if the following condition holds:

$$\int \pi_{n-1}(\boldsymbol{x}_{n-1}) K_n(\boldsymbol{x}_{n-1}, \boldsymbol{x}_n) \mathrm{d}\boldsymbol{x}_{n-1} = \int \pi_{n-1}(\boldsymbol{x}_n). \tag{4.31}$$

Details as to what constitutes a MCMC kernel will be given shortly. Chosing $L_{n-1}(\boldsymbol{x}_n, \boldsymbol{x}_{n-1})$ according (4.30) results in a very simple update equation for the weights [76]

$$\breve{w}_n(\boldsymbol{x}_{n-1}, \boldsymbol{x}_n) = \frac{\gamma_n(\boldsymbol{x}_{n-1})}{\gamma_{n-1}(\boldsymbol{x}_{n-1})}. \tag{4.32}$$

It is a known problem that the importance weights in such an sequential importance sampling scheme degenerate over time, i.e., the variance of the importance weights becomes larger and many particles with an extremely low importance weight will occur in the particle population [75, 90]. A remedy to this problem is resampling, which roughly speaking removes particles with low weights from the population while duplicating important particles with large weights. However, frequent resampling can reduce the informational content of the particle population. The so-called *effective sample size* (ESS) can be used to gauge the need for resampling. The ESS is defined as

$$\mathrm{ESS} = \frac{1}{\sum_{i=1}^{N_\mathrm{p}} (W^{(i)})^2}, \tag{4.33}$$

where $W^{(i)}$ denotes the normalized particle weight as defined in (4.20). The ESS can take values between 1 and N_p. A threshold for resampling of $\mathrm{ESS} = N_\mathrm{p}/2$ was used throughout this work.

In practice, the SMC scheme described above generally consists of a repetition of three basic steps, which are also summarized in Table 4.1. The first step entails reweighting of the particles using (4.32). Afterwards each particle is rejuvenated, i.e., perturbed using a MCMC kernel. Lastly, a resampling step is performed if the ESS falls below the resampling threshold.

So far it has not been discussed what constitutes a MCMC transition kernel or how to construct one. Essentially, an MCMC transition kernel is a *regular* conditional probability distribution [48] which fulfils certain requirements [146, 215, 275] and which can be used to describe the perturbation of a particle. Without going into the details, an example of the basic steps of a local random walk MCMC kernel are given in Table 4.2, instead of a formal mathematical definition. An example for a local proposal distribution $\eta(\boldsymbol{x}^*|\boldsymbol{x}_n^{(i)})$ is a Gaussian distribution

Sequential Monte Carlo algorithm

1. For $n = 0$, initialize particles $\{\boldsymbol{x}_1^{(i)}, w_1^{(i)}\}_{i=1}^{N_p}$ from $q_1(\boldsymbol{x})$. Set $n = 1$.
2. *Reweight* $w_n^{(i)} = w_{n-1}^{(i)} \frac{\gamma_n(\boldsymbol{x}_{n-1}^{(i)})}{\gamma_{n-1}(\boldsymbol{x}_{n-1}^{(i)})}$
3. *Rejuvenate* that is perturb each particle $\boldsymbol{x}_{n-1}^{(i)} \rightarrow \boldsymbol{x}_n^{(i)}$ using the MCMC Kernel $K_n(\boldsymbol{x}_{n-1}, \boldsymbol{x}_n)$
4. *Resample* if $\mathrm{ESS} < \mathrm{ESS}_{\mathrm{min}}$
5. if $n < t$ then $n = n + 1$ and goto step 2, else stop

Table 4.1 Basic steps of a Sequential Monte Carlo sampler.

Perturbation of a particle using an MCMC kernel

1. For $i = 1, \cdots, N_p$
2. draw a sample $\boldsymbol{x}^*$ from proposal distribution $\eta(\boldsymbol{x}^*|\boldsymbol{x}_n^{(i)})$
3. compute acceptance ratio: $\alpha(\boldsymbol{x}^*, \boldsymbol{x}_n^{(i)}) = \min\left\{1, \frac{\pi_n(\boldsymbol{x}^*)\eta(\boldsymbol{x}_n^{(i)}|\boldsymbol{x}^*)}{\pi_n(\boldsymbol{x}_n^{(i)})\eta(\boldsymbol{x}^*|\boldsymbol{x}_n^{(i)})}\right\}$
4. draw a sample $u^{(i)}$ from $\mathcal{U}(0, 1)$
5. if $u^{(i)} \leq \alpha(\boldsymbol{x}^*, \boldsymbol{x}_n^{(i)})$ then accept proposal, i.e., $\boldsymbol{x}_n^{(i)} = \boldsymbol{x}^*$, else reject, i.e., $\boldsymbol{x}_n^{(i)} = \boldsymbol{x}_n^{(i)}$

Table 4.2 Basic procedure of the MCMC step using a Metropolis-Hastings kernel [146, 215].

(other distributions are admissible too) with mean $\boldsymbol{x}_n^{(i)}$. Based on the steps described in Table 4.2, the probability distribution $K_n(\boldsymbol{x}_{n-1}, \boldsymbol{x}_n)$ then can be written as

$$\begin{aligned} K_n(\boldsymbol{x}_{n-1}, \boldsymbol{x}_n) = \eta(\boldsymbol{x}_n|\boldsymbol{x}_{n-1})\alpha(\boldsymbol{x}^*, \boldsymbol{x}_{n-1}) \\ + \left[1 - \int \eta(\boldsymbol{z}|\boldsymbol{x}_n)\alpha(\boldsymbol{z}, \boldsymbol{x}_n)\mathrm{d}\boldsymbol{z}\right] \mathbf{1}(\boldsymbol{x}_{n-1} = \boldsymbol{x}_n). \end{aligned} \tag{4.34}$$

The latter part of (4.34) denotes the rejection probability which usually cannot be computed analytically.

Putting all these things together, the result of a SMC scheme is a particulate approximation of the distribution π_t in the form

$$\pi_t(\boldsymbol{x}_t) \approx \sum_{i=1}^{N} W_t^{(i)} \delta_{\boldsymbol{x}_t^{(i)}}. \tag{4.35}$$

Estimates of any expectation of some function $\varphi(\cdot)$ with respect to π_t is also readily computed using

$$\mathbb{E}[\varphi(\mathbf{x})] \approx \sum_{i=1}^{N_\mathrm{p}} W_t^{(i)} \varphi(\boldsymbol{x}_t^{(i)}). \tag{4.36}$$

SMC is used in this work to sample from the posterior distribution of the Bayesian regression model described in Section 3.5.3. While the overall concept of SMC is described here, the particular variant is more advanced and, e.g., allows for an adaptive adjustment of the number of bridging distributions based on the ESS. Moreover, since the number of parameters in the regression model is not *a priori* fixed, the dimension of $\boldsymbol{x}_n$ can change and will depend on the training data. In order to account for the varying dimension of $\boldsymbol{x}_n$ in the SMC scheme, so called *reversible jump* MCMC kernels [128], that allow transdimensional jumps, are employed. In addition the proposal distribution of the kernels is adjusted to speed up the computation. For further details on the used algorithm, the reader is referred to [182, 183].

4.4 Classic reliability methods

As alternative to sampling based approaches, multiple so-called *reliability methods* have been developed to solve the reliability problem described in (4.4) and to compute the probability of failure in face of uncertain input parameters. A comprehensive introduction can be found in several textbooks, e.g., [87, 193, 212]. A shorter overview can be found in [320]. The so-called *first order reliability method* (FORM) and *second order reliability method* (SORM) are prominent examples of methods that can be used to solve the above mentioned type of stochastic problem. Briefly, these methods rely on the implicit definition of the failure domain through a limit state function which separates the safe domain from the failure domain. First, a transformation of variables is required which allows the conversion of the probability distributions of the random input quantities to a standard multivariate Gaussian distribution. Popular choices include the Rosenblatt [279] and the Nataf [225] transformation. Now, the so-called *design point*, which is defined as the point on the limit state surface closest to the origin in standard normal space, has to be determined by solving a constrained global optimization problem. Once the design point

has been found, the limit state surface is approximated by replacing the limit state functions with either a first (FORM) or a second order (SORM) expansion around the design point. The transformation of variables to standard normal space together with the first or second order approximation of the limit state function result in a simplified expression for the integral in (4.4), which then can be evaluated in closed form.

The major advantage of FORM and SORM is that the computational effort does not depend on the magnitude of the failure probability. However, there are also some significant drawbacks to these approaches, which are briefly mentioned in the following. For a more detailed comparison to sampling based reliability methods, the reader is referred to [290]. First challenges could arise in finding a suitable transformation of the random input variables to standard normal space. Moreover, to compute the design point, a constrained optimization problem must be solved. If these reliability methods are to be used in combination with complex finite element models with high stochastic dimension, two problems arise. First, derivatives with respect to the input parameters are difficult to obtain and approximation through finite-difference schemes is unfeasible. Second, design points obtained with the usual gradient based optimization schemes might not be unique. The primary reason to exclude classic reliability methods from this study, however, is that they do not provide probabilistic information beyond the failure probability. Furthermore, neither FORM or SORM allow an estimation of the accuracy of the computed failure probabilities.

4.5 Second order methods

Second order methods allow for the computation of mean and variance of the response quantity. Some of the oldest methods for UQ belong to this class, with development going back to the 1980s. The *pertubation method* was pioneered for linear structural mechanics in the early 1980s by Hisada and Nakagiri [154] and Handa and Anderson [142] and is based on a first-order Taylor expansion of the model $f(\mathbf{x})$ around the mean of the random inputs $\mathbf{x}$. For stochastic problems involving random fields, the method has been used together with a number of approaches to represent stochastic processes. In case of finite element analysis for linear elastic structures one variant, where stochastic element stiffness matrices are computed based on a weighted integral of the process over the element domain, goes by the name *weighted integral method* [78, 79, 81]. Another approach for low dimensional problems is the so-called *quadrature method*, whereby the integrals for mean and variance are evaluated based on some quadrature rule which depends on the chosen input distribution [23]. Thus, the method is technically not a purely second order approach. Second order approaches neglect nonlinear relations between model input and output, and thus accurate results can only be obtained if the coefficient of variation of the random input variables is small (c.f. Sudret and Der Kiureghian [320]), and only the first moments of the response are provided. Moreover, gradients of the model with respect to the random quantities are typically required. Due to these limitations, such methods are not considered in this work. If further information is desired, the reader can consult [320] for a more extensive overview of second order methods.

4.6 Surrogate based techniques

The overall cost of an UQ scheme in combination with complex forward models is mainly driven by the number of necessary forward model evaluations, which are often very expensive. Thus, a frequently applied approach to reduce the computational cost of UQ is the use of a surrogate model instead of the complex simulator, which could be an elaborate finite element model. When using a surrogate based approach, the overall UQ procedure comprises two steps. First, a surrogate model, which provides a cheap to evaluate approximation to the expensive computational model, is set up. Since the expensive model has to be evaluated numerous times during this setup phase to construct the surrogate, virtually all computational cost arise during this step. In a second step UQ is performed with, e.g., standard Monte Carlo, using the previously defined surrogate. Because the surrogate model is so cheap to evaluate, the computational cost associated with the sampling of the surrogate is negligible compared to the cost of setting up the surrogate. If the employed surrogate model provides an accurate approximation to the simulator, the obtained distribution or first moments of the quantity of interest will be very close to the result that would be obtained by sampling the expensive model directly. Note that for some combinations of surrogate model and distribution of the uncertain input parameters, the second step can be omitted if one is only interest in the first two moments of the response, because these are directly provided by the surrogate in closed form.

Plenty of different approaches to construct surrogate models have been proposed over the course of recent decades, and since they originated from very different fields of study, they go by very different names such as response surface, meta model, or emulator. Due to the large number of different approaches and variants of surrogate models used for UQ, it is well beyond the scope of this work to provide an overview of all available methods. Instead, the focus of this section is a short review and introduction to two particularly popular methods, or rather classes of methods. The first class of methods are based on the PCE and belong to the most prevalent methods for surrogate based UQ in engineering. The second class is based on GPs and constitutes a Bayesian approach, which is more rooted in the statistics community. The discussion, especially of the latter class, goes beyond a pure literature review, as GP based surrogates are also used in this work for UQ problems with low stochastic dimension (cf. Section 7.3). For a broader discussion of other surrogate models the reader is referred to [317, 318].

4.6.1 Surrogates based on Polynomial Chaos Expansion

Uncertainty quantification using PCE based surrogates has received considerable attention in recent years and a significant amount of literature is available on the subject. Here, only the very fundamentals of the approach are discussed. For a more detailed introduction the reader is referred to the textbooks [189, 364]. The goal of the PCE is to express the output of a simulator using multivariate polynomials that are orthogonal with respect to the joint probability of the random input parameters. The theory was first introduced by Wiener [358] for Gaussian random variables using multivariate Hermite-polynomials as basis and later applied in the context of stochastic finite elements in the seminal work of Ghanem and Spanos [117]. The theory was then generalized to non-Gaussian input variables using different types of orthogonal polynomials by Xiu and Karniadakis [366] and Soize and Ghanem [307]. Consequently, its often referred to as

generalized polynomial chaos expansion. In this work, *generalized* PCE is also simply referred to as PCE for the sake of conveniece.

The originally proposed solution scheme is based on a Galerkin procedure for the random dimensions and, hence, presents a natural extension of the finite element method to the random space. Although this approach has been applied to various problems [118, 178], it suffers from several drawbacks which have hampered its widespread use and render the method inapplicable to large scale problems with high stochastic dimension. First of all, it is an intrusive approach, which means that existing deterministic legacy code cannot be used and that application to another PDE requires a separate implementation for this particular problem. Moreover, extension to UQ regarding derived quantities such as strains, stresses, or functions thereof is not straightforward, nor is the extension to more challenging nonlinear problems such as nonlinear elasticity involving finite strain, contact, plasticity, or other nonlinearities [4, 12, 194].

To address these issues, so-called non-intrusive schemes based on the PCE have been developed, which permit the use of elaborate legacy codes and which can be applied to a wide range of problems including, e.g., large deformation plasticity [5], flow in complex geometries [289], and also some multiphysics problems such as coupled electromechanics [7] or fluid-structure interaction [362]. An apparently wide array of PCE based methods, which go by various different names, have been proposed in recent years. In this work it is distinguished between *non-intrusive projection methods* see, e.g., [119, 179, 189, 364] and *interpolatory collocation methods* see, e.g., [22, 135, 189, 364, 365], both of which are summarized under the umbrella term stochastic collocation methods by Xiu [364]. Another seemingly different approach, the so-called *regression approach* was introduced by Berveiller et al. [31], Choi et al. [64], Isukapalli et al. [164]. However, as shown in, e.g., [319], the non-intrusive projection approach and the regression approach can, from a statistical point of view, essentially both be interpreted as a variant of least squares regression using orthogonal polynomial basis functions with different design points for the model in random space, respectively. Moreover, different truncations of the PCE might be used. In the opinion of the author, the interpretation of discrete projection schemes as regression model with polynomial basis functions offers a nice statistical and more intuitive interpretation as to what constitutes non-intrusive UQ approaches based on PCE. Hence, the discrete projection and the regression viewpoint are briefly discussed and compared here. Furthermore, the advantages and drawbacks, as well as the specific properties which hinder an application of PCE approaches to the problems studied in this work are discussed here on the basis of the discrete projection approach and the related regression variant. With regard to the problems and examples studied in this work, the interpolatory collocation method offers no significant advantage over the discrete projection approach. Hence, a further discussion is deemed unnecessary and the reader is advised to consult the provided references for further information regarding this approach.

The fundamental concept of all PCE based UQ approaches is the representation of the model output as an expansion of polynomials, hence the name. Thus, the output of the model is projected onto a basis of orthogonal polynomials using the following expansion

$$\mathsf{y} = f(\mathbf{x}) \approx f_{\mathrm{PCE}}(\mathbf{x}) = \sum_{j=0}^{N_p} w_j \phi_j(\mathbf{x}). \tag{4.37}$$

Therein, $\phi_j(\boldsymbol{x})$ are multivariate polynomials, which are typically constructed from univariate polynomials with tensor products [189]. Suitable weights w_j of the polynomials have to be determined in the setup phase of the surrogate. The type of polynomial depends thereby on the probability distribution of the random inputs. The expected value of all polynomials is zero

$$\mathbb{E}[\phi_e(\mathbf{x})] = \int \phi_e(\boldsymbol{x}) p_{\mathbf{x}}(\boldsymbol{x}) \mathrm{d}\boldsymbol{x} = 0. \tag{4.38}$$

Moreover, since the polynomials are orthogonal, the following condition holds:

$$\int \phi_i(\boldsymbol{x}) \phi_j(\boldsymbol{x}) p_{\mathbf{x}}(\boldsymbol{x}) \mathrm{d}\boldsymbol{x} = \delta_{ij}. \tag{4.39}$$

Exploiting the orthogonality property (4.39), discrete projection schemes approximate the weights of the polynomial expansion by solving the orthogonal projection

$$w_e = \int f(\boldsymbol{x}) \phi_e(\boldsymbol{x}) p_{\mathbf{x}}(\boldsymbol{x}) \mathrm{d}\boldsymbol{x}, \tag{4.40}$$

using a numerical integration scheme. Employing either tensorized quadrature schemes, sparse grid cubature rules, or plain Monte Carlo, the above integral can be approximated as

$$w_e \approx \sum_{s=1}^{N_s} f(\boldsymbol{x}^{(s)}) \phi_e(\boldsymbol{x}^{(s)}) q^{(s)}. \tag{4.41}$$

Here, the $\boldsymbol{x}^{(s)}$ are the quadrature or sampling points and the $q^{(s)}$ denote the associated weights. For the sake of a consistent nomenclature, these points will also be referred to as design points from here on. Both, the location of the points and the magnitude of the weights depend on the employed quadrature scheme. The integrals to compute the weights can be solved very efficiently if the random input space is low-dimensional. However, if tensorized one-dimensional quadrature schemes are used to evaluate (4.41), the number of necessary model evaluations increases exponentially with the number of dimensions. This phenomenon is often referred to as *curse of dimensionality*. The use of integration schemes based on Smolyak sparse grids [305] can alleviate this problem to some extend at the cost of an additional approximation error [116, 189]. Nevertheless, due to the large number of required model evaluations for high dimensional problems, PCE based approaches offer computational savings only for problems with relatively few random input parameters.

The discrete projection approach can also be interpreted as fitting a particular polynomial regression model as a surrogate. For some choices of points in the random input space, at which the expensive simulator is evaluated, equivalence of the two seemingly different approaches can be shown. Starting point is again the assumption that the simulator output can be represented by orthogonal polynomials. However, due to the finite truncation of the expansion, the polynomials cannot exactly represent the simulator response and a truncation error ϵ_p has to be taken into account:

$$\mathsf{y} = f(\mathbf{x}) = \sum_{e=0}^{N_p} w_e \phi_e(\mathbf{x}) + \epsilon_p. \tag{4.42}$$

After introducing the notation

$$\boldsymbol{w} = [w_0, w_1, w_2, \cdots, w_p]^T, \tag{4.43}$$

$$\boldsymbol{\phi} = [\phi_1(\boldsymbol{x}), \phi_2(\boldsymbol{x}), \phi_3(\boldsymbol{x}), \cdots, \phi_p(\boldsymbol{x})]^T, \tag{4.44}$$

(4.42) can be rewritten as

$$\mathsf{y} = \boldsymbol{\phi}(\mathbf{x})^T \boldsymbol{w} + \epsilon_p. \tag{4.45}$$

As before, the goal is to determine the weights of the polynomials. One way this can be achieved is by asking the mean squared error to be minimal, which gives rise to the minimization problem

$$\boldsymbol{w}_{\text{LS}} = \min_{\boldsymbol{w}\in\mathbb{R}^p} \mathbb{E}\Big[\big(f(\mathbf{x}) - \boldsymbol{\phi}(\mathbf{x})^T \boldsymbol{w}.\big)^2\Big] \tag{4.46}$$

Taking the derivative and some algebraic rearrangement yield the following condition for the optimal choice of weights (see [319] for details)

$$\boldsymbol{w} = \mathbb{E}[\boldsymbol{\phi}(\mathbf{x})^T f(\mathbf{x})], \tag{4.47}$$

which is equal to (4.40) and hence demonstrates the principal equivalence of the two approaches.

In practical applications the expectation operator $\mathbb{E}$ is replaced by a discrete sum over a set of training samples $\{y^{(i)}, \boldsymbol{x}^{(i)}\}_{i=1}^{N_s}$ obtained from random sampling, e.g., MC or LHS or another quadrature scheme. Another option, that has been advocated in the past, is to chose the sampling points according to the roots of orthogonal polynomials [31, 164].

If the samples, i.e., the design points are obtained by random sampling, (4.46) simply becomes

$$\boldsymbol{w}_{\text{LS}} = \min_{\boldsymbol{w}\in\mathbb{R}^p} \frac{1}{N_s} \sum_{i=1}^{N_s} \Big[\big(f(\boldsymbol{x}^{(s)}) - \boldsymbol{\phi}(\boldsymbol{x}^{(s)})^T \boldsymbol{w}\big)^2\Big]. \tag{4.48}$$

Using the definition of the design matrix in (3.131), the least squares estimate for the weights is easily obtained by using (3.102)

$$\boldsymbol{w}_{\text{LS}} = [\boldsymbol{\Phi}\boldsymbol{\Phi}]^{-1}\boldsymbol{\Phi}\boldsymbol{y}, \tag{4.49}$$

where $\boldsymbol{y} = [f(\boldsymbol{x}^{(1)}), f(\boldsymbol{x}^{(2)}), \cdots f(\boldsymbol{x}^{(N_s)})]^T$. If the sample locations are determined by another, non-random integration scheme, the samples no longer all have the same weights. This can be accounted for by introducing a weight matrix $\boldsymbol{Q} = \text{diag}(q^{(1)}, q^{(2)}, \cdots, q^{(N_s)})$. The weights of the polynomials are then similarly determined using a weighted least squares approach

$$\boldsymbol{w}_{\text{LS}} = [\boldsymbol{\Phi}\boldsymbol{Q}\boldsymbol{\Phi}^T]^{-1}\boldsymbol{Q}\boldsymbol{\Phi}\boldsymbol{y}. \tag{4.50}$$

On an abstract level, non-intrusive spectral methods based on PCE expansion can be interpreted as regression using nonlinear orthogonal basis functions and a particular choice of design points or training samples to train the regression model. If seen from this perspective, it becomes apparent that low-order polynomials might not always be the optimal choice to represent complex nonlinear models. Moreover, PCE based surrogates do not offer a way to address the additional uncertainty introduced by evaluating the surrogate model instead of the simulator. Even if the the PCE surrogate matches the simulator exactly at the design points, the approximation provided by the surrogate does not necessarily match the simulator in between these points. This additional uncertainty cannot be accounted for in the usual PCE framework. However, this issue can be addressed by choosing a Bayesian approach based on GP models instead.

4.6.2 Surrogates based on Gaussian processes

Another popular approach to building surrogate models for the purpose of UQ is based on Gaussian process models. As before, the complex simulator is viewed as a function $f(\boldsymbol{x})$ which maps the inputs $\boldsymbol{x}$ into a scalar output y. For the purpose of UQ a cheap approximation $\mathsf{f}_{\mathrm{GP}}(\cdot)$ based on a Gaussian process is constructed using a set of design points and corresponding evaluations of the simulator at theses points $\mathcal{D} = \{\boldsymbol{x}^{(i)}, y^{(i)}\}_{i=1}^{N}$, which will be referred to as training samples. In contrast to the PCE approach, the idea to model the output of complex computer models using GPs originated in the statistics community [284] and was then later applied in he context of UQ and sensitivity analysis [148, 174, 234, 235]. In the context of modelling unknown functions in statistics, the approach dates even further back see, e.g., [40, 177, 227, 239]. Gaussian process modelling is also the basis of what is known as Kriging in the Geostatistics community [69, 210, 316].

The approach is very flexible and general in the sense that it can in principal be used in combination with a wide range of forward models. However, although it has been introduced over two decades ago and has some very appealing properties, its adoption in the engineering community is a relatively recent phenomenon and UQ using surrogate models based on GPs is still significantly less common than PCE based approaches.

The most important difference between surrogate models based on PCE is that GP models provide not just an approximation to $f(\boldsymbol{x}) \approx f_{\mathrm{GP}}(\boldsymbol{x})$ for an arbitrary input $\boldsymbol{x}$, but a distribution over functions, as explained in Section 3.5.2 on Gaussian process regression. In fact, it will become apparent in the following paragraphs that the GP regression approach explained above can be directly used to construct surrogate models for complex simulators and that the GP surrogate approach used in this work is essentially nothing but a regression model based on GPs. Instead of trying to establish a quantitive link between explanatory variables and some measurements, the goal is now to find a relationship between some model input parameters $\boldsymbol{x}$ and the model output $f(\boldsymbol{x}) = y$. As already mentioned, several different variants to construct GP surrogates exist, based on the choices for mean function, covariance function, and potential hyper-priors.

In case of modelling simulation models, i.e., computer experiments as opposed to "real" experiments, the measurements are often considered to be noise free, because the simulator is deterministic, in the sense that it always produces the same output y for a given input $\boldsymbol{x}$. From a theoretical point of view this is not a major problem. After putting a GP prior on $f_{\mathrm{GP}}(\boldsymbol{x})$ and evaluating the simulator at a set of design points to obtain a dataset $\mathcal{D} = \{\boldsymbol{x}^{(i)}, y^{(i)}\}_{i=1}^{n}$, computation of the posterior of $\mathsf{f}_{\mathrm{GP}}(\boldsymbol{x})$ in the noise free case is straightforward and merely entails conditioning of a multivariate Gaussian distribution on the set of training samples. The resulting posterior GP then interpolates the data-points exactly [361].

However, there are arguments against taking such an approach. Computation of the posterior entails inversion of the covariance matrix of the GP which is often ill-conditioned, especially for smooth covariance functions and hence the inversion can be numerically unstable [1, 226]. A frequently used remedy is to add a small so-called *nugget* term to the diagonal entries of the matrix to improve the condition number. Adding this nugget term is equivalent to the addition of an independent random noise term, as shown by Gramacy [125]. As a result the posterior no longer interpolates the data-points exactly, but rather constitutes a fit to "noisy" data, which, although the noise term is usually very small, brings us back to the realm of regression. There are

several other arguments that go beyond these computational issues. For instance, Gramacy and Lee [126] concluded that including and estimating a nugget or equivalently a random noise term often leads to surrogates with better statistical properties. They show that using a nugget term results in smoother estimates which provide better predictions, especially when data is scarce, i.e., when model evaluations are expensive and, thus, one is limited to a moderate number of evaluations of the simulator or when assumptions such as stationarity of the covariance function are violated.

In conclusion, the GP regression framework presented earlier is well suited to construct GP based surrogates for complex finite element models. The same approach was also used recently by [35], who extended the framework to the multi-output case, i.e., the case where the model output is a vector instead of a scalar. In the following, some general advantages of GP based surrogate models will be discussed along with the necessary steps to efficiently compute estimates for the usual quantities of interest in an UQ analysis, which include mean, variance, and quantiles of the distribution and the respective confidence bounds which can be calculated due to the Bayesian nature of this approach.

Starting point is the choice of an appropriate mean and covariance function for the GP. Common choices for mean function include constant or linear polynomials. For the covariance function, the predominant choice is the squared exponential covariance function as given in (3.60) or (3.61), which indicates a high degree of smoothness. Then, based on an initial set of training samples, the posterior GP is readily computed using (3.134). The design points are usually chosen according to some experimental design, e.g, LHS; however, purely randomly drawn samples from $p_{\mathsf{x}}(\boldsymbol{x})$ are also admissible, as are uniformly distributed points on a regular tensor grid or points from sparse grids. For a discussion on experimental designs in the context of computer experiments, see, e.g., [148, 284]. For now, it will be assumed that the posterior GP, given an initial set of training data $\mathcal{D}$ can be written as

$$\mathsf{y} = f(\mathbf{x}) \approx \mathsf{f}_{\mathrm{GP}}(\mathbf{x})|\mathcal{D}, \hat{\boldsymbol{\theta}} \sim \mathcal{GP}\Big(\tilde{m}(\mathbf{x}; \hat{\boldsymbol{\theta}}_m), \tilde{k}(\mathbf{x}, \mathbf{x}'; \hat{\boldsymbol{\theta}}_k)\Big), \tag{4.51}$$

where the vector of hyper-parameters $\hat{\boldsymbol{\theta}} = [\hat{\boldsymbol{\theta}}_m, \hat{\boldsymbol{\theta}}_k]$ is determined in this work by maximizing the marginal likelihood. $\tilde{m}(\boldsymbol{x}; \hat{\boldsymbol{\theta}}_m)$ and $\tilde{k}(\boldsymbol{x}, \boldsymbol{x}'; \hat{\boldsymbol{\theta}}_k)$ denote the posterior mean and covariance function given the design points, respectively. Thereby, the variance of the noise term is initially set to $10e-6$, resulting in a GP which almost exactly passes through the given data points.

From (4.51) it becomes clear that the GP surrogate provides more than just an approximation to $f(\mathbf{x})$, since it also provides a distribution around the mean, describing how close it is likely to be to the actual $f(\mathbf{x})$, i.e., the GP provides a measure of uncertainty from which confidence intervals for its estimation of $f(\mathbf{x})$ can be easily obtained. These confidence bounds are useful for several purposes. First, they provide the basis for what is called active learning or sequential experimental design, i.e., computing these confidence bounds can aid in the identification of regions in the input space with high uncertainty about the value of $\mathsf{f}_{\mathrm{GP}}(\cdot)$. After these regions have been identified, additional evaluations of the simulator in these regions can be performed, thereby improving the surrogate adaptively. Several approaches based on different utility functions have been proposed to perform such an active learning task. For instance MacKay [199] proposed an approach, referred to as *active learning MacKay* (ALM), in which the choice for the next design point is determined by the maximum predictive variance. An alternative approach, referred to as *active learning Cohn* (ALC) [66] in the following, choses the next sampling point

according to the expected change in predictive variance averaged over the whole input domain. The second benefit of having a predictive distribution rather than a simple deterministic surrogate is that confidence intervals can not only be computed for $\mathsf{f}_{\mathrm{GP}}(\boldsymbol{x})$, but also for all quantities derived from the surrogate, i.e., the approximations for mean, variance, or CDF of y. Using these confidence intervals, the accuracy of the surrogate can be judged and a decision whether further evaluations of the simulator are necessary can be made. The following paragraphs contain a brief description how to compute estimates for mean, variance, quantiles, CDF, and PDF as well as their respective confidence intervals using a GP based surrogate model.

For some combinations of covariance function of the surrogate and probability distribution of the uncertain model inputs $p_{\mathsf{x}}(\boldsymbol{x})$ it is possible to compute several statistical summaries such as mean and variance analytically [147, 172, 238], similar to PCE based surrogate models. In this work, however, the more general sampling based approach is used instead.

The simplest way to compute statistical summaries of y is to treat the GP surrogate like any other deterministic surrogate model, in the sense that the posterior mean $\tilde{m}(\mathsf{x};\hat{\boldsymbol{\theta}})$ is considered as approximation for $f(\mathsf{x})$. Then, all desired quantities can be computed by sampling of $\tilde{m}(\mathsf{x};\hat{\boldsymbol{\theta}})$. Because $\tilde{m}(\mathsf{x};\hat{\boldsymbol{\theta}})$ is very cheap to evaluate, any desired quantity can be determined by sampling to practically arbitrary precision. The problem with this approach is that it is based on the assumption that one knows the true value of $f(\boldsymbol{x})$ at all points $\boldsymbol{x}$ exactly. This is clearly not the case, since its value is only known at locations at which the simulator has been evaluated (assuming zero or negligible noise). By taking a Bayesian approach, this second level of uncertainty, often referred to as code uncertainty, can be quantified since $\mathsf{f}_{\mathrm{GP}}(\boldsymbol{x})$ is treated as a random function. As a result all summaries obtained using $\mathsf{f}_{\mathrm{GP}}(\boldsymbol{x})$ become random variables as well. This property can be exploited to compute confidence intervals for these quantities. For the computation of $\mathbb{E}[\mathsf{y}]$, $\mathbb{V}[\mathsf{y}]$, and quantiles of y, denoted by q from here on, the following three step procedure described by Oakley [232, 233] is adhered to in this work. The procedure is explained here using the example of the mean of y. However, the computation of estimates for all other quantities can be done accordingly. Since $\mathsf{f}_{\mathrm{GP}}(\boldsymbol{x})$ is a random function, the mean of y becomes a random variable:

$$\mathbb{E}_{\mathsf{x}}[\mathsf{f}_{\mathrm{GP}}(\mathsf{x})] = \mathsf{M}. \tag{4.52}$$

To compute mean, variance, and confidence intervals for this random variable, the following steps are performed:

1. **Step 1:** Generate N_{SAM} sample functions $f_{\mathrm{GP}}^{(\mathrm{j})}(\boldsymbol{x})$ from the posterior process $\mathsf{f}_{\mathrm{GP}}(\boldsymbol{x})$
2. **Step 2:** Compute the desired quantity of interest, in this case $\mathbb{E}_{\mathsf{x}}[f_{\mathrm{GP}}^{(\mathrm{j})}(\mathsf{x})] = M_{f_{\mathrm{GP}}^{(\mathrm{j})}}$ using Monte Carlo sampling (other quantities can also be assessed, e.g., the variance $\mathbb{V}_{\mathsf{x}}[f_{\mathrm{GP}}^{(\mathrm{j})}(\mathsf{x})] = V_{f_{\mathrm{GP}}^{(\mathrm{j})}}$, or some quantile $q_{f_{\mathrm{GP}}^{(\mathrm{j})}}$).
3. **Step 3:** Repeat steps 1 and 2 to obtain a sample from the distribution $p_{\mathsf{M}}(M)$, i.e., $M_{f_{\mathrm{GP}}^{(1)}}, M_{f_{\mathrm{GP}}^{(2)}}, \cdots, M_{f_{\mathrm{GP}}^{(\mathrm{L})}}$.

Based on this sample, one can compute estimates for, e.g., the mean, variance, or confidence intervals for the respective quantity of interest. Thus, an estimate for $\mathbb{E}[\mathsf{y}]$ can be readily calculated using

$$\hat{M} = \frac{1}{N_{\mathrm{SAM}}} \sum_{i=1}^{N_{\mathrm{SAM}}} M_{f_{\mathrm{GP}}^{(\mathrm{j})}}. \tag{4.53}$$

Similarly, the variance of $\mathbb{E}[\mathsf{y}]$ can be computed by

$$\hat{\sigma}^2_{\hat{M}} = \frac{1}{N_{\text{SAM}}} \sum_{i=1}^{N_{\text{SAM}}} (M_{f^{(\mathrm{j})}_{\text{GP}}} - \hat{M})^2 \tag{4.54}$$

which yields the following 95% confidence bounds for $\mathbb{E}[\mathsf{y}]$:

$$[M_{\text{cf,low}}, M_{\text{cf,up}}] = \hat{M} \pm 1.96\hat{\sigma}_{\hat{M}} \tag{4.55}$$

The same procedure can be applied to compute $\mathbb{V}[\mathsf{y}]$, q, and their respective confidence intervals.

For the procedure described above, sample functions, i.e., realizations of the posterior GP, have to be generated in an efficient manner. One cannot create exact realizations of $\mathsf{f}_{\text{GP}}(\cdot)$ since that would entail sampling $\mathsf{f}_{\text{GP}}(\cdot)$ at every point $\boldsymbol{x}$ in the sample space, which is infinite. Instead, a procedure to create approximate realizations described in [232] is employed in this work. Briefly, first a new set of simulation design points $(\boldsymbol{x}^{(1)'}, \boldsymbol{x}^{(2)'}, \cdots \boldsymbol{x}^{(N')'})$ which is distinct from the original set is chosen. Since the random vector of outputs $\mathbf{y}' = [\mathsf{f}_{\text{GP}}(\boldsymbol{x}^{(1)'}), \mathsf{f}_{\text{GP}}(\boldsymbol{x}^{(2)'}), \cdots \mathsf{f}_{\text{GP}}(\boldsymbol{x}^{(N)'})]^T$ has a multivariate Gaussian distribution according to (4.51), samples of $\mathbf{y}'$ are easily obtained by drawing from this multivariate Gaussian. In combination with the original set of design points, the data defines $\mathsf{f}^{(\mathrm{j})}_{\text{GP}}(\cdot)$ which still is a GP as defined in (4.51). Let the mean and covariance functions of the new process be $\tilde{m}^{(\mathrm{j})'}(\boldsymbol{x})$ and $\tilde{k}^{(\mathrm{j})'}(\boldsymbol{x}, \boldsymbol{x'})$, respectively. If the set of simulation design points is sufficiently large and the position of the points is well chosen, the variance of $\mathsf{f}^{(\mathrm{j})}_{\text{GP}}(\cdot)$ will be very small and $f^{(\mathrm{j})}_{\text{GP}}(\cdot)$ is approximated by $\tilde{m}^{(\mathrm{j})'}(\boldsymbol{x})$ with minimal error. Hence, $\tilde{m}^{(\mathrm{j})'}(\boldsymbol{x})$ can be used as approximate realization for $f^{(\mathrm{j})}_{\text{GP}}(\cdot)$.

Often, it is desired to obtain the full probability distribution of the model output in form of a CDF or PDF. It is relatively straightforward to compute these using the procedure based on approximate realizations of the posterior process described briefly above and in more detail in [232, 234]. The CDF of y is given by the following integral

$$\mathsf{F}_{\mathsf{y}}(y) = \int 1\big(\mathsf{f}_{\text{GP}}(\boldsymbol{x}) \leq y\big) p_{\mathbf{x}}(\boldsymbol{x}) \mathrm{d}\boldsymbol{x}, \tag{4.56}$$

and considered random because of the uncertainty in $\mathsf{f}_{\text{GP}}(\cdot)$. However, samples of $\mathsf{F}_{\mathsf{y}}(y)$ can be computed using realizations $f^{(\mathrm{j})}_{\text{GP}}(\cdot)$ of $\mathsf{f}_{\text{GP}}(\cdot)$ in combination with MC

$$F^{(\mathrm{j})}_{\mathsf{y}}(y) = \frac{1}{N_{\text{SAM}}} \sum_{i=1}^{N_{\text{SAM}}} 1\big(\tilde{m}^{(\mathrm{j})'}(\boldsymbol{x}^{(i)}) \leq y\big). \tag{4.57}$$

Having computed L realizations of $F^{(1)}_{\mathsf{y}}(y), F^{(2)}_{\mathsf{y}}(y), \cdots, F^{(\mathrm{L})}_{\mathsf{y}}(y)$, the sample mean can be used as an approximation for F_{y}

$$\hat{F}_{\mathsf{y}}(y) = \frac{1}{L} \sum_{j=1}^{L} F^{(\mathrm{j})}_{\mathsf{y}}(y). \tag{4.58}$$

Oakley and O'Hagan [234] advise that the sample median might be a better choice, because it is less affected by the potential skewness of the distribution of F_{y} at high and low values of y. In addition to mean and median, confidence bounds are also readily calculated using computed

samples $F_{\mathsf{y}}^{(\mathrm{j})}(y)$ either directly using the samples or by calculating the variance of F_{y} first. Analogous to the CDF it is trivial to compute estimates and confidence bounds for the corresponding empirical quantile function.

Estimation of the density function of $\mathsf{y}^{(\mathrm{j})} = f_{\mathrm{GP}}^{(\mathrm{j})}(\mathbf{x})$ is done in the same fashion. Because $f_{\mathrm{GP}}^{(\mathrm{j})}(\cdot)$ is so cheap to evaluate, a large number of samples $(\boldsymbol{x}^{*(1)}, \boldsymbol{x}^{*(2)}, \cdots, \boldsymbol{x}^{*(N)})$ drawn from $p_{\mathbf{x}}(\boldsymbol{x})$ and subsequent evaluation of $f_{\mathrm{GP}}^{(\mathrm{j})}(\boldsymbol{x}^{*(i)})$, which is approximated by $\tilde{m}^{(\mathrm{j})'}(\boldsymbol{x}^{(i)})$, provides sufficient data points to estimate $p_{\mathsf{y}}^{(\mathrm{j})}$. As before repeating this procedure yields a sample of density functions, based on which summaries such as mean and median as well as confidence bounds can be computed. With respect to the estimated median of the PDF it is important to note that it will not necessarily integrate to one, but still might provide a good graphical summary of $p_{\mathsf{y}}(y)$ and highlight important features such as multi-modality.

Overall, GP based surrogate models offer a very flexible framework to construct accurate surrogates for complex simulators, which can be treated as black box. Knowledge about the smoothness of the output quantity of interest can be readily incorporated by an appropriate choice for the covariance function. In contrast to deterministic surrogates, the GP approaches allow for the computation of confidence intervals for all assessed quantities, which can be used to assess whether further evaluations of the complex simulator are required or the accuracy has reached an acceptable level

The design points of PCE based surrogates are often chosen according to a tensor or sparse grid, matching a certain type of polynomial which in PCE schemes is linked to a certain probability distribution. In GP based approaches the design points are typically chosen more freely. In principle it is possible to use the GP surrogate build with a single set of design points with multiple different input distribution $p_{\mathbf{x}}(\boldsymbol{x})$. Of course the chosen experimental design will be suboptimal if used in combination with considerably different input distributions, but in some cases the accuracy will still be sufficient or at least provide a reasonable starting point if an adaptive scheme is used. Another advantage of using GPs over orthogonal polynomials is that it is a non-parametric approach in the sense that the model structure is not fixed or limited *a-priori* to, e.g., second or third order polynomials and, thus, offers significantly more flexibility.

The basic methodology as briefly presented here is quite mature and has been applied to a range of problems in the past. The overall approach has received considerable attention in recent years and has been applied to a variety of problems and extended in a number of ways, e.g., to handle multiple outputs, dynamic simulators, discontinuities in the relationship between model input and output, or to incorporate gradient information [35, 36, 67, 68, 85, 95, 127]. Also, since GP based approaches admit the incorporation of parametrized basis functions for its mean functions, orthogonal polynomials usually employed in PCE based approaches can be used as well, resulting in some kind of hybrid approach between PCE and GP as recently investigated by Kersaudy et al. [175]. Moreover, multi-fidelity ideas, which are based on the incorporation of information from low-fidelity versions of the simulator have been developed with the goal to reduce the required computational effort, see, e.g., [173, 188]. Because it is closely related to the approach and framework developed and used in this work, the multi-fidelity concept will be further discussed separately and in more detail in Section 5.3.3.

Overall, if the simulator is relatively well behaved and the stochastic dimension of the problem is low, surrogate models present a very convenient and efficient way to perform UQ and sensitivity analysis. However, aside from difficulties like capturing strong nonlinearities or discontinuities in the map from the random input to the model output, which can be addressed by

advanced techniques and adaptive schemes, the major fundamental disadvantage of surrogate models is the curse of dimensionality. This renders surrogate based UQ approaches infeasible for problems with high stochastic dimension, because the number of necessary model evaluations to train the surrogate grows extremely fast with the stochastic dimension of the problem [34, 98]. Simply speaking, setting up a surrogate model, no matter which kind, to represent a complex simulator implies determination of suitable parameters of the respective surrogate. For PCE based surrogates these are the weights of the polynomials and for GP based models these are weights for the basis function of the mean, which could also be polynomials, and the parameters of the covariance function. The higher the dimension of $\boldsymbol{x}$, the more parameters need to be estimated, which in turn requires more data. Consequently, setting up surrogate models for complex simulators in which uncertainties are characterized by random processes and fields is difficult since the representation of these uncertainties often leads to vectors $\boldsymbol{x}$ with thousands of entries.

5 Bayesian multi-fidelity Monte Carlo and its relation to other multi-fidelity approaches

The main purpose of the present chapter is the description of the developed Bayesian multi-fidelity Monte Carlo (BMFMC) framework for efficient UQ with large-scale models and high-stochastic dimension. A secondary aspect is the discussion of other multi-fidelity UQ approaches and their relation to the proposed approach.

Therefore, the underlying concept of using models with different levels of fidelity is introduced in Section 5.1, before the Bayesian multi-fidelity Monte Carlo approach is elaborated in Section 5.2. To put the proposed approach into context with other multi-fidelity approaches, the two most prominent multi-fidelity UQ schemes, the so-called *multi-level Monte Carlo* method and the concept of multi-fidelity GP surrogates, are briefly explained and their relation to the BMFMC approach is discussed in Section 5.3.

5.1 Multi-fidelity concept

In engineering applications UQ is usually performed in combination with elaborate computational simulation models which involve the numerical solution of a PDE. More often than not, it is possible to construct or conceive low-fidelity versions of these models, which are significantly cheaper to evaluate at the price of yielding a less accurate result. There are many different ways to create low-fidelity versions of complex computational models. For instance, one could use a numerical solution scheme with lower-fidelity. This can be obtained by using a coarser spatial and/or temporal discretization or the use of looser tolerances in the nonlinear or linear solver. Another option is the use of lower-fidelity mathematical/physical models, e.g., by considering linear instead of nonlinear elasticity, nonlinear elasticity instead of plasticity, or potential flow instead of Navier-Stokes flow. The computational costs can usually also be reduced by considering only parts of the system, omitting certain components for the benefit of shorter computation times at the cost of a less accurate solution. Reduced order models constructed using proper orthogonal decomposition [60, 359] or proper generalized decomposition [62] could, in principle, also be used as low-fidelity approximation for a complex high-fidelity finite element model. Last but not least, engineering insight or heuristics can, in some cases, yield very good low-fidelity approximations.

A low-fidelity model cannot be used directly in an UQ scheme by itself, because it provides a less accurate and possibly distorted result for the quantity of interest and potentially introduces very large modelling or discretization errors. Hence, any uncertainty distribution derived from the low-fidelity approximate model will be distorted and not provide correct information about

the systems of interest. On the other hand, high-fidelity models may provide an accurate assessment of the studied system, yet allow only a small number of model evaluations due to the associated high computational cost. Statistical summaries based on only few evaluations of the high-fidelity models are prone to sampling errors or, if surrogate models are used, interpolation errors. Multi-fidelity or multi-level UQ schemes hinge on the ability to create low-fidelity versions of the model and try to gain overall efficiency and accuracy by combining information from low-fidelity models and high-fidelity models using two or more levels of sophistication.

The overall idea is similar to that of geometric or algebraic multi-grid approaches for the solution of linear systems of equations [50]. However, as will be become clear shortly, several stochastic multi-fidelity approaches can make use of "coarse level" approximations to the "fine level" solution that are much worse than tolerable in deterministic multi-grid schemes. This leads to more flexibility in creating low-fidelity models.

5.2 Bayesian multi-fidelity Monte Carlo

In order to enable UQ for large-scale, complex computational models, a framework based on a multi-fidelity sampling strategy is developed in this work. Thereby, the main focus lies on systems for which surrogate models cannot be efficiently used due to a high stochastic dimension. The overall concept is to incorporate models with different levels of sophistication or fidelity in a sampling based UQ approach as proposed by Koutsourelakis [183]. Roughly speaking, the sampling is done on an inexpensive, approximate, low-fidelity model. Then, to account for the discrepancy between low-fidelity and high-fidelity solution a probabilistic correction factor in form of a conditional probability is used, for the calculation of which only few evaluations of the expensive high-fidelity model are required.

The basic premise of the BMFMC framework is the ability to construct two computational models for a given system of interest; an accurate, expensive high-fidelity model and a cheap, approximate low-fidelity version. The latter could be obtained, for instance, by creating a much coarser discretization. Suppose that one is interested in computing a particular quantity $y_{\mathrm{hi-fi}}(\mathbf{z})$ or rather its probability distribution, e.g., in the form of its density $p(y_{\mathrm{hi-fi}})$, or some statistics of the response, e.g., as given in (4.3) or (4.4). Here, let $\mathbf{z}$ denote the vector of random input parameters of the model instead of $\mathbf{x}$ to avoid confusion with spatial location. The case where the dimension of this vector is high, e.g., as it represents the random amplitudes of one or more discretized random fields is of particular interest, because it precludes the use of surrogate based techniques.

Analogous to $y_{\mathrm{hi-fi}}(\mathbf{z})$, the quantity of interest computed with the high-fidelity model, the corresponding quantity and its density computed using the low-fidelity model will be referred to as $y_{\mathrm{lo-fi}}(\mathbf{z})$ from here on. For example, if $y_{\mathrm{hi-fi}}$ is the von Mises stress at a particular location in the high-fidelity model, $y_{\mathrm{lo-fi}}$ denotes the von Mises stress evaluated at the same spatial location in the low-fidelity model. Based on the premise that the low-fidelity model is cheap to evaluate, the distribution $p(y_{\mathrm{lo-fi}})$ can be readily approximated using any kind of sampling algorithm such as direct Monte Carlo. While direct Monte Carlo is used throughout this work, it is important to note that other sampling techniques such as LHS, Quasi-Monte Carlo or SMC could be used as well [183].

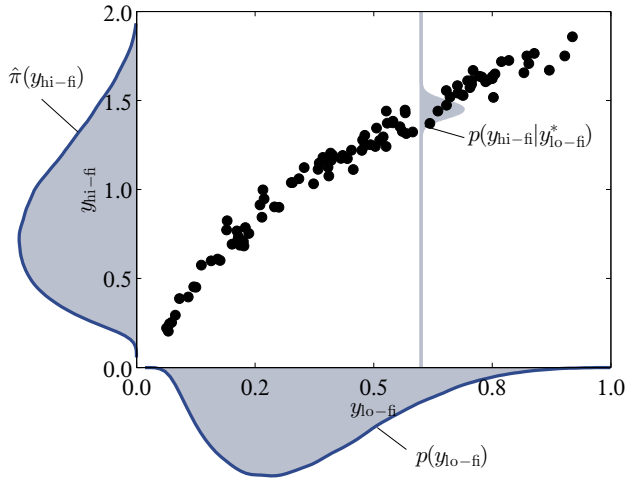

Figure 5.1 Principle of BMFMC approach. Probability distributions of low-fidelity and high-fidelity model are indicated through the respective densities in blue. Training samples which will be used to infer the conditional probability $p(y_{\text{hi-fi}}|y_{\text{lo-fi}})$ are shown as black dots. A conditional distribution $p(y_{\text{hi-fi}}|y^*_{\text{lo-fi}})$ is exemplarily shown for $y^*_{\text{lo-fi}}$ as well.

The second prerequisite is that the solution of the low-fidelity $y_{\text{lo-fi}}$ model provides sufficient stochastic information about the quantity of interest. This is a very weak requirement, since even crude approximations are admissible and it suffices if the low-fidelity model and the high-fidelity model have the same stochastic structure, i.e., both model outputs exhibit a similar dependence on the random input parameters. If this is the case, then a noisy statistical correlation between $y_{\text{lo-fi}}$ and $y_{\text{hi-fi}}$ as shown in Figure 5.1 can be observed. This correlation can be exploited if it can be captured as conditional probability distribution $p(y_{\text{hi-fi}}|y_{\text{lo-fi}})$. Then, $p(y_{\text{hi-fi}})$ can be readily computed, as illustrated in Figure 5.1, using

$$p(y_{\text{hi-fi}}) = \int p(y_{\text{hi-fi}}|y_{\text{lo-fi}})p(y_{\text{lo-fi}})\mathrm{d}y_{\text{lo-fi}}. \tag{5.1}$$

What is missing so far is the conditional distribution $p(y_{\text{hi-fi}}|y_{\text{lo-fi}})$. This conditional distribution can be inferred using a Bayesian regression model if data in form of a set of training samples $\{y_{\text{lo-fi}}(\boldsymbol{z}^{(\text{j})}), y_{\text{hi-fi}}(\boldsymbol{z}^{(\text{j})})\}_{j=1}^n = \{y^{(\text{j})}_{\text{lo-fi}}, y^{(\text{j})}_{\text{hi-fi}}\}_{j=1}^n$ is available. These training samples can be obtained by computing the quantity of interest on both the high-fidelity and the low-fidelity models for several realizations of the random input parameters $\boldsymbol{z}^{(\text{j})}$. A Bayesian regression model can then establish a probabilistic link between the low- and high-fidelity model, thus, allowing to compute either $p(y_{\text{hi-fi}})$ using (5.1), but also failure probabilities like $P(y \in \mathcal{A})$. Therefore, (4.4) is rewritten as

$$\begin{aligned} P\left[y_{\text{hi-fi}} \in \mathcal{A}\right] &= \mathbb{E}\left[P\left[y_{\text{hi-fi}} \in \mathcal{A}|y_{\text{lo-fi}}\right]\right] \\ &= \int P\left[y_{\text{hi-fi}} \in \mathcal{A}|y_{\text{lo-fi}}\right] p(y_{\text{lo-fi}})\mathrm{d}y_{\text{lo-fi}}. \end{aligned} \tag{5.2}$$

One interpretation of the regression model in combination with the information from the low-fidelity model is that of a data fit surrogate for the respective high-fidelity model. Another

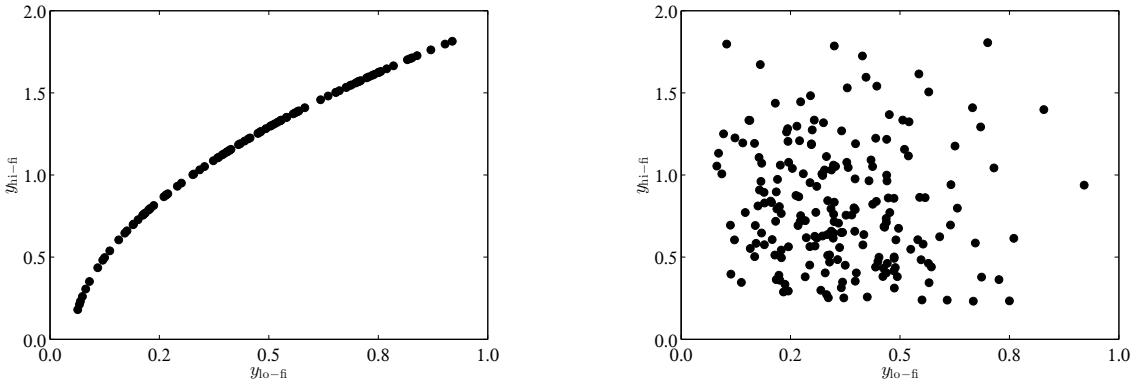

Figure 5.2 Two extreme scenarios for interrelation between high-fidelity and low-fidelity solution. (a) Direct one-to-one correspondence. (b) Statistical independence.

interpretation is that the regression model provides a probabilistic correction factor to account for the discrepancy between high- and low-fidelity solution. Thereby, it is important to note that this correlation can be exploited to predict $p(y_{\mathrm{hi-fi}})$ no matter how good the low-fidelity model approximates the high-fidelity model in a deterministic sense, meaning that large errors or discrepancies between the low-fidelity solution and the high-fidelity solution are admissible.

At this point it is helpful to consider the two most extreme cases which could possibly occur, to explore the limits of the proposed approach. These two cases are shown in Figure 5.2. The most favourable case where a direct one-to-one relationship exists between $y_{\mathrm{lo-fi}}$ and $y_{\mathrm{hi-fi}}$ is shown in Figure 5.2a. In this case it is obvious that it would be easy to come up with a functional relationship that could reproduce the interrelation between $y_{\mathrm{lo-fi}}$ and $y_{\mathrm{hi-fi}}$. In combination with $p(y_{\mathrm{lo-fi}})$ obtained from sampling, the calculation of $p(y_{\mathrm{hi-fi}})$ is trivial. The other extreme occurs if $y_{\mathrm{lo-fi}}$ and $y_{\mathrm{hi-fi}}$ are statistically independent, as shown in Figure 5.2b. In this case the low-fidelity model does not provide any information about the high-fidelity solution and cannot be used to expedite the computation of $p(y_{\mathrm{hi-fi}})$.

In order to facilitate the understanding for the reader, a sketch of the basic steps of the BMFMC approach is provided here, before a more detailed explanation of the individual steps is given. Starting with an existing accurate, high-fidelity model of a system of interest, an approximate low-fidelity model has to be constructed. This approximate model should have a similar stochastic structure as the high-fidelity model. However, it is not necessary that the approximate model provides an accurate approximation in a deterministic sense, as needed in deterministic multi-level/grid schemes. The only prerequisite is a mere statistical correlation between the high-fidelity and the approximate model. This very weak requirement offers a tremendous flexibility in the choice of approximate models. As shown in several numerical examples in the following chapters, the BMFMC approach also works if, e.g., a simpler physical model is used.

In the second step of the proposed approach the distribution $p(y_{\mathrm{lo-fi}})$ of the quantity of interest $y_{\mathrm{lo-fi}}$ has to be approximated by sampling the low-fidelity model. Independent of the particular choice of the sampling algorithm, computing $p(y_{\mathrm{lo-fi}})$ by sampling is much cheaper as compared

Bayesian multi-fidelity MC

1. Construct a low fidelity and a high-fidelity model of the system of interest, e.g., by creating a coarse and a fine discretization.
2. Compute $p(y_{\mathrm{lo-fi}})$ by sampling of the cheap low-fidelity model.
3. Select a very small subset of the samples $\{y^{(\mathrm{j})}_{\mathrm{lo-fi}}\}^n_{j=1}$, fully covering the (empirical) support of $p(y_{\mathrm{lo-fi}})$.
4. Compute corresponding high fidelity solution $\{y^{(\mathrm{j})}_{\mathrm{hi-fi}}\}^n_{j=1}$ for the selected subset of samples.
5. Use the samples $\{(y^{(\mathrm{j})}_{\mathrm{lo-fi}}, y^{(\mathrm{j})}_{\mathrm{hi-fi}})\}^n_{j=1}$ from both models as training data for a Bayesian regression model to obtain a (probabilistic) relationship between $y_{\mathrm{lo-fi}}$ and $y_{\mathrm{hi-fi}}$, i.e, $p(y_{\mathrm{hi-fi}}|y_{\mathrm{lo-fi}})$.
6. Approximate $p(y_{\mathrm{hi-fi}})$ and $P\left(y_{\mathrm{hi-fi}} \in \mathcal{A}\right)$ from $p(y_{\mathrm{hi-fi}}|y_{\mathrm{lo-fi}})$ and $p(y_{\mathrm{lo-fi}})$ using (5.1) and (5.2), respectively.

Table 5.1 Basic steps of the proposed BMFMC scheme. Taken from [32].

to sampling of the high-fidelity model. For the example problems considered in this work, low-fidelity models are between 10 and 1000 times cheaper to evaluate than the corresponding high-fidelity model.

Then, a small subset $\{y^{(\mathrm{j})}_{\mathrm{lo-fi}}\}^n_{j=1}$ of all computed samples is selected. Now, the high-fidelity solution $\{y^{(\mathrm{j})}_{\mathrm{hi-fi}}\}^n_{j=1}$ corresponding to the $\{y^{(\mathrm{j})}_{\mathrm{lo-fi}}\}^n_{j=1}$ is computed. The dataset $\{y^{(\mathrm{j})}_{\mathrm{lo-fi}}, y^{(\mathrm{j})}_{\mathrm{hi-fi}}\}^n_{j=1}$ is then used to train a Bayesian regression model which provides probabilistic information on $y_{\mathrm{hi-fi}}$ given $y_{\mathrm{lo-fi}}$. More specifically, the predictive distribution of the Bayesian regression provides the desired conditional probability distribution $p(y_{\mathrm{hi-fi}}|y_{\mathrm{lo-fi}})$. Once the conditional density $p(y_{\mathrm{hi-fi}}|y_{\mathrm{lo-fi}})$ is obtained, standard probability theory can be used to compute $p(y_{\mathrm{hi-fi}})$. Overall, the proposed BMFMC approach can be summarized in six basic steps, which are given in Table 5.1.

5.2.1 Sample selection

Assuming that the low-fidelity model has been evaluated N_{SAM} times, a small subset $\left\{y^{(\mathrm{j})}_{\mathrm{lo-fi}}\right\}^n_{j=1}$ of these computed samples is selected. For an accurate computation of $p(y_{\mathrm{hi-fi}})$ these samples should fully cover the support of $p(y_{\mathrm{lo-fi}})$, i.e., cover the whole range of values that $y_{\mathrm{lo-fi}}$ can take. Since usually only a particulate approximation of $p(y_{\mathrm{lo-fi}})$ is available, this range is approximated by the samples with the smallest and largest $y_{\mathrm{lo-fi}}$ value, respectively. For the examples considered in this work, 100-200 evenly distributed samples, which cover the range of all possible $y_{\mathrm{lo-fi}}$ values, yield consistent and excellent results.

However, it is noted that other more elaborate schemes to select the training samples can further reduce the number of evaluations of the high-fidelity model, especially if one is interested in estimating a small failure probability or say the 99 % quantile. Another scenario for more elaborate selection schemes is an extremely expensive high-fidelity model which severely limits the number of affordable model evaluations. In these situations more elaborate selection scheme could make a difference. To this end an adaption of the two stage design point selection procedure for GP surrogates to estimate percentiles of the distribution of interest as presented by Oakley [233] was investigated regarding its potential to further reduce the number of training points. Briefly, a preliminary version of the regression model is trained using an initial set of

very few training samples, say 10. Based on this preliminary regression model a rough approximation for the value of, e.g., the 99% quantile can be computed. In a second step, additional training samples are selected in the vicinity of the 99% quantile. Together with the initial set of training samples a second, more accurate version of the regression model can then be constructed, which is then used to produce a more accurate assessment of the 99% quantile. An initial assessment of this idea yielded interesting results. However, further research is deemed necessary before this approach can be reliably applied. Active learning approaches like ALM [199] and ALC [66] were also investigated [44], but it was found that the performance of the method based on a set of space filling samples is often hard to beat if a moderate number of high-fidelity model evaluations is affordable.

5.2.2 Bayesian regression models

Given that a set of training samples $\{y_{\mathrm{lo-fi}}^{(\mathrm{j})}, y_{\mathrm{hi-fi}}^{(\mathrm{j})}\}_{j=1}^{n}$ is available, a Bayesian regression model can be trained based on this data set. The predictive distribution of the regression model then provides the desired quantitative link $p(y_{\mathrm{hi-fi}}|y_{\mathrm{lo-fi}})$. A plethora of Bayesian regression approaches have been described in literature and are, in principle, applicable to this problem. Within the present work the regression approach proposed by Koutsourelakis [183] is used with minor modification as described in Section 3.5.3. The approach has several advantages, i.e., that marginally, meaning when all parameters are integrated out, also non-Gaussian distributions $p(y_{\mathrm{hi-fi}}|y_{\mathrm{lo-fi}})$ can be considered, even though the likelihood is considered to be Gaussian. Moreover, it is a very consistent fully Bayesian approach with prior distributions for all parameters and hyper-parameters, cf. [183]. In addition, it is extremely flexible and can also handle varying scales of fluctuation. The downside of the Koutsourelakis regression approach is that the posterior distribution of the parameters and the predictive distribution, i.e., $p(y_{\mathrm{hi-fi}}|y_{\mathrm{lo-fi}})$ cannot be computed in closed form and that consequently advanced Monte Carlo techniques, such as SMC, are needed to sample from the posterior. The basic principle of SMC samplers has been previously discussed in Section 4.3.2. For this task the SMC technique described in [182, 183] is employed. Although the cost associated with the inference of the posterior distribution of the parameters of the regression model are negligible compared to the cost of a single evaluation of any forward model considered in this work, simpler regression approaches are computationally faster. Perhaps more importantly other Bayesian regression approaches are easier to implement or third party libraries or packages can be used, facilitating the setup of a BMFMC framework. For this reason, examples where GP regression (see Section 3.5.2) is used instead of the Koutsourelakis regression approach are included in the following chapters. The particular version of GP regression used here is not a fully Bayesian approach and as a results the predictive distribution might tend to underestimate the uncertainty in the predictions [361]. For the examples in this work, significant differences in computed end results were not found. However, a more detailed comparison between different available regression models to address this issue should be investigated in future research.

5.2.3 Computing solution statistics of the high-fidelity model

Once the regression model has been trained, the original problem of computing statistics of the high-fidelity solver output based on the low-fidelity solution and the now available quantitative

link between low-fidelity and high-fidelity model can be tackled. By choosing a Bayesian approach levels of confidence can be assigned to the obtained estimates as well. The required steps differ depending on the particular regression approach that is used. In the following the steps to obtain the desired high-fidelity solution statistics based on the Koutsourelakis regression model are described in detail. Computing high-fidelity solution statistics based on a GP regression model is slightly simpler and the differences to Koutsourelakis regression model will also be briefly discussed in the following.

Based on the set of training samples the SMC algorithm yields a particulate approximation of the posterior density $\pi(\boldsymbol{\theta})$, where $\boldsymbol{\theta}(\omega)$ denote all parameters of the regression model (see (3.147)). Corresponding samples for the variance of the noise term ${\sigma_\epsilon}^2(\omega)$ can be readily drawn using the conditional posterior given in (3.162). Based on the Gaussian likelihood, the conditional distribution of $y_{\text{hi-fi}}$ given $\boldsymbol{\theta}$, σ_ϵ^2, and $y_{\text{lo-fi}}$ is given by

$$p(y_{\text{hi-fi}}|y_{\text{lo-fi}}) \approx p(y_{\text{hi-fi}}|y_{\text{lo-fi}}, \boldsymbol{\theta}, \sigma_\epsilon) = \frac{1}{\sqrt{2\pi}} \frac{1}{\sigma_\epsilon} \exp\left\{ -\frac{1}{2\sigma_\epsilon^2} \left(y_{\text{hi-fi}} - f(y_{\text{lo-fi}}, \boldsymbol{\theta})\right)^2 \right\} \tag{5.3}$$

with $f(y_{\text{lo-fi}}, \boldsymbol{\theta})$ defined according to (3.146). In order to obtain an estimate for the distribution $p(y_{\text{hi-fi}})$ one can integrate over the parameters $\boldsymbol{\theta}(\omega)$ and the variance of the noise ${\sigma_\epsilon}^2(\omega)$ to obtain the posterior mean estimate of the probability density of $y_{\text{hi-fi}}$, which will be referred to as $\hat{\pi}(y_{\text{hi-fi}})$ in order to distinguish between the distribution $p(y_{\text{hi-fi}})$ calculated directly with MC and the estimate computed by BMFMC. The posterior mean $\hat{\pi}(y_{\text{hi-fi}})$ can be computed using

$$\begin{aligned} \hat{\pi}(y_{\text{hi-fi}}) &= \mathbb{E}_{\boldsymbol{\theta}, \sigma_\epsilon, \mathrm{y}_{\text{lo-fi}}}[p(y_{\text{hi-fi}})] \\ &= \int p(y_{\text{hi-fi}}|y_{\text{lo-fi}}, \boldsymbol{\theta}, \sigma_\epsilon) p(y_{\text{lo-fi}}) \pi(\boldsymbol{\theta}, \sigma_\epsilon^2) \mathrm{d}\boldsymbol{\theta} \mathrm{d}\sigma_\epsilon^2 \mathrm{d}y_{\text{lo-fi}}. \end{aligned} \tag{5.4}$$

Using particulate approximations of $p(y_{\text{lo-fi}})$ and the joint posterior density $\pi(\boldsymbol{\theta}, \sigma_\epsilon^2)$

$$\begin{aligned} p(y_{\text{lo-fi}}) &\approx \sum_{i=1}^{N_{\text{SAM}}} W^{(i)} \delta_{y_{\text{lo-fi}}^{(i)}}(y_{\text{lo-fi}}), \\ \pi(\boldsymbol{\theta}, \sigma_\epsilon^{-2}) &\approx \sum_{l=1}^{N_{\text{particles}}} W^{(l)} \delta_{(\theta, \sigma_\epsilon)^{(l)}}(\boldsymbol{\theta}, \sigma_\epsilon^2), \end{aligned} \tag{5.5}$$

the posterior mean $\hat{\pi}(y_{\text{hi-fi}})$ can be readily approximated with

$$\hat{\pi}(y_{\text{hi-fi}}) \approx \sum_{l=1}^{N_{\text{particles}}} \sum_{i=1}^{N_{\text{SAM}}} W^{(l)} W^{(i)} \phi(y_{\text{hi-fi}} - f(y_{\text{lo-fi}}^{(i)}, \boldsymbol{\theta}^{(l)}), \sigma_\epsilon^{(l)})). \tag{5.6}$$

Here, ϕ denotes the Gaussian PDF as given in (5.3).

Another summary of interest is the probability of $y_{\text{hi-fi}}$ exceeding a specific threshold y_0. Given the model parameters $\boldsymbol{\theta}$ and the variance σ_ϵ^2 the probability of $y_{\text{hi-fi}}$ exceeding a specific threshold y_0 can be computed by

$$P\left(y_{\text{hi-fi}} < y_0; \boldsymbol{\theta}, \sigma_\epsilon\right) = \int q_{\mathcal{A}}(y_{\text{lo-fi}}; \boldsymbol{\theta}, \sigma_\epsilon) p(y_{\text{lo-fi}}) \mathrm{d}y_{\text{lo-fi}} \tag{5.7}$$

with $q_{\mathcal{A}}(y_{\mathrm{lo-fi}}, \boldsymbol{\theta}, \sigma_\epsilon)$ being defined as

$$\begin{aligned} q_{\mathcal{A}}(y_{\mathrm{lo-fi}}, \boldsymbol{\theta}, \sigma_\epsilon) &= \int_{y_0}^{\infty} p(y_{\mathrm{hi-fi}} | y_{\mathrm{lo-fi}}, \boldsymbol{\theta}, \sigma_\epsilon) dy \\ &= \Phi\left(\frac{f(y_{\mathrm{lo-fi}}, \boldsymbol{\theta}) - y_0}{\sigma_\epsilon}\right), \end{aligned} \tag{5.8}$$

where $\Phi(\cdot)$ is the standard normal CDF. The posterior mean approximation of $q_{\mathcal{A}}$, computed using the particulate approximation of $\pi(\boldsymbol{\theta}, \sigma_\epsilon^2)$, can be used to produce an estimate of the exceedance/failure probability for a specific value of $y_{\mathrm{lo-fi}}$

$$\begin{aligned} \mathbb{E}_{\boldsymbol{\theta},\sigma_\epsilon}[q_{\mathcal{A}}(y_{\mathrm{lo-fi}})] &\approx \hat{q}_{\mathcal{A}}(y_{\mathrm{lo-fi}}) \\ &= \sum_{l=1}^{N_{\text{particles}}} W^{(l)} \Phi\left(\frac{f(y_{\mathrm{lo-fi}}, \boldsymbol{\theta}^{(l)}) - y_0}{\sigma_\epsilon^{(l)}}\right). \end{aligned} \tag{5.9}$$

Substituting into (5.7) and using (5.5) yields an estimate for the failure probability in the sense that on average, given the training samples, the probability of $y_{\mathrm{hi-fi}}$ exceeding a threshold y_0 is given by:

$$\mathbb{E}_{\boldsymbol{\theta},\sigma_\epsilon,\mathrm{y}_{\mathrm{lo-fi}}}[P(y < y_0)] \approx \sum_{i=1}^{N_{\text{SAM}}} W^{(i)} \hat{q}_{\mathcal{A}}(y_{\mathrm{lo-fi}}^{(i)}) \tag{5.10}$$

Another advantage of the Bayesian approach is that in addition to point estimates like the posterior mean, confidence intervals can be estimated from the posterior, quantifying the uncertainties in the inferred parameters and hence in the regression model. P-quantiles $q_{\mathcal{A},p}(y_{\mathrm{lo-fi}})$ for the failure probability can be readily estimated using:

$$P\left(q_{\mathcal{A}}(y_{\mathrm{lo-fi}}) \leq q_{\mathcal{A},p}(y_{\mathrm{lo-fi}})\right) \approx \sum_{i=1}^{N_{\text{particles}}} W^{(i)} H\left(q_{\mathcal{A}}^{(i)}(y_{\mathrm{lo-fi}}) - q_{\mathcal{A},p}(y_{\mathrm{lo-fi}})\right) = p, \tag{5.11}$$

where $H(\cdot)$ denotes the heavyside function. To provide confidence intervals for exceedance probabilities in the following sections, $p = 1\%$ and $p = 99\%$ quantiles $q_{\mathcal{A},0.01}$ and $q_{\mathcal{A},0.99}$ are used.

The computation for the high-fidelity solution statistics is shown above specifically for the Koutsourelakis regression model based on a particulate approximations of the posterior distribution of its parameters. However, other Bayesian regression techniques can be used just as well. The technical steps involved might be a bit different, but the overall procedure remains the same. In order to put the steps described above in a more general context and explain the procedure if a GP based regression approach as discussed in Section 3.5.2 is used, it is helpful to think of $f(y_{\mathrm{lo-fi}}, \boldsymbol{\theta}(\omega))$ simply as a random function $\mathrm{f}(y_{\mathrm{lo-fi}})$ instead of a deterministic function with random parameters $\boldsymbol{\theta}(\omega)$. Then instead of integrating over all possible parameters weighted with their relative plausibility, one integrates over the distribution of the function. The concept of random function has been introduced before in the context of Gaussian processes. As explained in Section 3.5.2 the posterior process in GP regression can be interpreted as random function. Realization of this posterior process can be easily generated as described in Section 4.6.2. Based on these realizations $\{f^{(i)}(y_{\mathrm{lo-fi}})\}_{i=1}^{N_{\text{real}}}$ with equal weight $W^{(i)} = 1/N_{\text{real}}$, statistics

of the high-fidelity solution can be computed in the same fashion as described above, including confidence intervals. Integration with respect to σ_ϵ is not necessary, since the magnitude of the noise is not considered to be a random variable in the GP case, but determined using maximization of the marginal likelihood. Hence, the conditional distribution of $\mathrm{y}_{\mathrm{hi-fi}}$ given a realization $f^{(i)}$ is simply a Gaussian distribution.

5.2.4 General remarks

While it is difficult to provide general guidelines regarding how to construct good or optimal low-fidelity models for the BMFMC framework, it is important to mention that the suitability of a low-fidelity model and the applicability of the BMFMC scheme for a given pair of low-fidelity and high-fidelity model can be assessed based on the training samples alone; a full MC reference solution of the high-fidelity model is not necessary. Aside from a visual assessment of the interrelation between low-fidelity and high-fidelity solution, e.g., the correlation coefficient or the fraction of the variance of $y_{\mathrm{hi-fi}}$ that can be explained by the chosen regression model can provide a first indicator about the strength of the correlation. If the interrelation between the two models is similar to the one depicted in Figure 5.2b, the low-fidelity model does not provide sufficient information about the high-fidelity solver output and has to be discarded. One can then either try use another low-fidelity approximation or chose to perform sampling using the high-fidelity model. In any case, it is considered a major advantage of the method that it provides information about the limits of its own applicability.

While the BMFMC scheme is described here using one low-fidelity model, the use of multiple low-fidelity models is, in principle, also possible [183]. Multiple low-fidelity models could be considered in either a hierarchical or parallel fashion. The hierarchical approach is based on a sequence of models with increasing levels of sophistication or accuracy. The overall efficiency gain is thereby based on the notion that as the fidelity increases, the number of model evaluations needed to estimate the difference between the levels decreases, because the model discrepancy term becomes smoother and the magnitude of the difference becomes smaller. The idea to use a hierarchy of models has been employed in both Multi-level Monte Carlo (MLMC) [121] (cf. Section 5.3.1) and Gaussian process based surrogates [188] (cf. Section 5.3.3) and has proven to be an effective way to reduce computational costs. The second option would be to use multiple low-fidelity models in a parallel fashion. Thereby the different low-fidelity models are selected such that they capture different regimes of the system's response. However, the investigation of multi-model BMFMC schemes is beyond the scope of this work and will be subject of future research.

5.2.5 Efficient implementation

The BMFMC approach advocated in this work is a non-intrusive UQ scheme, since the approach does not necessitate modification of the code that is used to evaluate the forward model. Hence, BMFMC can be used in combination with elaborate and well tested legacy codes. BMFMC, in principle, only requires the ability to evaluate the forward model for a given set of input parameters. Nevertheless, it does not constitute a black box approach in a strict sense, since some knowledge about the model or system of interest is required to construct a suitable low-fidelity model. Although access and modification of the forward solver is not a necessity to use

the BMFMC scheme, the ability to modify the forward solvers source code can increase the overall efficiency of an UQ framework dramatically.

For instance, it is more efficient if the individual realizations of all uncertain and hence random properties can be generated at runtime as opposed to using separate input files. In case of uncertain constitutive properties this is relatively straightforward. After computing a realization of the random field describing the respective constitutive parameter, each element in the model is assigned the parameter value which corresponds to, e.g., its center location. For random geometries, however, things are not as easy.

Geometry and mesh adjustment at runtime Meshing, i.e., discretizing a geometry in space with finite elements is usually part of the preprocessing and more often than not performed with other software than the finite element solver. In any case, BACI does not have an integrated meshing package and third party packages are used to generate meshes. In this work, AAA models with an uncertain wall thickness are considered as examples for models with an uncertain geometry. Hence, one requirement of the developed UQ framework is the ability to efficiently generate realizations of the random AAA geometry and the corresponding finite element meshes. To avoid external tools in form of standalone mesh generation software or scripts, realizations of random geometries are created at runtime through a geometry and mesh adjustment step using a pseudo structure mesh movement algorithm. The approach was developed specifically for adjusting the wall thickness in relatively thin wall structures, but it could also be applied in other scenarios. To simplify the discussion of the geometry adjustment approach, consider the generic artery segment model depicted in Figure 5.3. The goal is to efficiently create versions of the depicted finite element model where the wall thickness is no longer uniform but varies spatially according to a realization of a random field. To achieve this, the first step is the computation of the value of the random field describing the thickness at all nodes on the outer surface of the wall. Next, a solid mechanics problem is set up with the aim to move the nodes on the outer surface using appropriate dirichlet boundary conditions such that the resulting local wall thickness matches the values of the random field. For this the nodes on the inner surface of the model are fixed through zero displacement dirichlet boundary conditions and the nodes on the outer surface of the model are moved in the direction of the local surface normal. The magnitude is thereby determined by the difference between current, uniform wall thickness and the desired local wall thickness prescribed by the realization of the random field. The position of the nodes between the two surfaces are adjusted accordingly by solving for equilibrium. To ensure a regular, uniform, and high-quality mesh, the outermost nodes are moved in multiple steps. An example of a resulting wall thickness distribution is shown in Figure 5.3b. The obtained deformed geometry is then used as reference configuration for the actual forward problem of interest.

Parameter continuation Sampling based UQ usually entails the repeated evaluation of a forward model with different sets of parameters. The fact that very similar forward problems have to be solved can be exploited for conservative forward problems by using numerical continuation schemes, which can help to reduce the overall computational effort associated with UQ. For instance all mechanical models of AAAs studied in this work are considered to be elasto-static problems, for which equilibrium solution is path independent and hence parameter continuation schemes can be used.

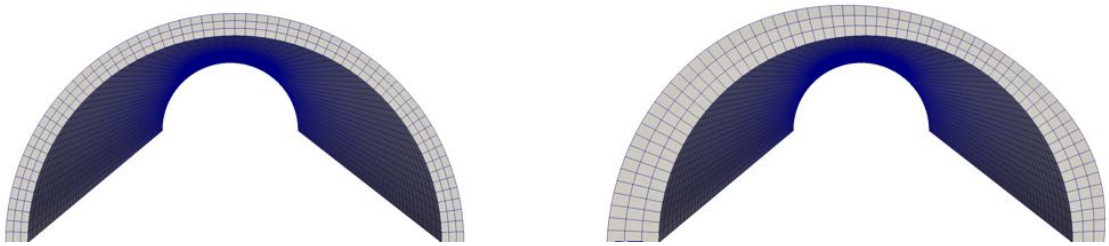

(a) (b)

Figure 5.3 Geometry adjustment based on pseudo structure mesh movement algorithm, shown for the example of a generic artery segment model. (a) Original geometry with uniform wall thickness. (b) Modified geometry with wall thickness adjusted to match realization of a random field.

To illustrate the continuation scheme it is helpful to first recap the discrete system of nonlinear equations resulting from the discretized static boundary value problem of nonlinear elastostatics derived in Section 2.1.4 which is repeated here to facilitate the discussion

$$\boldsymbol{r}(\boldsymbol{d}) = \boldsymbol{f}^{\mathrm{int}}(\boldsymbol{d}, \boldsymbol{p}) - \boldsymbol{f}^{\mathrm{ext}}(\boldsymbol{d}) = \boldsymbol{0}. \tag{5.12}$$

Herein, $\boldsymbol{r}$ denotes the residual vector, $\boldsymbol{f}^{\mathrm{int}}$ the internal forces, and $\boldsymbol{f}^{\mathrm{ext}}$ the external forces. Moreover, the implicit dependence of the internal forces on the constitutive parameters through the stress tensor is recognized here by introducing the vector $\boldsymbol{p}$, which contains all constitutive parameters for all elements. Thereby $\boldsymbol{p}$ could in turn depend on a set of random variables $\mathbf{z}$. Let $\boldsymbol{p}^{(1)}$ denote a particular set of parameters and $\boldsymbol{d}^{(1)}$ the corresponding solution of the boundary value problem determined through and incremental "load continuation scheme" as described in Section 2.2. Now, if the solution of the boundary value problem for a new set of constitutive properties $\boldsymbol{p}^{(2)}$ is sought - say the two vectors correspond to two different realizations of a random field - one could of course solve the nonlinear boundary value problem using the load incrementation procedure to obtain $\boldsymbol{d}^{(2)}$, as illustrated in Figure 5.4. Another option, since $\boldsymbol{d}^{(1)}$ is known, is to leave the load continuation parameter λ constant and use continuation in the material parameters instead. Therefore, the parameter $0 \leq \gamma \leq 1$ is introduced, which in turn is used to define the following sequence

$$\boldsymbol{p}_\gamma = (1-\gamma)\boldsymbol{p}^{(1)} + \gamma \boldsymbol{p}^{(2)}. \tag{5.13}$$

Now, instead of incrementally increasing the load factor λ and solving for static equilibrium, λ is set to 1 and a sequence of internal forces, defined through $\boldsymbol{f}^{\mathrm{int}}(\boldsymbol{d}, \boldsymbol{p}_\gamma)$, is used to transition incrementally to the static equilibrium solution $\boldsymbol{d}^{(2)}$, which corresponds to the constitutive properties $\boldsymbol{p}^{(2)}$ and the external loads $\boldsymbol{f}^{\mathrm{ext}}$.

Continuation in material properties is used here to improve the efficiency of the developed UQ framework. In practice, this means that a realization where all constitutive parameters are equal to their respective mean values is computed first. Then, based on this initial solution, continuation with respect to material parameters is performed to obtain solutions for all following

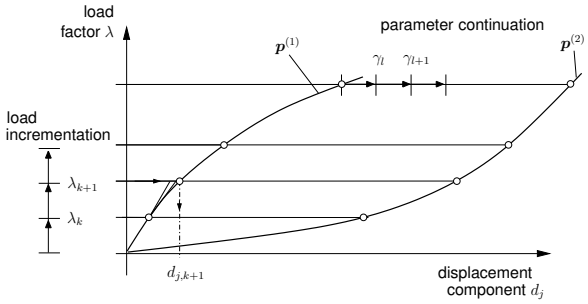

Figure 5.4 Illustration of the used parameter continuation scheme.

realizations. A prerequisite for this scheme to be more efficient is of course that the respective solutions are relatively close to each other. A related questions is how the necessary number of continuation steps can be determined. This question could be answered based on some sort of distance measure. An alternative is to employ an adaptive scheme, which adjusts the step size. A basic version of this approach is used in this work. The continuation scheme implemented within the scope of this work attempts to blend over to the next equilibrium in a preset number of steps. If the linear or nonlinear solver fails to converge, the step size is divided in half and a new attempt is made. Continuation schemes for constitutive properties have been previously used, e.g., within the scope of optimization problems, with the aim to identify some constitutive properties of the forward model, see [122]. To the knowledge of the author, parameter continuation schemes have not been applied in the context of an UQ framework, yet. Their use can significantly reduce the computational effort needed for the evaluation of the forward model, if model structure admits such a continuation approach.

Nested parallelism The solution time of many computational models to date, including the examples presented in the scope of this thesis, is often in the range of hours to days and their treatment usually requires multiple cores and parallel software architecture. In virtually all non-intrusive UQ schemes the forward model needs to be evaluated multiple times. Hundreds or thousands of evaluations are the norm rather than the exception. If these evaluations were performed sequentially, the actual time to solution would render UQ infeasible, even if only a modest number of forward model evaluations, say 100, is required. The use of approximate models as advocated in this work alleviates the problem, but the time to solution would still be impracticably large for many applications. Hence, the evaluations have to be carried out in a concurrent fashion. This problem can be solved by introducing a second level of parallelism in the code. By using what is referred to from here on as *nested parallelism*, parallel evaluation of multiple versions of the forward model is enabled within the same instance of the running code. This feature is particularly useful for embarrassingly parallel algorithms such as Monte Carlo, where instead of computing the samples sequentially, all samples are computed at the same time or at least in several strands. Of course, a similar speedup could be achieved by creating multiple instances of the software. However, while the integration of nested parallelism merely facilitates file handling and execution in case of direct Monte Carlo, it is crucial for more advanced sampling schemes like SMC, where communication between the otherwise independent groups is necessary to perform the resampling step, cf. Section 4.3.2. In any case, the software framework BACI was extended such that e.g., Monte Carlo simulations can be performed in a

parallel fashion using nested parallelism, such that the same framework will also permit the use of more advanced sampling schemes in the future.

5.3 Other multi-fidelity UQ approaches

The BMFMC approach is not the only method which uses models with different levels of fidelity to reduce the computational costs in an UQ scheme. Two other, prominent examples of multi-fidelity UQ schemes are introduced and discussed in the following and their relation to the BMFMC approach is explained. First, the so-called multi-level Monte Carlo technique is introduced. Then, the extension of GP based surrogates to multiple models with different fidelities is discussed. For the sake of completeness it is mentioned that a multi-fidelity framework for PCE based surrogates has also been proposed, see [224, 373].

5.3.1 Multi-Level Monte Carlo

Multi-level Monte Carlo (MLMC) is essentially a variance reduction technique based on the same idea as iterative multi-grid solvers for large systems of linear equations, i.e., finding the solution for a coarser version of the problem first and then applying correction steps to obtain the solution at a higher resolution. Multi-level Monte Carlo can be used to compute expectations more efficiently by decomposition of the problem into several sub-problems based on s so-called *levels* of the model. These levels could be created, e.g., by generating a hierarchy of meshes with increasing resolution. Then, based on the linearity of the expectation operator, instead of estimating the expectation of the quantity of interest $\mathbb{E}[\mathsf{y}_s]$ directly on the finest level using Monte Carlo, the expected value is computed based on the expectation on the coarsest level and several correction terms, which add the difference between the expectations computed on consecutive levels

$$\mathbb{E}[\mathsf{y}_s] = \mathbb{E}[\mathsf{y}_0] + \sum_{l=1}^{s} \mathbb{E}[\mathsf{y}_l - \mathsf{y}_{l-1}]. \tag{5.14}$$

In multi-level Monte Carlo these expectations are estimated independently through, e.g., the standard Monte Carlo estimate with N_l number of samples

$$\mathbb{E}[\mathsf{y}_l - \mathsf{y}_{l-1}] = \frac{1}{N_l} \sum_{i=1}^{N_l} \left(y_l^{(i)} - y_{l-1}^{(i)} \right). \tag{5.15}$$

Here $y_l^{(i)}$ and $y_{l-1}^{(i)}$ denote the quantity of interest computed on different levels but based on the same realization of random input quantities $\boldsymbol{z}^{(i)}$. Through an appropriate choice of the number of samples N_l needed to estimate the correction terms on each level, the overall variance of the multi-level estimator defined through the sum in (5.14) can be minimized for a fixed computational cost.

It has been shown that multi-level Monte Carlo can achieve a superior accuracy at the same computational cost as standard Monte Carlo if the two assumptions, that the accuracy and computational cost increase with the level and that the variance of the correction term decreases with increasing level, are fulfilled [120, 121]. Although estimation of a failure probability can be, in

principle, reformulated as an estimation of an expectation, calculation of a failure probability is not that simple using MLMC [99, 333].

Since its introduction for geometric integration by Heinrich [149], multi-level Monte Carlo has been applied to several problems, such as path simulations in finance [120], subsurface flow [25, 59, 65], and inviscid incompressible flow [218, 219]. To the knowledge of the author the method has not been applied to nonlinear structural mechanics yet. The multi-level Monte Carlo method has gained tremendous traction in recent years and several extensions have been proposed quite recently, see e.g., [121] for a detailed review including recent developments. For instance, Haji-Ali et al. [140] proposed the so called multi-index Monte Carlo methods which generalizes the concept of levels such that levels can be defined in multiple directions.

The generation of levels in MLMC is not restricted to a hierarchy of meshes with different resolutions. Using other techniques to construct cheap approximate solutions such as solving a simplified version of the problem at hand is also a valid approach [221], as long as the assumptions mentioned above are fulfilled. Nevertheless, MLMC is predominantly applied as a geometric multi-grid scheme in literature. For problems that rely on structured meshes or grids on regular domains, the generation of a hierarchy of grids is simple. However, practical engineering problems often rely on discretization schemes with unstructured meshes and, in addition, often feature very complex geometries. In biomedical applications with patient-specific models mesh generation often requires a fair amount of manual labour and is difficult to automize. In these scenarios the generation of many mesh levels is impractical and may be one of the reasons why MLMC has not been applied to problems with complex geometry yet.

5.3.2 Relationship between MLMC and BMFMC

The MLMC methodology can also be related to the Bayesian multi-fidelity approach advocated in this work. Because the BMFMC approach is based on two models with different levels of fidelity a comparison with a two-level MLMC approach is given here. In a two-level MLMC scheme the MLMC estimator for the expected value of $y_{\mathrm{hi-fi}}$ can be restated as a relationship between $y_{\mathrm{hi-fi}}$ and $y_{\mathrm{lo-fi}}$ using a very simple regression model. Essentially, the correction term between two consecutive levels can be also interpreted as the following linear model between two levels of fidelity

$$y_{\mathrm{hi-fi}} = f(y_{\mathrm{lo-fi}}) + \varepsilon = a y_{\mathrm{lo-fi}} + b + \varepsilon, \tag{5.16}$$

where the parameter $a = 1$ and the parameter b is estimated based on N_1 computed samples such that the error term is minimal in the least square sense. The gain in efficiency of this two level MLMC scheme is to a large extent determined by the variance in the error term, i.e,. magnitude of the average error, which among other things in this case depends on how close the actual relation between $y_{\mathrm{hi-fi}}$ and $y_{\mathrm{lo-fi}}$ is to the assumed relation $y_{\mathrm{hi-fi}} = 1 \cdot y_{\mathrm{lo-fi}} + b$.

In the opinion of the author a more detailed comparison between MLMC and BMFMC approach presents a very interesting direction of future research. However, investigations regarding this matter are beyond the scope of this work.

5.3.3 Multi-fidelity surrogate models based on Gaussian Processes

The extension of the GP surrogate framework to incorporate information from simulator evaluations with different levels of fidelity was originally proposed in the seminal work by Kennedy and O'Hagan [173] and later has been further developed in [188, 262]. Although the approach is very elegant and general, it has received comparatively little attention in the engineering community for the purpose of UQ so far, see [86] for an application to membrane deformation problems. From an engineering standpoint a related approach called the *model-correction-factor method* has been proposed, which applies the same idea to reliability analysis [88]. Anyway, similar to MLMC, the approach requires that at least one lower-fidelity version of the computational model can be constructed, the evaluation of which is computationally cheaper than the high-fidelity simulator. In addition the approach is based on the following assumptions, which are replicated here from [173] for the sake of completeness. The first assumption is that the output from the different models are correlated, i.e., share some basic features. Moreover, it is assumed that the models exhibit a degree of smoothness with respect to the uncertain input parameters, in the sense that output values are similar for similar input values. Lastly, it is assumed that prior beliefs about the model can be formulated as (stationary) Gaussian process and that the quantity of interest is a scalar value. The only difference to the single level GP surrogate is the first assumption, that the output from different versions of the simulator need to show some correlation, which intuitively makes sense given that the low-fidelity version is supposed to be an approximation to the next higher-fidelity simulator.

Instead of fitting a GP directly to the output y_s of the model with the highest fidelity, a GP surrogate for a low-fidelity model is constructed first, then a correction to account for the discrepancy between the levels or versions of the model is estimated separately. Various possibilities exist based on, e.g., the choice of covariance function, hyper-parameter and corresponding priors, and particular choice to model the discrepancy between the levels. Kennedy and O'Hagan [173] proposed the following relationship for two consecutive levels

$$\mathsf{g}_l(\boldsymbol{z}) = o_{l-1}\mathsf{g}_{l-1}(\boldsymbol{z}) + \mathsf{d}_l(\boldsymbol{z}), \tag{5.17}$$

where $\mathsf{g}_l(\boldsymbol{z})$ and $\mathsf{g}_{l-1}(\boldsymbol{z})$ are GP based surrogates for level l and $l-1$, respectively. The scalar o_{l-1} is referred to as regressive coefficient and accounts for the part of the difference between two consecutive levels which is proportional to the lower-fidelity solution. The remainder of the discrepancy is accounted for by $\mathsf{d}_l(\boldsymbol{z})$ for which, conditional on some hyper-parameters, a zero mean GP prior is used. The approach can be formulated, like MLMC, to incorporate information from s levels of fidelity. However, for ease of exposition, a restriction to two levels is made here to facilitate the discussion. In a two level scheme, first a GP surrogate for the low-fidelity model is constructed based on a set of design points. At these design points the low-fidelity model is evaluated to obtain a training data set $\{y_0, \boldsymbol{z}_0^{(i)}\}_{i=1}^{N_0}$. Subsequently, the correction term comprised of o_0 and $\mathsf{d}_l(\boldsymbol{z})$, which account for the difference between low-fidelity model and high-fidelity model are calculated. Both, o_0 and $\mathsf{d}_l(\boldsymbol{z})$ are estimated based on the output of the high-fidelity model evaluated at a subset of the aforementioned design points, which in combination with $\mathsf{g}_0(\boldsymbol{z})$ gives rise to the posterior GP $\mathsf{g}_1(\boldsymbol{z})$. This posterior GP is then used to make inference about the desired statistical summary of the quantity of interest, analogous to the procedures described in Section 4.6.2. The described approach can be also interpreted as a way to perform

implicit model calibration. If experimental data is available, it can be incorporated in the scheme at the highest level, thereby correcting for modelling errors between the high-fidelity simulator and an experiment. It is important to note that while the multi-fidelity approach might alleviate the curse of dimensionality, it does not resolve the fundamental problem that parameters of GP models in d-dimensional (if $\boldsymbol{z} \in \mathbb{R}^d$) space have to be trained. This entails estimation of parameters of, e.g., the covariance function, and the number of these parameters typically increases with the dimension. Thus, many data points are required in order to obtain reliable parameter estimates.

5.3.4 Relationship between GP surrogate models and BMFMC

To facilitate the following discussion of the relation between multi-fidelity GP surrogates and BMFMC let us assume that the regression model used in the BMFMC framework is based on a GP as well. In this case, although the BMFMC approach cannot be directly linked to the multi-fidelity framework described by Kennedy and O'Hagan [173], BMFMC it can be interpreted as GP surrogate model with a special, proxy-based, covariance function. Usually, the goal of the GP surrogate is to capture the relation between (random) model input parameters $\mathbf{z}$ and model output y. Thereby, based on the assumption that y varies smoothly with $\mathbf{z}$, the model is only evaluated at few points in the input space and y is interpolated in-between the chosen design points. The assumptions about the smoothness are made through the particular choice of covariance function $k(\boldsymbol{z}, \boldsymbol{z}')$. When the dimension of $\boldsymbol{z}$ becomes large, this approach becomes infeasible because it typically requires estimation of correlation parameters, e.g., ℓ_i, for each dimension.

If it were possible to come up with a different measure of similarity, which is based in a lower dimensional space, the problem of having to estimate correlation length parameters for each dimension could be circumvented. The output of a lower-fidelity model version can be interpreted as a proxy, which provides exactly this measure of similarity, in the sense that two high-fidelity model solutions are likely similar if the low-fidelity solutions are similar as well. This can be achieved by using a covariance function which depends on $y_{\mathrm{lo-fi}}(\boldsymbol{z})$ as argument, i.e., $k(y_{\mathrm{lo-fi}}(\boldsymbol{z}), y_{\mathrm{lo-fi}}(\boldsymbol{z}'))$. The advantage is that only a one-dimensional GP model needs to be trained, which obviously has fewer parameters than a d-dimensional model. The downside of this approach is that the relation between low-fidelity solution and high-fidelity solution is not a one-to-one relation, but contaminated with noise.

5.3.5 Combination of BMFMC with GP based surrogate models

As a consequence of the interpretation introduced above, it is possible to see that the BMFMC approach could be extended such that the low-fidelity model provides only partial information about the similarity of the high-fidelity model output and that the remaining information is provided by the distance with respect to certain components of $\boldsymbol{z}$. This would make sense in scenarios where it is possible to construct a cheap surrogate, which can only capture parts of the variability regarding a particular subset of $\boldsymbol{z}$. Another scenario is if the relationship between one component of the uncertain inputs and the high-fidelity model output is not smooth, but a cheap surrogate for this particular dependence is available. Splitting $\boldsymbol{z}$ into two parts, i.e.,

$\boldsymbol{z} = [\boldsymbol{z_1}, \boldsymbol{z_2}]$, some kind of mixed covariance function could be constructed

$$k(\boldsymbol{z}, \boldsymbol{z}') = k_1(y_{\mathrm{lo-fi}}(\boldsymbol{z_1}), y_{\mathrm{lo-fi}}(\boldsymbol{z_1'})) + k_2(\boldsymbol{z_2}, \boldsymbol{z_2'}). \tag{5.18}$$

This covariance function could be used in some kind of hybrid UQ scheme, i.e., a mixture between GP surrogate in the usual sense and the BMFMC approach advocated here. In the opinion of the author this kind of scheme could yield significant computational savings, especially if sensitivity analysis is considered in future applications as well.

6 Elicitation of probabilistic models for AAA wall properties based on experimental data

The present chapter addresses the estimation of probabilistic models of AAA wall properties, such as thickness, constitutive parameters, and failure measures. Thereby, a data-driven approach is pursued and elicitation of probabilistic models is based on a large database of *ex vivo* tensile tests, thickness measurements, and supplementary non-invasively measurable parameters. The results in presented in this chapter are largely based on the previous publication by the author [33].

The chapter commences with a brief discussion and overview of constitutive modeling of AAA wall and existing experimental and computational research regarding this subject. Furthermore, the need for probabilistic models for several patient-specific parameters is elaborated on the basis of experimental findings from both, own experiments and literature. After concluding that probabilistic models present the only coherent choice in view of uncertain patient-specific parameters, the remainder of the chapter addresses the estimation of suitable probabilistic models for patient-specific AAA wall parameters. The goal is to predict-patient specific parameters more accurately and with less uncertainty than predictions based on study population averages. This is achieved by using Bayesian regression techniques in combination with non-invasively assessable explanatory variables. Therefore, the two possible choices for a probabilistic model, i.e., random variable or random field, will be discussed and it will be shown that the simpler random variable model is overly simplistic for most AAA wall parameters and that the data indicates that the random field model is the more appropriate choice. Next, available experimental data, which was in parts gathered within the scope of this work, is harnessed to elicit probability distributions for several AAA wall parameters. These probability distributions might also vary depending on the location within the AAA geometry. Two options to obtain suitable probability distributions are investigated and compared. The first is fitting a probability distribution directly to the measurements of the respective parameter, while the second is to use supplementary, non-invasively available data to construct advanced Bayesian regression models based on Gaussian processes. The predictive distribution of these regression models provide the desired patient-specific, and possibly location dependent, probability distributions for the uncertain wall properties. For the purpose of comparison linear regression models based on the same data are constructed for all parameters as well. However, a Bayesian viewpoint is adopted for theses models as well.

It is shown that the predictive uncertainty can effectively be reduced, and the predictive assessment of several patient-specific parameters, most importantly for thickness and failure strength of the AAA wall, can be improved when additional non-invasively assessable parameters are taken into account for the prediction through regression models. Thereby, the more

elaborate Bayesian regression approach based on Gaussian processes consistently outperforms standard linear regression. Moreover, a comparison to a previously proposed statistical model for the wall strength is given later on in this chapter.

Aside from the first-order probability distribution of a random field describing a certain AAA wall parameter, the spatial correlation structure of the random field is another important characteristic which has to be estimated. In the context of UQ problems this is notoriously difficult because the data is rarely, if ever, sufficient to determine a correlation structure unequivocally [58]. Based on the assumption that the parameters vary smoothly in space, the correlation length of a relatively simple covariance structure can be estimated from the gathered experimental data. The details of the proposed procedure are described at the end of this chapter. The probabilistic predictions for AAA wall parameters and the estimated correlation structure will be combined to setup random fields describing uncertain input parameters of mechanical models of a AAAs. Several different choices will be compared and discussed based on UQ using these patient-specific AAA models in Chapter 7.

6.1 Mechanical modeling of AAA wall

In this work only purely elastic models of AAAs are considered and the aneurysmatic arterial wall is modeled as nonlinear hyper-elastic continuum. The consideration of growth and remodeling effects is beyond the scope of this work. However, it is important to acknowledge that these inelastic growth and remodeling effects govern the progression of the disease and the dynamics of the underlying mechanobiological processes. The mathematical and computational modeling of these processes is an area of active research, see, e.g., [10, 160] for an overview. Future work will likely encompass these phenomena as well.

That being said, the objective here is to define a suitable elastic model of the arterial wall which enables the computation of mechanical response quantities which are often related to AAA rupture risk. Although the actual failure mechanism is still debated in literature, popular choices for rupture risk indicators are often stress based, e.g., peak wall stress, both maximum normal stress or maximum von Mises stress, or the *rupture potential index* (RPI) proposed by Vande Geest et al. [337]. However, while many studies assess rupture potential by computing wall stresses based on an elastic model, it has been pointed out that the damage and failure process of soft tissue might be more involved and thus cannot be captured with purely elastic models employing a stress based failure criterion. Hence, other mechanical quantities such as peak strain or strain energy density are considered to be potential quantities of interest as well [107, 206, 251, 278, 345, 347].

In order to accurately compute stresses, strains, and strain-energy prevailing in the AAA wall, several patient-specific model input parameters are needed —most importantly the wall thickness, the parameters of a suitable constitutive law, and possibly failure measures such as the wall strength or failure tension. The computation of meaningful failure criterions based on mechanical quantities, such as the RPI, also requires knowledge of these input parameters. Unfortunately, the parameters cannot be exactly determined in a clinical setting and remain, to some extend, uncertain, which is the motivation for choosing a probabilistic model for these parameters. Below, the limitations of obtaining estimates for these parameters are discussed

and the methodology to infer probabilistic models for these parameters based on experimental data is explained.

6.1.1 Wall thickness

The wall thickness is obviously of paramount importance for the accurate simulation of the mechanical behavior of an AAA. Alas, unlike the overall geometry, the wall thickness and its regional distribution over the surface of the AAA can usually not be determined from standard clinical CT image data. Recently Shum et al. [302] and Martufi et al. [208] proposed an approach to estimate the wall thickness, including regional variations, from CT images and claim superior accuracy. If their findings can be replicated and confirmed, this approach could improve the accuracy of patient-specific AAA models. However, given that the resolution of current CT imaging systems is in the order of 1mm voxel size, it seems unlikely that the wall thickness will be determinable with negligible uncertainty.

The wall thickness could, in principle, also be quantified more accurately using, e.g., intravascular ultra-sound, but this would require an additional examination and is hitherto not part of the standard clinical routine. As a result, most researchers to date use a spatially constant uniform wall thickness estimated form a sample of *ex vivo* measurements and ignore the uncertainty about the true patient-specific wall thickness.

6.1.2 Constitutive models and parameters

A suitable constitutive model with patient-specific parameters is particularly important for the accurate computation of strain and strain-energy density computations. As will be discussed in more detail later on, the wall stress is relatively insensitive to variations of the constitutive parameters. Studies, such as [93, 277], claiming dramatic effects on wall stress usually neglect the prestressed state of the imaged AAA geometry and therefore obtain flawed results, which are additionally also more sensitive to variations in the constitutive parameters.

Nevertheless, an accurate, patient-specific constitutive model should be the basis for a computational investigation of AAAs. Several constitutive models for aneurysmatic arterial wall have been proposed by researchers in the past. A relatively simple isotropic constitutive model that is widely used because it captures the mechanical behavior of AAA tissue well, was introduced by Raghavan et al. [267] and Raghavan and Vorp [266]. It is based on the following strain-energy function

$$\Psi = \alpha(I_1 - 3) + \beta(I_1 - 3)^2, \tag{6.1}$$

with the constitutive parameters α and β. In the following, these two parameters will be referred to as α-stiffness and β-stiffness, respectively. The first invariant I_1 of the right Cauchy-Green strain tensor $\boldsymbol{C}$, which is defined in (2.13) and serves as a measure of deformation in (6.1). Throughout this work the constitutive model defined through (6.1) will be referred to as Raghavan & Vorp (R&V) material model, though a slightly different formulation is used. Modified to near incompressibility through an isochoric-volumetric split of the strain-energy function, the version of the R&V material used for all AAA finite element simulations in this work reads:

$$\Psi = \alpha(\bar{I}_1 - 3) + \beta(\bar{I}_1 - 3)^2 + \frac{\kappa}{\eta^2}(\eta \ln J + J^{-\eta} - 1), \tag{6.2}$$

where $\bar{I}_1$ is the first invariant of the isochoric Right-Cauchy-Green strain tensor and $J = \det \boldsymbol{F}$ is the determinant of the deformation gradient. The bulk modulus κ was set to $\kappa = \frac{2\alpha}{1-2\nu}$ using $\nu = 0.49$, and the parameter η is set to -2. Since its introduction the model has been adopted by many researchers and is still widely used in computational studies of AAA to date [92, 102, 103, 151, 204, 213, 273, 312].

Although some more recent studies based on biaxial tensile test have indicated that the constitutive behavior might be better captured with an anisotropic material model [241, 329, 338], the isotropic material law proposed by Raghavan and Vorp is used throughout this work for reasons elaborated in the following.

First of all the main goal of the present work is not the computation of rupture risk for AAA but the development of an efficient UQ framework which allows the consideration of complex mechanical models. Clearly, further research and development is needed until clinically relevant questions can be answered. In addition, the UQ framework developed in this work is by no means limited to isotropic material models and can readily be used in combination with complex anisotropic constitutive laws where, e.g., the fiber directions are modeled as random variable or random field.

Moreover, over the course of the past years a very large and unique experimental dataset has been collected at the Institute for Computational Mechanics. The dataset is comprised of uniaxial tensile test data of more than 200 specimens harvested from 80 patients. In addition, detailed patient information is available about the patients medical history, blood analysis data, and CT images, making it one of very few datasets of this kind and size world wide. Albeit the uniaxial tensile tests basically limit evaluation of the data to isotropic constitutive laws, having access to the raw experimental data including supplementary data on the patients medical history, blood analysis data, and CT image data, is considered a major benefit which is hard to neglect.

In addition to the arguments made above, biaxial tensile tests carried out with anisotropic porcine aorta by Trübswetter [330] revealed that the isotropic R&V material law performed only marginally worse in reproducing the constitutive behavior than a more complex anisotropic material law.

Lastly, while the reported average preferential stiffening direction is reported to be the circumferential direction, a closer look at the results from the biaxial tests in the study of Vande Geest et al. [338] and O'Leary et al. [241] reveals that only 17 of 26 and 20 of 28 tensile test specimens show this preferential stiffening direction, respectively. Biaxial tensile test were also conducted by Tong et al. [329]; however, they do not report results of individual specimens. These results indicate that the preferential stiffening direction and the corresponding fiber directions in the tissue exhibit a significant amount of variability and consequently would have to be considered uncertain in a numerical model. In addition, even if biaxial experimental data is available, the identification of the parameters of complex anisotropic constitutive laws through an optimization procedure is difficult. In fact, it becomes increasingly difficult the more parameters the constitutive model has. Without detailed *a priori* knowledge about the fiber direction it is difficult to determine contributions of the different components, i.e., isotropic contribution versus contribution of the fiber families, to the overall mechanical response of the tissue. Hence, even if biaxial tensile test are available, the parameters obtained from a parameter identification procedure will be afflicted with considerable uncertainty.

Aside from the choice of the particular constitutive model, the more fundamental problem is that tensile tests with AAA tissue require invasive excision of tissue samples and are thus only possible during elective repair or *post mortem*. Hence, for simulations performed with the goal to determine whether surgery is necessary or not, tensile test data is not available and thus the parameters of the used constitutive model, be it isotropic or anisotropic, will be uncertain. There has been some progress regarding *in vivo* characterization of constitutive properties based on pulse wave velocity or local changes in diameter of the aorta [16, 291, 342]. However, current *in vivo* approaches are not yet able to detect short scale spatial variations, nor has any of these approaches been successfully applied and validated for AAA or human aorta by tensile tests. In conclusion, patient-specific constitutive parameters cannot be accurately determined in a clinical setting. Taking population averaged parameters is also problematic since all studies that have been conducted to determine constitutive parameters found that these parameters vary significantly from patient to patient. Furthermore, the parameters exhibit spatial variations within a single patient as well [206, 241, 267–269, 274, 325, 329, 334, 338, 340]. In light of these arguments, the benefit of using anisotropic constitutive models seems questionable at this point.

6.1.3 Failure measures

In addition to wall thickness and constitutive properties, failure measures are needed to assess AAA rupture risk. Although stress based failure models might not be optimal to describe soft tissue damage and failure [206, 345], stress based failure measures are still widely used. A typical failure measure which can be derived from destructive tensile testing is the failure strength often also referred to as wall strength σ_{max}. It is usually determined as maximum first Piola-Kirchhoff stress during the destructive test

$$\sigma_{\text{max}} = \frac{F_{\text{max}}}{A_0}. \tag{6.3}$$

Here F_{max} is the maximum recorded force in the corresponding tensile test and A_0 is the initial cross-sectional area of the specimen. As this measure for wall strength is only useful in combination with knowledge about the wall thickness, or at least a model thereof, Raghavan et al. [268] introduced the failure tension T_{max} as a second failure measure for AAA wall. This failure measure is independent of the wall thickness, which is generally unavailable in clinical practice due to the aforementioned limitation of standard clinical image data. The failure tension can be computed as

$$T_{\text{max}} = \frac{F_{\text{max}}}{b_0}, \tag{6.4}$$

where b_0 is the specimen width in the undeformed configuration.

As with the constitutive parameters, the failure strength or the failure tension cannot be determined in a non-invasive fashion prior to surgery. Again population averaged values are unreliable due to the drastic variation between and also within patients [268, 269, 325]. This also pertains to the failure tension and it is not clear, at least from the dataset used in this study, that the failure tension can offer a more reliable prediction as compared to the wall strength.

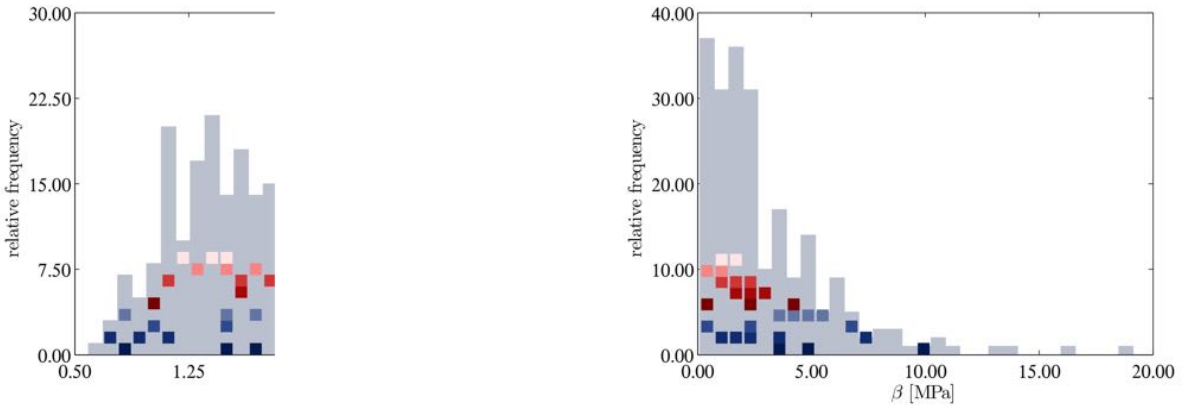

(a) **(b)**

Figure 6.1 Histogram of thickness measurements from tensile test specimens (a) and stiffness parameter β determined from tensile test (b). Intra-patient variability is shown by squares in the same color, which indicate measurements from specimens which were excised from the same patient.

6.2 Probabilistic models for uncertain patient-specific AAA wall parameters

In face of non determinable and hence uncertain patient-specific parameters the use of probabilistic models instead of using population averaged mean values is advocated in this work. Uncertain physical parameters such as the wall thickness can be modeled either as random variable or as a random field. In case the thickness is modeled as a random variable, the wall thickness of an AAA will be spatially constant. If the wall thickness is modeled as a random field, a spatially varying wall thickness will be obtained for each realization of the field. Hence, by representing an uncertain model parameter as a random field, the spatial, intra-patient variations of this quantity can be captured in a stochastic sense as well. Figure 6.1 depicts histograms of measured AAA wall thickness and the constitutive parameter β (R&V constitutive model, see (6.1)), which was obtained by fitting the R&V model to experimentally obtained stretch-stress curves. Squares with the same color indicate measurements taken from the same patient. Clearly, the intra-patient variations in these two parameters is significant and will have a considerable effect on the spatial distribution of computed mechanical quantities such as strains or stresses.

Before discussing the means by which probabilistic descriptions for the aforementioned wall parameters are estimated in this work, the requirements for the two different probabilistic model choices are briefly discussed, along with the assumptions to be made and the additional model parameters that have to be estimated.

6.2.1 Random variable models

Although the random variable model cannot capture intra-patient variations, the model is appealing due to its simplicity. A simple probability distribution, e.g., in form of a PDF, is used to describe the random behavior of the parameter. In the context of sampling based UQ schemes it thereby suffices that samples can be drawn form the distribution, and a closed form expression is not essential. Assuming that some measurements of the quantities to be described by a random variable are available, a PDF can be obtained either by fitting a parametric distribution such as a normal or a log-normal distribution to the data, or by using kernel density estimation. Through usage of specific types of distributions, constraints on the possible parameter range can be readily accounted for. For instance, all uncertain parameters studied in this work are positive by definition and hence the Gaussian distribution is not a suitable probabilistic model for these parameters. Distributions with a strictly positive support, such as the log-normal distribution, are often a more suitable choice.

6.2.2 Random field models

As discussed above for the random variable case, the Gaussian distribution is often not appropriate to describe uncertain physical parameters. Hence, non-Gaussian random fields are used within the scope of this work to describe uncertain wall parameters. Evidently, there is not enough data to fully infer the complete family of finite-dimensional probability distributions to describe a general non-Gaussian field in any practical setting. By making a number of assumptions about the properties of the field, the number of required parameters can be drastically reduced. In this work translation fields (cf. Section 3.3.2) are used for parameters that do not abide by a Gaussian distribution. In contrast to the covariance structure, which is assumed to be an isotropic, homogenous squared exponential covariance function, the mean function of the underlying Gaussian field is assumed to depend on the location in some cases. Based on these premises, the parameters of the first-order probability distribution, e.g., a log-normal distribution, as well as the correlation length parameter of the covariance function have to be estimated. Other more elaborate correlation structures are, in principle, also valid choices and might describe the actual spatial correlation of the parameters more accurately; however, it is very difficult to estimate the parameters of these covariance functions, especially in biomedical applications where experimental data is extremely scarce. Moreover, it would be interesting to compare several first-order distributions in addition to the log-normal one. This comparison, however, is too beyond the scope of this thesis and will likely be addressed in future work.

6.3 Inference of probability distributions for wall parameters

This section covers the estimation of probability distributions for the AAA wall's constitutive parameters, thickness, and failure probabilities based on experimental data. This problem can be interpreted as a prediction problem in the sense that the goal is to make probabilistic predictions about the wall properties, ideally on a patient-specific basis. These probabilistic predictions can be based on, e.g., previous measurements of these wall properties or on regression techniques,

which in combination with non-invasively available patient-specific data, provide a predictive distribution for the respective wall property of interest. Thereby, the aim is to minimize the predictive error and to reduce the remaining uncertainty about the patient-specific wall properties.

A multitude of other patient-specific parameters, such as blood analysis data, the patients medical history, and geometric features of the AAA are non-invasively assessable. If these parameters contain statistical information about, e.g., the wall strength or the wall thickness, it can be exploited using regression analysis. The idea is to use statistical tools to exploit non-invasively available information in order to infer patient-specific parameters that are needed for a more accurate patient-specific finite element model of an AAA, e.g., for the computational assessment of AAA rupture risk. This idea has been previously pursued by Vande Geest et al. [340] who suggested the use of linear regression to obtain a more accurate patient-specific prediction for the wall strength based on several non-invasively assessable parameters. By incorporating local thrombus thickness and normalized local AAA diameter in their statistical model, also regional variations of the wall strength can be captured and predicted. Along those lines, Maier [202] used regression for the construction of statistical models for other AAA wall parameters as well. A related approach was also recently proposed in [292], where the goal of the authors was the inference of parameter distributions of a constraint mixture model for the aortic wall based on measurement fitted values of these parameters and patient age. Here, a similar approach is followed and probabilistic models for the prediction of the aforementioned patient-specific parameters are created. However, in contrast to the studies by Vande Geest et al. [340] and Maier [202], a Bayesian viewpoint is adopted, resulting in probabilistic predictions allowing the computation of a confidence interval for all predictions, instead of a single deterministic number. This is considered a major advantage. Moreover, more advanced regression techniques are employed and a significantly larger patient population is considered. An extensive dataset based on 80 patients and 218 tensile test specimens was collected. In addition, 28 non-invasively assessable parameters, which can be used as explanatory variables in a regression model have been gathered.

After briefly reporting the results of 218 tensile tests with AAA wall specimens, the two main purposes of this section are as follows. First, it is shown that it is possible to exploit the statistical information which is encoded in the non-invasively accessible parameters to make probabilistic predictions for patient-specific constitutive parameters, wall thickness, failure tension, and wall strength using regression models. By comparison it is shown that linear regression, the often used and standard approach in biomedical engineering, is outperformed by the more elaborate Gaussian process regression. On average, the predictions for the patient-specific quantities obtained by Gaussian processes regression are more accurate as compared to predictions based on population average, as well as compared to the linear regression case. In addition, the variance of the predictive distribution obtained with the regression models is typically smaller compared to the parameter's variance of the study population, which implies that the uncertainty about these parameters is effectively reduced. The second goal is the replication of the findings from Vande Geest et al. [340]. Using the dataset collected at the Institute for Computational Mechanics predictions based on the model from [340] are computed. The results show that this model poorly predicts the data measured by the group of the author. The ensuing subsections and paragraphs contain a brief summary of the employed experimental methods, an overview of the study population, and a short description of the available explanatory parameters. The Results obtained with the regression techniques, which are described in Section 3.5, are presented in Section 6.3.3.

No. patients	80
No. tissue samples	132
No. tensile test specimens	218
No. experimentally determined parameters	5
No. potential explanatory parameters	28

Table 6.1 Summary of the size of experimental dataset. Taken from [33].

6.3.1 Experimental methods

6.3.1.1 Study population and tissue sampling

218 tensile tests were performed with samples from 80 AAA patients who underwent open repair. An overview of the study population size is given in Table 6.1 and a summary of the population characteristics is provided in Table 6.2. Complete blood analysis data and CT images were obtained as routine part of the preoperative preparation for 78 and 80 patients, respectively. The CT data was utilized as described in [273, 274] to create 3D reconstructions and finite element models of the AAA geometry including intraluminal thrombus (ILT). Orientation and location of the samples were indicated by the surgeon and recorded on images of 3D reconstructions or CT images of the AAA directly during surgery. In total, 132 tissue samples from different excision sites were obtained. For tensile testing, these samples were subdivided into 218 test specimens. The spatial position of an individual specimen was determined from its location within the tissue sample and the position of the sample which was recorded during surgery. Samples intended for mechanical evaluation were stored in lactated Ringers solution (130 mmol/l sodium chloride, 5 mmol/l potassium chloride, 2 mmol/l calcium chloride, 3 mmol/l sodium lactate) at $4\,^{\circ}\mathrm{C}$ and underwent mechanical testing at room temperature within 24 h after surgery. The study was approved by the ethics committee of the university hospital rechts der Isar, Technische Universität München, Germany.

6.3.1.2 Mechanical testing

All harvested samples of AAA wall were excised during open surgery and later subdivided into rectangular tensile test specimens with a length of 20-30 mm and a width of 8-10 mm. Prior to testing, the thickness of each specimen was measured using a Mitutoyo "Quick-Mini Series 700" digital thickness gauge (Mitutoyo, Kawasaki, Japan. Part-No. 700-118. Constant measuring force=0.5 N, measuring platen diameter=5 mm, accuracy = 20 μm) and averaged over five measuring points. Tensile tests were performed using either an ElectroForce 3100 (Bose Corporation, Eden Prairie, USA) or a Zwick/Roell mediX0.1 (Messphysik Materials Testing, Fürstenried Austria) tensile test machine. In both cases the same test protocol, which is described in [274], was used to determine elastic properties in a cyclic test. Subsequently, a destructive test was performed until failure. The failure load was thereby defined as maximum tensile force measured in this experiment. Specimens that slipped from the clamps during testing were excluded from the study, resulting in a total of 176 successful destructive tests.

	From	To	Mean±sd	Median
Age [years]	48	90	68.8±8.1	69
Max. AAA diameter [mm]	43	110	64.5±14.8	59
Max. ILT thickness[1] [mm]	0	46.2	22.8±9.77	22.4
Subrenal aortic diameter [mm]	28	82.6	45.8±10.3	43.4
Medical history	Yes		No	Unknown
Ruptured AAA	13		63	4
Chronic kidney disease (CKD)[2]	13		63	4
Diabetes mellitus (DM)[3]	8		67	5
Hypertension	52		23	5
Smoking status[4]	34		41	5
Coronary heart disease (CHD)	15		59	6
Peripheral vascular disease (PVD)	4		70	6

Table 6.2 Main characteristics of study population. No patient had known connective tissue disease. [1]78 AAAs had ILT. [2]Grouping for CKD was based on an estimated glomerular filtration rate (EGFR) according to the Kidney Disease Improving Global Outcomes (KDIGO) [331]: patients with EGFR<60ml/min (stage 3, 4 and 5) were considered as patients with CKD [328]. [3]Patients suffering from diabetes mellitus (DM) were defined by a fasting plasma glucose >126 mg/dl, or use of oral hypoglycemic agents or insulin [9]. [4]Patients were considered as smokers if they were active smokers or stopped smoking less than ten years ago [105]. Taken from Biehler et al. [33].

6.3.1.3 Evaluation of tensile tests

The stretch-stress curves obtained from cyclic testing were fitted to the hyperelastic, incompressible, isotropic R&V material model defined by the strain energy function given in (6.1). For each of the tested specimens the parameters α and β were determined from the measured force-displacement curves using a Levenberg-Marquardt curve fitting algorithm. The procedure is described in detail in [274]. In addition to the elastic properties, the two failure measures wall strength and failure tension defined in (6.3) and (6.4) were derived from destructive testing.

6.3.1.4 Non-invasively accessible explanatory parameters

A total of 28 non-invasively accessible parameters, which could potentially provide statistical information about the AAA wall properties, were considered. The parameters are shown in Table 6.3 and can be categorized into *patient characteristics* and *spatially distributed quantities* determined from medical images at the sample excision site. Patient characteristics include general patient information, the patient's medical history, and laboratory parameters obtained from blood analysis. Parameters from the latter category which vary spatially across the surface of the AAA are, e.g., the local ILT thickness and the euclidian distance to the bifurcation, as illustrated in Figure 6.2. All parameters are available either preoperatively in a clinical setting and hence can be collected with negligible additional costs or effort, or they can be obtained from a computer model of the AAA.

6.3.2 Regression models

In contrast to other studies employing regression models, the aim here is not information in the sense that the goal is to uncover a relationship between the explanatory variables and the *ex vivo* measured quantities, but rather prediction. The concern is not so much finding potential relationships - meaning which of the predictor variables explains or could cause a specific observable phenomenon - but rather to use the regression models to predict the quantities of interest for new unseen patients.

Based on the nomenclature defined in the Sections 3.4 and 3.5, the starting point for the regression analysis is the training data set $\mathcal{D}$ with n observations $\mathcal{D} = \{\boldsymbol{x}^{(i)}, y^{(i)}\}_{i=1}^{n} = (\boldsymbol{X}, \boldsymbol{y})$, where the input vector $\boldsymbol{x} \in \mathbb{R}^d$ contains d explanatory variables. Specifically, $\boldsymbol{x}$ contains the parameters, or a subset thereof, which are summarized in Table 6.3. The variable y denotes the measured output or target variable which we wish to predict, e.g., the wall thickness.

Patient characteristics			
general		***medical history***	
sex	f=0, m=1	chronic kidney disease (CKD)	no=0, yes=1
age	[years]	diabetes mellitus (DM)	no=0, yes=1
AAA-status	ele.=0, rpt.=1	hypertension	no=0, yes=1
max AAA diameter	[mm]	smoking status	no=0, yes=1
subrenal aortic diameter[1]	[mm]	Coronary heart disease (CHD)	no=0, yes=1
		Peripheral vascular disease (PVD)	no=0, yes=1
laboratory parameters			
creatinine[2]	mg/dl	sodium	[mmol/l]
erythrocytes	[Mio/μl]	urea	[mg/dl]
thrombocytes	[1000/μl]	mean corpuscular hemoglobin (MCH)	[pg/cell]
leukocytes	[1000/μl]	mean corpuscular	
hsCRP	[mg/l]	hemoglobin concentration (MCHC)	[gHb/100ml]
potassium	[mmol/l]	mean corpuscular volume (MCV)	[fl]

Spatially distributed quantities at the sample excision site[3]			
local geometrical data			
distance to bifurcation (see Figure 6.2)	[mm]	relative axial position (dist. to bi-	[-]
local thrombus thickness (see Figure 6.2)	[mm]	furcation divided by AAA length)	
local diameter	[mm]	relative thrombus thickness	[-]
local normalized diameter (NORD)	[-]	(local thrombus thickness divided	
(local ø divided by subrenal aortic ø)		by max thrombus thickness)	

Table 6.3 Categorized non-invasively accessible explanatory parameters used for statistical evaluation of AAA wall properties. Parameters are listed together with their unit or the statistical coding, e.g., no = 0; yes = 1. [1]If the aneurysm reached the renal arteries, the aortic diameter between the celiac artery and the superior mesenteric artery minus 2.5mm was used instead [203]. [2]Values from patients on dialysis (stage 5, EGFR$<$15 ml/min) were excluded. [3]All values at sample excision sites were automatically assessed from 3D reconstructed AAA. Taken from Biehler et al. [33]

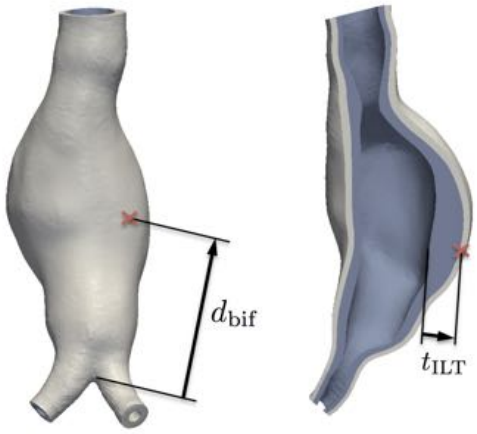

Figure 6.2 Reconstructed AAA geometry showing local thrombus thickness t_{ILT} and distance to the aortic bifurcation d_{bif}. Taken from Biehler et al. [33]

The goal is to make inference about the relationship between explanatory variables and target values. Typically, this relationship is not deterministic but can be characterized through a conditional probability distribution. In accordance to the Bayesian paradigm we do not only compute point estimates such as the mean value for the target variable, but rather consider probability distributions which reflect the remaining uncertainty in the target variable. Therefore, we assume that the explanatory variables can be related to the target variable via an additive error model

$$y = f(\boldsymbol{x}) + \epsilon, \tag{6.5}$$

where the random error ϵ contains not only the measurement error but also the contribution of other unknown or unmeasured variables to the target variable y. After the inference of a not necessarily deterministic function f and the magnitude of the error, we can make predictions for a new yet unseen test case $\boldsymbol{x}^*$ and compute the predictive, conditional distribution $p(y^*|\boldsymbol{x}^*, \mathcal{D})$. If the explanatory variables provide sufficient information about the target values, the variance of the predictive distribution will be small and the mean of the predictive distribution $\bar{y}^*$ will be close to the true value y of the target variable. If, on the other hand, y is significantly influenced by some other unknown parameter not included in $\boldsymbol{x}$, the predictions of the regression model will be poor, i.e., the error between predicted mean and true value will be large. Furthermore, the lack of predictive capability will be reflected by a large variance of the predictive distribution $p(y^*|\boldsymbol{x}^*, \mathcal{D})$. Note that all quantities that are assessed in this work are strictly positive and hence a logarithmic transformation, i.e., for the thickness t: $y = \log(t)$, is made to ensure that predictions are also strictly positive.

6.3.2.1 Linear regression

Linear regression is probably the most common regression technique in biomedical engineering and has been used previously to create a statistical model for the strength of AAA wall [340]. In contrast to Vande Geest et al. [340], a Bayesian viewpoint is adopted for linear regression here as well. The predictive distribution for a new test input $\boldsymbol{x}^*$ based on a training dataset

$\mathcal{D}$ has been derived in Section 3.5.1.1 along with the basics of this methodology. The mean is given in (3.121) while the squared scaled parameter of the predictive $t-$distribution and the corresponding 95% confidence interval is given in (3.122) and (3.124), respectively. However, for the sample size in this study $F_{\mathcal{T}}^{(-1)}(0.025, n-d)$, where $F_{\mathcal{T}}^{(-1)}$ denotes the inverse CDF of the t-distribution with $n-d$ degrees of freedom, is very close to 1.96; and hence the predictive distribution can be considered Gaussian with minimal error.

6.3.2.2 Gaussian process regression

As for linear regression, the basics of Gaussian process regression have been covered previously in Section 3.5.2. The mean, variance, and confidence interval of the Gaussian predictive distribution can be computed using (3.135), (3.136), and (3.142), respectively. For the purpose of estimating wall properties the combination of a linear ansatz for the mean function $m(\boldsymbol{x}) = \boldsymbol{\theta}_m^T \boldsymbol{x}$ and a covariance function from the Matérn family [209] as given in (3.65) is used here. All hyper-parameters and the variance of the noise are estimated based on maximizing the marginal likelihood as described in Section 3.5.2.1.

6.3.2.3 Assessment of predictive capabilities

The predictive error of the regression models is assessed by the standardized mean square error (SMSE), which is defined as the squared error between the mean prediction $\bar{f}^*$ and the measured target value $\tilde{y}^*$ averaged over all test cases n^* and normalized by the target variance

$$\text{SMSE} = \frac{\frac{1}{n^*}\sum_{i=1}^{n*}(\tilde{y}^{*\,(i)} - \bar{f}^{*\,(i)}))^2}{\sum_{j=1}^{n}\frac{1}{n}(y^{(j)} - \bar{y})^2}, \tag{6.6}$$

where $\bar{y}$ is the average of all target values in the training set. Using this error measure it is easy to see if a regression model performs better than simply using $\bar{y}$ as a guess for all test cases, in which case the SMSE is approximately one. Confidence regions for the predictions can be readily computed using (3.124) and (3.142) based on the predictive variance. Hence, in addition to the SMSE the standardized mean predictive variance

$$\sigma_{\text{s}}^{*\,2} = \frac{\frac{1}{n^*}\sum_{i=1}^{n*}(\sigma^{*\,(i)})^2}{\sum_{j=1}^{n}\frac{1}{n}(y^{(j)} - \bar{y})^2}, \tag{6.7}$$

is used to quantify the uncertainty in the predictions. Obviously, the standardized mean predictive variance should be smaller than one, indicating a narrower confidence region around the predictive mean than the one obtained directly from the target values $y^{(i)}$.

In order to compare the predictive capabilities of the two regression models a variant of leave-one-out cross-validation (LOOCV) is applied. All tensile test specimens from a single patient are used as test inputs or validation set, while the regression model is fitted to the data of the remaining patients. The standardized mean square error SMSE and standardized mean predictive variance are computed based on all specimens from the validation patient. Thus, these quantities are hereafter referred to as patient standardized mean square error (PSMSE) and patient standardized mean predictive variance $\sigma_{\text{P,s}}^{*\,2}$, respectively.

After performing the LOOCV scheme and having computed PSMSE and $\sigma_{\text{P,s}}^{*\,2}$ for every test patient, the arithmetic mean of these two quantities is computed. As the mean of the PSMSE

($\mathbb{E}$[PSMSE]) is prone to distortion by one or two particular bad cases, the median of this quantity ($\mathbb{MD}$[PSMSE]) is also reported. Furthermore, the percentage of the predictions that lie within the 95% confidence region is also reported. The true predictive root mean square error (RMSE), which is computed after the data has been transformed back to its original space, is also given to provide the reader with a sense of the true magnitude of the average predictive error. By fitting a normal distribution to the logarithm of the measured quantities, the trivial constant prediction model is obtained, which provides a constant prediction based on study population average, as well as an estimate for the variance of the measured parameters. In order to assess the benefit of the regression models over this constant prediction model, the error measures described above were computed for this approach as well, by applying the same LOOCV scheme.

6.3.2.4 Data selection and outliers

Amongst all potential explanatory variables a subset is chosen using a sequential forward feature selection algorithm. Starting from an empty set of explanatory variables, one predictor variable is added to the subset in each step until no further improvement, based on SMSE, in prediction of the dependent variable y is achieved. Feature selection was performed solely using standard linear regression; however, the same features were used to train the Gaussian process model in order to ensure comparability. Note that this comparison is not entirely fair. Maximizing the marginal likelihood can result in explanatory variables being effectively removed from the inference if a covariance function that implements automatic relevance determination, such as (3.65), is used [360]. While several other methods to determine a suitable subset of predictor variables were tried, the forward selection algorithm delivered the best results for the dataset and both regression methodologies. The full feature set was also used to train a Gaussian process model. The resulting predictions, however, were in general less accurate. For some of the patients in the database a subset of potential explanatory variables is missing for various reasons. Assuming that the data is missing at random, the corresponding specimens were excluded from the dataset (list wise deletion) for specimens with more than four missing entries. If fewer entries were missing, these were imputed with the population mean value of the respective variable. Moreover, severe y-space outliers were identified by a studentized residual larger than $F_{\mathcal{T}}^{(-1)}(0.0005, n-d)$ and excluded from the model.

6.3.3 Results

Before discussing the results obtained with the different regression models, the statistics of the tensile test results and the parameters of the fitted log-normal distributions are briefly reported. While the parameters α, β, and the thickness could be successfully measured for all 218 AAA wall specimens, the failure tension and the wall strength could only be determined for 176 specimens since some specimens slipped from the clamps. Thus, the statistics of the study population given below are based on 218 and 176 measurements, respectively. The experimental results are also summarized in Figure 6.3. Wall thickness ranged from 0.59 to 3.46 mm with a median of 1.56 mm and a mean $\pm$ SD of 1.65 $\pm$ 0.55 mm. The stiffness parameter α ranged from 0.00015 to 0.83323 MPa with a median of 0.079 MPa and a mean $\pm$ SD of 0.121 $\pm$ 0.128 MPa. The stiffness parameter β varied from 0.1 to 19.13 MPa with a median of 2.049 MPa and a mean $\pm$ SD of 2.985 $\pm$ 2.848 MPa. Failure tension varied from 0.54 to 2.63 N/mm with

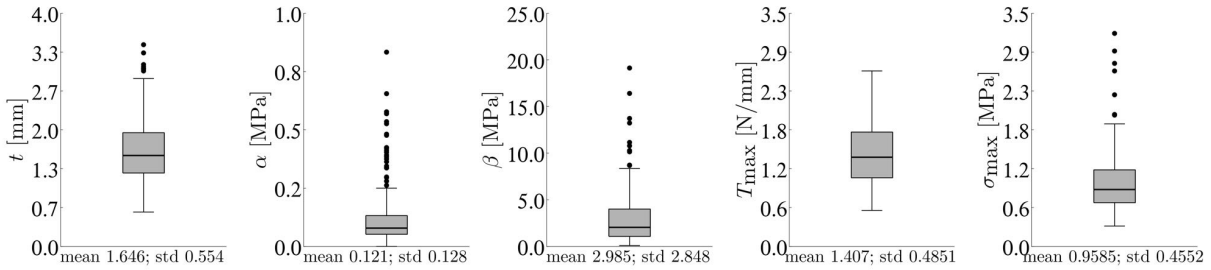

(a) wall thickness **(b)** α-stiffness **(c)** β-stiffness **(d)** failure tension **(e)** strength

Figure 6.3 Box-and-whisker plots summarizing experimentally measured wall thickness, α-stiffness, β-stiffness, failure tension and strength. Plots are based on 218 specimens for thickness, α-stiffness, β-stiffness; and 176 specimens for failure tension and strength. Taken from Biehler et al. [33].

quantity	μ	σ
α	-2.6031	1.1688
β	0.6724	0.9976
t	0.4434	0.3338
$T_{\max}$	-0.1326	0.4151
$\sigma_{\max}$	0.2821	0.3487

Table 6.4 Parameters of log-normal distribution fitted to tensile test data. $T_{\max}$ and $\sigma_{\max}$ denote failure tension and wall strength, respectively.

a median of 1.34 N/mm and a mean $\pm$ SD of 1.41 $\pm$ 0.49 N/mm. Wall strength ranged from 0.307 to 3.197 MPa, with a median of 0.835 MPa and a mean $\pm$ SD of 0.959 $\pm$ 0.46 MPa. The parameter estimates of log-normal distributions fitted to the data are summarized in Table 6.4.

In the following, the results of the regression analysis for each of the five measured quantities are reported and the predictive capabilities of linear regression and Gaussian process regression are compared. In addition, both approaches are compared with the trivial model which predicts based on mean and variance fitted to the log of the data directly. For each quantity, Tables 6.5 to 6.9 provide an overview of the computed error measures, allowing a quantitative comparison between the models. In the tables the abbreviations lognfit, lin, and gp, correspond to the constant prediction model, linear regression, and Gaussian process regression, respectively. Figures 6.4 to 6.8 show the model predictions as well as the measured values of the respective quantity of interest. It is important to emphasize that the patient for which predictions are made was not included in the training data set of the regression model. In other words, the data shown in the Figures arose not from one but multiple regression models. The mean value and the 95% confidence interval of the predictive distribution provided by the regression models are shown in the plots, visualizing the uncertainty in the predictions. For comparison, the mean and 95% confidence interval of the constant mean prediction model, fitted to all specimens, are given as well. Note that due to list wise deletion, the number of tensile test specimens included in the

regression analysis is reduced to 163 specimens from 55 patients for the elastic properties and 131 specimens from 53 patients for the failure measures, respectively.

The following paragraphs contain a detailed description of the results for: thickness, α-stiffness, β-stiffness, strength $\sigma_{\max}$, and failure tension $T_{\max}$. In Section 6.3.3.6 the wall strength model developed by Vande Geest et al. [340] is applied to the dataset of the Institute for Computational Mechanics and the results are compared with those from the regression models obtained in this work.

6.3.3.1 Thickness

Using the feature selection approach described above, the following features were included in the regression models: *sex, age, ruptured, subrenal diameter, CKD, DM, creatinin, erythrocytes,thrombocytes, sodium, urea, MCH, MCHC, distance to bifurcation, thrombus thickness,* and *NORD*. The units or the statistical encoding of these features is given in Table 6.3 Through dependence on *thrombus thickness, distance to bifurcation*, and *NORD* the predicted wall thickness will not be constant across the aneurysm, but will, as expected, feature regional variations.

reg. model	$\mathbb{E}[\text{PSMSE}]$	$\mathbb{MD}[\text{PSMSE}]$	$\mathbb{E}[\sigma^{*2}_{\text{P,s}}]$	in conf. reg.	RMSE [mm]
lognfit	1.000	0.716	1.000	0.909	0.577
lin	0.875	0.640	0.703	0.925	0.532
gp	0.719	0.421	0.521	0.906	0.486

Table 6.5 Comparison of regression models for the wall thickness. lognfit: constant prediction model; lin: linear regression; gp gaussian process regression; $\mathbb{E}[\text{PSMSE}]$, $\mathbb{MD}[\text{PSMSE}]$: mean and median of patient standardized mean square error, respectively; $\mathbb{E}[\sigma^{*2}_{\text{P,s}}]$: mean value of patient standardized mean predictive variance. In confidence region (conf. reg.) is the fraction of measurements that fall in the 95% confidence area of the regression model. RSME: root mean square error. Reproduced from Biehler et al. [33].

A visual comparison between model predicted and measured values is provided in Figure 6.4. Therein, two different representations of the same data are shown. In Figure 6.4a the individual specimens are sorted in ascending order according to the predicted thickness value. Figure 6.4b depicts the same data, but the specimens are ordered based on the measured thickness. Both of these representations are displayed because each of them conveys different information about the respective regression approach.

The order in Figure 6.4a provides a clearer visual illustration of the confidence area, which is shown in light red. The 95% confidence area obtained with Gaussian process regression is noticeably smaller than the light blue confidence region of the constant prediction model and the confidence region obtained with linear regression, shown in Figure 6.4c for comparison. Furthermore, the specimens with a measured thickness outside of the predicted confidence bounds can be easily identified at first glance in this figure.

In contrast, if the specimens are sorted in ascending order according to their measured thickness, a clearer picture of the predictive capability in terms of mean value is provided, cf. Figure 6.4b. If the curves for prediction average (red curve) and measured values (black dots) show the same trend, the selected features in combination with the chosen regression approach provide

information about the quantity of interest. However, due to the rather noisy data it cannot be expected that the average prediction curve matches the slope of the measured data exactly. This is especially true for values close to either the lower or the upper limit.

In addition to the qualitative assessment, a quantitative comparison of all error measures, shown in Table 6.5, indicates that both regression approaches result in superior predictions compared to the trivial constant prediction model. Thereby Gaussian process regression yields better results than linear regression. By using Gaussian process regression the median of the PSMSE is reduced from 0.716 to 0.421. The mean of $\sigma^{*2}_{\mathrm{P,s}}$, a measure for the predictive uncertainty, is also considerably smaller in the Gaussian process case. In comparison to the constant prediction model, the mean of $\sigma^{*2}_{\mathrm{P,s}}$ obtained with Gaussian process regression is approximately half as large. The fraction of measurements that lie outside of the 95% confidence interval, however, is almost the same for all cases.

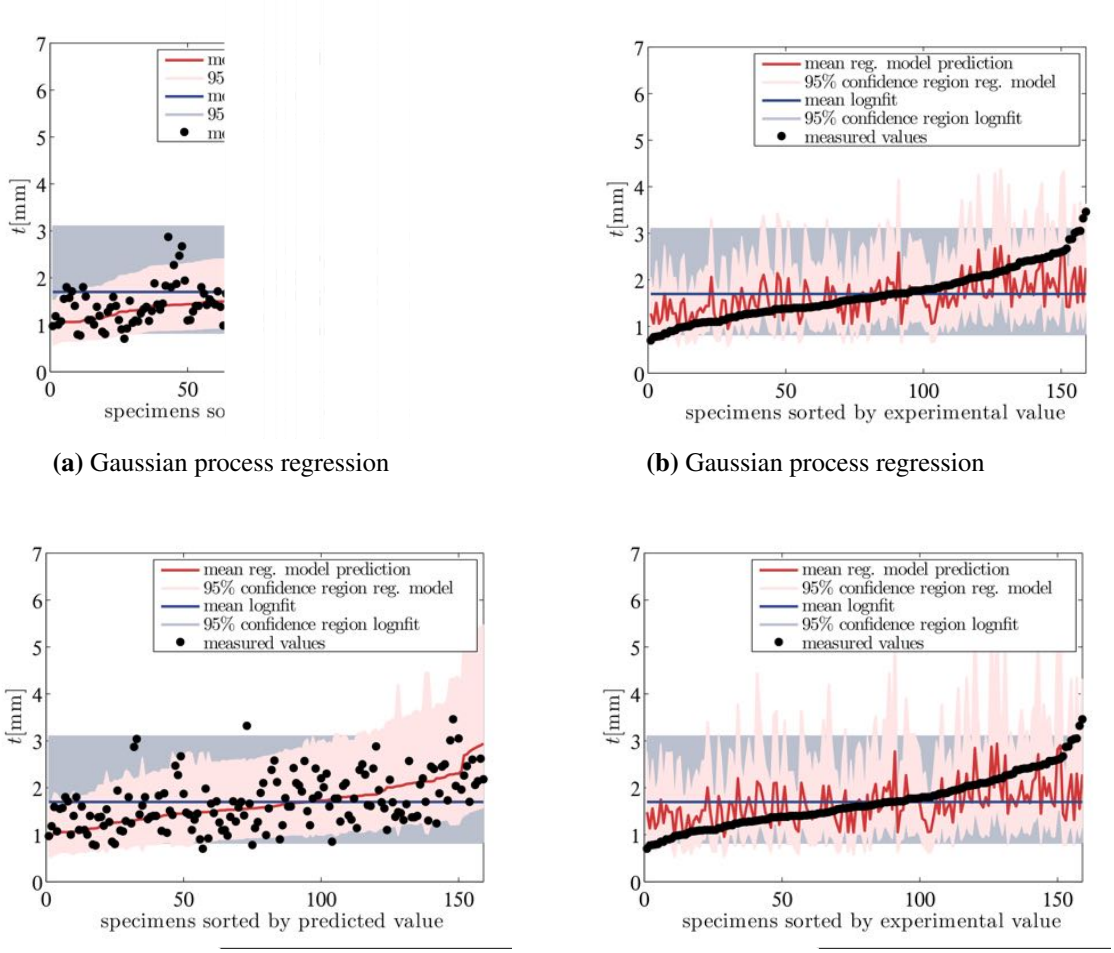

(a) Gaussian process regression

(b) Gaussian process regression

(c) Linear regression

(d) Linear regression

Figure 6.4 Model predicted vs. measured wall thickness. Top row: Gaussian process regression. Bottom row: linear regression. Taken from Biehler et al. [33].

6.3.3.2 Stiffness parameter α

As a result of the used feature selection procedure the following features were taken into account in the regression models: *age, ruptured, subrenal diameter, hypertension, smoking status, CHD, erythrocytes, hsCRP, sodium, urea,* and *MCV*. Although experimental results show spatial variations of α within the same aneurysm, the features listed above indicate that these intra-patient variations are random in the sense that they are not interrelated to one of the available spatially varying explanatory parameters.

Figure 6.5 shows the predicted and measured values for α-stiffness for both regression techniques. Again, the two sortings are provided to enable a quick visual comparison. Leaving very high values of α aside, the predictions capture the trend in the data well. A summary of the computed error measures is shown in Table 6.6. Based on mean value as well as on predictive variance, both regression techniques offer better predictive capabilities than the constant prediction model. Thereby, the Gaussian process approach performs better than linear regression. Using Gaussian process regression, the median of the PSMSE is 0.461 and the mean of $\sigma^{*2}_{\mathrm{P,s}}$ is 0.688. An improvement, considering that the respective values for the constant prediction model are 0.492 and 1, respectively.

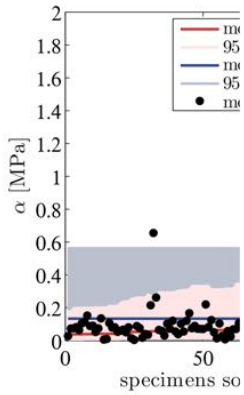

(a) Gaussian process regression

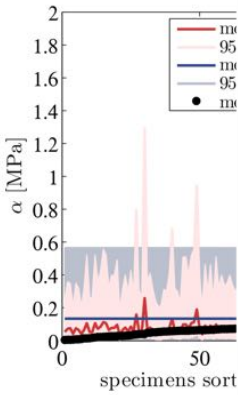

(b) Gaussian process regression

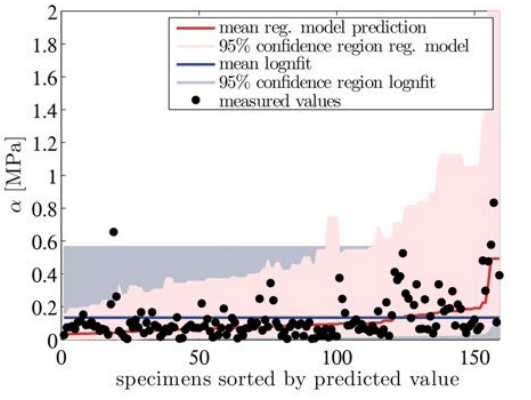

(c) Linear regression

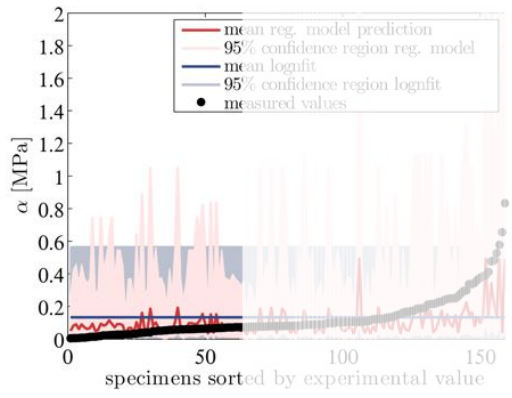

(d) Linear regression

Figure 6.5 Model predicted vs. measured α-stiffness. Top row: Gaussian process regression. Bottom row: linear regression. Taken from Biehler et al. [33].

reg. model	$\mathbb{E}[\text{PSMSE}]$	$\mathbb{MD}[\text{PSMSE}]$	$\mathbb{E}[\sigma^{*2}_{\text{P,s}}]$	in conf. reg.	RMSE [MPa]
lognfit	1.060	0.492	1.000	0.937	0.137
lin	0.914	0.549	0.810	0.937	0.111
gp	0.779	0.461	0.688	0.937	0.107

Table 6.6 Comparison of regression models for α-stiffness. Reproduced from Biehler et al. [33].

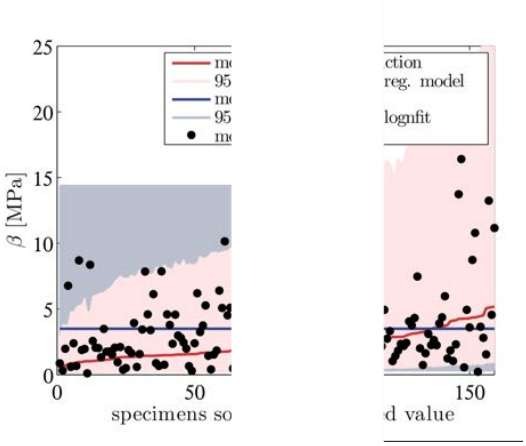

(a) Gaussian process regression

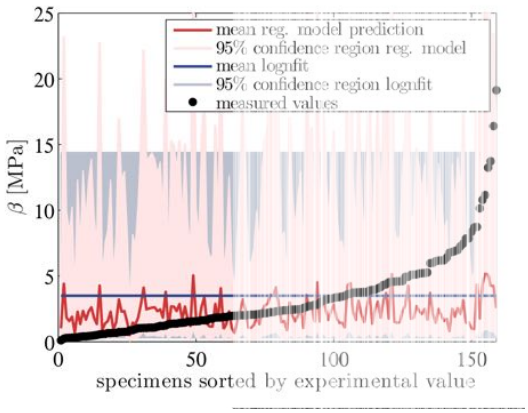

(b) Gaussian process regression

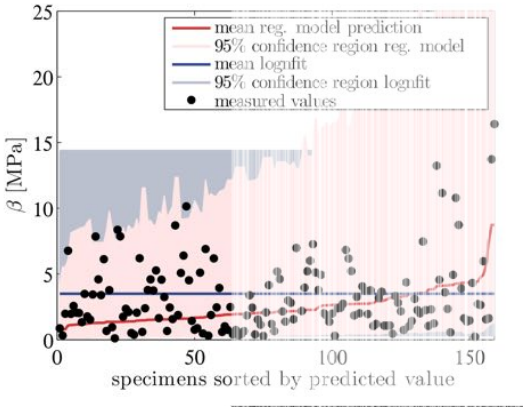

(c) Linear regression

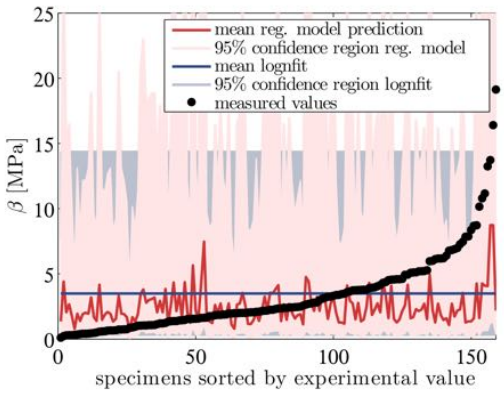

(d) Linear regression

Figure 6.6 Model predicted vs. measured β-stiffness. Top row: Gaussian process regression. Bottom row: linear regression. Taken from Biehler et al. [33].

6.3.3.3 Stiffness parameter β

Based on the feature selection approach the following features were included in the regression models: *age, ruptured, smoking status, CHD, PVD, erythrocytes, thrombocytes, urea, MCH, MCV,* and *relative thrombus thickness*. In contrast to α-stiffness, the predictions for β-stiffness depend on the *relative thrombus thickness* and thus show spatial variations across the geometry of the aneurysm. However, while the predictions for β using regression still offer some improvement in terms of error and predictive variance, the improvement is small and the error between predicted and measured β remains relatively large. As can be seen in Figure 6.6b and 6.6d both regression techniques fail in following the trend of the measured curve, indicating that the information in the explanatory variables is not sufficient to make accurate predictions.

reg. model	$\mathbb{E}[\text{PSMSE}]$	$\mathbb{MD}[\text{PSMSE}]$	$\mathbb{E}[\sigma^{*2}_{\text{P,s}}]$	in conf. reg.	RMSE [MPa]
lognfit	0.984	0.757	1.000	0.925	3.25
lin	0.934	0.710	0.983	0.931	3.07
gp	0.882	0.568	0.835	0.899	3.11

Table 6.7 Comparison of regression models for β-stiffness. Reproduced from Biehler et al. [33].

6.3.3.4 Failure tension

For the assessment of the failure tension the following features are considered: *ruptured, subrenal diameter, CHD, erythrocytes, leukocytes*, and *potassium*. Hence, the obtained regression models will predict a spatially constant tension because the explanatory variables included in the regression analysis do not depend on location.

A summary of the results and corresponding error measures is given in Figure 6.7 and Table 6.8. The mean of the PSMSE is smaller in the Gaussian process case; 0.920 compared to 1.030 for the constant prediction model. Again, linear regression performs not as well by a small margin. The predictive capability is also reflected by the increasing trend in the predictions in Figure 6.7b and Figure 6.7d. The biggest improvement, however, is achieved for the predictive variance, which is reduced to 0.722 in case of Gaussian process regression.

reg. model	$\mathbb{E}[\text{PSMSE}]$	$\mathbb{MD}[\text{PSMSE}]$	$\mathbb{E}[\sigma^{*2}_{\text{P,s}}]$	in conf. reg.	RMSE [N/mm]
lognfit	1.030	0.591	1.000	0.932	0.494
lin	0.956	0.621	0.804	0.947	0.448
gp	0.920	0.679	0.722	0.931	0.450

Table 6.8 Comparison of regression models for failure tension. Reproduced from Biehler et al. [33].

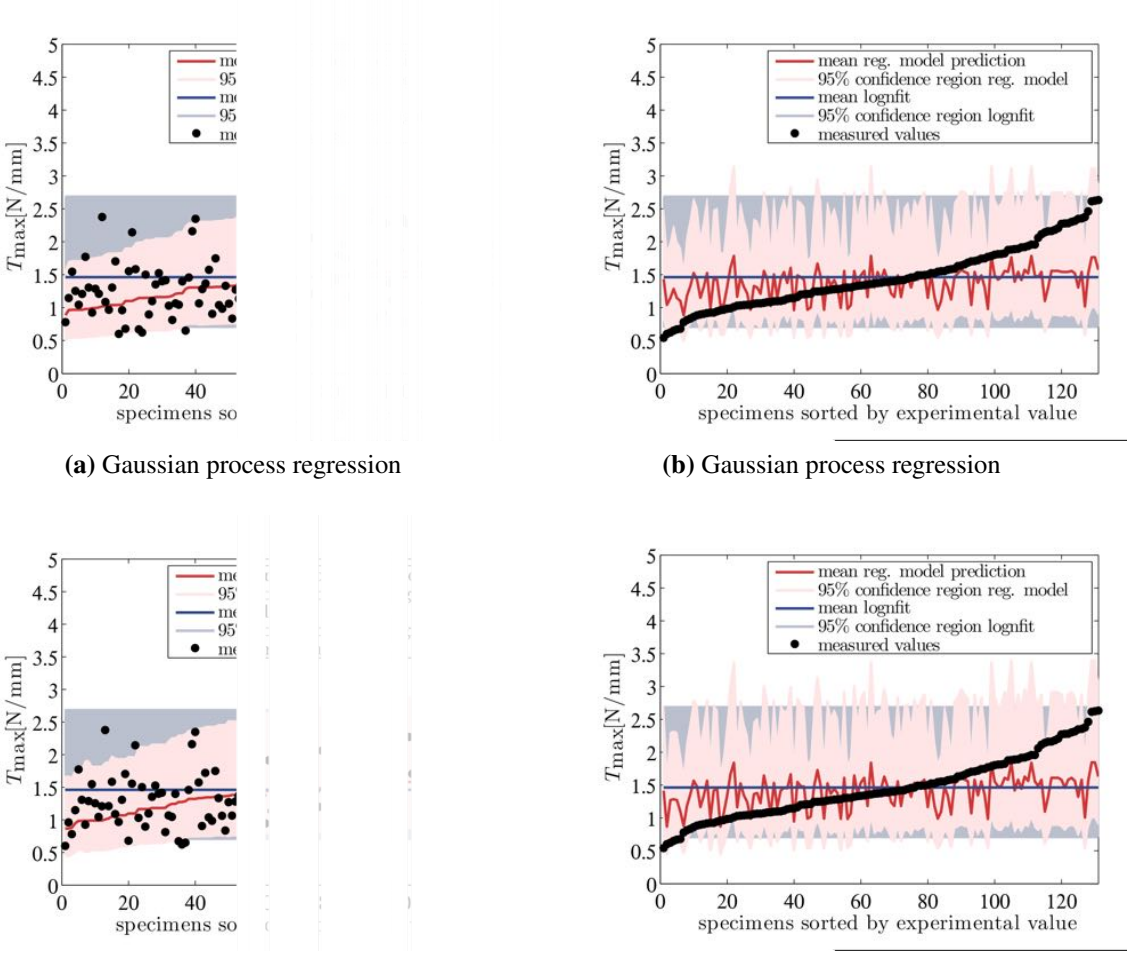

(a) Gaussian process regression

(b) Gaussian process regression

(c) Linear regression

(d) Linear regression

Figure 6.7 Model predicted vs. measured failure tension. Top row: Gaussian process regression. Bottom row: linear regression.Taken from Biehler et al. [33].

6.3.3.5 Strength

Based on the described feature selection approach the following parameters were considered in regression analysis to predict the strength of the AAA wall: *age, CKD, hypertension, erythrocytes, potassium, MCH, thrombus thickness*, and *NORD*. Note that *thrombus thickness* and *NORD* vary across the geometry of the aneurysm and hence spatially varying strength estimates are obtained with the regression models. In case of estimating wall strength, both regression models offer a significant improvement in accuracy compared to the constant prediction model, cf. Table 6.9 and Figure 6.8, respectively. Mean and median of the PSMSE are significantly reduced when using a regression technique to predict wall strength. Furthermore, the uncertainty in the predictions is reduced, as indicated by an average $\sigma^{*2}_{P,s}$ of 0.663 in the Gaussian process case. As in all other considered cases Gaussian process regression is superior to linear regression.

reg. model	$\mathbb{E}[\text{PSMSE}]$	$\mathbb{MD}[\text{PSMSE}]$	$\mathbb{E}[\sigma^{*2}_{\text{P,s}}]$	in conf. reg.	RMSE
lognfit	1.030	0.593	1.000	0.897	0.492
lin	0.905	0.418	0.825	0.916	0.464
gp	0.799	0.371	0.663	0.893	0.424

Table 6.9 Comparison of regression models for strength. Reproduced from Biehler et al. [33].

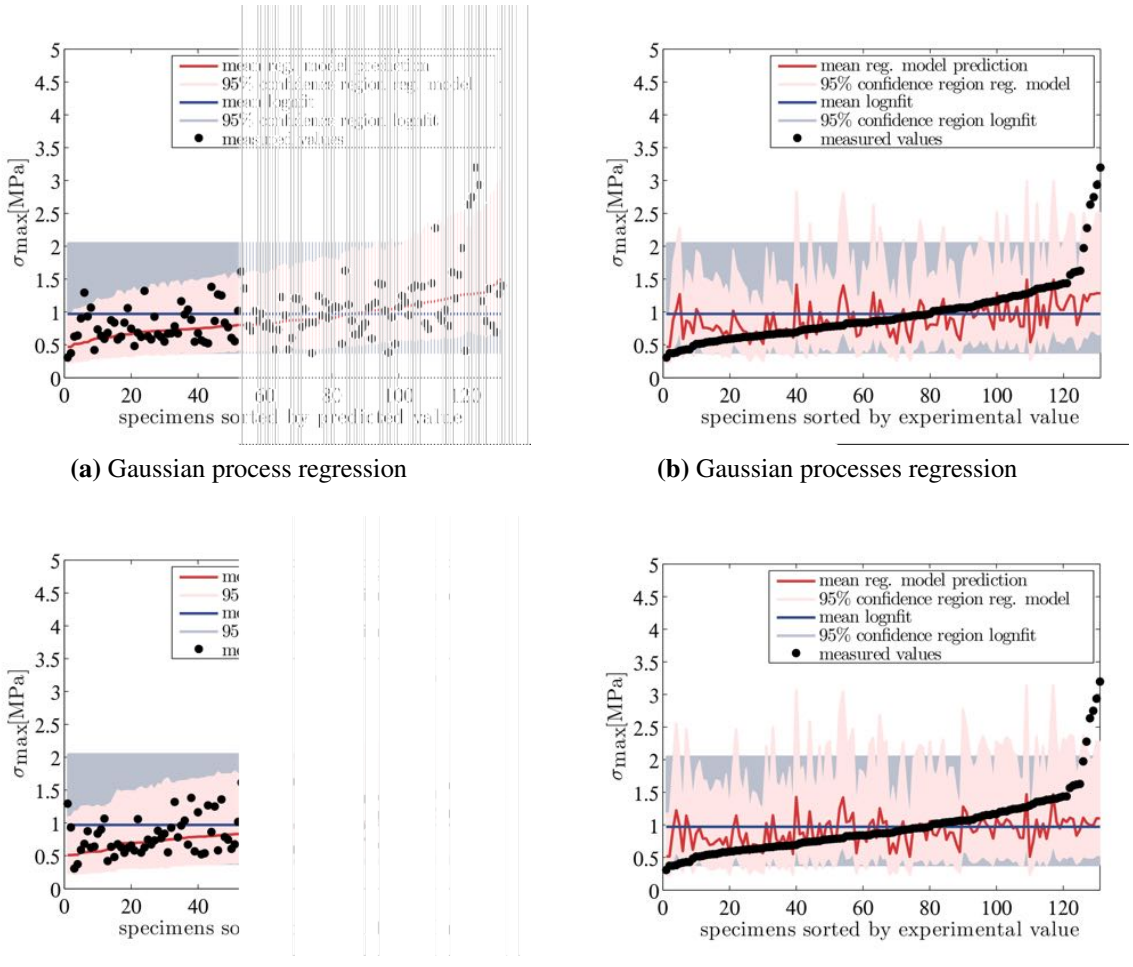

(a) Gaussian process regression

(b) Gaussian processes regression

(c) Linear regression

(d) Linear regression

Figure 6.8 Model predicted vs. measured strength. Top row: Gaussian process regression. Bottom row: linear regression. Taken from Biehler et al. [33].

6.3.3.6 Comparison to literature

Vande Geest et al. [340] used linear regression to predict the strength of aneurysmatic arterial wall based on their experimental results and patient database. They reported an estimate for the weights $\hat{\boldsymbol{w}}$ of their linear model. Furthermore, all explanatory variables considered in their model are also available for the study population considered here. Hence, their model, which is referred to as Vande Geest model from here on, can be used to predict the wall strength for the patient cohort and data studied in this work. The quality of the predictions made by the Vande Geest model is evaluated using experimental data from this study and the error measures defined above.

Since the full dataset that was used by Vande Geest et al. [340] is not available, only the mean of the predictive distribution can be computed. The comparison is thus limited to the PSMSE and RMSE. Of course, it would be interesting to try the predictive models developed in this work with the dataset that was used in [340] to enable a fair comparison. However, since the raw data is not available, such a comparison could not be performed.

According to the analysis in Vande Geest et al. [340] the following explanatory parameters are statistically linked to wall strength: *sex, thrombus thickness, NORD,* and *family history of AAA*. The last parameter is a binary variable providing information about previous incidence of AAA in at least one first degree family member of the patient. It is important to note that while this information is available for all our patients we chose not to include this parameter in the regression analysis because only one of our patients exhibits such a familial tendency. The two parameters *thrombus thickness* and *NORD* were found to be statistically linked to the wall strength in our regression analysis as well, indicating a potential relationship between those two parameters and the wall strength.

Table 6.10 shows the computed error statistics for predictions made by the Vande Geest model and the data set from the Institute of Computational Mechanics. For comparison the errors obtained with the trivial constant prediction model are repeated therein as well. The strength predictions obtained with the Vande Geest model for the patient database considered in this work are significantly worse than the predictions obtained with any of the other employed approaches. Even prediction based on mean value of the study population results in a more accurate estimate of the wall strength. The lack of an overall increasing trend for the predicted wall strength in Figure 6.9 also reveals the poor performance of the Vande Geest model on the dataset of the author's group.

reg. model	$\mathbb{E}[\text{PSMSE}]$	$\mathbb{MD}[\text{PSMSE}]$	$\mathbb{E}[\sigma^{*2}_{\text{P,s}}]$	in conf. reg.	RMSE [MPa]
lognfit	1.030	0.593	1.000	0.910	0.492
vdg	1.720	0.828	-	-	0.557

Table 6.10 Comparison of Vande Geest (vdg) model and lognfit model for the wall strength. Reproduced from Biehler et al. [33].

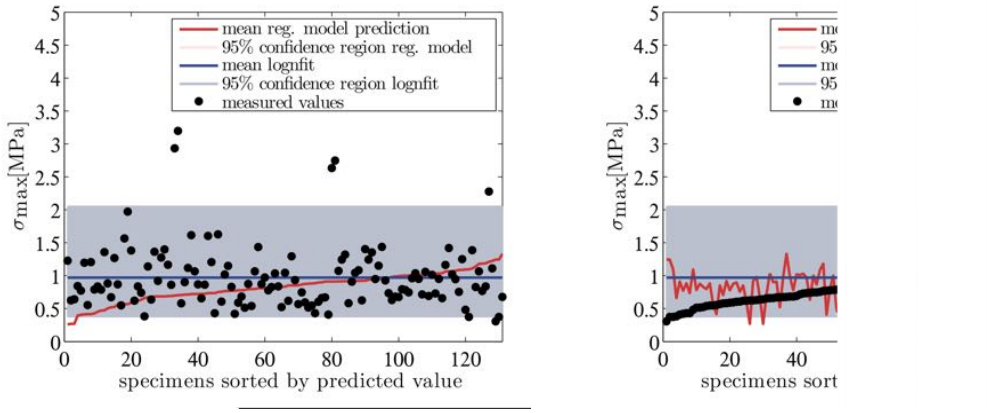

(a) Vande Geest model **(b)** Vande Geest model

Figure 6.9 Model predicted vs. measured strength using the model proposed by Vande Geest et al. [340]. Taken from Biehler et al. [33].

6.4 Estimating spatial correlation

So far the estimation of probability distributions for several wall parameters using different methods has been the focus of this chapter. These probability distribution can serve as estimate for the first-order probability distribution of a random field model of these quantities. Because these distributions originate from the predictive distribution of regression models which also take into account spatially varying quantities, the estimated probability distribution implicitly depends on the spatial location on the AAA surface through the local ILT thickness or the distance to the bifurcation. However, since a constant variance of the Gaussian error term is assumed, the variance on the log scale is constant and only the mean of the predictive distribution depends on the spatial location.

A random field model for these quantities requires specification of the spatial correlation structure. A data-driven estimate for the correlation length is missing thus far. Based on the assumption that the uncertain parameters vary smoothly in space, a squared exponential covariance function is deemed adequate throughout this work. In order to obtain an estimate of the correlation length, it is assumed that the spatial distribution of the logarithm of the relevant wall quantities are realizations of a GP with squared exponential covariance structure and that furthermore, the parameters of this process are the same for all patients in the studied dataset. Upon these assumptions, an estimate for the correlation length based on the correlation coefficient of measurements from adjacent test specimens from the same tissue sample can be obtained.

The following paragraphs describe the procedure used to obtain an estimate of the correlation length for α, β, and the wall thickness t, based on the dataset described in the previous section. In contrast to the regression models only data obtained by direct thickness measurements or tensile testing is needed. Missing non-invasively assessable parameters are no longer an issue and hence experimental data from all 80 patients, i.e.,132 tissue samples and 218 test specimens, comprise the initial dataset used in this case. Out of the 132 samples, 49 were large enough to supply more than one specimen, resulting in 135 specimens from 41 patients for which at

least one other specimen from the same sample was available. Measurements from all those specimens were sorted into a two row matrix such that each column contained measurements from two adjacent specimens. Subsequently, the correlation coefficient between the rows of the matrix was computed to obtain an estimate for the correlation coefficient of log α, log β, and log t between adjacent tissue specimens.

Assuming the same isotropic squared exponential auto-covariance function for all patients, the correlation length, being the only parameter, can be computed if the value of auto-covariance function can be estimated for a particular distance between points as explained in the following.

The functional form of the squared exponential auto-covariance is given in (3.60) and repeated here to facilitate the ensuing discussion

$$k(\boldsymbol{x}, \boldsymbol{x}') = \sigma_{\mathsf{G}}^2 \exp\big(-\frac{\|\boldsymbol{x} - \boldsymbol{x}'\|^2}{\ell^2}\big). \tag{6.8}$$

For a stationary field, the corresponding correlation coefficient function as defined in (3.53) becomes

$$\rho(\boldsymbol{\tau}) = \exp\big(-(\frac{\|\boldsymbol{\tau}\|}{\ell})^2\big), \tag{6.9}$$

where $\boldsymbol{\tau}$ is the lag vector, i.e., distance between two points $\boldsymbol{x}$ and $\boldsymbol{x}'$. Let $\tilde{\rho}$ be a known correlation coefficient corresponding to an arbitrary but fixed distance $\tilde{\boldsymbol{\tau}}$

$$\tilde{\rho} = \exp\big(-(\frac{\|\tilde{\boldsymbol{\tau}}\|}{\ell})^2\big), \tag{6.10}$$

then the correlation length of the process can be easily inferred. First taking the logarithm on both sides yields

$$\log(\tilde{\rho}) = -(\frac{\|\tilde{\boldsymbol{\tau}}\|}{\ell})^2. \tag{6.11}$$

Algebraic rearrangement results in the following expression for ℓ:

$$\ell = \frac{\|\tilde{\boldsymbol{\tau}}\|}{\sqrt{-\log(\tilde{\rho})}}. \tag{6.12}$$

Here, $\tilde{\rho}$ is the correlation coefficient computed based on all adjacent tissue specimens in the dataset, and $\tilde{\boldsymbol{\tau}}$ is an estimate for the distance between adjacent specimens. Based on the dimensions of the tensile test specimens with a length of 20-30 mm and a width of 8-10 mm, two estimates, 10 and 15 mm, for the average distance between two adjacent specimens were used to compute a correlation length according to (6.12). The resulting estimates for the different wall parameters are summarized in Table 6.11.

quantity	$\tilde{\tau}$ [mm]	ℓ [mm]
$\log \alpha$	10	13.66
$\log \alpha$	15	20.49
$\log \beta$	10	11.33
$\log \beta$	15	17.00
$\log t$	10	20.07
$\log t$	15	30.10

Table 6.11 Estimated correlation lengths for stochastic processes of different quantities.

It is important to stress that the estimates of the correlation length given in Table 6.11 are based on several simplifying assumptions and should be considered rough estimates rather than absolute values. However, often even less information about the correlation structure and its parameters is known due to lack of data, and investigations are often restricted to parameter studies or parameter estimates based on educated guesses [58].

If more measurements from individual patients spread across the AAA were available, correlation length estimates could be determined by performing GP regression or interpolation solely with spatial location as "explanatory variable". A procedure frequently used in geostatistics to estimate soil properties based on several measurements at a set of locations, see, e.g., [316] for a more detailed discussion. Alas, in case of estimating AAA wall properties the available data is too sparse to apply this procedure and one has to resort to estimation based on the correlation coefficient between adjacent specimens to obtain an estimate for the correlation length.

6.5 Discussion and conclusions

The obtained results demonstrate that information encoded in non-invasively available data can be exploited by regression models to achieve a more accurate prediction of patient-specific parameters such as constitutive parameters, thickness, failure tension, and strength. Moreover, by employing the proposed regression models, the predictive uncertainty in these parameters can be reduced. Linear and Gaussian process regression were used and the results of both methodologies were compared to the simplest model, which makes predictions based on the mean value and the variance of the data. The results show that both regression approaches are able to predict the respective quantities of interest more accurately, especially in case of wall thickness, α-stiffness, and strength. Thereby, Gaussian process regression consistently outperformed the simple linear regression approach, indicating that a simple linear model is not flexible enough to represent the data.

Although predictions based on the mean value of the respective predictive distribution are more accurate than the prediction based on the population mean, it is crucial to reemphasize the importance of the probabilistic interpretation of the regression analysis at this point. The variance of the error in (6.5) cannot just be ascribed to measurement error, but has to be considered as margin of uncertainty, which originates from the influence of other unknown parameters or random fluctuations in the quantity of interest. Regression can provide a probability distribution for the quantity of interest, e.g., the wall thickness from which a confidence interval can be com-

puted. According to the obtained results this interval most likely contains the true value of the thickness. It was found that the confidence intervals obtained with Gaussian process regression are in general tighter than the ones obtained with the other prediction approaches. The benefit of using Gaussian process regression is thus not only a more accurate point estimate for the respective quantity of interest, but, more importantly, also a reduction in predictive uncertainty. The improvement in predictive accuracy offered by regression models depends on the quantity that one wishes to predict. For the constitutive parameter β and the failure tension the improvement is not as significant as for the other parameters.

The spatial correlation of quantities measured at different locations was estimated using measurements from adjacent tissue specimens. In combination with the obtained predictive distributions, random field models for the studied wall parameters can be specified. Resulting in data-driven, patient-specific, stochastic models for several mechanical wall parameters, which can be used in computational UQ studies with patient-specific AAA models.

It is important to note that although the uncertainty in some of the patient-specific parameters can be reduced using elaborate regression techniques in combination with other non-invasively accessible, patient-specific parameters, the remaining uncertainty is not negligible. In the opinion of the author, a meaningful computational assessment of AAA rupture risk based on mechanical failure criteria such as peak wall stress is only possible if these uncertainties are considered in the computational model and thorough UQ is performed.

The probabilistic output of the regression model is considered the starting point for a probabilistic description of the input parameters, e.g, the wall thickness in a finite element model. Reduced uncertainty in model input parameters will translate to tighter confidence intervals in computed model output. Hence, mechanical quantities which are related to AAA rupture risk, such as peak wall stress, can be predicted with less uncertainty. In the following chapter patient-specific finite element models of AAAs with uncertainty in the input parameters are investigated. Different stochastic models are examined and the influence of several parameters, e.g., correlation length on the computed results is studied. Moreover, several stochastic thickness models based on the findings in this chapter are compared

The study by Vande Geest et al. [340] provides the only other published statistical model for the strength of the AAA wall. Their model was applied to the dataset of the Institute of Computational Mechanics and used to obtain wall strength predictions which were then compared to wall strength measurements. Overall, the predictive capability of the Vande Geest model could not be replicated with the database used in this work. This can have several reasons, such as differing experimental setup, slightly different methods to determine *NORD* and *thrombus thickness*, and the relatively small number of tissue samples used to set up the regression model. For further improvement of these kinds of statistical models a large database would be a plus, and likely produce more accurate and reliable predictions.

As in the study conducted by Vande Geest et al. [340], the tissue samples that were used in this study have been excised during open surgical repair. Hence, most of the samples originate from the anterior region of the aneurysm. A limitation that has to be kept in mind.

7 The impact of uncertainties in computational models of AAAs

In the context of computational cardiovascular modeling the problem of missing or uncertain patient-specific model input parameters is generally recognized. Nevertheless, very few researchers have addressed this problem by applying uncertainty quantification methods to investigate the impact of uncertain input parameters on the quantities of interest in computational models of the cardiovascular system or components thereof. In addition, existing research regarding UQ in cardiovascular mechanics is limited to either idealized geometries or uncertainties modeled as independent random variables as opposed to correlated random fields.

So far the study of uncertain parameters in reduced dimensional models of arteries and arterial networks has attracted the most attention amongst researchers [61, 96, 136, 157, 158, 192, 367]. Osnes and Sundnes [244] investigated the influence of uncertain material properties in a simplified generic heart model, while uncertainty in blood viscosity and its impact on, e.g., wall shear stress in an idealized portal vein model was investigated by Pereira et al. [252]. Regarding AAA, Sankaran and Marsden [289] investigated idealized geometries of AAAs considering parametric uncertainties such as the radius, and [253] examined patient-specific AAA geometries with a random variable model for the wall thickness.

To the knowledge of the author, the study by Biehler et al. [32] was the first to perform UQ in combination with 3D nonlinear patient-specific finite element models of AAAs and is also the only one considering spatially correlated random quantities. Based in parts on the work presented in [32], the BMFMC approach is applied here to large-scale, nonlinear, patient-specific models of AAAs. Thereby, uncertainties in constitutive parameters as well as the wall thickness are considered and the impact of these uncertainties on mechanical quantities usually related to AAA rupture potential, such as von Mises stress, strain or strain energy density is studied. To this end data-driven probabilistic models based on the findings presented in the previous chapter are employed. In particular for the wall thickness several different probabilistic models are compared. To capture intra- as well is inter-patient variations these quantities are modeled as random fields, a comparison to a simpler random variable model is provided for the wall thickness as well. The use of random field models for uncertain model input parameters leads to systems with very high stochastic dimension, rendering surrogate based UQ techniques inapplicable. It is shown that the BMFMC approach is able to reproduce the MC reference solution at a fraction of the computational costs and delivers accurate results even if strongly simplified low-fidelity models are used. Thereby, the computational costs of UQ can be reduced to an acceptable level even for large-scale, nonlinear, and complex biomechanical problems with uncertainties modeled as random fields.

Thus, the purpose of this Chapter is twofold. On the one hand, the efficiency and accuracy of the novel BMFMC approach is shown for large-scale nonlinear models. On the other hand, in addition to the methodological aspects presented in this chapter, the uncertainties in the simu-

lation results of patient-specific AAA models are quantified, and the possible ramifications for patient-specific computational assessment of AAA rupture potential are discussed. Although patient-specific models of AAA are considered here, it is stressed that the approach is very general and can be applied to a wide range of problems and is by no means limited to this particular application. For instance, the use of the BMFMC approach for UQ in reduced dimensional models of the human respiratory system is shown in Chapter 8.

The outline of the present chapter is as follows. First, a brief description of the process used to generate and setup patient-specific AAA finite element models is given in Section 7.1. The proposed BMFMC approach is applied to several large-scale, nonlinear, patient-specific finite element models of AAAs. First models with an uncertain constitutive parameter are considered in Section 7.2, then the impact of an uncertain wall thickness is studied in Section 7.3. A demonstration that the proposed approach can also handle models with multiple sources of uncertainties is given in Section 7.4. Based on the obtained results, the implications regarding computational rupture risk assessment of AAAs are discussed in Section 7.5.1, followed by some remarks on methodological aspects in Section 7.5.2.

7.1 From imaging to simulation

Based on CT image data, AAA finite element models with patient-specific geometries are created using an existing workflow which has been previously described in detail by Maier et al. [203] and Reeps et al. [273]. Briefly, the first step of the process entails segmentation of the blood lumen and, if present, ILT in the CT images to generate a 3D reconstruction of the geometry of the aneurysm. Using these reconstructions, a finite element mesh is generated using either Harpoon (Sharc Ltd, Manchester, UK) or CUBIT (Sandia National Laboratories, Albuquerque, NM, USA). Since the arterial wall thickness cannot be clearly identified in the images due to resolution limitations, a spatially constant wall thickness is initially extruded from the *abluminal* surface of the ILT.

Simple clamped boundary conditions are used at the inlet and the outlets of the aneurysms. To mimic the load exerted by the blood pressure an orthogonal pressure follower load is imposed on the luminal surface of the ILT. If no ILT is present, pressure is applied on the luminal surface of the vessel wall. The shear stresses induced by the blood flow are negligible compared to the pressure load and a full fluid-structure-interaction simulation is not required.

Since the geometries of the aneurysms are obtained from *in vivo* CT images, the imaged configuration is not stress free but represents a loaded spatial configuration. In order to obtain meaningful results this prestressed state has to be accounted for. To imprint the stresses from an assumed diastolic pressure of 87 mmHg in the *in vivo* imaged state, the MULF scheme described in Section 2.2.2 is used. The obtained prestressed state implicitly defines a stress free reference geometry, while neglecting growth and remodeling processes in the wall. This implicitly defined geometry of course depends on the properties of the arterial wall and the ILT. Hence, if some of the wall properties are considered random, this geometry depends on the particular realization of the random quantities. After the prestressing phase the *luminal* pressure is increased to a systolic pressure of 121 mmHg, thereby taking into account the imprinted stresses and strains acting on the imaged configuration. Throughout this work the blood pressure is considered to be known and any uncertainties regarding patient specific blood pressure are neglected. In future

work, the model could be refined by using patient-specific measured blood pressure values. In addition, fluctuations in blood pressure could be considered in an uncertainty analysis as well.

Lastly, constitutive properties have to be assigned to the ILT and the arterial wall. The ILT forms through the coagulation of blood and is present in the vast majority of aneurysms [137, 143]. In literature it is predominantly described as heterogenous, isotropic hyper-elastic material. It was found that the stiffness of ILT varies regionally with respect to radial position [108, 242, 329, 339, 353]; however, ventral to dorsal regional variations have been reported as well [56]. If modeled as hyper-elastic continuum, a two-fold stress shielding effect can be ascribed to the ILT. Because its presence results in a reduced lumen with a smaller radius, the resulting load exerted by the intraluminal pressure is smaller as compared to an aneurysm with the same shape but without ILT. Secondly, it has a load bearing capacity which further reduces the load on the wall. Several constitutive laws have been proposed to model ILT behaviour, see [202] for a comparison. In this work the constitutive model proposed by Gasser et al. [108] was chosen, which written in invariants and modified to slight compressibility reads

$$\Psi(\bar{I}_1, \bar{I}_2, J) = c(\bar{I}_1{}^2 - 2\bar{I}_2 - 3) + \frac{\kappa}{\eta^2}(\eta \ln J + J^{-\eta} - 1). \tag{7.1}$$

Although the constitutive parameters of the ILT are afflicted with uncertainty and usually not exactly known in clinical practice, deterministic but spatially varying constitutive parameters are used in the AAA models considered in this work. Gasser et al. [108] distinguishes three layers of ILT for which the material parameter c is reported. Here the value of the material parameter c is continuously interpolated from the luminal to the abluminal surface of the thrombus as described by Maier [202], using the values reported in [108] for luminal ($c_{\text{lum}} = 2.62$ kPa), medial ($c_{\text{med}} = 1.98$ kPa), and abluminal ($c_{\text{ablum}} = 1.73$ kPa) layer. The values for the parameters $\kappa = 8\frac{c}{1-2\nu}$, $\nu = 0.48$, and $\eta = -2$ were also chosen according to Maier [202].

Constitutive models for AAA wall have been previously discussed in Section 6.1.2 and the SEF given in (6.2), which is repeated here for convenience, is used throughout this work as constitutive model for aneurysmatic arterial wall

$$\Psi(I_1, J) = \alpha(\bar{I}_1 - 3) + \beta(\bar{I}_1 - 3)^2 + \frac{\kappa}{\eta^2}(\eta \ln J + J^{-\eta} - 1). \tag{7.2}$$

For this material a bulk modulus $\kappa = \frac{2\alpha}{1-2\nu}$ with $\nu = 0.49$ was used throughout this work and $\eta = -2$. While the material parameters of ILT are also afflicted with considerable uncertainties, the restriction to uncertain wall parameters is made in this work for ease of exposition. Future research will likely encompass uncertain ILT parameters as well.

After the reconstruction of the AAA geometry, generation of a finite element mesh and definition of boundary conditions as well as constitutive properties, all necessary components for the deterministic boundary value problem described in Section 2.1.4 are defined.

7.2 AAA models with uncertain constitutive parameters

As demonstration of the capabilities of the BMFMC approach, UQ is performed using two realistic AAA models with patient-specific geometries from the database of the Institute of Computational Mechanics. These AAA models serve as showcase examples for large-scale

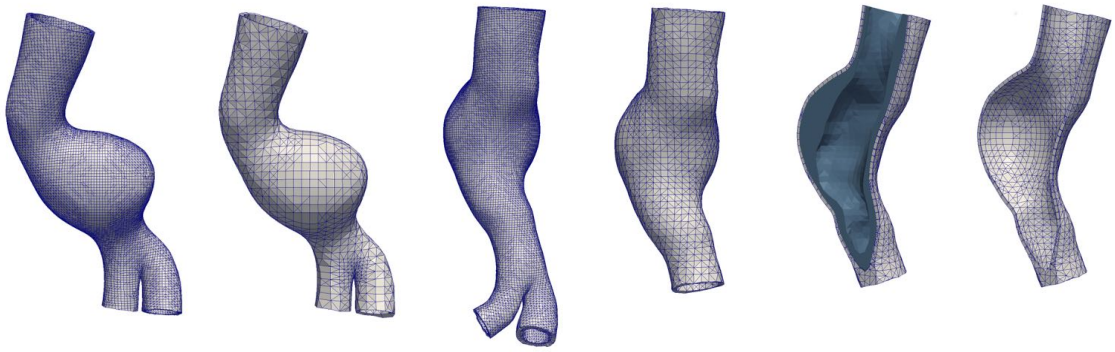

Figure 7.1 High-fidelity and corresponding low-fidelity AAA finite element models based on patient-specific geometries. (a) Male67 high-fidelity model. (b) Male67 low-fidelity model. (c) Male71 high-fidelity model. (d) Male71 low-fidelity model. (e) Cross-sectional view of male71 low-fidelity model with ILT. (f) Cross-sectional view of male71 low-fidelity model without ILT. Reproduced from [32].

nonlinear solid mechanics problems with uncertain constitutive properties. The properties of the two models, which are referred to as male67 and male71 in the following, are described in the next section, along with the generation of suitable low-fidelity versions of these models. In order to obtain a reference solution for comparison to the proposed BMFMC approach, direct MC is performed with all high-fidelity finite element models with a sample size of $N_{\mathrm{SAM}} = 50000$.

7.2.1 Patient-specific finite element models

As described above, the geometry of the lumen and, if present, the ILT were reconstructed from CT data. The model male71 exhibits ILT while male67 does not. The wall thickness is considered to be deterministic and set to 1.57 mm, constant throughout the models. High-fidelity finite element models are generated with a mesh size of roughly 1mm. These hybrid finite element discretizations are shown in Figure 7.1a and 7.1c and consist of 15228 (male67) and 169791 (male71) linear hexahedra-, wedge- and tetrahedra-shaped elements. Resulting in a problem size of 61674 and 292044 degrees of freedom, respectively. For the aneurysm male67, a low-fidelity model, which is shown in Figure 7.1b, is constructed by coarsening the discretization. Using an element size of approximately 3 mm, the resulting coarser model has 2670 elements and 8679 degrees of freedom. For the aneurysm male71 two low-fidelity models were created. For the first low-fidelity model a coarser discretization and a truncated geometry was used as depicted in Figure 7.1d and 7.1e. This simplification results in a finite element model with 19579 elements and 25875 degrees of freedom. Secondly, to further reduce the computational effort, another approximate model was created using model reduction in the sense that the ILT was omitted entirely in addition to a coarser discretization and geometric truncation, see Figure 7.1d and 7.1f. Therein, the size reduces to 3164 elements and 10320 degrees of freedom. The reduction in model size and complexity yields a tremendous reduction in computational costs. For the aneurysms male67 and male71 coarsening of the discretization and model reduction yield a low-fidelity model that is between 10 and 50 times cheaper than the original high-fidelity model.

model	solution time (CPU seconds)	degrees of freedom
male67 high-fidelity	2000	61674
male67 low-fidelity	195	8679
male71 high-fidelity	10800	292044
male71 low-fidelity with ILT	400	25875
male71 low-fidelity without ILT	215	10320

Table 7.1 Size of studied AAA finite element models and computing times for the evaluation of the models. Reproduced from [32].

The CPU time required to compute one sample of the different models along with the numbers of degrees of freedom are summarized in Table 7.1. A 6 core Intel Xeon 3.2 GHz workstation with 12 GB memory was used to establish the solution times of the different models. The simulations were computed on one core, except the high-fidelity model of the male71 aneurysm, for the solution of which four cores were used.

7.2.2 Stochastic models for constitutive parameters

As discussed in Chapter 6 the material properties of AAAs are subject to large inter- and intra-patient variations in all of the material properties. Hence, a random field approach to formulate a stochastic material law for the aneurysmatic arterial wall is deemed more adequate than a random variable model. A homogenous, univariate, log-normal three-dimensional random field is used to describe the inter- and intra-patient variations of the constitutive parameter β of the constitutive law for the AAA wall given in (7.2). The parameter β was chosen because it was found that β exhibits a larger variance as well as a greater variation between individual patients as compared to α. Hence, as a first step towards a fully probabilistic constitutive framework, the parameter β was chosen to be modeled as a random field and the remaining constitutive parameters are set to deterministic population averaged mean values.

Using a sampling based UQ approach requires the generation of realizations of the random field. Here the spectral representation method is used in combination with translation process theory to generate realizations of a log-normal three-dimensional random field. First, a realization of a Gaussian random field is created using (3.85), which is then mapped into a realization of a non-Gaussian field using (3.90) and the spectral matching procedure described in Section 3.3.4.

The spectral representation method requires two probabilistic characteristics of the random field the first-order probability distribution and the covariance function. Based on the consideration in Chapter 6 and on the reasonable assumption that the constitutive parameter β varies smoothly in space, a squared exponential covariance function was chosen for the underlying Gaussian process

$$k(\boldsymbol{\tau}) = \exp\Big[-\big(\frac{\|\boldsymbol{\tau}\|}{\ell}\big)^2\Big]. \tag{7.3}$$

In addition, a log-normal distribution is used as first-order probability distribution, i.e., $p(\beta) = \log\mathcal{N}(\mu_\beta, \sigma_\beta)$ with the parameters $\mu_\beta = 1.0857$ and $\sigma_\beta = 0.9205$. The remaining parameters of

the constitutive model are set to $\alpha = 0.059$ MPa and $\kappa = 5.9$ MPa, respectively. These values are parameter estimates obtained by fitting a log-normal distribution to experimentally obtained data as described in Chapter 6. However, because a preliminary dataset, which differs from the one used in Chapter 6 and contains fewer patients, was available at the time this particular work was done, the parameters μ_β, σ_β, and α are slightly different from the values reported in Chapter 6 in Table 6.4. The simulations which are discussed in the following could, of course, be repeated with the updated values. However, in the opinion of the author the fundamental conclusions drawn from the results will remain the same and the enormous computational costs associated with repeating the MC simulation to obtain another reference solution cannot be justified.

To study the sensitivity with respect to the unknown correlation length ℓ in (7.3), three random field models with different correlation lengths $\ell = 12.5$ mm, $\ell = 25$ mm and $\ell = 50$ mm are investigated. The chosen range covers random fields which exhibit rather short scale fluctuations as well as highly correlated random fields with a correlation length in the range of the diameter of a typical aneurysm. Moreover, the chosen values cover the range that was estimated based on experimental data in Section 6.4.

With the non-Gaussian random field defined above, the constitutive law for the aneurysmatic arterial wall is extended to incorporate the uncertainty in the parameter $\beta = \beta(\boldsymbol{x}, \mathbf{z})$. The constitutive parameter is a function of spatial location $\boldsymbol{x}$ and the realizations of the random phase angles $\boldsymbol{z}^{(\mathrm{j})}$. Once a sample of random phase angles is drawn, a realization of the three dimensional random field is computed and the constitutive parameter $\beta(\boldsymbol{x}, \boldsymbol{z}^{(\mathrm{j})})$ can be evaluated at the midpoint of each element in the AAA wall. This value is then assigned to the element as local constitutive parameter. Note that other possibilities to obtain an element based constitutive parameter exist. For instance, one could also compute some form of average based on evaluations at the nodes or the Gauss points of an element. However, for the considered examples the ratio between element size and correlation length is small enough to warrant the chosen approach. The full stochastic version of the strain-energy function, which now depends on the location $\boldsymbol{x}$ as well as on the vector of random phase angles $\mathbf{z}$ then reads

$$\Psi(\bar{I}_1, J, \boldsymbol{x}, \mathbf{z}) = \alpha(\bar{I}_1 - 3) + \beta(\boldsymbol{x}, \mathbf{z})(\bar{I}_1 - 3)^2 + \frac{\kappa}{\eta^2}(\eta \ln J + J^{-\eta} - 1). \tag{7.4}$$

7.2.3 Results

In this section the impact of the uncertain constitutive parameter β on the relevant mechanical quantities such as Cauchy von Mises stress (σ_{vM}), Euler-Almansi von Mises strain (e_{vM}), and strain energy Ψ is first discussed on the basis of MC reference simulations. Thereby, the influence of the correlation length on the distributions of these quantities is investigated. Subsequently, in Section 7.2.3.2 the results of the employed BMFMC approach are compared to the MC reference solution and the accuracy and efficiency of the multi-fidelity approach is examined.

7.2.3.1 Monte Carlo reference solution

As expected, in spite of drastic variations in the wall stiffness the overall spatial pattern of the von Mises stress is still largely determined by the geometry of the aneurysm and rather insen-

sitive to variations in β. Nevertheless, a slight dependency on the correlation length was found, where a smaller correlation length leads to greater variations in the overall stress pattern. Figure 7.2 shows the von Mises stress and strain resulting from five different showcase realizations of the stochastic constitutive law for the male71 aneurysm. The samples in Figure 7.2 were computed with a correlation length of $\ell = 12.5$ mm for which the resulting stress pattern exhibits the largest variations. However, the overall spatial pattern of the stress remains remarkably similar for all depicted realizations of the random field. Moreover, if the correlation length of the random field is increased, the variations in the spatial stress pattern become even less significant. This is in agreement with theoretical mechanical considerations, as the stress state in the aneurysm wall is dominated by in plane membrane stress, which is determined mostly by the overall geometry of the aneurysm and the traction boundary conditions.

In contrast to the spatial stress pattern the spatial strain pattern of the samples very significantly indicate a strong dependency between local stiffness of the wall and local strain. Unlike in the stress pattern, regions with high strain are not determined by the overall shape or the geometry of the aneurysm but rather by regions with low wall stiffness, as shown in Figure 7.2c. The male67 aneurysm shows similar behavior and is hence not shown here.

In addition to this qualitative assessment the empirical probability distributions of the stress obtained through MC were examined at several locations across the aneurysms, see Figure 7.3. The mechanical quantities of interest were evaluated at single elements at these specific locations. Figure 7.4 shows the empirical probability densities of the von Mises stress, von Mises strain, and strain-energy at two locations on the male67 aneurysm. Location 1, shown in Figure 7.3a, is located in the neck of the aneurysm above the sack. Location 2 is at the right lateral, distal end of the AAA sack, see Figure 7.3a. Both locations are in regions that exhibit high wall stress. For the other aneurysm male71, Figure 7.5 shows the probability densities evaluated at location 3, located at the center of the dorsal side of the aneurysm sack in the high stress region, and at location 4, located at the ventral side of the aneurysm sack in a low stress region with thick ILT underneath the AAA wall, see Figure 7.3b and 7.3c. All empirical densities are plotted for the different correlation lengths of the random field in the stochastic constitutive model. In addition to the mean and COV, the 95% quantiles are provided for each of the distributions in Figures 7.4 and 7.5.

The obtained distributions for the stresses confirm the qualitative assessment that the stresses are only mildly affected by the local stiffness of the wall. The COVs of the stress distributions are below 0.12. If only the locations 1, 2, and 3, which all lie in high stress regions of the respective AAAs, are considered, the maximum COV of the stress distribution is 0.07. In addition, these three elements show smaller COVs of the stress with increasing correlation length of the random field. In contrast to this, the COV of the stress at location 4, which lies in a region with thick ILT and low wall stress, is less influenced by the correlation length. The 95% quantile of the stress distributions, as a "worst case" estimate, is approximately 2%-19% higher than the respective mean value, see Figure 7.4a, 7.4b, 7.5a and 7.5b. This provides further evidence that uncertainties in the constitutive parameter β result in only moderate uncertainty in the computed stresses.

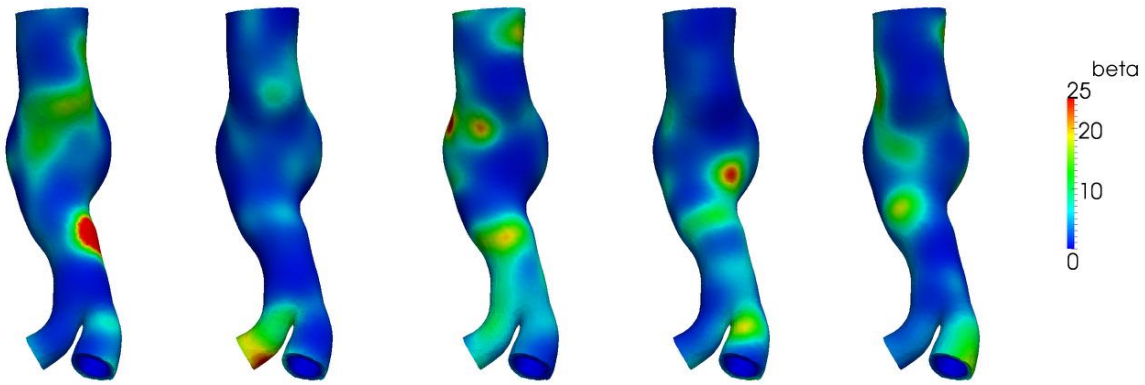

(a)

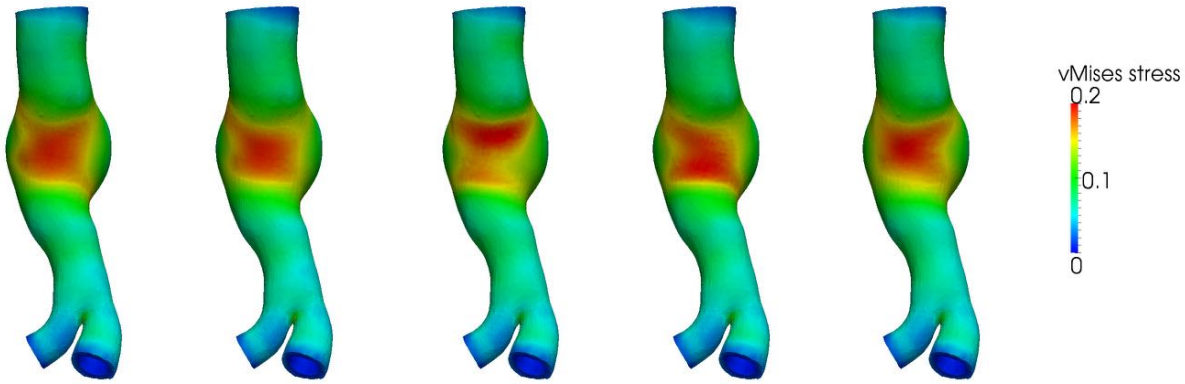

(b)

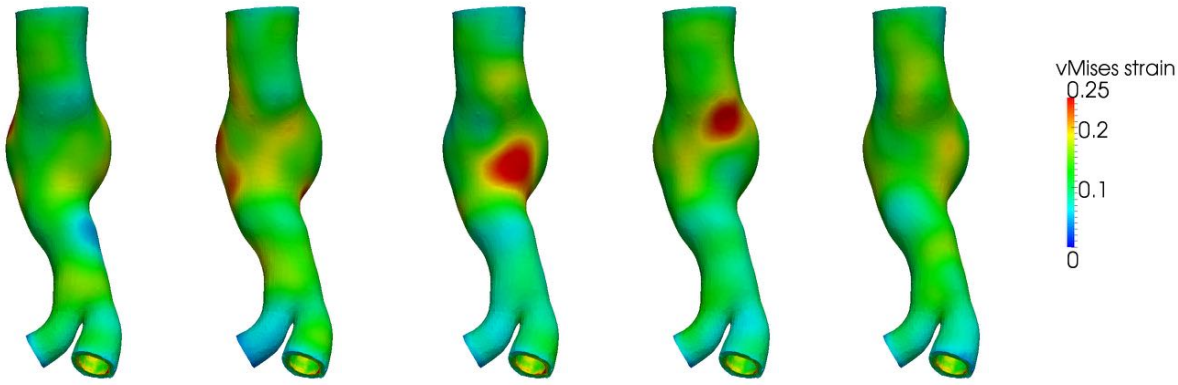

(c)

Figure 7.2 Simulation results of male71 aneurysm for five different realizations of the random field with a correlation length of $\ell = 12.5$ mm. Realizations of random field describing β [MPa] are shown in (a) and the resulting von Mises stresses [MPa] and von Mises strains are shown in (b) and (c), respectively. Taken from [32].

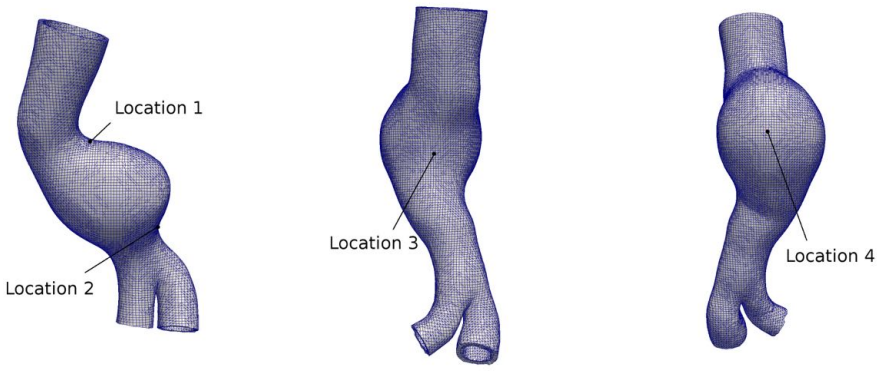

Figure 7.3 Locations within AAA wall at which mechanical quantities are evaluated. (a) Shows locations 1 and 2 in anterior view of male67 patient, while (b) shows location 3 in posterior view of the male71 patient. Location 4 is shown in (c) in anterior view of the male71 aneurysm. Taken from [32].

While this appears to be consistent with the findings from Raghavan and Vorp [266] it should be stressed that Raghavan and Vorp only considered mild parameter variations within the 95% confidence interval of their estimated mean value and not within the complete range of measured values. Furthermore, they did not consider spatial intra-patient variations of the constitutive parameters nor did they consider the prestressed state of the aneurysm or ILT. Findings that are similar to the ones discussed above have also been reported for intracranial aneurysms by Ma et al. [198] and Miller and Lu [216]. These two studies also indicate only a mild dependence of the wall stresses on the constitutive parameters, however, only spatially homogenous parameters were considered therein as well. The results show that the wall stresses are only mildly sensitive to variations in the constitutive parameter β. This holds especially for the rather long scale spatial heterogeneity obtained with the longer correlations lengths of the random field, see Figure 7.4a. The sensitivity of the stress state on the material properties typically increases as the random field exhibits strong spatial gradients in the parameter field as one moves to smaller correlation lengths indicating, that only strongly localized variations in this parameter have a significant effect on the stresses. This insensitivity, in spite of strongly localized variations in β, can be ascribed to the prestressed state of the imaged geometry. The prestress in the *in vivo* imaged configuration of cardiovascular structures has to be accounted for in order to obtain meaningful simulation results, as has been pointed out in numerous publications [111, 112, 216, 311]. All techniques to account for this essentially approximate a stress state that equilibrates with the external load given the spatial configuration. The boundary conditions in a typical cardiovascular problem resemble those termed statically determinate. Dominated by traction boundary conditions emulating luminal blood pressure, the Dirichlet boundary conditions applied far away from the region of interest have only minor influence. Thus, in prestressed cardiovascular structures which are predominantly loaded by traction boundary conditions the overall stress state, which is largely determined by the prestress, is governed by simple equilibrium of internal stress with the external loading and therefore is relatively insensitive to variations in the constitutive parameters.

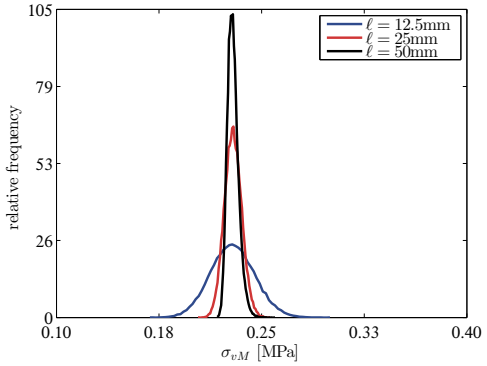

ℓ [mm]	Mean [MPa]	COV [-]	95% q. [MPa]
12.5	0.22885	0.069787	0.2555
25	0.2291	0.027649	0.23973
50	0.22913	0.018063	0.23656

(a) Von Mises stress at location 1

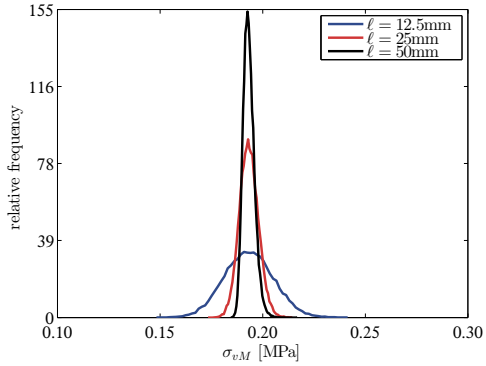

ℓ [mm]	Mean [MPa]	COV [-]	95% q. [MPa]
12.5	0.19323	0.06153	0.21291
25	0.19323	0.023991	0.20099
50	0.19323	0.014449	0.19819

(b) Von Mises stress at location 2

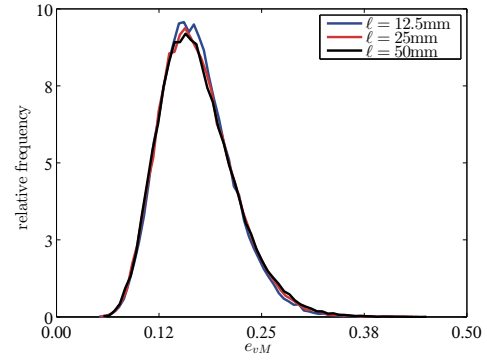

ℓ [mm]	Mean [MPa]	COV [-]	95% q. [MPa]
12.5	0.17012	0.25189	0.24732
25	0.17106	0.26318	0.25225
50	0.17156	0.26887	0.25561

(c) Von Mises strain at location 1

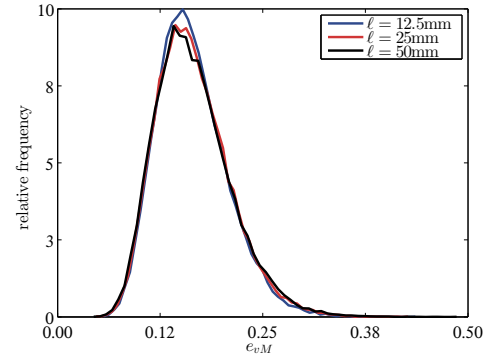

ℓ [mm]	Mean [MPa]	COV [-]	95% q. [MPa]
12.5	0.16386	0.26131	0.24127
25	0.16506	0.27175	0.24609
50	0.16522	0.27973	0.24961

(d) Von Mises strain at location 2

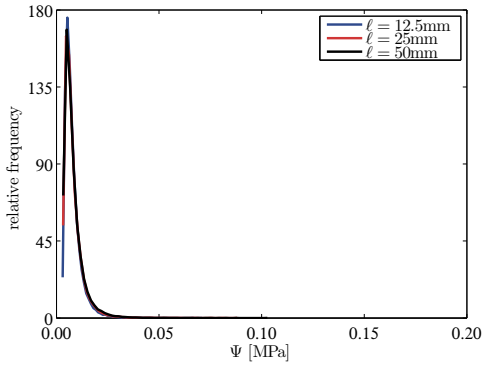

ℓ [mm]	Mean [MPa]	COV [-]	95% q. [MPa]
12.5	0.0077964	0.51794	0.015418
25	0.0079977	0.57488	0.016421
50	0.0081013	0.61197	0.017119

(e) Strain-energy at location 1

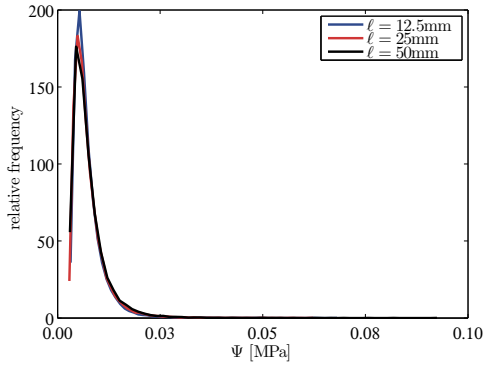

ℓ [mm]	Mean [MPa]	COV [-]	95% q. [MPa]
12.5	0.0072272	0.48373	0.013766
25	0.0073936	0.52661	0.014598
50	0.007467	0.56652	0.015236

(f) Strain-energy at location 2

Figure 7.4 MC reference solution for male67 aneurysm. Reproduced from [32].

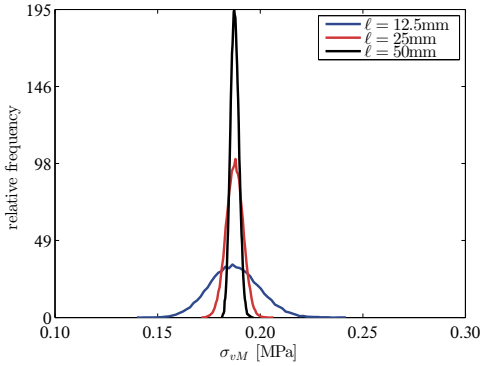

ℓ [mm]	Mean [MPa]	COV [-]	95% q. [MPa]
12.5	0.1873	0.064839	0.20773
25	0.18744	0.021768	0.1941
50	0.18757	0.01084	0.19102

(a) Von Mises stress at location 3

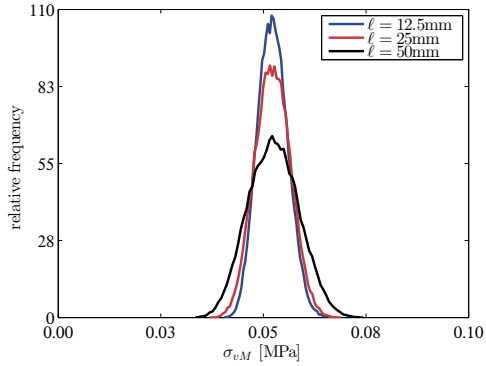

ℓ [mm]	Mean [MPa]	COV [-]	95% q. [MPa]
12.5	0.052291	0.069736	0.058451
25	0.052241	0.08211	0.059319
50	0.052482	0.11542	0.062647

(b) Von Mises stress at location 4

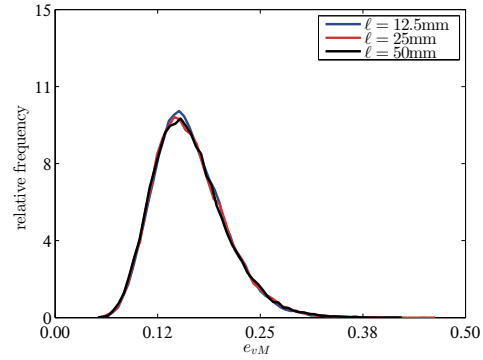

ℓ [mm]	Mean [MPa]	COV [-]	95% q. [MPa]
12.5	0.16404	0.2601	0.24097
25	0.16412	0.26746	0.24324
50	0.16387	0.26948	0.24422

(c) Von Mises strain at location 3

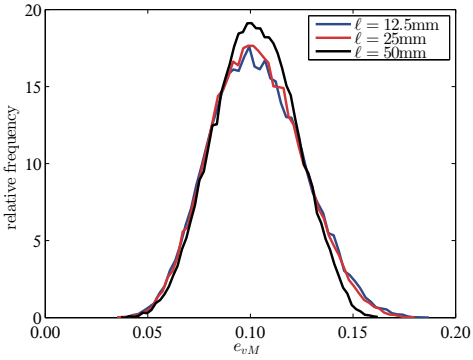

ℓ [mm]	Mean [MPa]	COV [-]	95% q. [MPa]
12.5	0.10335	0.21759	0.14183
25	0.10307	0.21143	0.14039
50	0.10237	0.19122	0.13486

(d) Von Mises strain at location 4

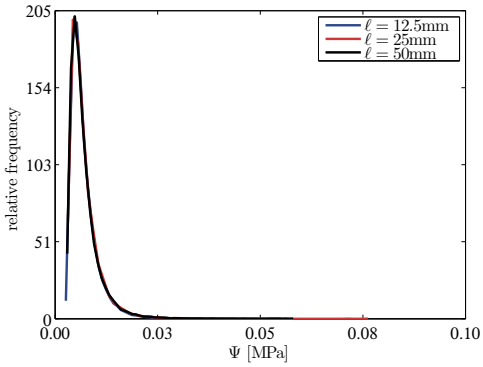

ℓ [mm]	Mean [MPa]	COV [-]	95% q. [MPa]
12.5	0.0068995	0.47871	0.013142
25	0.0069712	0.51633	0.013604
50	0.0069634	0.5216	0.01371

(e) Strain-energy at location 3

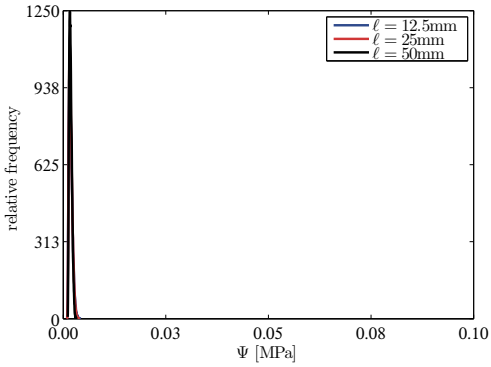

ℓ [mm]	Mean [MPa]	COV [-]	95% q. [MPa]
12.5	0.0018184	0.24358	0.0026554
25	0.0018084	0.23154	0.0026
50	0.0017859	0.18306	0.0023953

(f) Strain-energy at location 4

Figure 7.5 MC reference solution for male71 aneurysm. Reproduced from [32].

In contrast to the stresses, the strain and strain-energy exhibit large COVs and are therefore drastically affected by the constitutive parameter β. The probability distributions depicted in Figure 7.4c-7.4f and Figure 7.5c-7.5f reveal the large variations in local strain and strain-energy. With COVs up to 0.28 and 0.6, respectively, the strains and strain-energy exhibit significantly larger COVs than the stresses, rendering a statement about the true strain state of the aneurysm difficult when facing uncertain constitutive parameters. Whereas the distributions of the stresses are symmetric, both, strains and strain energy exhibit skewed distributions. The contour plots in Figure 7.2c reveal a close dependence between low β value and high local strain and vice versa and the overall spatial pattern of the strain depends mostly on the realization of the random field and not on the geometry of the aneurysm. Since the local stress state is mostly dictated by the given spatial configuration and external load, local strains depend predominantly on the local stiffness. The softer the wall, the higher the strains need to be in order to reach a certain "predetermined" stress level.

Comparing the probability densities of the strain and strain-energy at different correlation lengths in Figures 7.4c-7.4f and Figure 7.5c-7.5f, respectively, there is no noticeable difference between the three assumed correlation lengths. The variance of these probability distributions is virtually independent from the chosen correlation length for both, strains and strain-energy. If the 95% quantiles are used as an estimate for a worst case scenario and compared to the mean values, it becomes evident that strain is potentially 60-70% higher than the mean value and thus could be dramatically underestimated in deterministic models with population averaged constitutive parameters. In case of the strain-energy, the margin of uncertainty is even larger with a COV of typically more than 0.5, which results in a 95% quantile that is more than twice as high as the mean value.

The explanation for these very large COVs is once again the non-stress-free *in vivo* imaged configuration of the aneurysm. The combination of a known deformed configuration and the load case leading to this configuration results in a computed stress state which is only mildly sensitive to variations and uncertainties in the constitutive parameter β. This is not the case for the computation of the strain state. With a stress state that is to a large extent determined by the geometry of the aneurysm the strains become very sensitive to the local stiffness of the AAA wall. Assuming that the local stress state is dictated by the geometry and hence more or less fixed, the strain state that corresponds to this stress state depends on β. Low local stiffness will result in very high local strains and vice versa. Thus, any uncertainty in β directly translates to uncertainty in the strain state, inhibiting an accurate prediction of the strains if the stress free geometry and the constitutive properties are unknown or uncertain. The same argument holds if the strain-energy is considered as quantity of interest. As a result, the distributions of the strains and strain energy, evaluated at specific locations in the wall, exhibit very high COVs.

7.2.3.2 Bayesian multi-fidelity Monte Carlo

To demonstrate the efficiency and accuracy of the proposed BMFMC framework, a subset of the results from the previous section is chosen. Four examples which are summarized in Table 7.2 are considered, examining von Mises stress and strain at distinct locations of the two AAA models as quantities of interest. Moreover, different correlation lengths of the random field are taken into account, and different approximation schemes for the low-fidelity models are considered as well.

example	patient	quantity	location	ℓ	approximation scheme
1	male67	σ_{vM}	2	25 mm	coarsening
2	male71	σ_{vM}	3	25 mm	coarsening
3	male71	σ_{vM}	3	12.5 mm	coarsening & no ILT
4	male71	e_{vM}	4	25 mm	coarsening & no ILT

Table 7.2 Examples considered to demonstrate capabilities of BMFMC approach. Reproduced from [32].

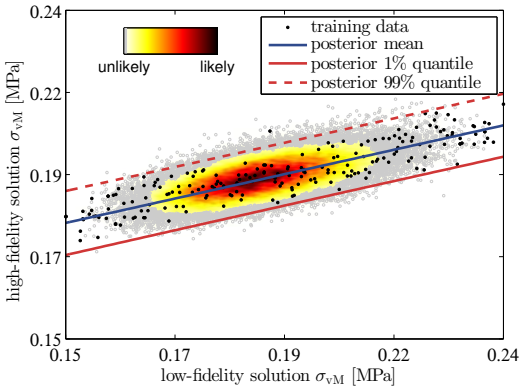

(a) Example 1: low-fidelity vs. high-fidelity solution, male67 aneurysm, $\ell = 25$ mm, σ_{vM} at location 2.

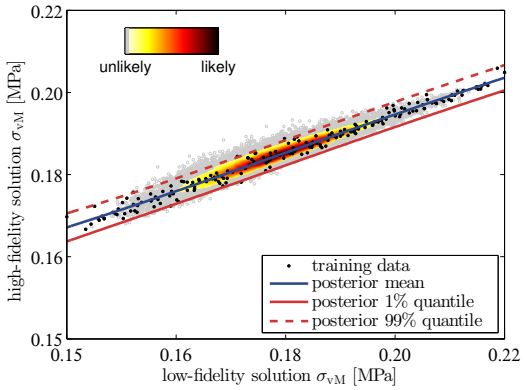

(b) Example 2: low-fidelity vs. high-fidelity solution, male71 aneurysm, $\ell = 25$ mm, σ_{vM} at location 3.

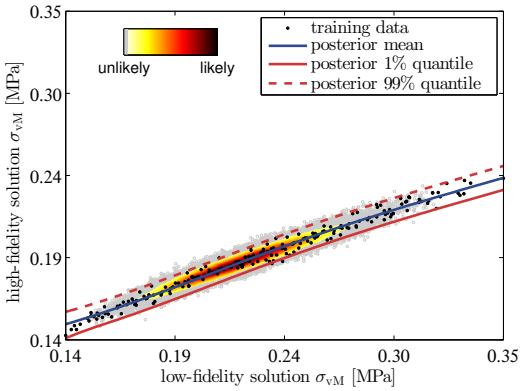

(c) Example 3: low-fidelity vs. high-fidelity solution, male71 aneurysm, $\ell = 12.5$ mm, σ_{vM} at location 3.

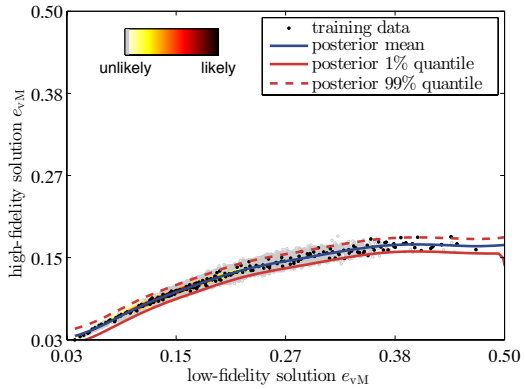

(d) Example 4: low-fidelity vs. high-fidelity solution, male71 aneurysm, $\ell = 25$ mm, e_{vM} at location 4.

Figure 7.6 Comparison between low-fidelity solution and high-fidelity solution. In addition to the posterior mean and the 1% and 99% quantiles of $p(y_{\text{hi-fi}}|y_{\text{lo-fi}})$ the figures show the used training samples (black dots) as well as all 50000 samples as color-coded 2d histogram. Reproduced from [32].

	MC reference			posterior mean BMFMC			relative error [%]		
	mean	COV	95% q.	mean	COV	95% q.	mean	COV	95% q.
Ex. 1	0.1932	0.0239	0.1983	0.1928	0.0259	0.2012	0.21	8.26	1.45
Ex. 2	0.1874	0.0217	0.1939	0.1872	0.0223	0.1940	0.12	2.70	0.05
Ex. 3	0.1872	0.0648	0.2073	0.1871	0.0653	0.2080	0.10	0.86	0.34
Ex. 4	0.1030	0.2114	0.1430	0.1023	0.2139	0.1395	0.71	1.20	2.44

Table 7.3 Comparison between MC reference solution and posterior mean BMFMC solution. Taken from [32].

After computing 50000 MC samples using the low-fidelity models, 200 of those were selected and the corresponding high-fidelity samples were taken from the MC reference solution. The 200 samples were selected such that they evenly cover the entire support of the particulate approximation of $p(y_{\text{lo-fi}})$, as described in Section 5.2.1. This set of training samples was used to determine the posterior density $\pi(\boldsymbol{\theta}, \sigma_\epsilon^2)$ of the parameters of the Koutsourelakis regression model and the variance of the noise term. Subsequently, this distribution is used to compute the conditional probability distribution $p(y_{\text{hi-fi}}|y_{\text{lo-fi}})$. Figure 7.6 shows a comparison between the solution of the low-fidelity model and the high-fidelity solution for all four examples. The color coded 2D histograms, based on all 50000 MC samples show the interrelation between the quantity of interest computed on the approximate and the high-fidelity model, respectively. The training samples that were used to infer the parameters of the regression model are shown in Figure 7.6 as black dots. The obtained posterior mean as well as the 1% and 99% quantiles of $p(y_{\text{hi-fi}}|y_{\text{lo-fi}})$ are also depicted in Figure 7.6.

In all four cases the posterior mean of $p(y_{\text{hi-fi}}|y_{\text{lo-fi}})$ captures the interrelation between the approximate and high-fidelity solution very well. Furthermore, the computed quantiles readily provide confidence intervals, which contain virtually all MC samples with very few exceptions. The reason for the noisy relationship between $y_{\text{lo-fi}}$ and $y_{\text{hi-fi}}$ is that the coarsening of the discretization yields larger discretization errors and therefore spurious effects due to the coarser discretization appear. Moreover, the coarser mesh is unable to resolve the finer details of the random field which results in a smeared, less detailed solution. It was found that these effects are more distinct if the quantity of interest is the von Mises stress as compared to von Mises strain.

While the first two examples show an almost linear relation between low-fidelity and high-fidelity solution, example three and particularly example four exhibit a distinct nonlinear dependency. The nonparametric Bayesian regression model is able to capture these nonlinear interrelations as well. It also can be seen in Figure 7.6, especially for the latter two examples, that the lack of ILT in the low-fidelity model leads to significant differences in the overall magnitude between the stresses computed with the approximate and the high-fidelity model, respectively. In fact, the stress and strain are considerably higher in the low-fidelity model, due to the lack of ILT. By comparing the two densities $p(y_{\text{lo-fi}})$ and $p(y_{\text{hi-fi}})$, as shown in Figure 7.7, this difference becomes even more apparent.

The posterior mean approximation $\hat{\pi}(y_{\text{hi-fi}})$ is computed for all examples using (5.4) and depicted in Figure 7.7 together with $p(y_{\text{lo-fi}})$ and the MC reference solutions of the high-fidelity model $p(y_{\text{hi-fi}})$. Despite the differences between $p(y_{\text{lo-fi}})$ and $p(y_{\text{hi-fi}})$, the posterior mean approximation $\hat{\pi}(y_{\text{hi-fi}})$ is in excellent agreement with the MC reference solution for all examples.

example	patient	approximation scheme	cost MC	cost BMFMC
1	male67	coarsening	50000	5075
2	male71	coarsening	50000	2051
3	male71	coarsening & no ILT	50000	1195
4	male71	coarsening & no ILT	50000	1195

Table 7.4 Comparison of computational costs between direct MC and BMFMC approach. Costs are given as equivalent number of calls to the respective high-fidelity model. Taken from [32].

Table 7.3 lists the mean, COV and 95% quantile for both the MC reference $p(y_{\text{hi-fi}})$ and the posterior mean approximation $\hat{\pi}(y_{\text{hi-fi}})$. Additionally, the relative error between the MC reference and the BMFMC approach is given, thus allowing a quantitative assessment of the accuracy. For the mean value a relative error below 1% is achieved for all examples. The error of the estimation of the COV and the 95% quantile is slightly higher. However, considering the crude low-fidelity models and the gain in computational efficiency, the accuracy is more than sufficient for biomedical applications.

The ability to obtain an accurate estimate for the complete PDF, rather than just the first moments is a major advantage, because the probability that the quantity of interest exceeds a certain threshold y_0 can be computed. Although the exact definition of a failure threshold can be difficult in biomechanical systems, such a failure probability is a valuable tool in many applications including rupture risk stratification of AAAs. Under the assumption that a suitable failure threshold y_0 can be defined, the probability that a threshold y_0 is exceeded, is computed using (5.10). Figure 7.8 depicts the posterior mean failure probability computed for a range of failure thresholds y_0 for the chosen examples. Again an excellent agreement with the MC reference solution is achieved, at a fraction of the computational cost, see Table 7.4. In addition, credible intervals which are also shown in Figure 7.8 can be computed using (5.11). The intervals are an indicator for the accuracy of the computed failure probability estimate based on the training data. As depicted in Figure 7.8, the provided bounds contain the MC reference solution.

The computational efficiency of the method depends on the ability to create cheap low-fidelity models which still provide "enough" relevant information. In the examples considered here the ratio of computational effort required to compute one sample of the accurate and the low-fidelity model, respectively is between 10.2 and 50. A ratio of 50, accomplished by using a coarser discretization and omitting the ILT in the low-fidelity model, results in a tremendous reduction of the computational effort, see Table 7.4. Compared to direct MC using the high-fidelity model the total computational effort is reduced by a factor of 42. As the male67 patient does not exhibit ILT and merely a coarser discretization was used to create the low-fidelity model, the computational cost for the male67 aneurysm is reduced by a factor of 10 compared to direct MC. However, the vast majority of AAAs in the patient database exhibit ILT and especially for large AAA, which are computationally expensive, being able to omit the ILT in the model will result in even greater savings. However, it is pointed out that omitting the ILT in the low-fidelity model is obviously only a viable option as long as no uncertainties in the ILT properties itself are considered in the UQ analysis.

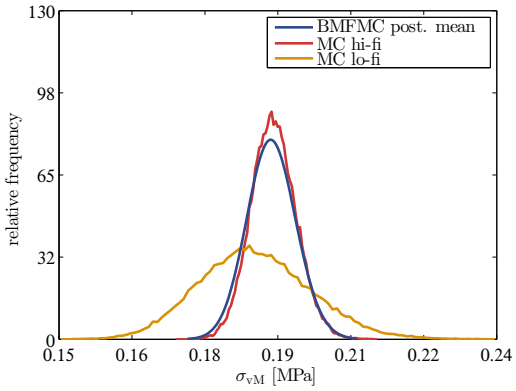

(a) Example 1: male67, $\ell = 25$, σ_{vM} at location 2.

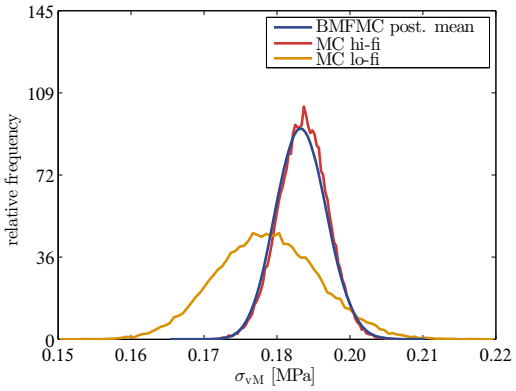

(b) Example 2: male71, $\ell = 25$, σ_{vM} at location 3.

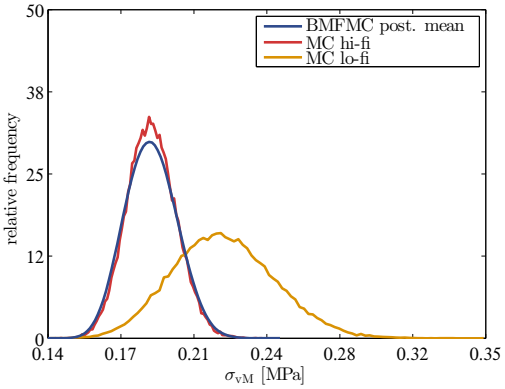

(c) Example 3: male71, $\ell = 12.5$, σ_{vM} at location 3.

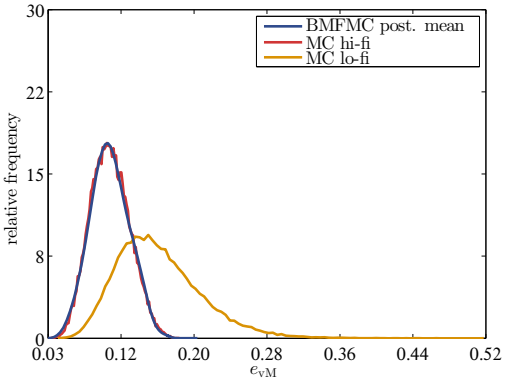

(d) Example 4: male71, $\ell = 25$, e_{vM} at location 4.

Figure 7.7 Exemplary comparison of empirical densities from low-fidelity model $p(y_{\text{lo-fi}})$, high-fidelity model $p(y_{\text{hi-fi}})$ and posterior mean BMFMC approximation $\hat{\pi}(y_{\text{hi-fi}})$. Reproduced from [32].

It is important to stress the fact that the low-fidelity model does not have to be accurate, as in deterministic multi-level or multi-grid schemes. As shown in Figure 7.7, low-fidelity models without ILT yield significantly higher values for strain and stress due to the missing support of ILT for the AAA wall. Additionally, no restrictions to the interrelation between the low-fidelity and high-fidelity model apply. Even highly nonlinear interrelations are detected and accurately reproduced by the Koutsourelakis regression model, the complexity of which is determined by the information provided by the training samples. Whereas inaccurate low-fidelity models and nonlinear interrelations do not adversely affect the accuracy of the approach per se, coarsening of the discretization yields less detailed smeared out results due to the coarser representation of the random field, a larger discretization error, and potentially aggravates spurious numerical effects such as volumetric locking. This results in a noisier relationship between the low-fidelity and the accurate model, i.e., a higher variance of the conditional probability distribution $p(y_{\text{hi-fi}}|y_{\text{lo-fi}})$. As the variance increases, the credible intervals of the regression function $f(y_{\text{lo-fi}}, \boldsymbol{\theta})$ will become larger too. Thus, the accurate prediction of the quantity of interest on the

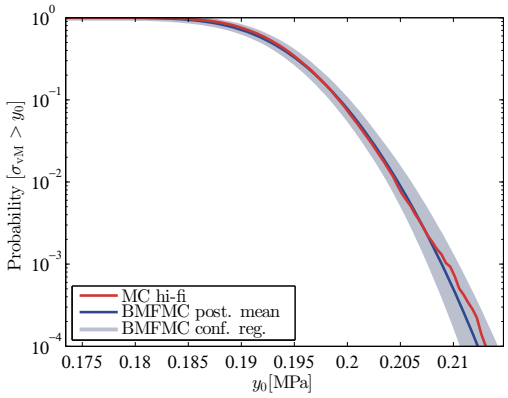

(a) Example 1: male67, $\ell = 25$, σ_{vM} at location 2.

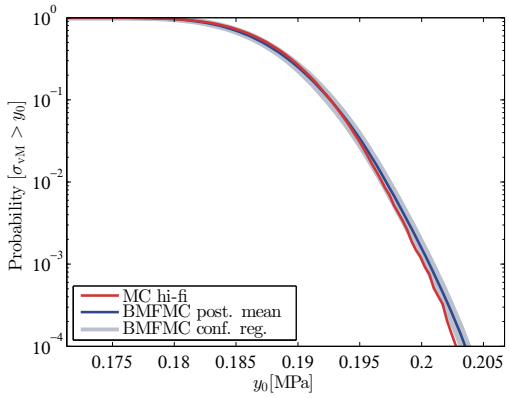

(b) Example 2: male71, $\ell = 25$, σ_{vM} at location 3.

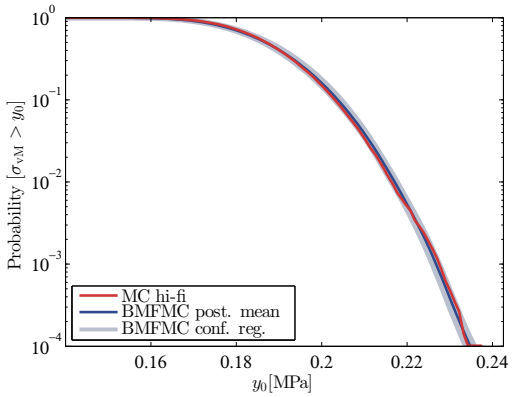

(c) Example 3: male71 $\ell = 12.5$, σ_{vM} at location 3.

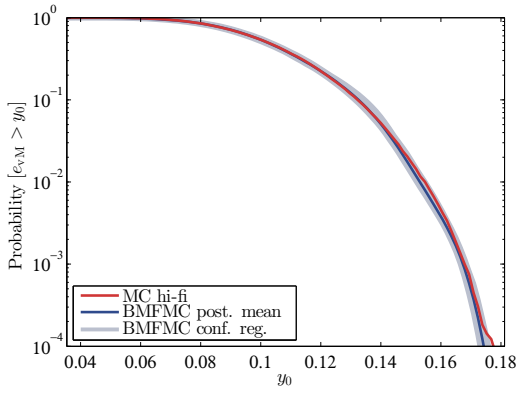

(d) Example 4: male71 $\ell = 25$, e_{vM} at location 4.

Figure 7.8 Probability of exceeding a local failure threshold y_0 for a given quantity of interest. Comparison of MC reference solution to posterior mean approximation and posterior quantiles. Reproduced from [32].

high-fidelity model becomes more difficult. While a set of 200 training samples was used here and with that excellent agreement with the MC reference solution was achieved, the amount of training data needed depends on a number of factors, i.e., the required accuracy, the employed low-fidelity model, the quantity of interest, and the statistic to be estimated. Hence, it is difficult to provide an *a priori* estimates of how many samples are needed to achieve a given accuracy. However, monitoring the credible intervals of $f(y_{\text{lo-fi}}, \boldsymbol{\theta})$ while more training points are added can aid in deciding whether adding more training samples, which entails evaluating the high-fidelity model, justifies the additional effort associated with evaluation of the forward model.

Efficiency gains through parameter continuation Using the continuation scheme for elastic properties described in Section 5.2.5 the computational costs can be further decreased. For instance, for the high-fidelity model of the male71 patient the computational cost for one forward model evaluation can be reduced roughly by a factor of 3 to an average of 3800 CPU

seconds. The computational cost for one evaluation of the low-fidelity model (version without ILT) reduces to a mere 95 CPU seconds. Of those 95 s 75 s are spent computing the realization of the random field using the spectral representation method. As a result the total computational cost for the BMFMC scheme add up to 1531 CPU hours which is equivalent to 510 full evaluations of the full high-fidelity forward model. Thus the BMFMC scheme is about a 100 times cheaper than MC without parameter continuation. Due to the comparatively large effort to compute realizations of the random field, the one way to achieve an additional speedup is the use of a faster approach for the computation of random field realizations. It was found that the computation of realizations based on the Fourier series expansion of random fields described in Section 3.3.3.3 is significantly faster and thus this approach is mostly used in examples considered in the following sections.

7.3 AAA models with uncertain wall thickness

The present section shows that the BMFMC approach can also be used to investigate the impact of an uncertain wall thickness. Moreover, a global quantity - the peak wall stress - instead of a local quantity of interest is investigated here. As in the previous section, two patient-specific geometries of real AAAs are used to demonstrate the capabilities of the method with real world examples. Another major focus of this section is the comparison of different data-driven stochastic wall thickness models. Three probabilistic wall thickness models with different levels of sophistication are investigated here and the resulting probability distribution for the peak wall stress is computed for both patients. Thereby, the data-driven probabilistic wall models are based on experimental data and the obtained results in Chapter 6. More specifically, two probabilistic wall models, a random variable and a random field model, whose parameters are based on study population measurements of the wall thickness are used. In addition, a second random field model, which takes non-invasively available predictors for the wall thickness into account, is also included. Because some of these predictor variables are not available for the patients investigated in the last section, two different AAA geometries are considered here.

The probability distribution of the peak wall stress in each AAA model is computed using the BMFMC approach in case the wall thickness is described by a random field and a MC reference solution with 20000 samples is provided for comparison. If the wall thickness is described by a simple random variable, the stochastic dimension of the problem is one and hence a surrogate model will need fewer model evaluations than the BMFMC approach. For this reason a GP based surrogate was used to perform UQ for the simpler random variable case. The used GP surrogate approach is described in detail in Section 4.6.2. For the example considered here, a GP with a squared exponential covariance function was used, the hyper-parameters of which are determined by marginal likelihood maximization.

In contrast to the previous section where the Koutsourelakis regression approach was used, a GP based regression model as described in Section 3.5.2 was used here to compute the necessary conditional probability distribution $p(y_{\text{hi-fi}}|y_{\text{lo-fi}})$. The GP based regression model is significantly easier to implement and thus presented here as an alternative. Nevertheless, it is acknowledged that further research should include a more detailed comparison between different regression approaches.

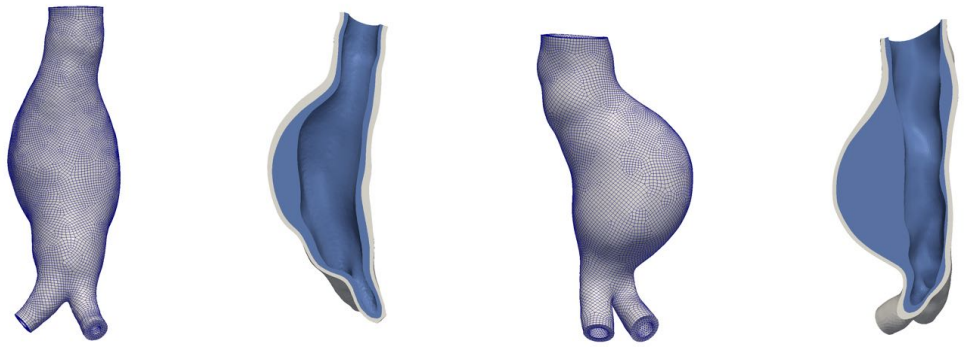

(a) (b) (c) (d)

Figure 7.9 Discretization and geometry of high-fidelity patient-specific AAA models of patients female48 (a) and male65 (c). Both AAA feature ILT which is shown in blue in the cross-sectional views for patient female48 (b) and patient male65 (d).

7.3.1 Patient-specific finite element models

Two finite element models, which are referred to from here on as female48 and male65, were created using the process described in Section 7.1. The resulting high-fidelity versions of the models are depicted in Figure 7.9. As can be seen in the cross-sectional views provided in Figure 7.9, both AAAs exhibit ILT. The models consist of 124962 (female48) and 111442 (male65) linear hexahedral and tetrahedral elements, resulting in a problem size of 374886 and 334326 degrees of freedom, respectively. The ILT is meshed exclusively using tetrahedral elements, whereas the wall consists of three layers of hexahedral elements. Because the nodes at the interface match exactly, the two triangular surface elements belonging to two tetrahedral volume elements can be directly tied to one quadrilateral surface element, which belongs to one hexahedral volume element of the wall. This direct mesh tying approach introduces a small error since the discretizations do not match at this artificial interface. To ensure that this error is insignificant, this direct mesh tying approach was compared to a consistent mortar mesh tying approach [97] to couple ILT and wall together. The differences were found to be negligible.

If the wall thickness is modeled by a discretized random field, the thickness $t_{\text{stoch}}(\boldsymbol{x}, \mathbf{z})$ becomes a function of location $\boldsymbol{x}$ and a number of random variables collectively denoted as $\mathbf{z}$. Using the geometry adjustment algorithm described in Section 5.2.5 realizations of the random geometry are generated at runtime. Once a realization $t_{\text{stoch}}(\boldsymbol{x}, \boldsymbol{z}^{(i)})$ of the random field describing the wall thickness is computed and evaluated at the nodes on the outer surface of the AAA, the positions of all nodes in the wall are adjusted accordingly.

At this point it is important to note that the wall thickness is not altered at the bifurcation of the AAAs nor in its direct vicinity. The wall thickness is considered constant up to approximately 15 mm above the bifurcation point, because geometry alterations in the vicinity of the bifurcation could not be performed without resulting in self-intersecting geometries. Kinks in the geometry are avoided by gradually blending between constant wall thickness and stochastic wall thickness in a transition zone above the bifurcation.

model	solution time (CPU seconds)	degrees of freedom
female48 high-fidelity	24100	374886
female48 low-fidelity	27	-
male65 high-fidelity	19716	334326
male65 low-fidelity	18	-

Table 7.5 Size of female48 and male65 AAA finite element models and solution times for one solve of the forward model. The computational for the high-fidelity model also includes the additional effort for the geometry adjustment step.

After the geometry adjustment step, the actual boundary value problem of interest is solved and the von Mises stress field $\boldsymbol{\sigma}^{(i)}_{t_{\text{stoch}}}(\boldsymbol{x})$ corresponding to a particular realization of the thickness $t_{\text{stoch}}(\boldsymbol{x}, \boldsymbol{z}^{(i)})$ can be computed subsequently. The boundary conditions described in the previous Section were used for the AAAs considered here as well. The quantity of interest studied in the following examples is the maximum von Mises stress. In order to avoid numerical artefacts, the 99 % quantile of the von Mises stress of all wall elements is taken instead of the true maximum in all following simulations.

Regarding the low-fidelity versions of the model, a different approach as compared to the one described in Section 7.2 was taken. Instead of using a coarser discretization, essentially the simple rule of thumb - that the stress in the wall is roughly inversely proportional to the local wall thickness - is used for the construction of a low-fidelity solution. In order to compute a low-fidelity approximation to the von Mises stresses in the AAA wall for a realization $t_{\text{stoch}}(\boldsymbol{x}, \boldsymbol{z}^{(i)})$, the von Mises stress $\boldsymbol{\sigma}_{t_{\text{const}}}(\boldsymbol{x})$, which is computed based on a simulation with spatially uniform wall thickness t_{const}, is simply multiplied with the local ratio between t_{const} and $t_{\text{stoch}}(\boldsymbol{x}, \boldsymbol{z}^{(i)})$

$$\boldsymbol{\sigma}_{t_{\text{stoch}}}(\boldsymbol{x}, \boldsymbol{z}^{(i)}) = \boldsymbol{\sigma}_{t_{\text{const}}}(\boldsymbol{x}) \frac{t_{\text{const}}}{t_{\text{stoch}}(\boldsymbol{x}, \boldsymbol{z}^{(i)})}. \tag{7.5}$$

Thus, after the high-fidelity model is solved once to compute the von Mises stress for all elements in the AAA wall based on a uniform wall thickness, (7.5) is used to compute a low-fidelity approximation for the von Mises stress. The computational cost associated with the evaluation of this low-fidelity "model" are close to zero, since computing one sample only requires the generation of a realization of the random field describing the wall thickness $t_{\text{stoch}}(\boldsymbol{x}, \boldsymbol{z}^{(i)})$ and one scalar multiplication for each element within the wall using (7.5). Doing so not even requires an update of the geometry of the model and the geometry adjustment step can be omitted as well. Details about the computational effort for each model are given in Table 7.5. The described procedure, which is referred to as *scaled-thickness* approach from here on, results in low-fidelity "models" which are approximately 993 and 1095 times cheaper then the corresponding high-fidelity version of the model. The stated solution times are averaged values obtained using a computing platform with Intel Xeon E5-2680 processors. For all models considered in this section, 8 cores were used for the evaluation of the forward models.

While uncertainty in the wall thickness is considered in this section, the constitutive properties are considered to be deterministic and study population average values according to the results in Chapter 6 were chosen for the constitutive parameters, i.e, $\alpha = 0.121$ MPa and $\beta = 2.98$ MPa.

7.3.2 Stochastic models for the wall thickness

In Chapter 6 the construction of data-driven, predictive models for several mechanical parameters, which govern the mechanical behaviour of the AAA wall, have been constructed and discussed. It has been shown that the predictive uncertainty can be reduced by taking non-invasively assessable, patient-specific parameters into account. In this section different stochastic models based on the findings in Chapter 6 for the wall thickness are investigated and the impact on the probability distribution of the peak wall stress within the AAA wall is studied. Three different probabilistic wall thickness models are considered here, two random field models and one random variable model. Thereby, all models are based on a log-normal distribution for the wall thickness. For both random field models, a squared exponential covariance function is employed. Based on the results in Section 6.4 the correlation length ℓ was set to 25 mm, the average of the two estimates provided in Table 6.11. A sensitivity study regarding the correlation length is beyond the scope of this work but should be subject of future research. The correlation lengths given in Table 6.11 were estimated based on a logarithmic transformation of the data. Hence, the probabilistic models for the thickness are simply based on a Gaussian random field model for the logarithm of the thickness. Consequently, the first-order probability distribution of random field describing the thickness is log-normal. While the type of (first-order) probability distribution is the same for all probabilistic models, the parameters of the log-normal probability distribution are not. Based on the results presented and discussed in Chapter 6, the different model versions along with the respective parameter choices are given in the following.

- **Model A:** Log-normal random field model based on fitting a Gaussian distribution to study population measurements of the logarithm of the wall thickness. The resulting log-normal random field has a spatially constant mean and the parameters of the log-normal distribution are $\mu_t = 0.4434$ and $\sigma_t = 0.3338$, respectively.

- **Model B:** Random field model based on the predictive distribution of the GP based Bayesian regression model discussed in Chapter 6, which takes into account non-invasively available information. The parameter $\mu_t(\boldsymbol{x})$ of the first-order log-normal distribution thereby depends on the spatial location through several spatially varying, non-invasively assessable parameters. Thus, a closed form expression is not provided. The second parameter was set to $\sigma_t = 0.246$, according to the obtained results in Chapter 6.

- **Model C:** Random variable model based on the study population measurements of the wall thickness using the same distribution parameters as in model A. However, since model C is based on a random variable, the resulting wall thickness will be spatially constant across the AAA, thus neglecting a spatial, intra-patient variations in wall thickness.

As discussed in Section 6.3.3.1, the predictive distribution for the wall thickness provided by the regression model is more accurate and the predictive variance, i.e., the predictive uncertainty, is smaller as compared to the variance estimated directly from study population measurements. By conducting an UQ analysis using both model A and model B, the benefit of using regression model based probabilistic predictions for the wall thickness can be assessed. Although the data indicates that random variable models are overly simplistic, as they cannot capture intra-patient variations of the wall thickness, a random variable model is included for comparison with the more complex random field models. Through comparison with the results obtained with the

probabilistic model C, the necessity of the more complex random field models A and B can be judged.

It is noted that the particular choice of random field models is based on the assumption that the amount of intra-patient variations or uncertainty is equal to the total amount of variability. Other models are, of course, conceivable, such as a mixture between a random field with smaller variance capturing the intra-patient variability in combination with a random variable for the mean to model inter-patient variations.

To generate realizations of the random field, the Fourier series expansion given in (3.79) was used. Compared to the spectral representation method, a major advantage of this approach is that realizations of random fields can be computed much faster. The truncation threshold in (3.80) was set to 250, resulting in a stochastic dimension of the UQ problem of 5112. Using this truncation threshold approximately 95% of the variability of the field is retained by the expansion.

7.3.3 Results

Using the two patient-specific AAA models female48 and male65, the impact of an uncertain wall thickness on the peak wall stress is investigated and the results obtained with three different probabilistic wall models are compared. For wall thickness model A and B the uncertainty is propagated using BMFMC and for wall thickness model C a GP based surrogate is used. The discussion of the results is divided into three parts. First, the solution obtained with the proposed BMFMC is compared to a MC reference solution and the accuracy and efficiency of the BMFMC approach is discussed. Then, the results computed with the GP surrogate are provided and advantages of the method are illustrated. This discussion of the methodological aspects is followed by a comparison of peak wall stress distributions computed based on all three probabilistic wall models and both patients.

7.3.3.1 Bayesian multi-fidelity Monte Carlo

The two random field based probabilistic wall models A and B in combination with two patient-specific AAA geometries yield four different model variants. UQ was performed with all of these four model versions using both MC and the Bayesian multi-fidelity approach. A brief summary of the accuracy of BMFMC for all four model versions is provided in Table 7.6. In all cases an excellent agreement with the MC reference solution is achieved. The posterior mean approximation reproduces the MC reference with very small error in all examined quantities.

In Table 7.6 estimates for mean, COV, and 95% quantile of the peak wall stress based on the high-fidelity MC reference $p(y_{\text{hi-fi}})$ and posterior mean approximation $\hat{\pi}(y_{\text{hi-fi}})$ of the BMFMC scheme are provided for all four examples under investigation. A relative error significantly below 1% is achieved in most cases.

Because the BMFMC approach performs very similar with all four model versions only two showcase examples are discussed in more detail. The female48 aneurysm with stochastic wall model A and the male65 aneurysm with wall model B are considered in the following. The low-fidelity version of all models is based on the scaled thickness approach described above. For all versions 20000 samples were computed for the high-fidelity and the low-fidelity model, respectively. As described in Section 5.2.1 200 informative training samples were selected to

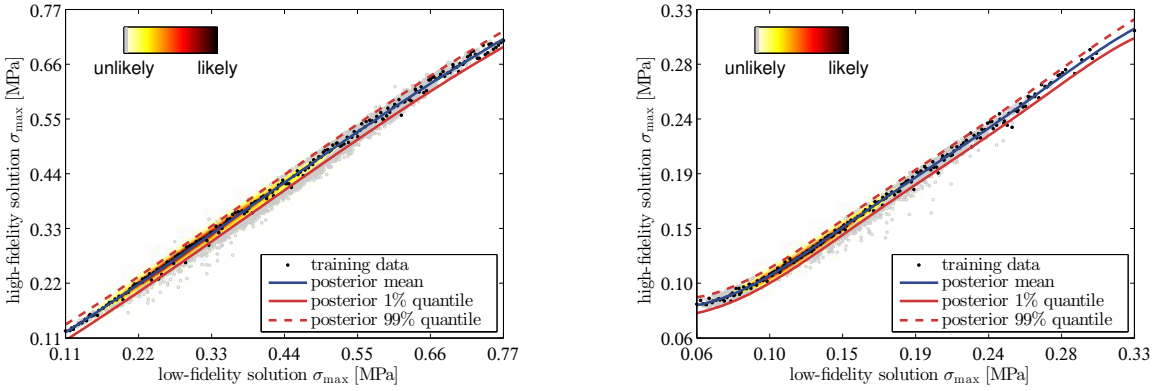

(a) female48 model A

(b) male65 model B

Figure 7.10 Comparison between low-fidelity solution and high-fidelity solution. In addition to the posterior mean and the confidence region of the predictive distribution $p(y_{\text{hi-fi}}|y_{\text{lo-fi}})$, the figures show the used training samples as black dots.

	MC reference			posterior mean BMFMC			relative error [%]		
	mean	COV	95% q.	mean	COV	95% q.	mean	COV	95% q.
female48 m. A	0.3323	0.2917	0.5168	0.3324	0.2929	0.5191	0.036	0.358	0.445
female48 m. B	0.2142	0.2144	0.2977	0.2147	0.2113	0.2979	0.244	1.446	0.035
male65 m. A	0.2043	0.2951	0.3202	0.2037	0.2926	0.3207	0.297	0.844	0.151
male65 m. B	0.1350	0.2015	0.1857	0.1351	0.2004	0.1857	0.028	0.515	0.027

Table 7.6 Comparison between MC reference solution and BMFMC approximation for the two considered patients and both random field based probabilistic wall models (m.).

train a GP based regression model, which then provides the conditional probability distribution $p(y_{\text{hi-fi}}|y_{\text{lo-fi}})$. In Figure 7.10 a comparison between the solution of the high-fidelity and the low-fidelity model is shown for both examples. The training samples that were used to setup the regression model are shown as black dots in the plots and show interrelation between low-fidelity and high-fidelity model output. This interrelation is well captured by the conditional distribution provided by the GP regression model, the posterior mean prediction of which is shown in blue in Figures 7.10a and 7.10b. Moreover, the confidence interval of $p(y_{\text{hi-fi}}|y_{\text{lo-fi}})$ is shown in addition to the mean.

The noise level is noticeably smaller as compared to the examples with an uncertain constitutive parameter studied in Section 7.2. Moreover, the relationship between low-fidelity and high-fidelity solution is very close to linear, except for the areas corresponding to the tails of the distribution, where a slight deviation from an otherwise linear relation is discernible. In addition, the slope of the interrelation is close to one, indicating that the chosen low-fidelity model yields indeed very accurate results by itself.

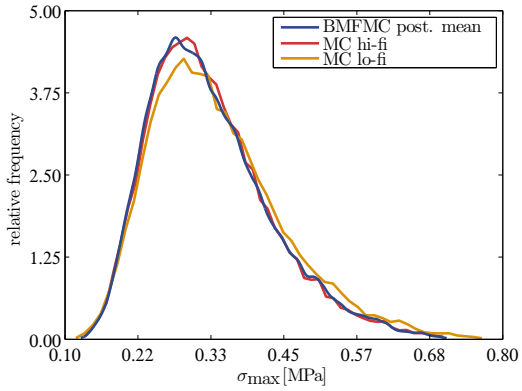

(a) PDF estimates: female48 aneurysm, wall model A.

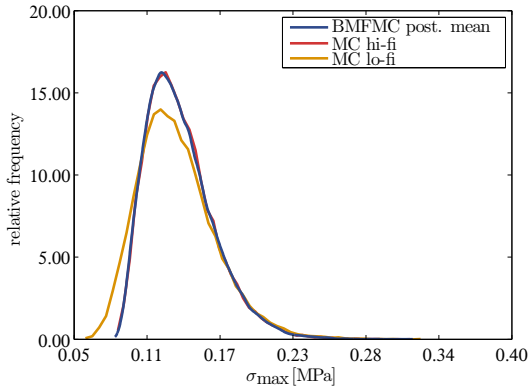

(b) PDF estimates: male65 aneurysm, wall model B.

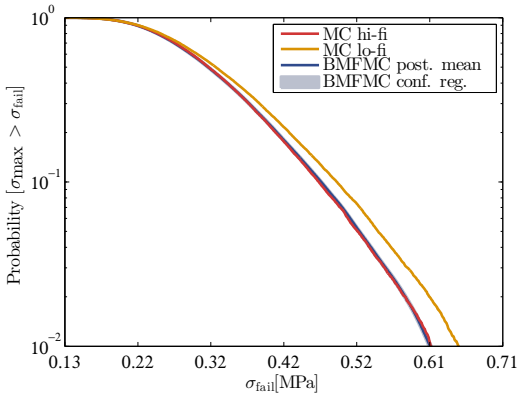

(c) Failure probability: female48 aneurysm, wall model A.

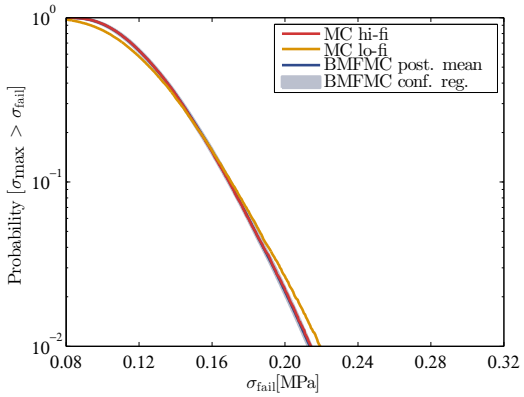

(d) Failure probability: male65 aneurysm, wall model B.

Figure 7.11 Exemplary comparison between high-fidelity MC solution (red), low-fidelity MC solution (yellow), and BMFMC solution (blue) for female48 aneurysm with wall model A and male65 aneurysm with wall model B. Top: estimated PDFs for peak wall stress. Bottom: failure probability based on peak wall stress.

In fact, at first glance one might argue that the chosen examples are not the best showcase for the BMFMC method because the peak wall stress computed with the low-fidelity model is so accurate that statistics based on the low-fidelity solution alone might be sufficient. However, comparing the plots in Figure 7.10a and 7.10b it becomes evident that the accuracy of the low-fidelity models varies and depends on the examined example. Without having an accurate high-fidelity solution for comparison, it is difficult to provide an a priori estimate of the error introduced by the low-fidelity model. Moreover, while the differences seem small in the representation in Figure 7.10, the discrepancy in accuracy between low-fidelity model and high-fidelity model is more pronounced if the probability distributions are compared. Figure 7.11 depicts the estimated densities $p(y_{\text{hi-fi}})$ and $p(y_{\text{lo-fi}})$ for both the high-fidelity solution and the corresponding low-fidelity solution. Especially for the first example, the error in statistical summaries estimated directly from low-fidelity model output are significant. Using BMFMC the

example	patient	low-fidelity model	cost MC	cost BMFMC
1	female48	scaled thickness	20000	222
2	male65	scaled thickness	20000	218

Table 7.7 Comparison of computational costs between direct MC and Bayesian multi fidelity MC approach. Costs are given as equivalent number of evaluations of the respective high-fidelity model.

discrepancy between low-fidelity and high-fidelity model can be accounted for, and the probability distribution estimates obtained with BMFMC, which are also shown in Figure 7.11, match the MC high-fidelity reference extremely well.

Under the assumption that a failure threshold σ_{fail} can be specified, the failure probability $P(\sigma_{\max} > \sigma_{\text{fail}})$ can be computed. Figure 7.11 depicts the posterior mean BMFMC failure probability computed for a range of failure thresholds σ_{fail} for the studied examples. Again, an excellent agreement with the MC reference solution is achieved. In addition, credible intervals are also shown in Figure 7.11. Due to the low noise level in the interrelation between the low-fidelity solution and the high-fidelity solution, these credible intervals are very tight. The failure probabilities based on the low-fidelity solution alone are also shown in Figure 7.11. In particular for the female48 aneurysm with wall model A, the failure probability computed based on the low-fidelity solution alone differs markedly from the MC reference.

While the BMFMC solution matches the high-fidelity MC reference solution very well, the computational savings achieved by using the BMFMC solution are enormous, as can be seen in Table 7.7, which provides a summary of the computational cost. The low-fidelity model of the male65 patient is about 1095 times cheaper than the high-fidelity model. The result is an overall cost for UQ using BMFMC which is equivalent to a mere 222 evaluations of the forward model, as compared to 20000 for a regular MC scheme. Thus, the proposed BMFMC scheme is about 90 times cheaper, while delivering results that match those of standard MC. As can be inferred from Table 7.7, the computational savings obtained for the second patient are similar. The overall efficiency of the scheme could be further improved if the parameter continuation scheme described in Section 5.2.5 would be extended to cope uncertain geometries as well. Moreover, the use of fewer training samples would further reduce the computational cost. It is noted that the construction of low-fidelity models which are a 1000 times cheaper to evaluate and at the same time are almost as accurate as the high-fidelity model is probably an exception, rather than the norm.

7.3.3.2 Gaussian process surrogate model

In case the wall thickness is modeled as random variable, the stochastic problem at hand only has one stochastic dimension and hence surrogate models present the more efficient UQ approach, compared to MC or BMFMC. In one dimension it is very easy to create a surrogate model to mimic the behavior of the finite element model of the AAA. Thereby it is important to note that the surrogate only needs to capture the dependence between peak wall stress and wall thickness. The finite element models of the patients female48 and male65 were evaluated using 25 different uniform wall thicknesses ranging from 0.57 mm to 4.45 mm, thereby covering the range of all

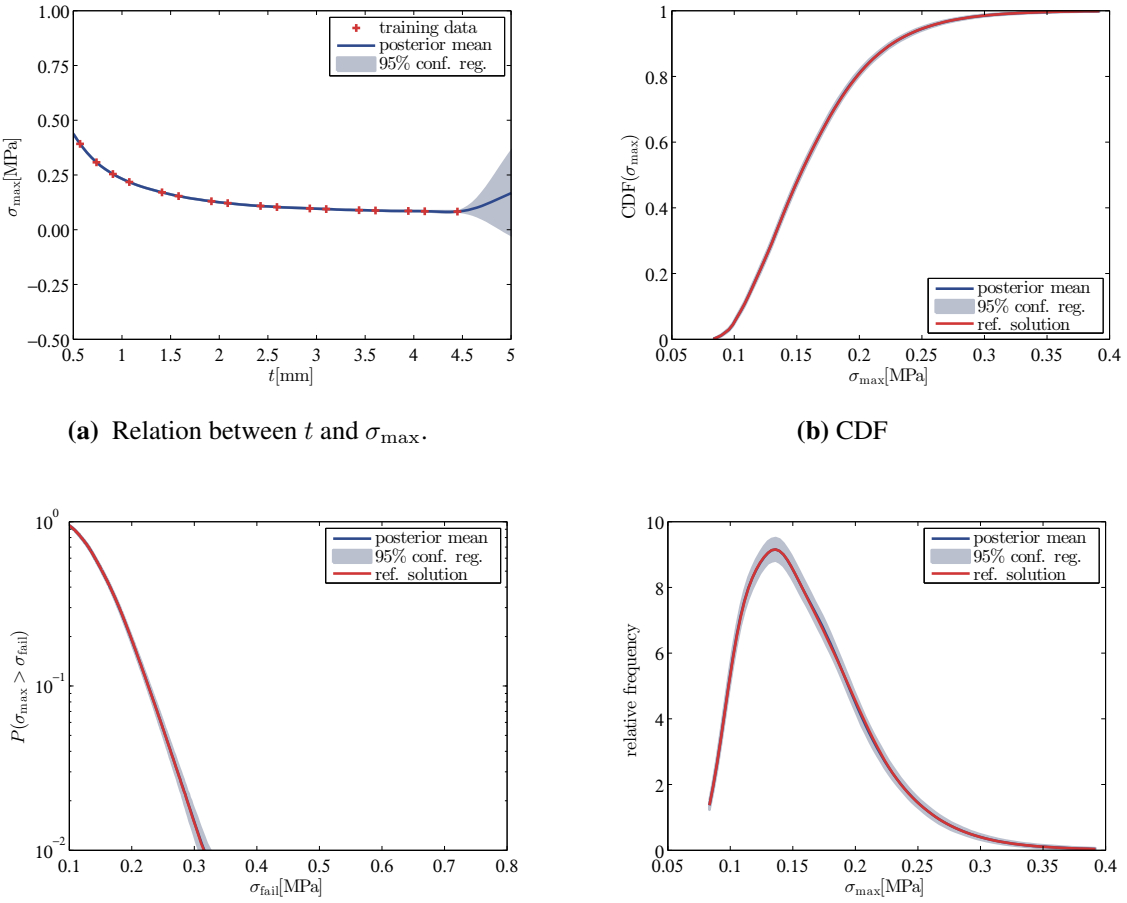

(a) Relation between t and $\sigma_{\max}$.

(b) CDF

(c) Failure probability

(d) PDF

Figure 7.12 Gaussian process based surrogate model for $\sigma_{\max}$ in male65 model with uncertain wall thickness, based on 17 design points. (a) Relationship between wall thickness and peak wall stress. (b) Estimated CDF. (c) Estimated failure probability. (b) Estimated PDF.

experimentally measured values and more than 99% of the support of the log-normal distribution describing the random fluctuations in wall thickness.

Based on these 25 design points, a GP was fitted to the data, linking wall thickness to peak wall stress in the AAA models. This GP was then used to obtain a reference solution for the probability distribution of $\sigma_{\max}$ using the procedures described in Section 4.6.2. Without conducting a rigorous convergence analysis, the accuracy of GP surrogates constructed with fewer design points were investigated by comparison to this reference solution in order to estimate the number of design points necessary for an accurate, yet efficient, UQ analysis.

Starting with only three design points, the GP surrogate was trained based on these points and estimates for CDF and PDF were computed. Then additional design points were added incrementally. It was found that the use of 17 design points in the setup phase of the GP surrogate produced results that are in excellent agreement with the reference solution and no significant

improvement could be achieved through the addition of more design points. Consequently 17 design points were considered sufficient for the examples considered in this work.

Figure 7.12 shows the GP surrogate for the male65 aneurysm based on 17 design points as well as the resulting estimates for CDF, PDF, and failure probability, i.e., $P(\sigma_{\max} > \sigma_{\text{fail}})$. The mean estimate is provided along with 95% confidence regions, respectively. In addition the reference solution based on 25 design points is provided as well. The design points which were used to train the GP are shown as red crosses in Figure 7.12 and the resulting posterior mean and 95% confidence region are shown in blue and light blue, respectively. For wall thickness values smaller than 4.5 mm the confidence region is so small that it is barely visible in the plot, indicating that the addition of further design points is unnecessary. Although the predictive uncertainty for thickness values larger than 4.5 mm is significant, the studied probability distribution assigns virtually zero mass to values greater than 4.5 and hence adding design points in this domain would not alter the results. Nevertheless, it is important to note that the provision of a confidence measure is one of the major advantages of GP based surrogate approaches, because many other surrogate models do not provide estimates of their accuracy.

As shown in Figure 7.12 the mean estimates for CDF, PDF, and failure probability are virtually indistinguishable from the reference solution. Moreover, the 95% confidence regions for all computed summaries are very small, indicating that 17 design points are sufficient for the examined example.

The results for the second example, the female48 aneurysm, are similar and hence a detailed discussion is omitted here for the sake of brevity. A summary of the results for the female48 aneurysm along with a comparison to other wall thickness models is provided in the next section.

Although 17 model evaluations do not pose a significant computational burden for the patient-specific AAA models considered in this section, it is noted that several ways to further reduce the computational effort without compromising accuracy exist. One way is the use of information from low-fidelity models as outlined in Section 5.3.4. Another option would be to use a formulation which admits the incorporation of gradient information as described in [73, 95]. The implementation of a parameter continuation scheme would also further expedite the computation of multiple realizations of the wall thickness.

7.3.3.3 Comparison of different stochastic thickness models

Having discussed the methodological aspects in the previous two sections, the present section addresses the comparison of the different probabilistic stochastic wall thickness models from a mechanical point of view. First, the results obtained with the simplest stochastic wall model C are discussed. As expected and shown in Figure 7.13, the magnitude of the wall stress decreases with increasing wall thickness. The clearly nonlinear relationship between the peak stress and the wall thickness can also be seen in Figure 7.12a. Since the simple random variable model results in a spatially constant wall thickness across the geometry of the aneurysm, the spatial stress pattern remains similar for different values of the wall thickness. This pattern is determined by the overall geometry of the AAA with the local ILT thickness also having a significant impact on wall stress. While only the stress pattern of the male65 aneurysm is shown in Figure 7.13, the female48 aneurysm behaves in the same fashion and hence a contour plot of the stresses is omitted.

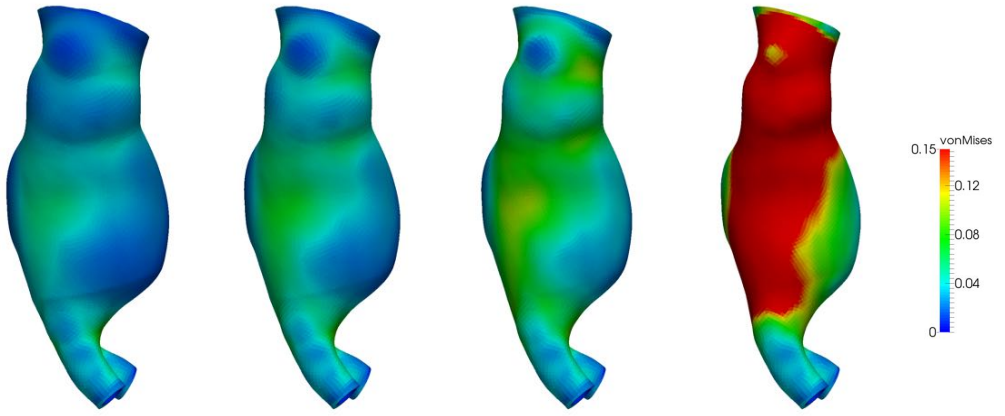

(a) $t = 4.45$ mm **(b)** $t = 3.44$ mm **(c)** $t = 2.43$ mm **(d)** $t = 1.41$ mm

Figure 7.13 Computed von Mises stresses for different uniform wall thickness values for male65 aneurysm. Stresses are shown in MPa.

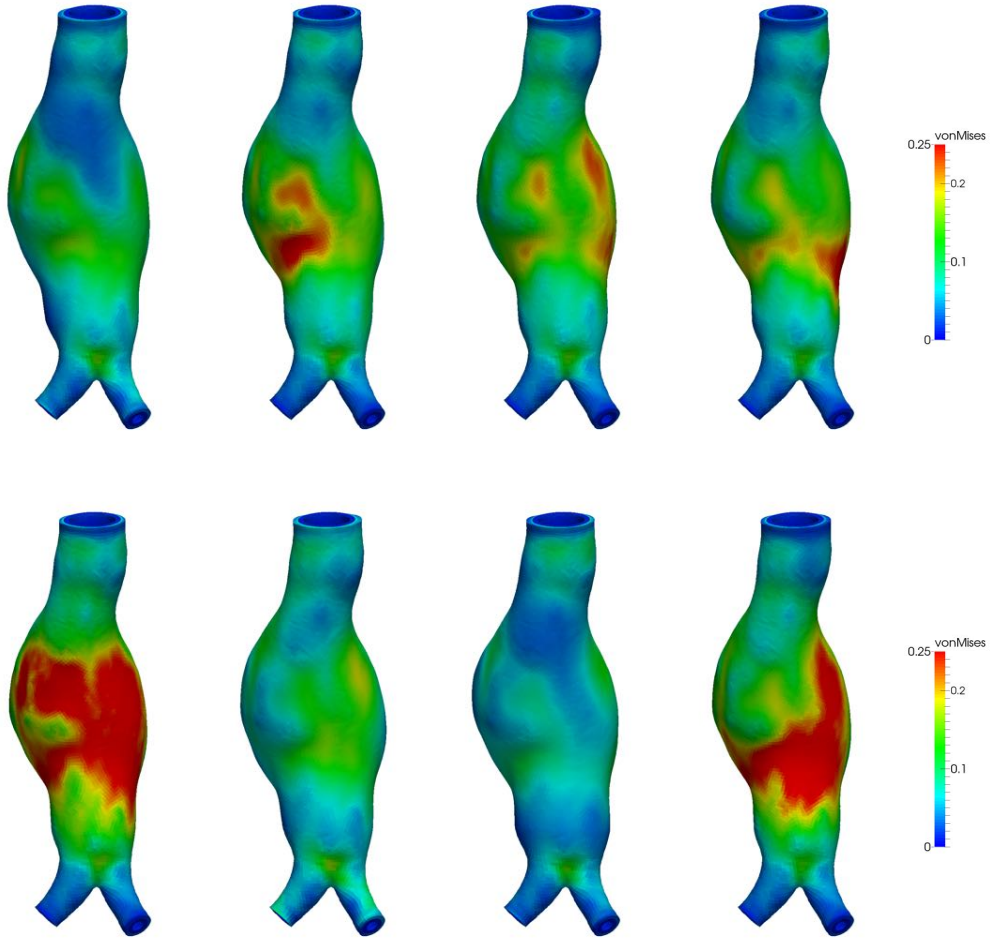

Figure 7.14 Von Mises stresses in female48 aneurysm wall for eight MC samples based on stochastic wall model B. Stresses are shown in MPa.

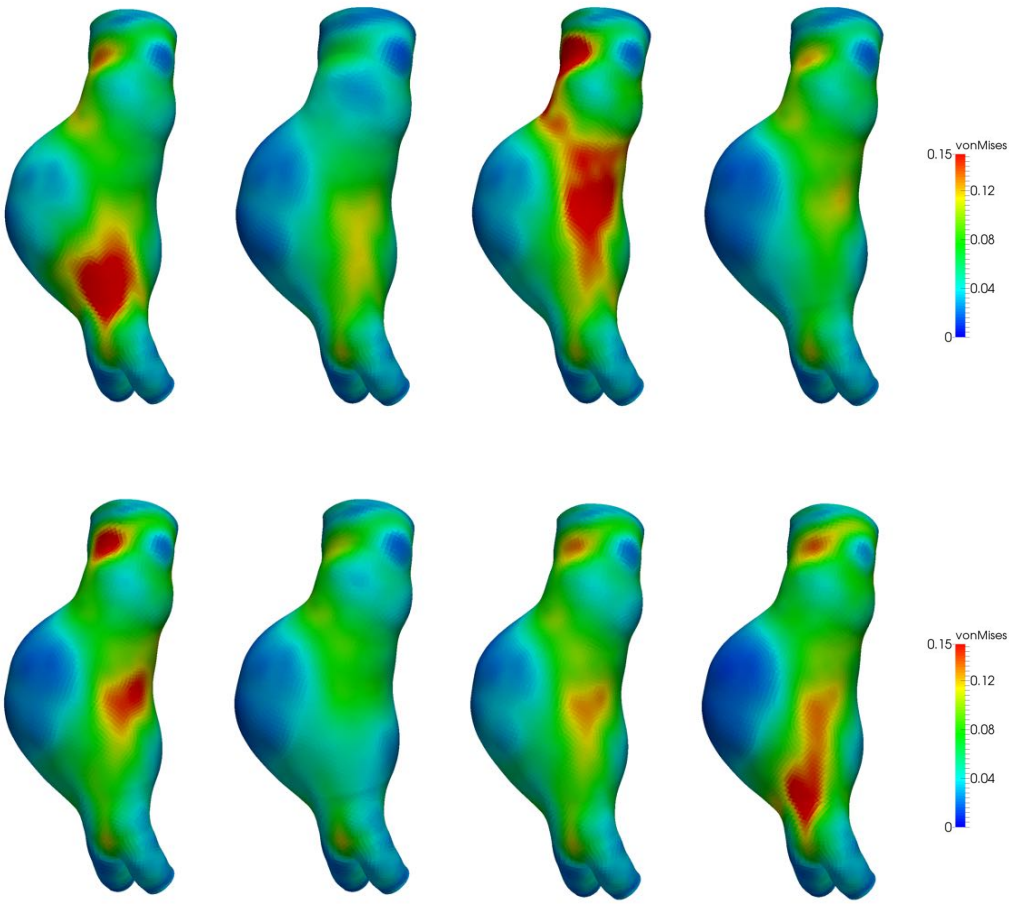

Figure 7.15 Von Mises stresses in male65 aneurysm wall for eight MC samples based on stochastic wall model B. Stresses are shown in MPa.

In contrast, if the uncertain wall thickness is modeled by a random field, the spatial stress pattern is, in addition to the geometry of arterial wall and ILT, drastically influenced by the spatial wall thickness distribution of the realization of the random field describing the wall thickness. The spatial stress pattern varies significantly between realizations, as shown in Figures 7.14 and 7.15, which depict the von Mises stress for eight different realizations of the stochastic wall thickness for both studied patients. In both Figures the realizations are based on the probabilistic wall model B. Based on this qualitative comparison alone, the differences between an uncertain but spatially constant wall thickness and an uncertain wall thickness model which takes into account spatial variation, i.e., intra-patient variations, as well, become apparent.

Qualitatively, stochastic wall model A and B yield similar results, in the sense that both stochastic wall models result in an overall wall stress pattern that is heavily influenced by the particular realization of the wall thickness. Quantitatively though, the results for model A and B are different. Figure 7.16 shows a comparison between the computed probability distributions of $\sigma_{\max}$ for all three wall models and for both patients. In the left column of Figure 7.16 estimates of the PDFs are shown and in the right column failure probabilities are plotted. In addition, Table

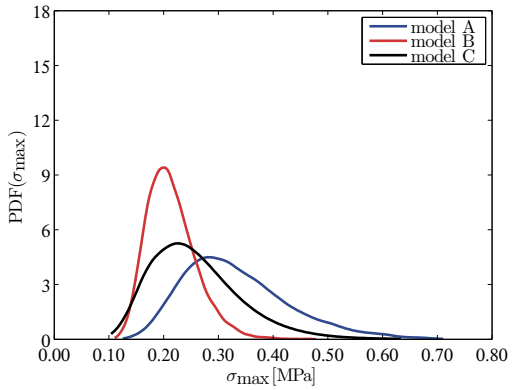

(a) PDFs of σ_{max} female48 aneurysm

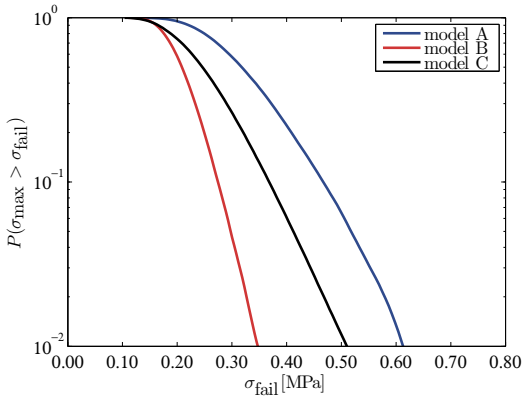

(b) Failure probability female48 aneurysm

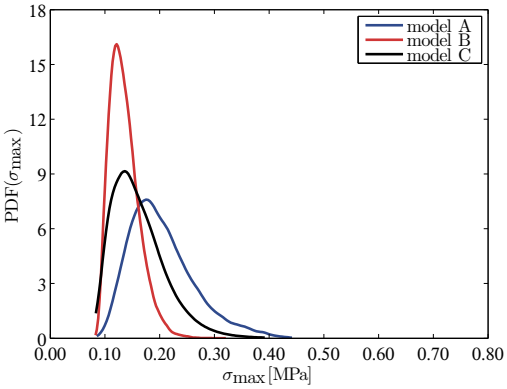

(c) PDFs of σ_{max} male65 aneurysm

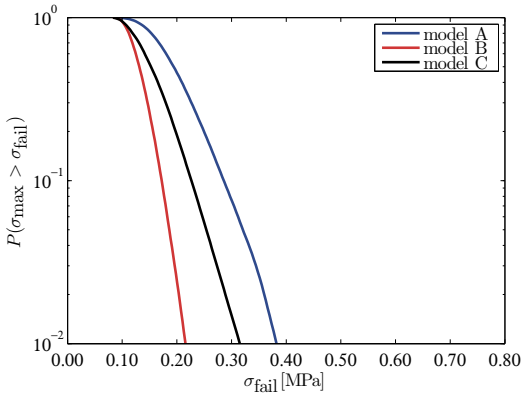

(d) Failure probability male65 aneurysm

Figure 7.16 Comparison of distribution of σ_{max} for the three considered stochastic wall models. PDFs and failure probability for female48 aneurysm are shown in the top row. PDFs and failure probability for male65 aneurysm are shown in the bottom row.

7.8 provides a summary of computed mean, variance, and 95% quantile of all distributions. In comparison with wall model A, wall model B yields lower mean values for the peak wall stress. The expected value of the peak wall stress is reduced from 0.332 MPa (model A) to 0.215 MPa (model B) for the female48 aneurysm and from 0.204 MPa to 0.135 MPa for the male65 aneurysm, cf. Table 7.8. Moreover, the variance of the peak wall stress, in other words the uncertainty about the peak wall stress, is markedly smaller if the simulations are performed with wall model B as compared to model A. In face of an uncertain wall thickness the 95% quantile of the peak wall stress could serve as a worst case estimate. As can be seen in Table 7.8 these values are significantly higher than the expected value. Also regarding this metric, wall model B leads to significantly lower values. Under the assumption that a failure threshold σ_{fail} can be specified, an exceedance probability, which is shown for a range of thresholds in Figure 7.16, can be computed. As can be seen in Figure 7.16, the wall thickness model has a drastic influence on the computed failure probability as well. The reduced output uncertainty

patient	model	$\mathbb{E}[\sigma_{\max}]$ [MPa]	$\mathbb{V}[\sigma_{\max}]$ [MPa^2]	95% quantile of $\sigma_{\max}$ [MPa]
female48	model A	0.332	0.0094	0.519
female48	model B	0.215	0.0021	0.298
female48	model C	0.259	0.0069	0.412
male65	model A	0.204	0.0036	0.321
male65	model B	0.135	0.0007	0.186
male65	model C	0.161	0.0024	0.254

Table 7.8 Comparison of mean value, variance, and 95% quantile of peak wall stress for different stochastic wall thickness models.

of the stress is the result of a reduced uncertainty in wall thickness, highlighting the benefit and potential of the data-driven stochastic wall model B developed in Chapter 6. The lower expected value of $\sigma_{\max}$ can also be attributed to the improved stochastic wall thickness model. For the studied patients, the predictive distribution of the regression models has a higher mean value across the whole geometry of the AAAs, compared to study population average predictions. However, results might be different for other AAAs.

Regarding a comparison between random variable model A and the random field model C it is noted that, although the variance of the thickness is the same in model A and model C, the random field model results in greater expected values, variance and 95% quantile of the peak wall stress, cf. Table 7.8. This effect occurs in both of the studied patients. Despite the fact that model A and model C have the same variance, the probability for a region with very thin wall thickness, which in turn results in high stresses, is much higher in the random field case (model A). As a result, the computed peak wall stress is, on average, higher. Neglecting intra-patient variations in thickness and opting for the random variable model in an UQ analysis seems questionable in light of these results.

Finally, it is important to reemphasize, although this result was expected, that the peak wall stress is very sensitive to variations in wall thickness. Hence, uncertainty in wall thickness translates to a considerable uncertainty in computed wall peak stress. Reliable simulation results and computational AAA rupture risk stratification consequently require a consideration of these uncertainties.

7.4 Models with multiple sources of uncertainties

Although the stochastic dimension in the examples considered this far was very high, all examples were limited to one uncertain physical parameter. The aim of the present section is to demonstrate in a proof of concept fashion that problems with more than one uncertain physical parameter, all of which are modeled as random fields, can be tackled with the BMFMC approach.

In case of multiple uncertain model parameters, each of those can be modeled individually as random field using the approaches for the generation of realizations described in Section 3.3.3 if the parameters are uncorrelated. If these parameter are correlated, cross-correlated random vector fields should be used as a probabilistic model. However, the generation of non-

Gaussian cross-correlated random vector fields is more involved and an area of ongoing and vivid research. In this work a restriction to random fields which are not cross-correlated is made for ease of exposition and to avoid speculation about potential cross-correlation structures between different model parameters. Nevertheless, references to the literature regarding the generation of non-Gaussian cross-correlated random vector fields can be found in Section 3.3.5. While sample generation certainly will be more involved in the cross-correlated random vector field case, the author does not see a reason why the proposed BMFMC should not work in this case as well.

7.4.1 Examples

Generic artery In addition to the uncertain constitutive parameter β an uncertain wall thickness is considered as well. Therefore, the model of a hollow cylinder with a radius of 15 mm and a length of 200 mm that can be interpreted as a model of a generic artery is exemplarily considered here. As with the patient-specific AAA models simple clamped boundary conditions are applied at the in- and outlets of the artery segment and a traction orthogonal to the deformed configuration is imposed, to mimic a luminal blood pressure of 160 mmHg on the inner surface of the cylinder. To reduce the computational burden only the upper half of the cylinder is considered and symmetry boundary conditions are applied on the cut surfaces. Note that due to the asymmetric spatial distribution of the uncertain properties the deformation of the full cylinder will in general not be symmetric and computing only half the model will introduce an error. However, as this example is shown here in a mere proof of concept fashion, this sacrifice is made for the benefit of shorter computation times. The stochastic constitutive law described in Section 7.2.2 is used as stochastic material model for the wall of the cylinder. The wall thickness of the cylinder is also modeled by a log-normal random field, realizations of which are also computed using (3.85) and (3.90). For the sake of brevity a restriction to one variant of this example is made, i.e., for both fields a squared exponential covariance function with a correlation length of $\ell = 25$ mm is considered. The parameters of the marginal log-normal distribution of the random field describing the wall thickness are set to $\mu_t = 0.447$ and $\sigma_t = 0.333$, respectively. These parameters result in a spatially varying wall thickness that covers roughly the range between 0.5 and 4 mm. In this example, it is assumed that the two fields describing the constitutive parameter β and the wall thickness, respectively, are not cross-correlated.

As before two models of different fidelity are created. A high-fidelity model, a realization of which is shown in the left part of Figure 7.17, with 24000 elements and 98532 degrees of freedom, and a low-fidelity approximate model, shown in the right part of Figure 7.17. The low-fidelity model consists of 300 elements and 2046 degrees of freedom. To further reduce the computational cost of the low-fidelity model only a reduced luminal pressure is applied. By applying only half the load, the number of necessary load steps in the nonlinear solution scheme is cut in half as well. The result is a low-fidelity model which is approximately 120 times cheaper to evaluate than the corresponding high-fidelity model. Of course, the reduced load will result in a dramatic underestimation of, e.g., the wall stress computed with the low-fidelity model. The resulting CPU times required for one model evaluation along with the numbers of degrees of freedom are summarized in Table 7.9 for the two models. Simulations of the low-fidelity model were computed on one core, whereas for the high-fidelity model four cores were used.

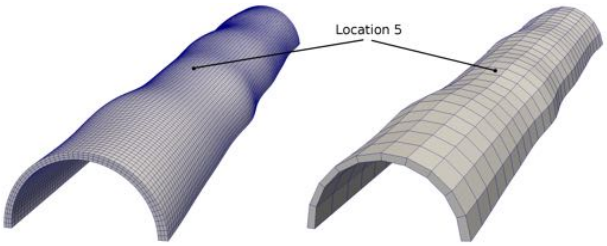

Figure 7.17 One realization of high-fidelity (left) and low-fidelity (right) finite element model of the generic artery example.

model version	solution time (CPU seconds)	dofs
high-fidelity	4800	98532
low-fidelity	42	2046

Table 7.9 Generic artery example: size of studied finite element models in degrees of freedom (dof) and solution times for one sample.

For the sake of brevity the results of the BMFMC approach are discussed based on one quantity of interest. Here the von Mises stress at a specific location was chosen. The location is indicated in Figure 7.17 as location 5 and will be referred to as such from here on. The overall procedure is the same as described before for the patient-specific examples. A MC reference solution for the low and high-fidelity model was computed using 50000 samples. Then, as described previously, 200 samples from both models are used as training data to infer the conditional probability distribution $p(y_{\text{hi-fi}}|y_{\text{lo-fi}})$, which then allows us to compute the approximation $\hat{\pi}(y_{\text{hi-fi}})$.

Patient-specific example As showcase patient-specific example the male71 patient is considered here. The model setup for the high-fidelity as well as the low-fidelity model is the same as described in Section 7.2. For maximum efficiency the low-fidelity model obtained through coarsening of the discretization and omitting the ILT is used here. The difference here is that both constitutive parameters α and β are considered uncertain and are modeled by random fields. The parameters provided in Table 6.4 are used for mean and standard deviation for a Gaussian random field for the log of both parameters, resulting in a log-normal random field for both material parameters. For both fields a correlation length of 12.5 mm was chosen and the two random fields are considered to be independent. Realizations are computed using the Fourier series expansion given in 3.79. The truncation threshold n_k was set to 220, such that the truncated expansion accounts for more than 90% of the variability of the fields. 20000 samples were computed for both models to obtain a MC reference solution in addition to the BMFMC solution for comparison. To further reduce the computational costs the parameter continuation scheme described in Section 5.2.5 was used in the computation.

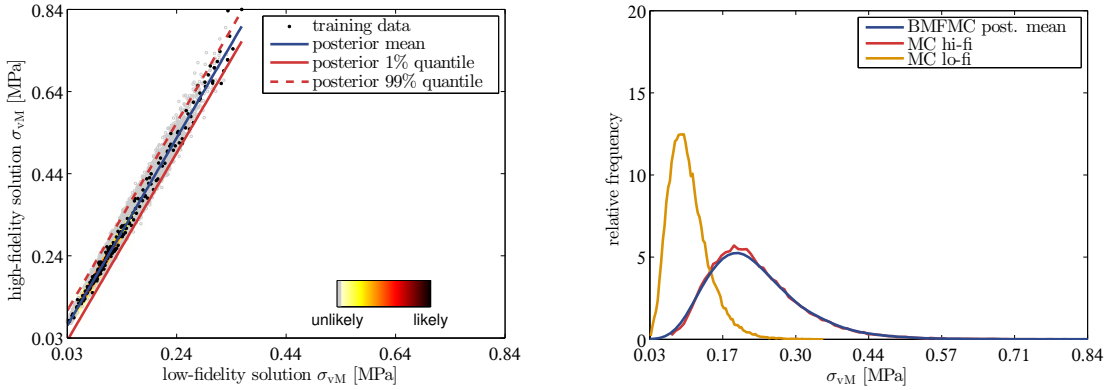

(a) low-fidelity vs. high-fidelity solution.

(b) Empirical PDFs of σ_{vM} at location 5.

Figure 7.18 BMFMC results for generic artery with uncertain constitutive parameter and wall thickness. (a) Comparison between low-fidelity solution and high-fidelity solution at location 5. (b) Comparison between computed densities for σ_{vM} at location 5 from low-fidelity model $p(y_{\text{lo-fi}})$, high-fidelity model $p(y_{\text{hi-fi}})$ and posterior mean approximation $\hat{\pi}(y_{\text{hi-fi}})$.

7.4.2 Results

Generic artery The plots in Figure 7.18 provide a summary of the results. In Figure 7.18a a comparison between the solution of the low-fidelity model and the corresponding solution of the high-fidelity model is shown. In this example the relationship is essentially linear. Furthermore, it can be seen that the stress values computed by the low-fidelity model are obviously considerably lower than the ones computed with the high-fidelity model due to the reduced pressure which is applied to the low-fidelity model. This difference is also evident in the computed histograms which are shown in Figure 7.18b. The distribution of the stress computed with the coarse model is shifted to the left compared to the MC reference solution. However, the magnitude of the stress is mainly determined by the local wall thickness and this dependency can also be captured by the coarser model with reduced load. Hence, the posterior mean approximation $\hat{\pi}(y_{\text{hi-fi}})$, computed using the BMFMC approach, matches the MC reference solution $p(y_{\text{hi-fi}})$ very well. The relative errors in mean, COV, and 95% quantile are 0.059%, 1.44%, and 0.63%, respectively. Using the BMFMC approach the computational costs can be reduced to the equivalent of approximately 640 full evaluations of the high-fidelity model. As expected, the results show a high variability of the stress at the evaluated location (COV = 0.369) due to the variable wall thickness.

Patient-specific example For the comparison between MC reference and BMFMC the von Mises stress at location 4 (see Figure 7.3) and the peak von Mises stress occurring within the AAA wall are evaluated. Again, note that the 99% quantile instead of the true maximum was used. The relationship between low-fidelity and high-fidelity model, the probability densities, and failure probabilities are shown in Figure 7.19. The left column shows the results for the von Mises stress at location 4 while the right column shows the results for the maximum von Mises stress.

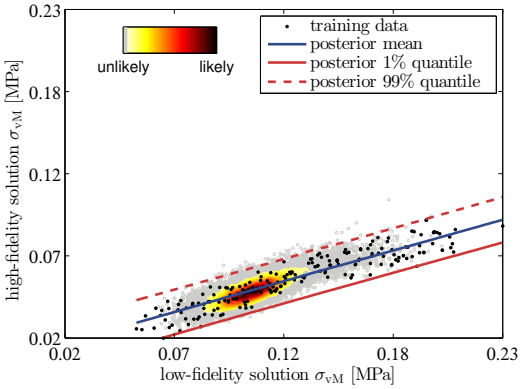

(a) low-fidelity vs. high-fidelity solution σ_{vM} at location 4.

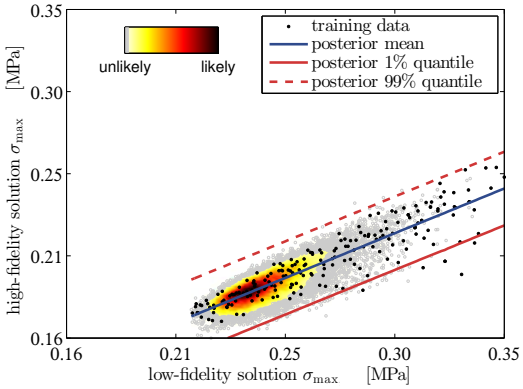

(b) low-fidelity vs. high-fidelity solution σ_{max}.

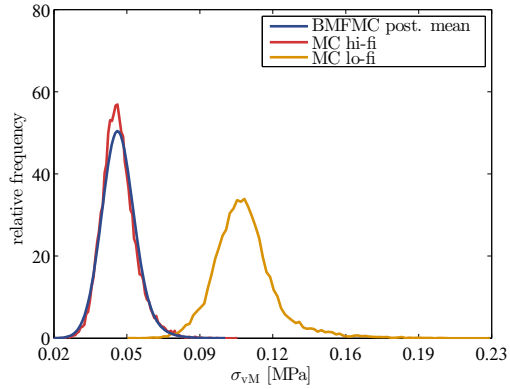

(c) PDF of σ_{vM} at location 4.

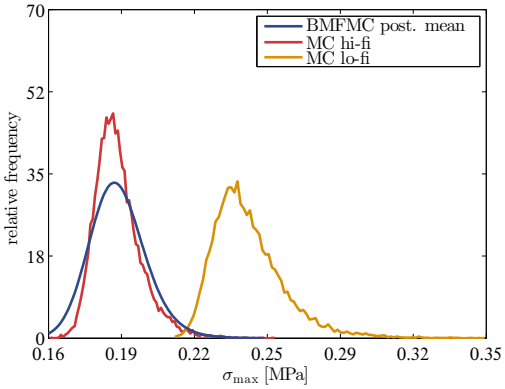

(d) PDF of $\sigma_{\text{vM,max}}$.

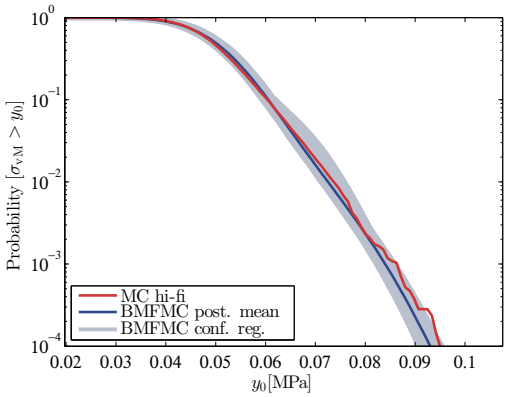

(e) Failure probability based on σ_{vM} at location 4.

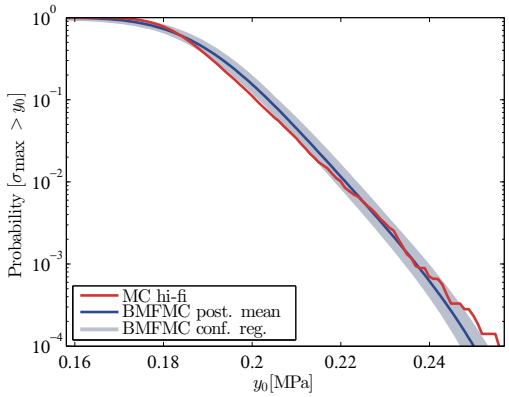

(f) Failure probability based on σ_{max}.

Figure 7.19 BMFMC results for male71 patient with uncertainty in both constitutive parameters. Top row: Comparison between low-fidelity solution and high-fidelity solution of σ_{vM} at location 4 (a) and $\sigma_{\text{vM,max}}$ (b). Middle row: Comparison between densities from low-fidelity model $p(y_{\text{lo-fi}})$, high-fidelity model $p(y_{\text{hi-fi}})$, and posterior mean approximation $\hat{\pi}(y_{\text{hi-fi}})$ for σ_{vM} at location 4 (c) and $\sigma_{\text{vM,max}}$ (d). Bottom row: probability of exceeding a failure threshold. Comparison of MC reference solution to BMFMC posterior mean approximation and posterior quantiles for σ_{vM} at location 4 shown in (e) and $\sigma_{\text{vM,max}}$ (f).

In both cases the relationship between low-fidelity model and high-fidelity model is essentially linear with a considerable amount of noise. On average the results obtained with the low-fidelity model show higher values due to the omitted ILT in the low-fidelity model. Especially for the von Mises stress at location 4, the agreement between the MC and the BMFMC solution is excellent, as can be seen by comparing the probability densities in Figure 7.19c.

For the peak wall stress the results are still good, but there exists a noticeable difference between the MC reference solution and the BMFMC estimate. The difference in the distributions can be also seen when comparing failure probability in Figure 7.19e and 7.19f. The BMFMC deviates from the MC reference solution and the computed confidence interval does not contain the MC reference solution for a considerable range of failure thresholds y_0. Table 7.10 shows a comparison of mean, COV, and 95% quantile of the respective quantity of interest computed with both MC and BMFMC. The relative error between the two solution methods is also provided. For the von Mises stress at location 4, the small relative errors reported in Table 7.10 confirm the previous visual assessment of an excellent agreement between MC reference and BMFMC solution. For the peak wall stress, the mean and 95% quantile show a very small error with 0.142 % and 1.115 %, respectively. The COV, however, shows a larger error and the BMFMC estimate deviates perceptively (18.1%) from the MC reference solution.

An explanation for the impaired performance can be found through a closer examination of the relationship between low-fidelity and high-fidelity model output in Figure 7.19b. In addition to the used training samples, posterior mean and quantiles of the regression model a 2D color coded histogram depicts the relation between low-fidelity and high-fidelity model. The histogram reveals that the conditional distribution $p(y_{\text{hi-fi}}|y_{\text{lo-fi}})$ is not symmetric but skewed and that the variance of the distribution is not constant but varies with $y_{\text{lo-fi}}$.

The inference of the parameters of the regression is based on a Gaussian likelihood with a constant variance, in the sense that it does not depend on $y_{\text{lo-fi}}$. In other words, the regression approach is based on the assumption of a homoscedastic and Gaussian error or noise term. Both of the assumptions are clearly not fulfilled in the peak wall stress example given here leading to an impaired performance of the method. In the absence of a reference solution examination of the regression residuals can provide insights regarding the validity of the made assumptions. The residual, i.e., the difference between actual ($y^{(i)}_{\text{hi-fi}}$) and corresponding posterior mean prediction ($\hat{y}^{(i)}_{\text{hi-fi}}$) can be readily computed for each of the training samples. If the noise is Gaussian, the residuals will also approximately follow a Gaussian distribution which can be visually assessed in a so called normal probability plot.

QOI	MC reference			posterior mean BMFMC			relative error [%]		
	mean	COV	95% q.	mean	COV	95% q.	mean	COV	95% q.
σ_{vM} at loc. 4	0.0500	0.1626	0.0644	0.0500	0.1675	0.0643	0.074	2.985	0.190
$\sigma_{\text{vM,max}}$	0.1876	0.0549	0.2068	0.1880	0.0649	0.2091	0.142	18.072	1.153

Table 7.10 Comparison between MC reference solution and BMFMC approach.

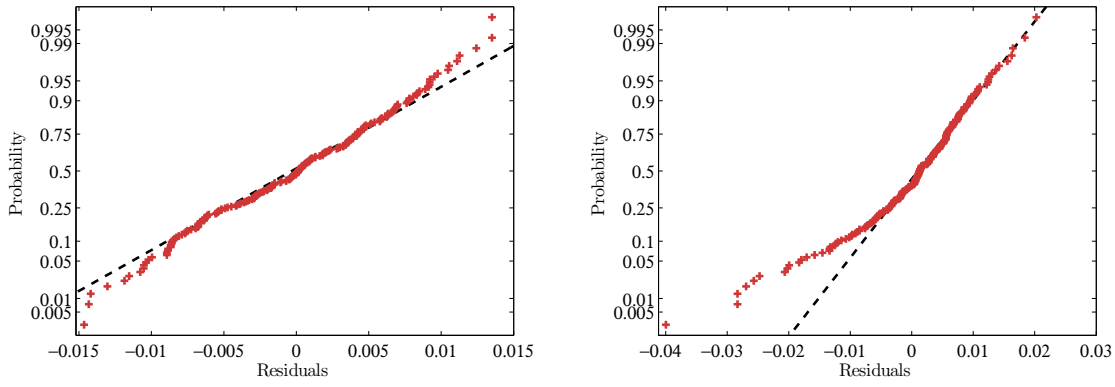

Figure 7.20 Normal probability plot of residuals between posterior mean prediction of high-fidelity result by regression model and actual high-fidelity results. Plot in (a) shows residuals of σ_{vM} at location 4, whereas (b) shows residuals for peak wall stress $\sigma_{\max}$.

Normal probability plots for the residuals of the two examples studied here are shown in Figure 7.20. The normal probability plot of the residuals of the von Mises stress at location 4 resembles a straight line, indicating approximately Gaussian distributed residuals. In contrast, residuals obtained for the peak wall stress example deviate substantially from a straight line suggesting a departure from normality. It is emphasized that the training samples alone are sufficient for this assessment and a MC reference solution is not needed. This is important because it means that problematic cases with, e.g., highly skewed noise can be detected without having a high-fidelity Monte Carlo reference solution. Consequently, the low-fidelity model could be discarded or another likelihood function could be used. Another option is to choose to use current setup nonetheless, while being aware of the limitations and the possibility that the method will not provide optimal results.

Regarding the computational costs, the solution time for one sample of the low-fidelity model could be reduced to a mere 32 CPU seconds using the parameter continuation scheme. The generation of random field realizations is significantly cheaper if the Fourier expansion is used and hence the solution time for the low-fidelity model could be further reduced. In combination with the high-fidelity model the simple parameter continuation scheme used here sometimes needed more continuation steps to converge because the solution of the different realizations of the problem were ”further apart” from the initial solution. Roughly a factor of 2.7 compared to the computational effort associated with the regular nonlinear solution scheme was achieved. More elaborate, truly adaptive continuation schemes could perhaps improve the performance and should be investigated in the future. The computational cost of the BMFMC scheme for this example are approximately 217 CPU hours for the 200 high-fidelity solutions plus 178 CPU hours for the 20000 low-fidelity examples, resulting in less than 400 CPU hours in total. Compared with the computational cost of 60000 CPU hours of a standard MC scheme without parameter continuation, the employed BMFMC scheme is roughly 150 times cheaper and the total computational cost amounts to 134 evaluations of the high-fidelity model.

7.5 Concluding remarks

In this chapter the BMFMC framework was applied to complex nonlinear biomechanical models with patient-specific geometries and uncertain constitutive parameters or geometry. Thereby, uncertain parameters were modeled as three dimensional non-Gaussian random field, leading to a high stochastic dimension of the problem at hand. By combining multi-fidelity sampling with non-parametric Bayesian regression the full probability distribution function of the quantities of interest can be approximated at a fraction of the computational costs, compared to direct sampling of the accurate, high-fidelity model. It was shown that the BMFMC approach achieves an excellent agreement with MC reference solutions. In addition, the remarkable efficiency of the BMFMC approach can, for certain types of problems, be further improved if parameter continuation schemes are used. In this case, the computational costs of UQ can often be reduced to the equivalent of a few hundred runs of the high-fidelity model. This renders UQ for complex biomechanical problems feasible on standard computing platforms.

All further conclusions derived from the results in this chapter are subdivided into two parts. First, the implications of the obtained results for computational rupture risk assessment of AAAs are discussed in the next section. Then, conclusions regarding the methodological aspects of BMFMC are drawn.

7.5.1 Implications for computational rupture risk assessment of AAAs

Considering the above results with regard to reliable AAA rupture risk assessment, it is concluded that purely deterministic models are not sufficient for the accurate patient-specific assessment of AAA rupture potential. While stress based failure or rupture models [100, 109, 203, 337] are rather insensitive to uncertainties in constitutive parameters, uncertainty in wall thickness severely affects the spatial stress pattern and the peak wall stress.

By comparing a random variable with random field wall thickness models it could be shown that neglecting intra-patient variations leads to different results and that the variability is potentially underestimated when using a random variable model. Furthermore, the comparison of different data-driven random field wall thickness models has shown that harnessing all non-invasively available data for the construction of patient-specific stochastic wall thickness models results in reduced uncertainty of the computed peak wall stress for the examples considered here. The utilization of these types of probabilistic model should be extended to other uncertain parameters as well. First and foremost, a probabilistic wall strength model should be considered. In combination with stochastic wall strength models a stochastic failure measure could be defined, which could in turn result in a more reliable estimate of AAA rupture risk. A first step in this direction was recently done by Polzer and Gasser [253], who combined the probability distribution of the peak wall stress and a probability distribution of the wall strength to compute a probabilistic failure measure. However, both the wall thickness and the wall strength were modeled as random variable and the wall thickness was considered as the only source of uncertainty.

While only isotropic constitutive laws were considered in this work, it should be pointed out that the proposed approach can of course also be applied if more complex, e.g. anisotropic, constitutive models are used. Although many of the conducted studies assess rupture potential

by computing wall stresses based on an elastic model, including anisotropic ones, it has been pointed out previously that the damage and failure process of soft tissue is more involved and cannot be captured with purely elastic models employing a von Mises stress based failure criterion [107, 206, 251, 278, 345, 347]. These advanced tissue damage and failure models, e.g., based on the evolution of the isochoric stored strain-energy of the material, as proposed by Simo [303] and applied to AAAs by Marini et al. [206] require accurate prediction of the prevailing strain and strain-energy. Thus, constitutive properties will have a greater influence on the results as compared to the situtations where the wall stress is the only quantity of interest.

However, regarding mechanical properties of the AAA wall, the more important limitation which has to be pointed out is that it is well known that several growth and remodeling processes constantly rebuild and transform the tissue in the arterial wall. Hence, cardiovascular structures such as AAAs are subject to ongoing growth and remodeling processes. Therefore, localized areas with high strain or stress are likely to be remodeled diminishing such peaks in the tissue. However, the issue of uncertain model input parameters persists if growth and remodeling processes are considered and uncertainty quantification remains essential in order to provide reliable results and confidence bounds.

Therefore, detailed statistical and probabilistic models based on empirical data and rigorous UQ is the only way to obtain meaningful and reliable results in lack of truly patient-specific parameters Future research should include studies in which all uncertain model input parameters are taken into account. Aside from uncertainties in constitutive properties of the wall and the wall thickness, this includes uncertainties regarding the ILT as well as boundary conditions. Cross correlations between different parameters should, of course, be considered as well.

7.5.2 Methodological aspects

It has been shown that the BMFMC approach yields accurate results at drastically reduced costs for various examples. One of the major advantages of the approach is the tremendous flexibility regarding the construction of low-fidelity models. In this chapter low-fidelity models based on a coarser discretization, model reduction, and a quasi analytic scaled-thickness model have been used to demonstrate this capability. It was shown that the method yields accurate results even if the low-fidelity model provides only a very poor approximation and the difference between low-fidelity solution and high-fidelity solution is large.

Although it is difficult to judge a priori whether a low-fidelity model is suitable for use within the BMFMC approach, it is crucial to stress that the adequacy of the model can be judged without having a full MC reference solution of the high-fidelity model. While a clear interrelation between low-fidelity and high-fidelity model existed in all examples shown in this work this might not always be the case. However, the full statistical toolkit can be utilized to assess the validity and quality of the chosen regression approach in combination with the available training data. The definition of a full set of validation steps and heuristics should be considered in future research to provide guidelines or threshold for the acceptance or rejection of a specific low-fidelity in the BMFMC scheme. In addition, more detailed guidelines or an adaptive scheme to determine the number of necessary training samples based on the statistical summary of interest and on the strength of the correlation between low-fidelity and high-fidelity solution would be beneficial in order to maximize the efficiency of the BMFMC approach.

For the examples studied in this chapter, both of the employed regression approaches investigated in combination with the BMFMC scheme generally provided very good results. An exception was the example where the conditional probability distribution $p(y_{\text{hi-fi}}|y_{\text{lo-fi}})$ was highly skewed and the magnitude of the variance term was dependent on $y_{\text{lo-fi}}$. In these cases the assumption of a Gaussian likelihood with input independent variance, which is made in both the GP regression and the Koutsourelakis regression approach, can result in impaired performance of the BMFMC approach because the conditional distribution cannot be accurately captured. For these scenarios different regression approaches with a more flexible error term to allow for skewed distributions and variable variance have to be investigated. Several formulations and concept for this task have been proposed in literature, see, e.g., [181, 248, 321, 351, 352, 371]. The investigation and comparison of these approaches is, however, beyond the scope of this work but should be considered in future research.

Aside from exploiting cheap low-fidelity models, it was demonstrated that exploiting the problem structure and using continuation in material properties further expedite the solution of a UQ problem. It is noted that this strategy could be applied in many UQ schemes and is not limited to the presented multi-fidelity approach advocated here. The performance of the continuation scheme depends on the difference between the solution for the different realizations and the used reference solution. The greater the difference the more continuation steps are required. The use of more elaborate continuation schemes would likely further reduce the computational effort compared to the relatively simple approach employed here.

Lastly, it is emphazised that the developed geometry adjustment algorithm is crucial for the study of uncertain geometries. Generating realizations of the random geometry in a separate preprocessing step and having separate input files for each realization would be impractical even if only a moderate number of samples are needed. Moreover, it is stressed that the actual time to solution is drastically reduced due to ability to compute samples, i.e., to solve the forward problem, in a concurrent fashion on high performance computing platforms. While plain MC sampling can be parallelized simply by running multiple instances of the code, this is no longer the case for advanced sampling schemes such as SMC, which requires some communication between strands to perform, e.g., resampling steps. This is important as SMC schemes present another option to further improve the efficiency of the developed framework [183], especially if one is interested in estimating very small failure probabilities.

8 Uncertainty quantification in reduced order lung models

Acute Lung Injury (ALI) and Acute Respiratory Distress Syndrome (ARDS) are both life threatening diseases. Their treatment requires mechanical ventilation, which can lead to further damage of the lung due to overinflation, barotrauma, and cyclic closing and reopening of the alveoli [265]. The damage caused by mechanical ventilation is generally referred to as Ventilatory Associated Lung Injury (VILI). Mortality rates as high as 49% and 59% for ALI and ARDS, respectively [332], have spurred a tremendous amount of research to enhance the understanding of the nature of the lung damage and to improve mechanical ventilation protocols. Besides *in vivo* and *ex vivo* experiments, computational studies based on numerical models of the entire lung or parts thereof have contributed to a deeper understanding of the underlying phenomena which govern the onset of VILI.

Research indicates that amongst other factors the amount and rate of local mechanical deformation, i.e., strain in the tissue plays a major role in inflammatory processes and ultimately tissue damage [229, 259]. A recently developed comprehensive computational model of the entire human lung allows the computation of these mechanical quantities based on patient-specific lung models [162, 163, 282]. This model can reproduce patient-specific pulmonary physiology and capture local and global pulmonary phenomena and quantities and therefore can be used to study both spontaneous breathing and mechanical ventilation. One of the long term goals of this research aims at the optimization of mechanical ventilation protocols to minimize tissue damage and improve mortality rates. One of the remaining challenges is the personalization of these models regarding, for instance, constitutive parameters. Estimates for these parameters are available from calibrating the model to experimentally measured pressure-volume curves while the patient undergoes mechanical ventilation [281]. Moreover, the relative stiffness of the lung tissue in different regions of the lung can be estimated from CT image data based on the Hounsfields scale or from *ex vivo* uniaxial tensile tests [28, 272]. However, with regard to a particular patient undergoing mechanical ventilation, no exact data is available and considerable uncertainty remains.

In this chapter, the sensitivity of the simulation results with respect to uncertainties in one constitutive parameter is investigated based on a patient-specific, reduced dimensional lung model in a mechanical ventilation scenario. Aside from quantifying the impact of an uncertain stiffness parameter on local and maximum occurring strain within the lung, another major goal of this chapter is to demonstrate that the BMFMC approach can be applied in many circumstances and is not tailored or limited to nonlinear solid mechanics applications.

The remainder of this chapter is as follows. First the anatomy of the lung and the model building process from imaging to simulation model is briefly described in Sections 8.1 and 8.2, respectively. Then, the reduced dimensional lung model is introduced in Section 8.3, followed by the chosen patient-specific example and the description of the stochastic constitutive law in

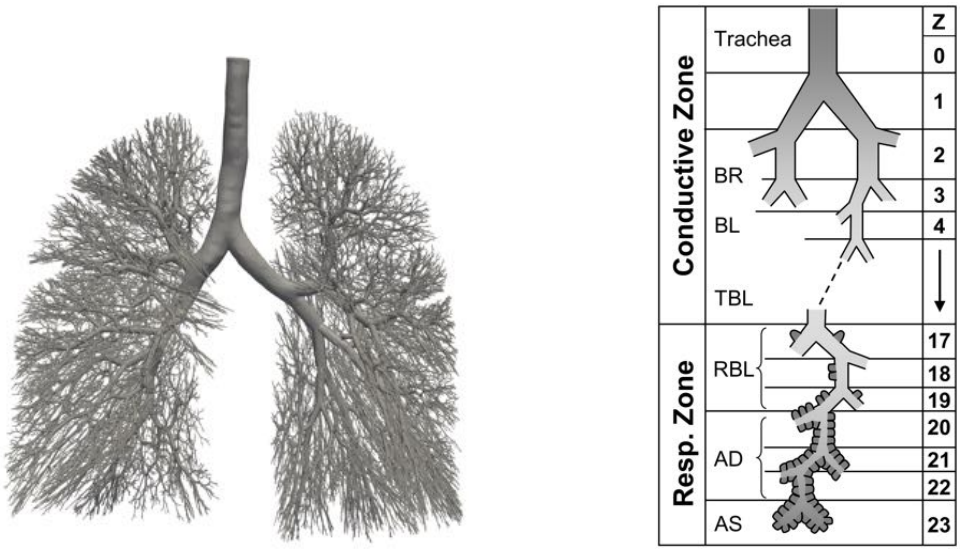

Figure 8.1 Airways of the human lung (a) 3D representation of a 16 generation airway tree of conducting airways, taken from [162]. (b) Human airways according to Weibel's model, adopted from [354]. Abbreviations: Z=airway generation; BR = bronchus; BL=bronchiole; TBL = terminal bronchiole; RBL= respiratory bronchiole; AD= alveolar duct; AS = alveolar sac.

Section 8.4. Therein, the used high- and low-fidelity models are described as well. The results of the performed UQ analysis are reported and discussed in Section 8.5. Conclusions are drawn in Section 8.6.

8.1 Anatomy of the human lung

An extensive introduction and overview of the anatomy and physiology is beyond the scope of this work and the inclined reader is referred to, e.g., [313, 354], for a thorough introduction to the topic. However, the most important aspects of the anatomy of the lung along with the nomenclature necessary to understand the ensuing description of the computational model, are briefly introduced in this section.

The two human lungs with the right and the left lung are composed of three and two lobes, respectively. Both lungs are encapsulated by a thin fluid-filled space called *pleural space*. A thin two-layered membrane structure, called *pleura* encapsulates the pleural space and is attached to the lung on the *proximal* side of the fluid and to the chest wall on the other, *distal* side of the pleural space. At the bottom the lungs are constrained by the diaphragm. While it is usually distinguished between upper and lower respiratory tract, only the lower tract will be described in the following. The lower respiratory tract is comprised of a tree of conducting and respiratory airways and a 3D representation of such a tree is depicted in Figure 8.1. The figure also shows a detailed schematic of the different generations within the lower respiratory tract. The conducting airways, starting with the trachea, ramify into smaller airways and the 1st through 16th generation of these airways form the dead zone in which no gas exchange

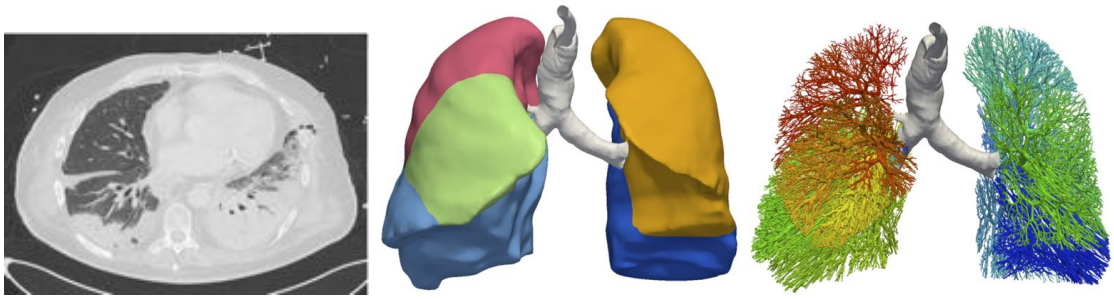

(a) (b) (c)

Figure 8.2 From CT scan to simulation model: (a) Exemplary slice of end-expiratory CT data and (b) segmented 3D lung geometry from CT data. (c) Segmented lower generations and space-filling higher generations of conducting airway. Taken from [281].

occurs [141]. The respiratory zone, where the gas exchange occurs, consists of up to another 7 generation of respiratory airways referred to as acini. The acini are composed of *terminal bronchioles*, *alveolar ducts*, and *alveoli*, as shown in Figure 8.1b.

8.2 From imaging to simulation — reduced order model of the respiratory system

The computational models used here are built for the purpose of simulating mechanical ventilation. Thereby, the goal is to obtain detailed information about the local mechanical state of the lung tissue based on a prescribed pressure at the tracheal inlet. Therefore, the air flow in the conducting airways and the deformation of the acini resulting from the inflow of air has to be modelled. For this, the geometry of the airway tree and a mathematical model for the flow in the airways is needed. The overall geometry of the lung models considered in this study are based on segmented 3D lung geometries from patient-specific CT scans as shown in Figure 8.2. While the lobes and lower generation airways can be segmented from the image data, higher generation airways and acini cannot. The higher generation airways are generated using a space filling tree algorithm described in [163, 323]. The airways are generated recursively by splitting each parent branch into two daughter branches until the peripheral airways reach either a length below 1.2 mm, a radius below 0.2 mm, or the 17th generation. Thereby, the radii of the two daughter branches is not the same but a scaling of the radius for the left and right branch of the tree is 0.876 and 0.686 with respect to the radius of the parent branch. This ratio was chosen according to [205] based on observation in the human body. An example of an airway tree generated with the algorithm is shown in Figure 8.2. For further details regarding the generation of conducting airways trees using space filling algorithms the reader is referred to [163, 323].

With the geometry set up, a flow model is needed. Fully resolved 3D flow models based on the Navier-Stokes equations could be applied; however, their evaluation is to expensive. Moreover, it has been shown that state-of-the-art reduced 0D models for the flow within the airway tree can provide accurate results in these scenarios. Using a reduced dimensional flow model, the desired insight into, e.g., local strain distribution, or over-straining of the acini can be obtained

at an acceptable computational cost. The 0D models for the airways and the acini which are used in this work and briefly described in the following are based on [162, 163, 282]. Therein, the employed model is described in more detail.

8.3 Mathematical model of the human lung

8.3.1 Reduced dimensional airway model

A reduced dimensional model based on the integration of the Navier-Stokes equations can be derived if some assumptions about the geometry of the airways and about the flow in the airways can be made. Specifically, it is assumed that that airways have axis-symmetric cross-sections and negligible curvature. In addition, it is assumed that the flow in the airways has an axis-symmetric velocity profile and that the compliance of the airway wall can be described by a linear elastic constitutive model. Reduced dimensional models can then be obtained by first integrating along the radial direction of the airways and subsequently along the axial direction of the airways as well. For further details on the derivation of the reduced dimensional problem the reader is referred to, e.g, [8, 162]. The resulting equations for the 0D airway according to [163, 281, 282] are given as

$$\begin{aligned} C\frac{dP_{\mathrm{in}}}{dt} + Q_{\mathrm{out}} - Q_{\mathrm{in}} &= 0, \\ I\frac{dQ_{\mathrm{out}}}{dt} + RQ_{\mathrm{out}} + P_{\mathrm{out}} - P_{\mathrm{in}} &= 0. \end{aligned} \tag{8.1}$$

In analogy to components in an electric circuit, C denotes the capacitive, I the inductive, and R the resistive part of the system. The pressure and flow rate at the in and outlets are denoted by P_{in},P_{out} and Q_{in},Q_{out}, respectively. The capacitive part represents the effects of airways compliance and the inductive term is used to take inertial effects of both the air and the airway wall into account. The resistive term is used to model dissipative effects that occur to due air viscosity. A suitable nonlinear resistance model that takes into account turbulent as well as geometric losses within the airway tree, was developed in [249] later and refined in [336] and is used in this work.

8.3.2 Acinar model

A reduced model for the acinus is attached at all terminal ends of the airway tree. The acinar model is based on a four-element Maxwell model, which has been developed in [163] and is shown in Figure 8.3b. The model links the flow rate of air into an alveolar duct model, shown in Figure 8.3a, to the prevailing pressure difference between acinar pressure (P_{a}) and pleural or inter-acinar pressure ($P_{\mathrm{pl/intr}}$) through several maxwell elements consisting of springs and dashpots, cf. Figure 8.3b. Each acinus is assumed to be comprised of a tree of alveolar ducts as shown in Figure 8.3c.

The chosen Maxwell model corresponds to a visco-elastic material model for the acinar tissue. Thereby, nonlinear constitutive behavior of the tissue can be captured by using a nonlinear model for the spring E_1 [282]. An Ogden-type material was chosen here because it can capture

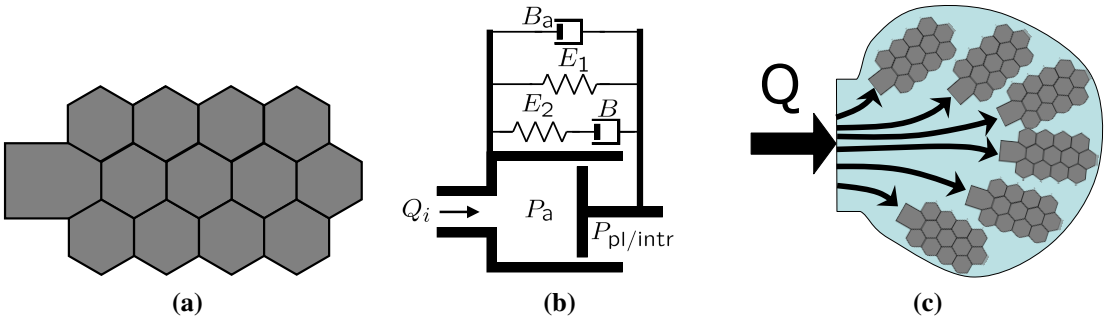

Figure 8.3 Acinus model (a) schematic of an alveolar duct; (b) four element Maxwell model of an alveolar duct, with acinar pressure (P_a), pleural/inter-acinar pressure ($P_\mathrm{pl/intr}$), and flow rate (Q_i); (c) schematic of an acinus filled with a tree of alveolar ducts. Taken from [282].

the volumetric part of the nonlinear constitutive behavior of lung tissue well [28, 272]. Based on an Ogden-type [236] strain-energy function

$$\Psi_\mathrm{ogd} = \frac{\kappa}{\eta^2}(\eta \ln(J) + J^{-\eta} - 1), \tag{8.2}$$

which depends on the Jacobian J of the deformation gradient $\boldsymbol{F}$ and has two constitutive parameters κ and η, the following relation between volumetric deformation of the acini and pressure can be derived

$$P_\mathrm{a} - P_\mathrm{pl/intr} = \frac{\kappa}{\eta}\left(\frac{V_\mathrm{a}}{V_\mathrm{a,0}}\right)^{-1}\left(1 - \left(\frac{V_\mathrm{a}}{V_\mathrm{a,0}}\right)^{-\eta}\right). \tag{8.3}$$

Therein, P_a and $P_\mathrm{pl/intr}$ denote alveolar pressure and the ambient pressure outside the aveolar duct, respectively. The volumetric deformation is given by the quotient between initial volume of the acinus $V_\mathrm{a,0}$ and the current volume of the acinus V_a, i.e., $\varepsilon_\mathrm{vol} = V_\mathrm{a}/V_\mathrm{a,0}$.

8.3.3 Inter-acinar dependencies

Within the lung, neighbouring alveoli and acini cannot deform independent of each other. Since the walls of adjacent alveoli are attached to each other, the individual alveoli and hence also the acini compete essentially for the same volume during expansion and the dynamics of an alveolus is affected by those in its vicinity. Taking this interplay into account is important, in particular for lungs which are heterogeneously distended due to gravitational effects, dynamic non-uniformity of ventilation, or locally varying tissue stiffness. An approach to emulate this behaviour in pure reduced dimensional models was recently described by Roth et al. [282], who suggested the use of inter-acinar linker elements to capture the interactions between adjacent acini. The approach, which is also used in this work, is based on creating a inter-acinar linker element between all neighbouring acini pairs whose distance between their respective centers of gravity is smaller than 1.2 times the sum of their radii. In a second step, the outermost acini interacting with the pleural space are detected in order to be able to prescribe suitable boundary conditions for the problem which mimics the ribcage. This way interactions between adjacent acini can be modelled and their combined volume can be constrained. As explained in detail

in [282], the acini are coupled together based on the balance of forces at their interface, which leads to the following interdependence model for an individual acinus i

$$P_{\mathrm{intr},i} - \frac{P_{\mathrm{pl}}}{N_{\mathrm{adj},i}} - \sum \frac{P_{\mathrm{intr},j}}{N_{\mathrm{adj},i}} = 0, \tag{8.4}$$

where $N_{\mathrm{adj},i}$ is the number of adjacent acini or pleural spaces for acinus i.

8.3.4 Pleural pressure

A lung volume dependent pleural pressure model is used to replicate the constraining effect of the ribcage. Here the following pleural pressure model according to Harris [144] is used:

$$P_{\mathrm{pl}} = P_{\mathrm{pl}}^0 + b_{\mathrm{p}} V_{\mathrm{CP_p}} + c_{\mathrm{p}} e^{(d_{\mathrm{p}} V_{\mathrm{CP_p}})}. \tag{8.5}$$

Therein $V_{\mathrm{CP_p}} = (V - V_{\mathrm{R}})/(V_{\mathrm{TLC}} - V_{\mathrm{R}})$ denotes the *percentile vital capacitance*. The parameters $V_{\mathrm{TLC}} = 6.95\,\mathrm{l}$ and $V_{\mathrm{R}} = 1.95\,\mathrm{l}$ denote the so-called total *lung capacitance* and *residual volume*, respectively. The remaining model parameters of the pleural pressure model were obtained by fitting (8.5) to the measurements given in [144] and were accordingly set to $P_{\mathrm{pl}}^0 = -9.772$ $\mathrm{cmH_2O}$, $b_{\mathrm{p}} = 20.435$ $\mathrm{cmH_2O}$, $c_{\mathrm{p}} = -33.383$ $\mathrm{cmH_2O}$, and $d_{\mathrm{p}} = -7.686$.

8.4 Patient-specific lung model

Based on the process outlined above, a patient-specific lung model is constructed based on CT image data. The CT scans were taken at a predefined positive end-expiratory pressure (PEEP), which corresponds to an end-expiratory lung volume (EELV). In order to apply the BMFMC scheme for UQ, two versions of the model are created. A physiological high-fidelity model with 16 airway generations and 31975 acini. A 3D visualization of the model is depicted in Figures 8.4a and 8.4b. For the low-fidelity version of the model, which is shown in Figure 8.4c and 8.4d, the last five airway generations were omitted and acini are attached at the 12th airway generation. This results in a model with 2039 acini. In order to obtain the same acinar volume, the acini in the low-fidelity model are significantly larger than in the high-fidelity model, cf. Figure 8.4, and no longer have a physiological size.

Mechanical ventilation is simulated by prescribing a pressure P_{t} at the tracheal inlet. The prescribed curve is based on a real mechanical ventilation protocol, which is depicted in Figure 8.5. Before the periodic ventilation pressure curve can be applied, the pleural pressure P_{pl} and the PEEP are ramped up to physiological conditions, which is also shown in Figure 8.5. Usually, to account for transient effects due to the viscosity of the system two breathing cycles are simulated. One ventilation cycle takes $3.1\mathrm{s}$, which together with the ramp up phase results in a total simulated time of 9.3 s for two simulated ventilation cycles.

The maximum pressure of 25 $\mathrm{cmH_2O}$ at the tracheal inlet is reached at 4.4 s and 7.5 s, respectively. For all simulations a time step size of $0.01\mathrm{s}$ was used, which results in 930 time steps for one complete simulation of two ventilation cycles. For the high-fidelity model the computation of 930 time steps requires a total of 98 CPU hours, whereas the low-fidelity model can be solved in a mere 1.1 CPU hours, cf. Table 8.1. Furthermore, the since BMFMC scheme permits the use of very approximate solutions, simulations with the low-fidelity model up to $t = 3.5\mathrm{s}$ were found to be sufficient. This further reduces the computational effort to 0.38 CPU hours.

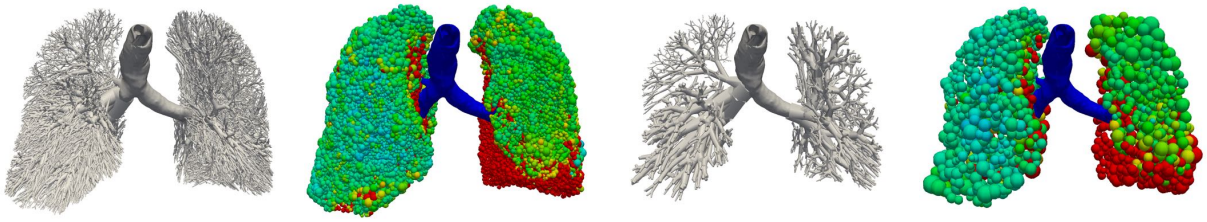

(a) **(b)** **(c)** **(d)**

Figure 8.4 High-fidelity and low-fidelity version of the studied patient-specific lung model. (a) shows a 16 generation airway tree and (b) the corresponding acini. (c) shows a reduced 12 generation airway tree and (c) the acini of the low-fidelity model.

No. generations	No. elements	No. nodes	No. of procs	Total CPU hours
17	280263	107527	6	98 h
12	19241	7376	2	1.1 h
12 up to time step 350	19241	7376	2	0.38 h

Table 8.1 Comparison of model size and corresponding CPU time for the lung models with different number of airway generations.

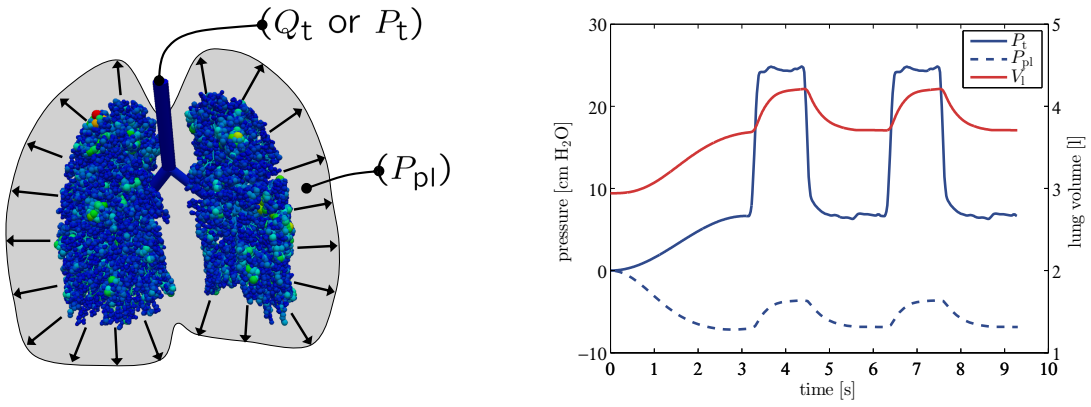

(a) **(b)**

Figure 8.5 Applied boundary conditions in the lung model. (a) Schematic of applied tracheal P_t and pleural P_{pl} pressure boundary conditions. (b) Temporal development of applied tracheal pressure and resulting pleural pressure. Additionally, the resulting time dependent lung volume is show. The curve is based on a deterministic simulation with average value for κ.

Probabilistic constitutive parameter As proposed in [281], a heterogenous tissue stiffness is used in the lung model considered here. Based on the Hounsfield units (HU) in the corresponding CT image data, the acinar stiffness parameter κ is set according to the HU of voxel the acinus falls into, using

$$\kappa = \kappa_0(1 + \frac{\text{HU}}{\text{HU}_{\text{avg}}}). \tag{8.6}$$

Here, HU_{avg} denotes the average HU for lung tissue (in the scan used here, $\text{HU}_{\text{avg}} = -597$) and κ_0 denotes the baseline tissue stiffness. By using this approach, collapsed regions of the lung or areas with accumulated fluid are assigned a higher tissue stiffness due to higher HU values. For the second constitutive parameter η a spatially constant value was assumed. In order to obtain physiological results, patient-specific values for the two parameters κ_0 and η are estimated. Given that a four quasi-static measurements of the patient's P-V curve are available, patient-specific values for the two parameters can be calculated, such that the applied tracheal pressure and resulting volume of the lung in the model match the actual measurements, see [281] for a more detailed description. For the patient considered here, this led to the parameter estimates $\kappa_0 = 1900$ Pa and $\eta = -5.0$. The remaining parameters of the Maxwell model are chosen according to [163].

One cannot expect that the heterogenous acinar stiffness distribution obtained with the simple HU mapping procedure described in (8.6) exactly represents the ground truth. Using UQ it is possible to investigate the sensitivity of the reduced lung model output to variations in acinar stiffness. Thereby, the difference in acinar stiffness between healthy and collapsed regions of the lung as well as local variations can be investigated. Here, the heterogenous acinar stiffness obtained with (8.6) is superimposed with a random field, which describes local spatial fluctuations in acinar stiffness. In future research uncertainty with respect to stiffness differences between healthy and diseased tissue or other model parameters could be considered as well.

In any case, for the model under investigation in this work, a nonlinear acinar stiffness parameter κ is modelled as a three dimensional log-normal random field, with a spatially variable median μ_κ obtained from (8.6) and a scale parameter σ_κ. Realizations of the field are obtained by computing a realization of a Gaussian random field for the logarithm of κ using (3.79) under the assumption of a squared exponential covariance function as given in (3.60) and a correlation length of $\ell = 50$ mm. The truncation threshold in (3.79) is set to n_k = 250, resulting in 13704 terms in the expansion accounting for more than 95% of the total variability of the random field. Two variants of the stochastic stiffness model were investigated, model A where $\sigma_\kappa = 0.025$ and model B where $\sigma_\kappa = 0.15$. Both models are also summarized in Table 8.2. Detailed data regarding variability of lung tissue stiffness is extremely scarce and the employed scale parameters, which are based on the variability of existing preliminary experimental data [28, 272], have thus to be considered a rough first estimate.

model variant	correlation length	μ_κ	σ_κ
model A	50 mm	HU dependent	0.025
model B	50 mm	HU dependent	0.15

Table 8.2 Parameters of random field model for different model variants of patient-specific lung model.

8.5 Results

In this Section the impact of an uncertain acinar stiffness parameter κ on the maximum acinar strain and the tidal volume is investigated for both of the described model variants. As in the previous Chapter, the results are presented and discussed in two parts. First, the results are presented from a mechanical point of view on the basis of a Monte Carlo analysis. Then, results obtained with the BMFMC approach are discussed.

Due to the extremely high cost of the high-fidelity lung model Monte Carlo solution is limited to 1000 samples of the high-fidelity model, which is not sufficient to accurately estimate small exceedance or failure probabilities. However, a 1000 samples are sufficient to obtain an initial estimate of the variability of the results and, most importantly, to demonstrate that the BMFMC approach is also applicable to reduced order models of the lung.

8.5.1 Monte Carlo Solution

Figure 8.6 depicts a few example realizations of the random field describing κ (model B) and the corresponding volumetric acinar strain at maximum inspiration, i.e., at $P_{\mathrm{t}} = 25$ cmH_2O and $t = 7.5$s. It can be seen that local acinar strain is clearly interrelated with local stiffness parameter κ. Thereby, areas with a low κ value correspond to areas with high volumetric strain. In spite this clear connection between local κ and local strain values, the maximum occurring strain within the model does not always occur at the location where the stiffness parameter κ is minimal. This can be seen in Figure 8.7, in which the maximum occurring strain is plotted against the strain at the acinus with minimum κ. If the location of the maximum strain were to correspond to the location with minimum κ, the two plots would show a straight line. As can be seen in Figure 8.7 this is not the case. Especially for model A, the maximum strain does frequently not occur at the location with the lowest stiffness.

The reason for that is a combination of airway dynamics, inter-acinar dependencies, and gravitational effects. These characteristics essentially damp the dependence of local strain on local stiffness. In particular gravity seems to have a shifting effect on the location of the maximum strain. In virtually all cases where maximum strain does not correspond to the location of minimum κ, the location of the maximum occurring strain is located above the location of the minimum of κ. Moreover, it has been observed that the location of the maximum strain jumps over the course of a simulation. Future research will have to clarify whether the use of different ventilation manoeuvres, e.g., high-frequency oscillatory ventilation, can alter either the location or the magnitude of the maximum occurring strain or both.

Figure 8.8b and 8.9b show a histogram of the maximum strain, for model A and model B, respectively. In particular for model A, where the variance of the random field describing κ is small, the variability of maximum occurring strain is also very small. The maximum strain obtained with a deterministic κ, obtained by using (8.6) without added random fluctuations, is very close to the mean value of the uncertainty distribution obtained with the probabilistic stiffness model A. As could be expected, the variability of the maximum strain is larger if probabilistic stiffness model B is used. Here, the difference between maximum strain obtained using a deterministic κ ($\varepsilon_{\mathrm{vol,max}} = 1.7982$) is significantly lower than the mean value of the distribution of the maximum strain ($\mathbb{E}[\varepsilon_{\mathrm{vol,max}}] = 1.9033$).

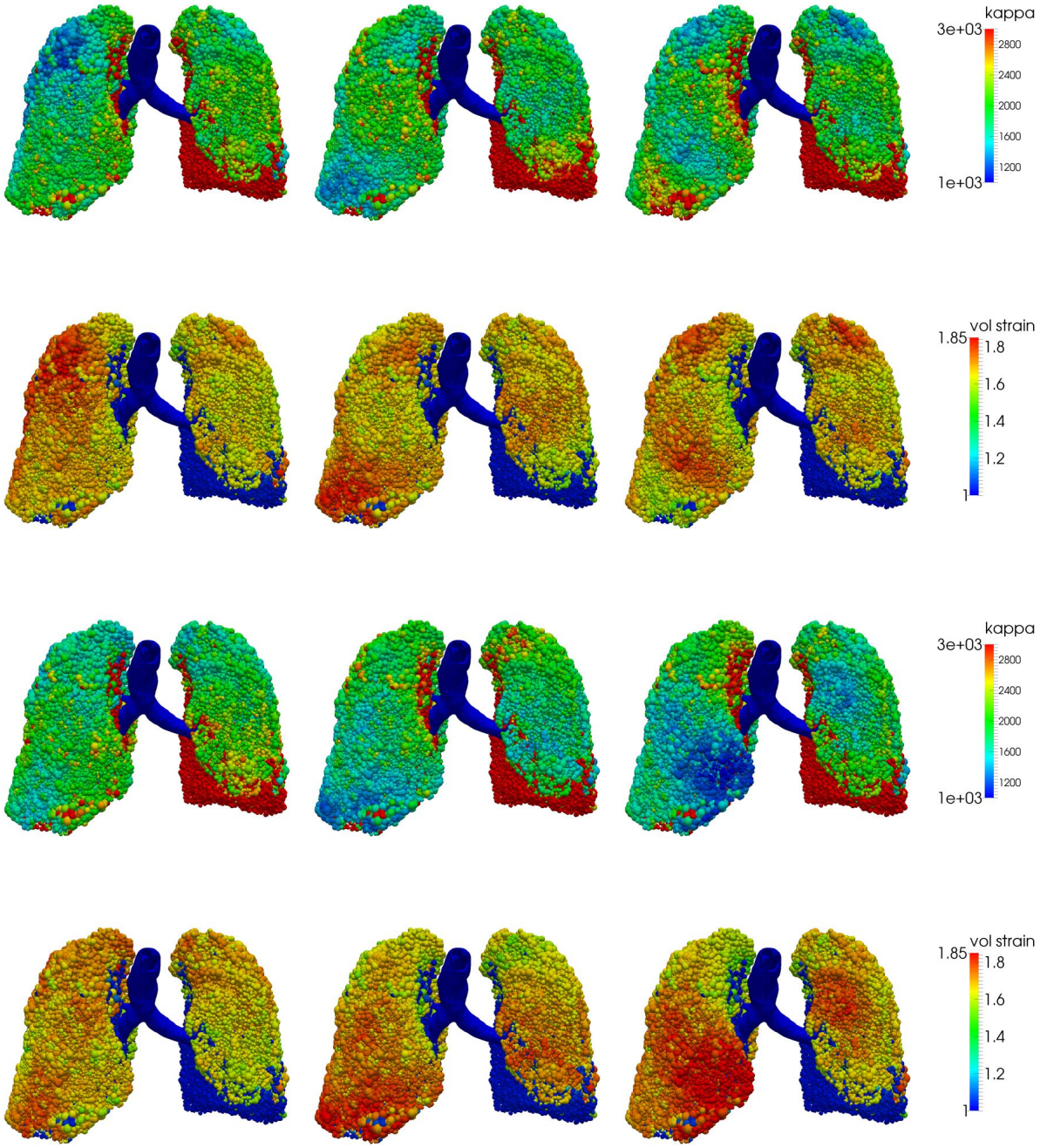

Figure 8.6 Six sample realizations of probabilistic stiffness model B and corresponding acinar strain at maximum inspiration at $t = 7.5$. First and third row show spatial κ distribution (color scale in Pa). Second and forth row show the corresponding strain distributions.

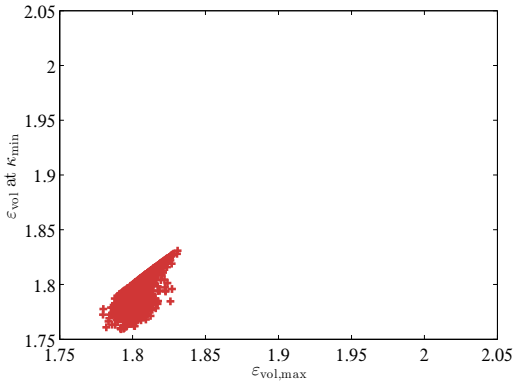

(a) acinar stiffness model A

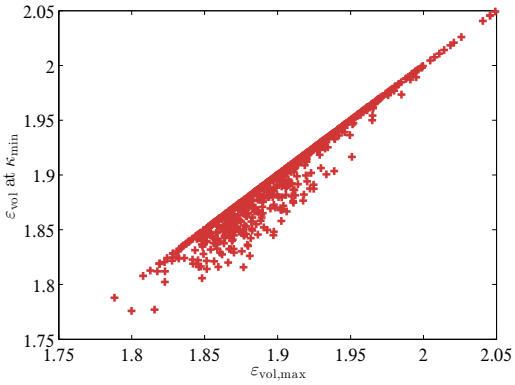

(b) acinar stiffness model A

Figure 8.7 Comparison of maximum occurring acinar strain and acinar at the location of minimum κ.

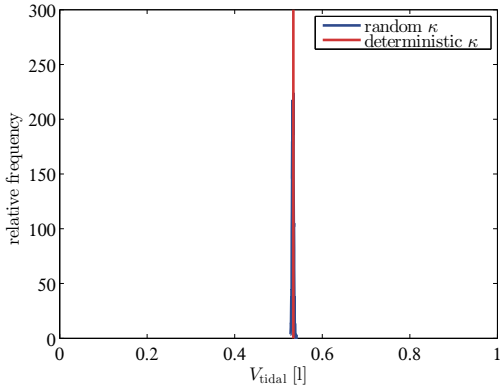

(a)

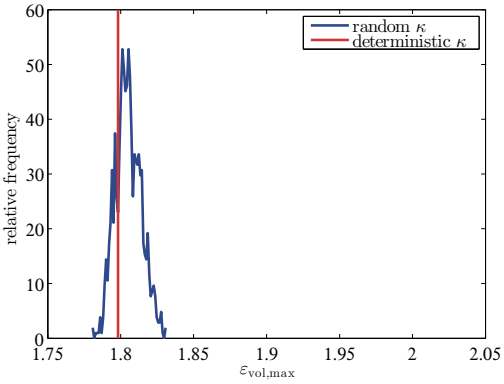

(b)

Figure 8.8 Histograms of tidal volume (a) and maximum acinar strain (b) for acinar stiffness model B.

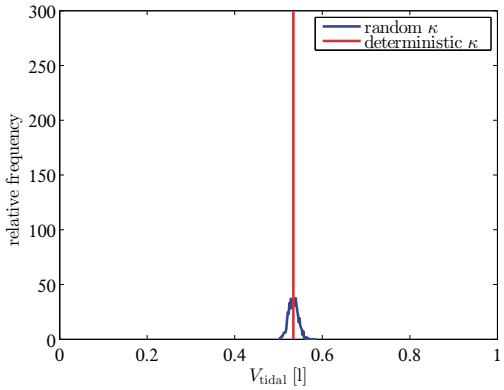

(a)

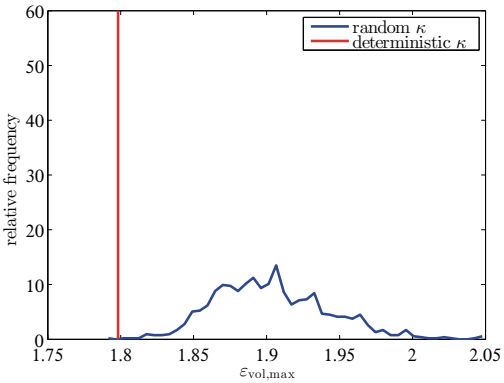

(b)

Figure 8.9 Histograms of tidal volume (a) and maximum acinar strain (b) for acinar stiffness model B.

	MC reference			BMFMC posterior mean			relative error [%]		
	mean	COV	95% q.	mean	COV	95% q.	mean	COV	95% q.
model A	1.8052	0.0048	1.8204	1.8055	0.0045	1.8192	0.0195	6.9039	0.0670
model B	1.9033	0.0205	1.9696	1.9045	0.0215	1.9787	0.0657	4.6866	0.4589

Table 8.3 Comparison between MC reference solution and BMFMC approximation for the considered example model and both random field based probabilistic acinar stiffness models.

The tidal volume V_{tidal} shows a similar behavior and is relatively insensitive to fluctuations in acinar stiffness. Moreover, the mean value of the tidal volume is very close the tidal volume obtained in a deterministic simulation even if acinar stiffness model B is used.

It is important to emphasize that the locally occurring maximum strain values, computed with the finite element model, are different from maximum volume averaged strain values which are computable in an usual clinical setting based on tidal volume and functional residual capacity. For the model under investigation here, the maximum occurring volume averaged strain is $\varepsilon_{\text{avg,max}} = 1.48$, which is significantly lower than the values for local strain reported here. Note that this value for the volume averaged strain corresponds to an average, deterministic κ.

8.5.2 Bayesian multi-fidelity Monte Carlo

In order to demonstrate that the BMFMC framework is indeed a very general approach, it is applied here to estimate the distribution of the maximum strain in combination with both probabilistic stiffness models A and B. The highest strain values occur at maximum inspiration which corresponds to $t = 4.4$ s and $t = 7.5$ s for the first and second breath, respectively. To ensure that the true maximum is used the maximal occurring strain value in time and space is taken as maximum strain in the high-fidelity solution. The low-fidelity model is only simulated up to $t = 3.5$ s and the maximum strain is evaluated at this point in time, to further reduce the computational effort. As a result the maximum strain values computed with the low-fidelity model are significantly lower than the corresponding values computed with the high-fidelity model. This is shown in Figure 8.10, which depicts the correlation between high-fidelity and low-fidelity solution for the two considered model variants A and B as two-dimensional histogram. In addition, the posterior mean prediction and the 1% and 99% quantiles of the regression model are shown in Figure 8.10. Here a GP based regression approach was used. Due to the high computational costs associated with the evaluation of the high-fidelity model and to show that the BMFMC method can also be used if only few evaluations of the high-fidelity model are available, a subset of only 50 training samples was used to train the GP regression model.

In Figure 8.11 a comparison of estimated PDFs for high-fidelity, low-fidelity, and posterior mean BMFMC approximation shown for the two model variants. Failure probabilities are shown as well. Thereby, it is important to keep in mind that the MC reference is based on only 1000 samples. The BMFMC approach matches the MC reference solution rather well. This can also be seen by comparison of mean and COVs as given in Table 8.3. The agreement of the estimated mean values is excellent while the estimated COVs show somewhat larger errors compared to the MC reference.

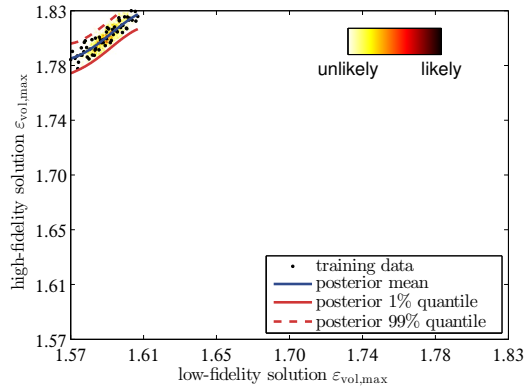

(a) Acinar stiffness model A

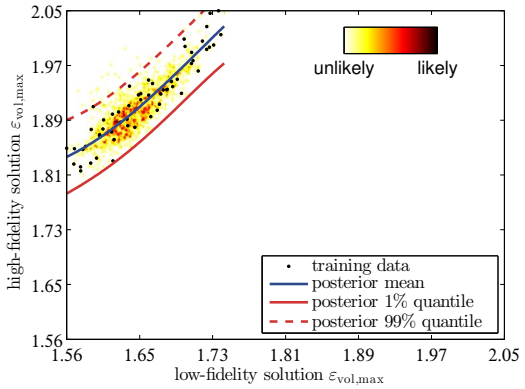

(b) Acinar stiffness model B

Figure 8.10 Comparison between low-fidelity solution and high-fidelity solution. In addition to the posterior mean and confidence region of the predictive distribution $p(y_{\text{hi-fi}}|y_{\text{lo-fi}})$ the figures show the used training samples as black dots.

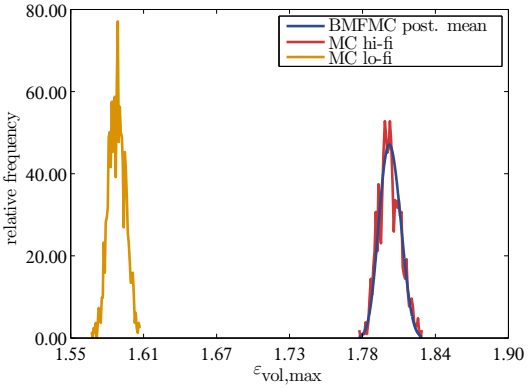

(a) PDF estimates for acinar stiffness model A.

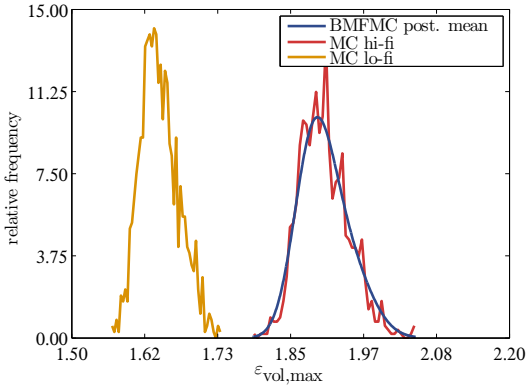

(b) PDF estimates for acinar stiffness model B.

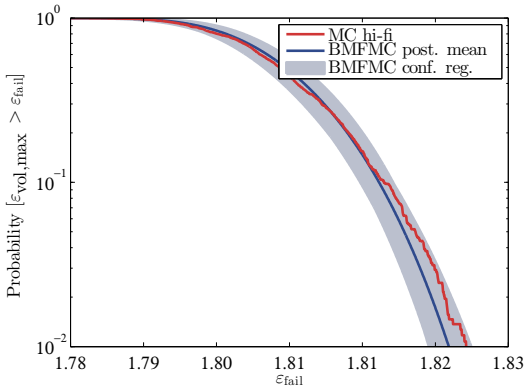

(c) Failure probability for acinar stiffness model A.

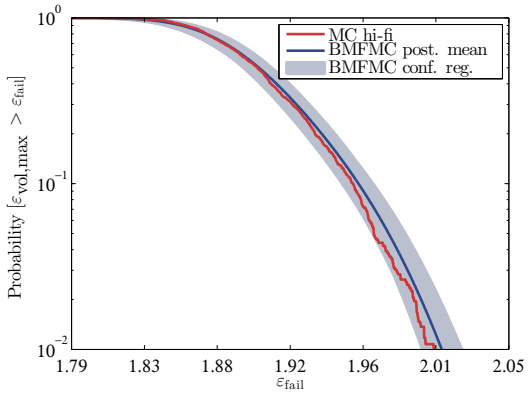

(d) Failure probability for acinar stiffness model B.

Figure 8.11 Exemplary comparison between high-fidelity Monte Carlo solution (red), low-fidelity Monte Carlo solution(yellow), and BMFMC solution (blue) for patient-specific lung model with acinar stiffness model A and model B. Top: estimated PDFs for maximum acinar strain. Bottom: failure probability based on maximum acinar strain threshold.

As can be seen in Figure 8.11a and 8.11b the confidence regions of the BMFMC approach are also rather large as a result of the noisy relationship and the few training samples used. The variance of the conditional probability distribution $p(y_{\text{hi-fi}}|y_{\text{lo-fi}})$ compared to the total variability of the high-fidelity solution is high compared to previous examples in the preceding chapter. One reason for high amount of noise, which has a detrimental effect on the accuracy of the BMFMC method, is the overall very low variability of the solution. Another factor might be the way the low-fidelity model is constructed and the random field is evaluated. Reducing the number of airway generations leads to larger acini. In addition, this truncation of the tree results in acini being at different locations than in the high-fidelity model. Evaluating the random field and assigning a value to each acinus based on averaging over the acinus volume instead of assigning a value based on evaluation of the field at a single point, as it is done in the considered examples, could help to reduce the noise.

Regarding the computational costs, the BMFMC scheme with 50 training sample is roughly 19 times cheaper than the direct MC with 1000 samples. The cost of BMFMC is the equivalent to 54 high-fidelity model evaluations, which amounts to saving more than 90000 CPU hours.

8.6 Concluding remarks

UQ was performed using a state of the art, patient-specific, reduced order model the lung. Thereby, one stiffness parameter was considered uncertain and modelled as three dimensional random field. The maximum acinar strain was found to be not very sensitive with respect to the considered uncertain stiffness model because inter-acinar linkers, adequate boundary conditions to model the rib-cage, and gravitational effects damp the effect of local variations in acinar stiffness. Nevertheless, the deterministic model tends to underestimate the maximum strain compared to the mean value obtained with UQ.

Future work should include further investigations regarding the most suitable probabilistic model for the stiffness parameter κ, as well as other uncertain parameters. Moreover, the lung model should be extended to include reopening effects of the collapsed lung regions.

Most importatnly, it was demonstrated that the developed BMFMC framework is applicable to various types of problems and not limited to solid mechanics problems. In order to be used efficiently BMFMC requires that a cheap to evaluate low-fidelity model can be created, which has a similar stochastic structure. The presented examples show that a suitable cheap low-fidelity model can also be constructed for reduced dimensional models of the human respiratory system, which demonstrates the general applicability of the proposed BMFMC approach.

9 Summary and Outlook

Within the scope of this work a framework for UQ in large-scale, nonlinear models with high-stochastic dimension could be successfully developed and implemented. The main focus of this work was the independent conception and implementation of a UQ framework, as well as a subsequent application to exemplary biomedical problems. The present summary wraps up the methodic and scientific progress and provides a glimpse into one scenario of the uncertain future that lies ahead.

9.1 Conclusions

One major goal, the development of a general, efficient UQ framework for complex models, this work set out to achieve, was accomplished. Two components comprise this framework. The first component admits a mathematical description of uncertainty in form of random variables or random fields. It is thereby emphasized, that uncertain parameters can be modelled by three-dimensional, non-Gaussian random fields within the developed framework. The use of random field models, especially if these fields are multi-dimensional, leads to a high stochastic dimension of the problem, which precludes the application of surrogate techniques. Hence, other techniques to propagate the uncertainties through the computational models have to be used. To this end, a novel and efficient multi-fidelity sampling scheme was adopted and a framework based on this approach was implemented. By combining multi-fidelity sampling with non-parametric Bayesian regression, it was possible to approximate the full probability distribution function of the respective quantities of interest at a fraction of the computational costs as compared to direct sampling of the accurate high-fidelity model. Furthermore, is was shown that the presented approach achieves an excellent agreement with MC reference solutions. To further reduce the computational burden, a parameter continuation scheme was developed which enables the exploitation of the typical sampling problem structure, i.e., the repeated simulation of very similar problems. The sampling procedures were implemented allowing simultaneous solution of multiple instances of the forward model within the same instance of the software, thus allowing for an easy extension to more advanced sampling schemes. Furthermore, the developed Bayesian multi-fidelity Monte Carlo (BMFMC) framework is complemented with a surrogate modelling approach based on GPs for problems with low stochastic dimension.

The exemplary application of the developed framework to computational models of AAAs goes well beyond showcase numerical examples but rather aims to provide the first steps towards a fully probabilistic treatment of computational models of AAAs. In the opinion of the author rigorous UQ regarding the multitude of uncertain model input parameters provides a way to further strengthen the trust in computational models of AAAs for the purpose of assessing AAA rupture potential. Within the scope of this work, multiple approaches to obtain patient-specific probabilistic models for several of the mechanical input parameters were developed and

applied. For instance, harnessing a large database of experimental data, which was in part gathered during this work, and using state of the art Bayesian regression approaches to make use of non-invasively available factors resulted in superior probabilistic predictions for several uncertain mechanical quantities. It could be shown that the predictions using this novel approach were more accurate than predictions based on population averages and, more importantly, that the probabilistic predictions based on the Bayesian regression models, taking non-invasively assessable parameters into account, resulted in reduced uncertainty about several mechanical quantities as compared to their assessment based on measurements of these mechanical quantities alone.

Using the obtained probabilistic models, realistic simulations of several patient-specific AAAs with uncertain input parameters were set up and the impact of several uncertain input parameters, such as constitutive parameters and wall thickness, on mechanical quantities that are typically related to AAA rupture risk could be quantified. The results showed that the impact on these quantities can be dramatic, highlighting, once more, the need for rigorous UQ. Several different probabilistic models were compared, e.g., to gauge the need for random field models to capture intra-patient variations of the uncertain model input parameters. The results showed that a simple random variable model for the wall thickness leads to a different peak wall stress distribution, compared to a random field thickness model, indicating that a simple random variable model is not sufficient.

The examples showed that the developed BMFMC approach can be used to assess local quantities, e.g., stresses at specific locations as well as global quantities, e.g., the maximum von Mises stress. Furthermore, it was shown that the BMFMC approach is very versatile and that it can be employed in complex scenarios making use of a variety of low-fidelity approximations of the high-fidelity model. Moreover, it was shown that low-fidelity models are by no means limited to coarser discretizations. In addition, the application to a completely different physical problem, the reduced dimensional modelling of the human lung, underscores once more the generality of the approach.

9.2 Outlook

Overall, the results obtained with BMFMC approach are very promising and in the opinion of the author, the approach has the potential to enable and facilitate UQ for a broad range of problems. However, there are some open questions which have to be pointed out and should be addressed in future work. This is the aim of the present section. In addition, this section provides an outlook on possible directions of future research. An outlook for the general methodology will be provided first, followed by some ideas regarding the computational rupture risk assessment of AAAs.

9.2.1 Methods

While the results obtained with the BMFMC approach presented in the examples throughout this work show generally a very good agreement with direct MC, it is important to point out that further research is needed to determine the optimal ratio between high-fidelity and low-fidelity samples. In others words, given a certain amount of computational resources, what is

the optimal number of samples on each level to get the most accurate result? The answer to this question will of course depend on the chosen low-fidelity model and the desired statistic.

Regarding the probabilistic models of the uncertain input parameters an obvious step to extent the current framework is the consideration of cross-correlated non-Gaussian random vector fields, e.g., following the ideas recently described in [63, 101, 296]. Often, when multiple uncertain physical parameters are considered, these parameters exhibit some degree of spatial correlation as well as cross-correlation between different parameters. This correlation should be reflected by the probabilistic models of uncertain input parameters in an UQ framework.

The sampling procedure itself could be improved by employing more advanced sampling schemes, e.g., LHS or quasi Monte Carlo. On the other hand, the cost for the evaluation of a forward model likely could be reduced by extending and improving the parameter continuation scheme used in the present work.

Regarding the used regression models to compute the conditional probability distribution between low-fidelity and high-fidelity model only models based on a Gaussian likelihood, i.e., a Gaussian error term have been investigated. Future research should include investigation of more elaborate non-Gaussian and also non-symmetric noise models to improve the accuracy of the approach and make it more robust against outliers. Multiple regression models could be trained and subsequently compared to evaluate their performance. The model yielding the best results should then be used in the BMFMC scheme to compute the desired high-fidelity solution statistic.

The extension of the BMFMC scheme to compute sensitivity measures is also in interesting direction of future research. The computational savings are likely even greater than in the case where one is interest just in the probability distribution of the quantity of interest. Thereby, the computation of sensitivity measures regarding multiple uncertain parameters modelled as random fields or a combination of random fields and random variables would be of particular interest.

Based on preliminary investigations, the use of multiple low-fidelity models or the briefly mentioned combination or hybrid (cf. Section 5.3.5) between a multi-fidelity and a surrogate approach, presents, in the opinion of the author, another promising direction of future research. Thereby, a low-fidelity model would provide only incomplete information about the high-fidelity model masking all mathematical dimensions of the problem belonging to the random field representation of one or more physical parameters. The low-fidelity model would effectively lump all random variables describing the variation of one physical parameter into a single dimension represented by the output of a low-fidelity model. Other random dimensions could be directly captured by the surrogate model. One of the benefits of this approach would be the ability to compute sensitivity measures with respect to the different uncertain physical parameters based on existing ideas for the efficient computation of sensitivity measures for GP based surrogates [235].

9.2.2 Applications

Regarding the computational assessment of AAA rupture potential, the logical next steps include an extension of the presented simulations to include uncertainties in all constitutive parameters, including the parameters of the ILT as well as the wall thickness. Possible correlations between the parameters should also be considered. Moreover, a probabilistic wall strength

model should be used. This would then allow for the computation of an actual rupture risk, similar to the probabilistic rupture risk index recently proposed in [253]. Of course this risk has to be understood as conditional on the assumption that the mechanical behaviour of the AAA can be accurately described with an elastic model. This, however, might not be the case. Aside from more elaborate elastic models, which, e.g., includes anisotropic materials, research including growth and remodelling effects presents another possible avenue of future research. The problem of uncertain model input parameters, however, persist when growth and remodelling approaches are used.

Apart from AAA models, the BMFMC methodology has, in the opinion of the author, a tremendous potential in many biomedical or general engineering applications. Consider for instance computational models of arterial blood flow. Due to the high costs associated with a full three-dimensional treatment of these kinds of problems researchers frequently employ reduced dimensional models, which have shown good performance in many cases at a fraction of the computational costs. Grinberg et al. [136] reports a ratio of computational effort of 18000 between 3D and 1D models This enormous difference in computational cost could likely be exploited in a BMFMC based UQ scheme, allowing accurate UQ with respect to quantities which can only be accurately assessed using the full 3D model.

They same rationale of course applies to other applications of UQ in computational fluid dynamics. If simplified flow models, e.g. potential flow, can be successfully used as low-fidelity approximation for the instationary solution of the Navier-Stokes equations, the cost for UQ in computational fluid dynamics problems could be potentially reduced by orders of magnitude.

A Probability distributions

Distribution	Notation	Parameters
Uniform	$\mathsf{x} \sim \mathcal{U}(a, b)$ $p_{\mathsf{x}}(x) = \mathcal{U}(x\|a, b)$	boundaries a, b, with $b > a$
Normal	$\mathsf{x} \sim \mathcal{N}(\mu, \sigma^2)$ $p_{\mathsf{x}}(x) = \mathcal{N}(x\|\mu, \sigma^2)$	mean μ standard deviation $\sigma > 0$
Multivariate Normal	$\mathbf{x} \sim \mathcal{N}(\boldsymbol{\mu}, \boldsymbol{\Sigma})$ $p_{\mathbf{x}}(\boldsymbol{x}) = \mathcal{N}(\boldsymbol{x}\|\boldsymbol{\mu}, \boldsymbol{\Sigma})$ (implicit dimension d)	mean $\boldsymbol{\mu}$ symmetric, pos. semidefinite $d \times d$ covariance matrix $\boldsymbol{\Sigma}$
log-Normal	$\mathsf{x} \sim \log\mathcal{N}(\mu, \sigma^2)$ $p_{\mathsf{x}}(x) = \log\mathcal{N}(x\|\mu, \sigma^2)$	location μ, scale $\sigma > 0$ of associated normal
Gamma	$\mathsf{x} \sim \mathrm{Gamma}(a, b)$ $p_{\mathsf{x}}(x) = \mathrm{Gamma}(x\|a, b)$	shape $a > 0$ inverse scale $b > 0$
Inverse-Gamma	$\mathsf{x} \sim$ Inv-Gamma$(a, b)(a, b)$ $p_{\mathsf{x}}(x) =$ Inv-Gamma$(a, b)(x\|a, b)$	shape $a > 0$ scale $b > 0$
Scaled inverse-chi-square	$\mathsf{x} \sim$ Inv-$\chi^2(\nu, s^2)$ $p_{\mathsf{x}}(x) =$ Inv-$\chi^2(x\|\nu, s^2)$	degrees of freedom $\nu > 0$ scale $s > 0$
Exponential	$\mathsf{x} \sim$ Expon(b) $p_{\mathsf{x}}(x) =$ Expon$(x\|b)$	inverse scale $b > 0$
t	$\mathsf{x} \sim \mathcal{T}(\nu, \mu, \sigma^2)$ $p_{\mathsf{x}}(x) = \mathcal{T}(x\|\nu, \mu, \sigma^2)$	degrees of freedom $\nu > 0$ location μ, scale $\sigma > 0$
Poisson	$\mathsf{x} \sim$ Poisson(λ) $p_{\mathsf{x}}(x) =$ Poisson$(x\|\lambda)$	'rate' $\lambda > 0$

Table A.1 Probability distributions used in this work. Table adopted from [115].

Density function	Mean and Variance
$p_{\mathsf{x}}(x) = \frac{1}{b-a}, x \in [a,b]$	$\mathbb{E}[\mathsf{x}] = \frac{a+b}{2}$ $\mathbb{V}[\mathsf{x}] = (b-a)^2/12$
$p_{\mathsf{x}}(x) = \frac{1}{(2\pi\sigma^2)^{1/2}} \exp(-\frac{1}{2\sigma^2}(x-\mu)^2)$	$\mathbb{E}[\mathsf{x}] = \mu$ $\mathbb{V}[\mathsf{x}] = \sigma^2$
$p_{\mathbf{x}}(\boldsymbol{x}) = \frac{1}{(2\pi)^{d/2}} \frac{1}{\lvert\boldsymbol{\Sigma}\rvert^{1/2}} \exp(-\frac{1}{2}(\boldsymbol{x}-\boldsymbol{\mu})^T \boldsymbol{\Sigma}^{-1}(\boldsymbol{x}-\boldsymbol{\mu}))$	$\mathbb{E}[\mathbf{x}] = \boldsymbol{\mu}$ $\mathbb{V}[\mathbf{x}] = \boldsymbol{\Sigma}$
$p_{\mathsf{x}}(x) = 1/(x\sigma\sqrt{2\pi}) \exp(-\frac{(\log x-\mu)^2}{2\sigma^2})$	$\mathbb{E}[\mathsf{x}] = \exp(\mu + \sigma^2/2)$ $\mathbb{V}[\mathsf{x}] = (\exp(\sigma^2-1)) \exp(2\mu+\sigma^2)$
$p_{\mathsf{x}}(x) = \frac{b^a}{\Gamma(a)} x^{a-1} e^{-bx}, x > 0$	$\mathbb{E}[\mathsf{x}] = \frac{a}{b}$ $\mathbb{V}[\mathsf{x}] = \frac{a}{b^2}$
$p_{\mathsf{x}}(x) = \frac{b^a}{\Gamma(a)} x^{-(a+1)} e^{-b/x}, x > 0$	$\mathbb{E}[\mathsf{x}] = b/(a-1)$ $\mathbb{V}[\mathsf{x}] = (b^2)/((a-1)^2(a-2))$
$p_{\mathsf{x}}(x) = \frac{(\nu/2)^{-\nu/2}}{\Gamma(\nu/2)} s^\nu x^{-(\nu/2+1)} e^{\nu s^2/(2x)}, x > 0$	$\mathbb{E}[\mathsf{x}] = \frac{\nu}{\nu-2} s^2$ $\mathbb{V}[\mathsf{x}] = \frac{2\nu^2}{(\nu-2)^2(\nu-4)}$
$p_{\mathsf{x}}(x) = be^{-bx}, x > 0$	$\mathbb{E}[\mathsf{x}] = \frac{1}{b}$ $\mathbb{V}[\mathsf{x}] = \frac{1}{b^2}$
$p_{\mathsf{x}}(x) = \frac{\Gamma((\nu+1)/2)}{\Gamma(\nu/2)} \sqrt{\pi\nu\sigma^2} \left(1 + \frac{1}{\nu}\frac{(x-\mu)^2}{\sigma^2}\right)^{-(\nu+1)/2}$	$\mathbb{E}[\mathsf{x}] = \mu$, for $\nu > 1$ $\mathbb{V}[\mathsf{x}] = \frac{\nu}{\nu-2}\sigma^2$, for $\nu > 2$
$p_{\mathsf{x}}(x) = \frac{1}{x!} \lambda^x \exp(-\lambda)$ $x = 0, 1, 2, ..., n$	$\mathbb{E}[\mathsf{x}] = \lambda$ $\mathbb{E}[\mathsf{x}] = \lambda$

Bibliography

[1] R. Ababou, A. C. Bagtzoglou, and E. F. Wood, On the condition number of covariance matrices in kriging, estimation, and simulation of random fields, *Mathematical Geology* **26**, 99–133, 1994.

[2] P. Abrahamsen, A review of Gaussian random fields and correlation functions, Technical report, Norwegian Computing Center, Oslo, Norway, 1997.

[3] M. Abramowitz and I. A. Stegun, *Handbook of mathematical functions: with formulas, graphs, and mathematical tables*, Dover, 1964.

[4] S. Acharjee and N. Zabaras, Uncertainty propagation in finite deformations–A spectral stochastic Lagrangian approach, *Computer Methods in Applied Mechanics and Engineering* **195**, 2289–2312, 2006.

[5] S. Acharjee and N. Zabaras, A non-intrusive stochastic Galerkin approach for modeling uncertainty propagation in deformation processes, *Computers & Structures* **85**, 244–254, 2007.

[6] R. J. Adler, *The geometry of random fields* , Wiley, 1981.

[7] N. Agarwal and N. R. Aluru, Stochastic modeling of coupled electromechanical interaction for uncertainty quantification in electrostatically actuated MEMS, *Computer Methods in Applied Mechanics and Engineering* **197**, 3456–3471, 2008.

[8] J. Alastruey, K. H. Parker, and J. Peiró, Lumped parameter outflow models for 1-D blood flow simulations: effect on pulse waves and parameter estimation, *Communications in Computational Physics* **4**, 317–336, 2008.

[9] K. G. M. M. Alberti and P. Z. Zimmet, Definition, Diagnosis and Classification of Diabetes Mellitus and its ComplicationsPart 1: Diagnosis and Classification of Diabetes Mellitus Provisional Report of a WHO Consultation, *Diabetic Medicine* **15**, 539–553, 1998.

[10] D. Ambrosi, G. A. Ateshian, E. M. Arruda, S. C. Cowin, J. Dumais, A. Goriely, G. A. Holzapfel, J. D. Humphrey, R. Kemkemer, E. Kuhl, and , Perspectives on biological growth and remodeling, *Journal of the Mechanics and Physics of Solids* **59**, 863–883, 2011.

[11] D. Ambrosi, A. Quarteroni, and G. Rozza (eds.), *Modeling of Physiological Flows*, Volume 5, Springer, 2012.

[12] M. Anders and M. Hori, Three-dimensional stochastic finite element method for elasto-plastic bodies, *International Journal for Numerical Methods in Engineering* **51**, 449–478, 2001.

[13] C. Andrieu, N. De Freitas, and A. Doucet, Robust full Bayesian learning for radial basis networks, *Neural computation* **13**, 2359–2407, 2001.

[14] C. Andrieu, N. de Freitas, A. Doucet, and M. I. Jordan, An Introduction to MCMC for Machine Learning, *Machine learning* **50**, 5–43, 2003.

[15] G. L. Ang, A. H.-S. Ang, and W. H. Tang, Optimal importance-sampling density estimator, *Journal of Engineering Mechanics* **118**, 1146–1163, 1992.

[16] H. Astrand, J. Stålhand, J. Karlsson, M. Karlsson, B. Sonesson, and T. Lanne, In vivo estimation of the contribution of elastin and collagen to the mechanical properties in the human abdominal aorta: effect of age and sex, *Journal of Applied Physiology* **110**, 176–187, 2011.

[17] S. K. Au and J. L. Beck, A new adaptive importance sampling scheme for reliability calculations, *Structural Safety* **21**, 135–158, 1999.

[18] S. K. Au and J. L. Beck, Important sampling in high dimensions, *Structural Safety* **25**, 139–163, 2003.

[19] S. K. Au and J. L. Beck, Subset simulation and its application to seismic risk based on dynamic analysis, *Journal of Engineering Mechanics* **129**, 901–917, 2003.

[20] S. K. Au, J. Ching, and J. L. Beck, Application of subset simulation methods to reliability benchmark problems, *Structural Safety* **29**, 183–193, 2007.

[21] S.-K. Au and J. L. Beck, Estimation of small failure probabilities in high dimensions by subset simulation, *Probabilistic Engineering Mechanics* **16**, 263–277, 2001.

[22] I. Babuška, F. Nobile, and R. Tempone, A stochastic collocation method for elliptic partial differential equations with random input data, *SIAM Journal on Numerical Analysis* **45**, 1005–1034, 2007.

[23] H. Baldeweck, *Méthodes des éléments finis stochastiques. Applications a la geotechnique et a la mecanique de la rupture*, PhD thesis, Université d'Evry Val d'Essonne, 1999.

[24] J. M. Ball, Convexity conditions and existence theorems in nonlinear elasticity, *Archive for rational mechanics and Analysis* **63**, 337–403, 1976.

[25] A. Barth, C. Schwab, and N. Zollinger, Multi-Level Monte Carlo Finite Element method for elliptic PDE's with stochastic coefficients, *Numerische Mathematik* **119**, 123–161, 2011.

[26] T. Bayes and R. Price, An essay towards solving a problem in the doctrine of chances, *Philosophical Transactions (1683-1775)*, 370–418, 1763.

[27] P. Beaurepaire, M. A. Valdebenito, G. I. Schuëller, and H. A. Jensen, Reliability-based optimization of maintenance scheduling of mechanical components under fatigue, *Computer Methods in Applied Mechanics and Engineering* **221**, 24–40, 2012.

[28] A. Bel-Brunon, S. Kehl, C. Martin, S. Uhlig, and W. A. Wall, Numerical identification method for the non-linear viscoelastic compressible behavior of soft tissue using uniaxial tensile tests and image registration–Application to rat lung parenchyma, *Journal of the Mechanical Behavior of Biomedical Materials* **29**, 360–374, 2014.

[29] T. Belytschko, W. K. Liu, B. Moran, and K. Elkhodary, *Nonlinear finite elements for continua and structures*, Wiley, 2nd Edition, 2013.

[30] D. P. Bertsekas and J. N. Tsitsiklis, *Introduction to Probability*, Athena Scientific, 2002.

[31] M. Berveiller, B. Sudret, and M. Lemaire, Stochastic finite element: a non intrusive approach by regression, *European Journal of Computational Mechanics/Revue Européenne de Mécanique Numérique* **15**, 81–92, 2006.

[32] J. Biehler, M. W. Gee, and W. A. Wall, Towards efficient uncertainty quantification in complex and large-scale biomechanical problems based on a Bayesian multi-fidelity scheme, *Biomechanics and Modeling in Mechanobiology* **14**, 489–513, 2015.

[33] J. Biehler, S. Kehl, M. W. Gee, F. Tanios, J. Pelisek, A. Maier, C. Reeps, H. H. Eckstein, and W. A. Wall, Probabilistic non-invasive prediction of wall properties of abdominal aortic aneurysms using Bayesian regression, *Biomechanics and Modeling in Mechanobiology*, 2015. Submitted.

[34] I. Bilionis and N. Zabaras, Multidimensional adaptive relevance vector machines for uncertainty quantification, *SIAM Journal on Scientific Computing* **34**, B881–B908, 2012.

[35] I. Bilionis and N. Zabaras, Multi-output local Gaussian process regression: Applications to uncertainty quantification, *Journal of Computational Physics* **231**, 5718–5746, 2012.

[36] I. Bilionis, N. Zabaras, B. A. Konomi, and G. Lin, Multi-output separable Gaussian process: Towards an efficient, fully Bayesian paradigm for uncertainty quantification, *Journal of Computational Physics* **241**, 212–239, 2013.

[37] P. Billingsley, *Probability and measure*, John Wiley & Sons, 3rd Edition, 1995.

[38] C. M. Bishop, *Pattern Recognition and Machine Learning*, Springer, 2006.

[39] J. D. Blankensteijn, S. E. C. A. de Jong, M. Prinssen, A. C. van der Ham, J. Buth, S. M. M. van Sterkenburg, H. J. M. Verhagen, E. Buskens, D. E. Grobbee, and Dutch Randomized Endovascular Aneurysm Management (DREAM) Trial Group, Two-year outcomes after conventional or endovascular repair of abdominal aortic aneurysms., *The New England journal of medicine* **352**, 2398–2405, 2005.

[40] B. Blight and L. Ott, A Bayesian approach to model inadequacy for polynomial regression, *Biometrika* **62**, 79–88, 1975.

[41] P. Bocchini and G. Deodatis, Critical review and latest developments of a class of simulation algorithms for strongly non-Gaussian random fields, *Probabilistic Engineering Mechanics* **23**, 393–407, 2008.

[42] E. Boileau, P. Nithiarasu, P. J. Blanco, L. O. Müller, F. E. Fossan, L. R. Hellevik, W. P. Donders, W. Huberts, M. Willemet, and J. Alastruey, A benchmark study of numerical schemes for one-dimensional arterial blood flow modelling, *International Journal for Numerical Methods in Biomedical Engineering* **31**, n/a–n/a, 2015. doi: http://dx.doi.org/10.1002/cnm.2732.

[43] J. Bonet and R. D. Wood, *Nonlinear continuum mechanics for finite element analysis*, Cambridge University Press, 1997.

[44] F. Bott, *Determination of optimal sampling points in multi-fidelity uncertainty quantification scheme using an active learning approach*, Bachelor thesis, Technischen Universität München, 2014.

[45] U. Bourgund and C. G. Bucher, *Importance Sampling Procedure Using Design Points (ISPUD)-a User's Manual*, Institute of Engineering Mechanics, University of Innsbruck, 1986.

[46] J.-M. Bourinet, F. Deheeger, and M. Lemaire, Assessing small failure probabilities by combined subset simulation and support vector machines, *Structural Safety* **33**, 343–353, 2011.

[47] M. J. Bown, A. J. Sutton, P. R. F. Bell, and R. D. Sayers, A meta-analysis of 50 years of ruptured abdominal aortic aneurysm repair, *British Journal of Surgery* **89**, 714–730, 2002.

[48] L. Breiman, *Probability and stochastic processes: with a view toward applications*, Houghton Mifflin, 1969.

[49] D. C. Brewstera, J. L. Cronenwett, J. W. Hallett, K. W. Johnston, W. C. Krupski, and J. S. Matsumura, Guidelines for the treatment of abdominal aortic aneurysms: Report of a subcommittee of the Joint Council of the American Association for Vascular Surgery and Society for Vascular Surgery, *Journal of Vascular Surgery* **37**, 1106–1117, 2003.

[50] W. L. Briggs and S. F. McCormick, *A Multigrid Tutorial*, SIAM, 2000.

[51] L. C. Brown and J. T. Powell, Risk factors for aneurysm rupture in patients kept under ultrasound surveillance. UK Small Aneurysm Trial Participants, *Annals of surgery* **230**, 289–296, 1999.

[52] P. M. Brown, D. T. Zelt, and B. Sobolev, The risk of rupture in untreated aneurysms: The impact of size, gender, and expansion rate, *Journal of Vascular Surgery* **37**, 280–284, 2003.

[53] C. G. Bucher, Adaptive sampling—an iterative fast Monte Carlo procedure, *Structural Safety* **5**, 119–126, 1988.

[54] C. G. Bucher, Asymptotic sampling for high-dimensional reliability analysis, *Probabilistic Engineering Mechanics* **24**, 504–510, 2009.

[55] R. E. Caflisch, Monte Carlo and quasi-Monte Carlo methods, *Acta numerica* **7**, 1–49, 2008.

[56] S. Celi, P. Losi, and S. Berti, Investigation on regional variation of intraluminal thrombus: A mechanical and histological study, *Bioinspired, Biomimetic and Nanobiomaterials* **1**, 183–194, 2012.

[57] F. Cérou, P. Del Moral, T. Furon, and A. Guyader, Sequential Monte Carlo for rare event estimation, *Statistics and Computing* **22**, 795–808, 2012.

[58] D. C. Charmpis, G. I. Schuëller, and M. F. Pellissetti, The need for linking micromechanics of materials with stochastic finite elements: A challenge for materials science, *Computational Materials Science* **41**, 27–37, 2007.

[59] J. Charrier, R. Scheichl, and A. L. Teckentrup, Finite element error analysis of elliptic PDEs with random coefficients and its application to multilevel Monte Carlo methods, *SIAM Journal on Numerical Analysis* **51**, 322–352, 2013.

[60] A. Chatterjee, An introduction to the proper orthogonal decomposition, *Current science* **78**, 808–817, 2000.

[61] P. Chen, A. Quarteroni, and G. Rozza, Simulation based uncertainty quantification of human arterial network hemodynamics, *International Journal for Numerical Methods in Biomedical Engineering* **29**, 698–721, 2013.

[62] F. Chinesta, P. Ladeveze, and E. Cueto, A short review on model order reduction based on proper generalized decomposition, *Archives of Computational Methods in Engineering* **18**, 395–404, 2011.

[63] H. Cho, D. Venturi, and G. E. Karniadakis, Karhunen–Loève expansion for multi-correlated stochastic processes, *Probabilistic Engineering Mechanics* **34**, 157–167, 2013.

[64] S.-K. Choi, R. V. Grandhi, and R. A. Canfield, Structural reliability under non-Gaussian stochastic behavior, *Computers & Structures* **82**, 1113–1121, 2004.

[65] K. A. Cliffe, M. B. Giles, R. Scheichl, and A. L. Teckentrup, Multilevel Monte Carlo methods and applications to elliptic PDEs with random coefficients, *Computing and Visualization in Science* **14**, 3–15, 2011.

[66] D. A. Cohn, Neural network exploration using optimal experiment design, *Neural Networks* **9**, 1071–1083, 1996.

[67] S. Conti, J. P. Gosling, J. E. Oakley, and A. O'Hagan, Gaussian process emulation of dynamic computer codes, *Biometrika* **96**, 663–676, 2009.

[68] S. Conti and A. O'Hagan, Bayesian emulation of complex multi-output and dynamic computer models, *Journal of statistical planning and inference* **140**, 640–651, 2009.

[69] N. Cressie, *Statistics for spatial data*, Wiley, 1991.

[70] M. A. Crisfield, An arc-length method including line searches and accelerations, *International Journal for Numerical Methods in Engineering* **19**, 1269–1289, 1983.

[71] K. R. Dalbey and L. Swiler, Gaussian process adaptive importance sampling, *International Journal for Uncertainty Quantification* **4**, 133–149, 2014.

[72] T. A. Davis, Algorithm 832: UMFPACK V4.3 - an unsymmetric-pattern multifrontal method, *ACM Transactions on Mathematical Software (TOMS)* **30**, 196–199, 2004.

[73] J. H. de Baar, T. P. Scholcz, C. V. Verhoosel, R. P. Dwight, A. H. Van Zuijlen, and H. Bijl, Efficient uncertainty quantification with gradient-enhanced kriging: Applications in fsi, In J. Eberhardsteiner, H. J. Böhm, and F. G. Rammerstorfer (eds.), *6th European Congress on Computational Methods in Applied Sciences and Engineering*, 2012.

[74] S. De Putter, B. Wolters, M. Rutten, M. Breeuwer, F. A. Gerritsen, and F. N. van de Vosse, Patient-specific initial wall stress in abdominal aortic aneurysms with a backward incremental method, *Journal of Biomechanics* **40**, 1081–1090, 2007.

[75] P. Del Moral, *Feynman-Kac Formulae*, Springer, 2004.

[76] P. Del Moral, A. Doucet, and A. Jasra, Sequential Monte Carlo samplers, *Journal of the Royal Statistical Society: Series B (Statistical Methodology)* **68**, 411–436, 2006.

[77] A. P. Dempster, Upper and lower probabilities induced by a multivalued mapping, *The Annals of Mathematical Statistics* **38**, 325–339, 1967.

[78] G. Deodatis, Bounds on response variability of stochastic finite element systems, *Journal of Engineering Mechanics*, 1990.

[79] G. Deodatis, Weighted integral method. I: stochastic stiffness matrix, *Journal of Engineering Mechanics* **117**, 1851–1864, 1991.

[80] G. Deodatis and R. Micaletti, Simulation of highly skewed non-Gaussian stochastic processes, *Journal of Engineering Mechanics* **127**, 1284, 2001.

[81] G. Deodatis and M. Shinozuka, Weighted integral method. II: response variability and reliability, *Journal of Engineering Mechanics*, 1991.

[82] A. Der Kiureghian and O. Ditlevsen, Aleatory or epistemic? Does it matter?, *Structural Safety* **31**, 105–112, 2009.

[83] A. Der Kiureghian and P.-L. Liu, Structural reliability under incomplete probability information, *Journal of Engineering Mechanics* **112**, 85–104, 1986.

[84] B. G. DeRubertis, S. M. Trocciola, E. J. Ryer, F. M. Pieracci, J. F. McKinsey, P. L. Faries, and K. C. Kent, Abdominal aortic aneurysm in women: Prevalence, risk factors, and implications for screening, *Journal of Vascular Surgery* **46**, 630–635.e1, 2007.

[85] F. A. DiazDelaO and S. Adhikari, Gaussian process emulators for the stochastic finite element method, *International Journal for Numerical Methods in Engineering* **87**, 521–540, 2011.

[86] F. A. DiazDelaO and S. Adhikari, Bayesian assimilation of multi-fidelity finite element models, *Computers & Structures* **92-93**, 206–215, 2012.

[87] O. Ditlevsen and H. O. Madsen, *Structural reliability methods*, Wiley, 1996.

[88] O. Ditlevsen and T. A. Nielsen, Model-Correction-Factor Method in Structural Reliability, *Journal of Engineering Mechanics* **120**, 1–10, 1994.

[89] A. Doucet and N. de Freitas, *Sequential Monte Carlo Methods in Practice*, Springer, 2001.

[90] A. Doucet, M. Briers, and S. Sénécal, Efficient block sampling strategies for sequential Monte Carlo methods, *Journal of Computational and Graphical Statistics* **15**, 2006.

[91] P. S. Douglas, G. Pontone, M. A. Hlatky, M. R. Patel, B. L. Norgaard, R. A. Byrne, N. Curzen, I. Purcell, M. Gutberlet, G. Rioufol, U. Hink, H. W. Schuchlenz, G. Feuchtner, M. Gilard, D. Andreini, J. M. Jensen, M. Hadamitzky, K. Chiswell, D. Cyr, A. Wilk, F. Wang, C. Rogers, and B. De Bruyne, Clinical outcomes of fractional flow reserve by computed tomographic angiography-guided diagnostic strategies vs. usual care in patients with suspected coronary artery disease: the prospective longitudinal trial of FFR CT: outcome and resource impacts study, *European Heart Journal* **36**, 3359–3367, 2015.

[92] B. J. Doyle, A. Callanan, and T. M. Mcgloughlin, A comparison of modelling techniques for computing wall stress in abdominal aortic aneurysms, *BioMedical Engineering OnLine* **6**, 137–161, 2007.

[93] B. J. Doyle, A. Callanan, P. A. Grace, and E. G. Kavanagh, On the influence of patient-specific material properties in computational simulations: A case study of a large ruptured abdominal aortic aneurysm, *International Journal for Numerical Methods in Biomedical Engineering* **29**, 150–164, 2012.

[94] V. Dubourg, B. Sudret, and F. Deheeger, Metamodel-based importance sampling for structural reliability analysis, *Probabilistic Engineering Mechanics* **33**, 47–57, 2013.

[95] R. P. Dwight and Z.-H. Han, Efficient uncertainty quantification using gradient-enhanced kriging, In *50th AIAA/ASME/ASCE/AHS/ASC Structures, Structural Dynamics, and Materials Conference*, 2009.

[96] V. G. Eck, J. Feinberg, H. P. Langtangen, and L. R. Hellevik, Stochastic sensitivity analysis for timing and amplitude of pressure waves in the arterial system, *International Journal for Numerical Methods in Biomedical Engineering* **31**, n/a–n/a, 2015. doi: http://dx.doi.org/10.1002/cnm.2711.

[97] A. Ehrl, A. Popp, V. Gravemeier, and W. A. Wall, A dual mortar approach for mesh tying within a variational multiscale method for incompressible flow, *International Journal for Numerical Methods in Fluids* **76**, 1–27, 2014.

[98] M. S. Eldred and C. G. Webster, Evaluation of non-intrusive approaches for Wiener-Askey generalized polynomial chaos, In *49th AIAA/ASME/ASCE/AHS/ASC Structures, Structural Dynamics, and Materials Conference, 16th AIAA/ASME/AHS Adaptive Structures Conference,10th AIAA Non-Deterministic Approaches Conference, 9th AIAA Gossamer Spacecraft Forum, 4th AIAA Multidisciplinary Design Optimization Specialists Conference*, 2008.

[99] D. Elfverson, F. Hellman, and A. Målqvist, A multilevel Monte Carlo method for computing failure probabilities, *arXiv.org preprint*, 2014. URL http://arxiv.org/abs/1408.6856.

[100] P. Erhart, A. Hyhlik-Dürr, P. Geisbüsch, D. Kotelis, M. Müller-Eschner, T. C. Gasser, H. von Tengg-Kobligk, and D. Böckler, Finite Element Analysis in Asymptomatic, Symptomatic, and Ruptured Abdominal Aortic Aneurysms: In Search of New Rupture Risk Predictors, *European Journal of Vascular and Endovascular Surgery* **49**, 239–245, 2015.

[101] R. V. Field Jr and M. Grigoriu, A method for the efficient construction and sampling of vector-valued translation random fields, *Probabilistic Engineering Mechanics* **29**, 79–91, 2012.

[102] M. F. Fillinger, M. L. Raghavan, S. P. Marra, J. L. Cronenwett, and F. E. Kennedy, In vivo analysis of mechanical wall stress and abdominal aortic aneurysm rupture risk, *Journal of Vascular Surgery* **36**, 589–597, 2002.

[103] M. F. Fillinger, S. P. Marra, M. L. Raghavan, and F. E. Kennedy, Prediction of rupture risk in abdominal aortic aneurysm during observation: wall stress versus diameter, *Journal of Vascular Surgery* **37**, 724–732, 2003.

[104] L. Formaggia, A. Quarteroni, and A. Veneziani (eds.), *Cardiovascular Mathematics: Modeling and simulation of the circulatory system*, Springer, 2010.

[105] S. H. Forsdahl, K. Singh, S. Solberg, and B. K. Jacobsen, Risk Factors for Abdominal Aortic Aneurysms A 7-Year Prospective Study: The Tromsø Study, 1994–2001, *Circulation* **119**, 2202–2208, 2009.

[106] D. Gamerman and H. F. Lopes, *Markov chain Monte Carlo: stochastic simulation for Bayesian inference*, CRC Press, 2006.

[107] T. C. Gasser and G. A. Holzapfel, A rate-independent elastoplastic constitutive model for biological fiber-reinforced composites at finite strains: continuum basis, algorithmic formulation and finite element implementation, *Computational Mechanics* **29**, 340–360, 2002.

[108] T. C. Gasser, G. Görgülü, M. Folkesson, and J. Swedenborg, Failure properties of intraluminal thrombus in abdominal aortic aneurysm under static and pulsating mechanical loads, *Journal of Vascular Surgery* **48**, 179–188, 2008.

[109] T. C. Gasser, M. Auer, F. Labruto, J. Swedenborg, and J. Roy, Biomechanical Rupture Risk Assessment of Abdominal Aortic Aneurysms: Model Complexity versus Predictability of Finite Element Simulations, *European Journal of Vascular and Endovascular Surgery* **40**, 176–185, 2010.

[110] M. W. Gee, C. M. Siefert, J. J. Hu, R. S. Tuminaro, and M. G. Sala, ML 5.0 smoothed aggregation user's guide, Technical report, SAND2006-2649, Sandia National Laboratories, 2006.

[111] M. W. Gee, C. Reeps, H. H. Eckstein, and W. A. Wall, Prestressing in finite deformation abdominal aortic aneurysm simulation, *Journal of Biomechanics* **42**, 1732–1739, 2009.

[112] M. W. Gee, C. Förster, and W. A. Wall, A computational strategy for prestressing patient-specific biomechanical problems under finite deformation, *International Journal for Numerical Methods in Biomedical Engineering* **26**, 52–72, 2010.

[113] A. Gelman, Prior distributions for variance parameters in hierarchical models (comment on article by Browne and Draper), *Bayesian analysis* **1**, 515–534, 2006.

[114] A. Gelman and J. Hill, *Data analysis using regression and multilevel/hierarchical models*, Cambridge University Press, 2006.

[115] A. Gelman, J. B. Carlin, H. S. Stern, D. B. Dunson, A. Vehtari, and D. B. Rubin, *Bayesian data analysis*, CRC press, 2013.

[116] T. Gerstner and M. Griebel, Numerical integration using sparse grids, *Numerical algorithms* **18**, 209–232, 1998.

[117] R. G. Ghanem and P. D. Spanos, *Stochastic finite elements: a spectral approach*, Springer (reissued by Dover Publications, 2002), 1991.

[118] R. G. Ghanem, Ingredients for a general purpose stochastic finite elements implementation, *Computer Methods in Applied Mechanics and Engineering* **168**, 19–34, 1999.

[119] D. M. Ghiocel and R. G. Ghanem, Stochastic finite-element analysis of seismic soil-structure interaction, *Journal of Engineering Mechanics* **128**, 66–77, 2002.

[120] M. B. Giles, Multilevel Monte Carlo path simulation, *Operations Research* **56**, 607–617, 2008.

[121] M. B. Giles, Multilevel Monte Carlo methods, *Acta numerica* **24**, 259–328, 2015.

[122] N. H. Gokhale, P. E. Barbone, and A. A. Oberai, Solution of the nonlinear elasticity imaging inverse problem: the compressible case, *Inverse Problems* **24**, 045010–27, 2008.

[123] I. G. Graham, F. Y. Kuo, J. A. Nichols, R. Scheichl, C. Schwab, and I. H. Sloan, Quasi-Monte Carlo finite element methods for elliptic PDEs with lognormal random coefficients, *Numerische Mathematik* **131**, 329–368, 2014.

[124] L. L. Graham, K. Gurley, and F. Masters, Non-Gaussian simulation of local material properties based on a moving-window technique, *Probabilistic Engineering Mechanics* **18**, 223–234, 2003.

[125] R. B. Gramacy, Bayesian treed Gaussian process models, PhD thesis, University of California, Santa Cruz, 2005.

[126] R. B. Gramacy and H. K. H. Lee, Cases for the nugget in modeling computer experiments, *Statistics and Computing* **22**, 713–722, 2010.

[127] R. B. Gramacy and H. K. Lee, Bayesian treed Gaussian process models with an application to computer modeling, *Journal of the American Statistical Association* **103**, 1119–1130, 2008.

[128] P. J. Green, Reversible jump Markov chain Monte Carlo computation and Bayesian model determination, *Biometrika* **82**, 711–732, 1995.

[129] R. M. Greenhalgh, Comparison of endovascular aneurysm repair with open repair in patients with abdominal aortic aneurysm (EVAR trial 1), 30-day operative mortality results: randomised controlled trial, *The Lancet* **364**, 843–848, 2004.

[130] R. M. Greenhalgh, L. C. Brown, J. T. Powell, S. G. Thompson, D. Epstein, and M. J. Sculpher, Endovascular versus open repair of abdominal aortic aneurysm., *The New England journal of medicine* **362**, 1863–1871, 2010.

[131] M. Grigoriu, *Applied non-Gaussian processes*, Prentice Hall, 1995.

[132] M. Grigoriu, Simulation of stationary non-Gaussian translation processes, *Journal of Engineering Mechanics* **124**, 121–126, 1998.

[133] M. Grigoriu, *Stochastic calculus: Applications in science and engineering*, Springer, 2002.

[134] M. Grigoriu, Evaluation of Karhunen–Loève, spectral, and sampling representations for stochastic processes, *Journal of Engineering Mechanics* **132**, 179–189, 2006.

[135] M. Grigoriu, *Stochastic systems: uncertainty quantification and propagation*, Springer, 2012.

[136] L. Grinberg, E. Cheever, T. Anor, J. R. Madsen, and G. E. Karniadakis, Modeling Blood Flow Circulation in Intracranial Arterial Networks: A Comparative 3D/1D Simulation Study, *Annals of Biomedical Engineering* **39**, 297–309, 2010.

[137] T. A. S. Guimarães, G. N. Garcia, M. B. Dalio, M. Bredarioli, C. A. P. Bezerra, and T. Moriya, Morphological aspects of mural thrombi deposition residual lumen route in infrarenal abdominal aorta aneurisms, *Acta Cirurgica Brasileira* **23**, 151–156, 2008.

[138] K. R. Gurley and A. Kareem, A conditional simulation of non-normal velocity/pressure fields, *Journal of Wind Engineering and Industrial Aerodynamics* **77**, 39–51, 1998.

[139] K. R. Gurley, M. A. Tognarelli, and A. Kareem, Analysis and simulation tools for wind engineering, *Probabilistic Engineering Mechanics*, 1997.

[140] A.-L. Haji-Ali, F. Nobile, and R. Tempone, Multi-Index Monte Carlo: When Sparsity Meets Sampling, *arXiv.org preprint*, 2014. URL http://arxiv.org/abs/1405.3757v5.

[141] J. E. Hall, *Guyton and Hall textbook of medical physiology*, Elsevier, 2010.

[142] K. Handa and K. Anderson, Applications of finite element methods in the statistical analysis of structures, In T. Moan and M. Shinozuka (eds.), *Third Int. Conf. on Structural Safety and Reliability*, pages 409–420.

[143] S. S. Hans, O. Jareunpoon, M. Balasubramaniam, and G. B. Zelenock, Size and location of thrombus in intact and ruptured abdominal aortic aneurysms, *Journal of Vascular Surgery* **41**, 584–588, 2005.

[144] R. S. Harris, Pressure-Volume Curves of the Respiratory System, *Respiratory Care* **50**, 78–99, 2005.

[145] T. Hastie, R. Tibshirani, and J. Friedman, *The elements of statistical learning*, Springer, 2nd Edition, 2009.

[146] W. K. Hastings, Monte Carlo sampling methods using Markov chains and their applications, *Biometrika* **57**, 97–109, 1970.

[147] R. G. E. Haylock, *Bayesian inference about outputs of computationally expensive algorithms with uncertainty on the inputs*, PhD thesis, University of Nottingham, 1997.

[148] R. G. E. Haylock and A. O'Hagan, On inference for outputs of computationally expensive algorithms with uncertainty on the inputs, *Bayesian statistics 5*, 629–637, 1996.

[149] S. Heinrich, Multilevel Monte Carlo methods, In S. Margenov, J. Waśniewski, and P. Yalamov (eds.), *Large-Scale Scientific Computing*, pages 58–67, Large-Scale Scientific Computing, 2001.

[150] J. C. Helton and F. J. Davis, Latin hypercube sampling and the propagation of uncertainty in analyses of complex systems, *Reliability Engineering & System Safety* **81**, 23–69, 2003.

[151] M. S. Heng, M. J. Fagan, J. W. Collier, G. Desai, P. T. McCollum, and I. C. Chetter, Peak wall stress measurement in elective and acute abdominal aortic aneurysms, *Journal of Vascular Surgery* **47**, 17–22, 2008.

[152] M. A. Heroux, AztecOO User's guide, Technical report, SAND2004-3796, Sandia National Laboratories, 2007.

[153] M. A. Heroux, R. A. Bartlett, V. E. Howle, R. J. Hoekstra, J. J. Hu, T. G. Kolda, R. B. Lehoucq, K. R. Long, R. P. Pawlowski, E. T. Phipps, and , An overview of the Trilinos project, *ACM Transactions on Mathematical Software (TOMS)* **31**, 397–423, 2005.

[154] T. Hisada and S. Nakagiri, Stochastic finite element method developed for structural safety and reliability, In T. Moan and M. Shinozuka (eds.), *Third Int. Conf. on Structural Safety and Reliability*, pages 409–417, 1981.

[155] G. A. Holzapfel, *Nonlinear solid mechanics*, Wiley, 2000.

[156] T. Homma and A. Saltelli, Importance measures in global sensitivity analysis of nonlinear models, *Reliability Engineering & System Safety* **52**, 1–17, 1996.

[157] W. Huberts, C. de Jonge, W. P. M. van der Linden, M. A. Inda, K. Passera, J. H. M. Tordoir, F. N. van de Vosse, and E. M. H. Bosboom, A sensitivity analysis of a personalized pulse wave propagation model for arteriovenous fistula surgery. Part B: Identification of possible generic model parameters, *Medical Engineering and Physics* **35**, 827–837, 2013.

[158] W. Huberts, C. de Jonge, W. P. M. van der Linden, M. A. Inda, J. H. M. Tordoir, F. N. van de Vosse, and E. M. H. Bosboom, A sensitivity analysis of a personalized pulse wave propagation model for arteriovenous fistula surgery. Part A: Identification of most influential model parameters, *Medical Engineering and Physics* **35**, 810–826, 2013.

[159] T. J. R. Hughes, *The finite element method: linear static and dynamic finite element analysis*, Dover, 2000.

[160] J. D. Humphrey and G. A. Holzapfel, Mechanics, mechanobiology, and modeling of human abdominal aorta and aneurysms **45**, 805–814, 2012.

[161] J. D. Humphrey and K. R. Rajagopal, A constrained mixture model for growth and remodelling of soft tissues, *Mathematical Models and Methods in Applied Sciences* **12**, 407–430, 2002.

[162] M. Ismail, *Reduced Dimensional Modeling of the Entire Human Lung*, PhD thesis, Technische Univesität München, 2014.

[163] M. Ismail, A. Comerford, and W. A. Wall, Coupled and reduced dimensional modeling of respiratory mechanics during spontaneous breathing, *International Journal for Numerical Methods in Biomedical Engineering* **29**, 1285–1305, 2013.

[164] S. S. Isukapalli, A. Roy, and P. G. Georgopoulos, Stochastic response surface methods (SRSMs) for uncertainty propagation: application to environmental and biological systems, *Risk analysis* **18**, 351–363, 1998.

[165] L. Jaulin, *Applied interval analysis: with examples in parameter and state estimation, robust control and robotics*, Springer, 2001.

[166] H. Jeffreys, An Invariant Form for the Prior Probability in Estimation Problems, *Proceedings of the Royal Society A: Mathematical, Physical and Engineering Sciences* **186**, 453–461, 1946.

[167] H. Jeffreys, *The theory of probability*, Oxford University Press, 1998.

[168] W. Jeong and K. Rhee, Hemodynamics of Cerebral Aneurysms: Computational Analyses of Aneurysm Progress and Treatment, *Computational and Mathematical Methods in Medicine* **2012**, 1–11, 2012.

[169] M. Kac and A. Siegert, An explicit representation of a stationary Gaussian process , *The Annals of Mathematical Statistics* **18**, 438–442, 1947.

[170] K. Karhunen, Über lineare Methoden in der Wahrscheinlichkeitsrechnung, *Annales Academiae Scientiarum Fennicae Series A. 1* **37**, 3–79, 1947.

[171] L. S. Katafygiotis and K. M. Zuev, Geometric insight into the challenges of solving high-dimensional reliability problems, *Probabilistic Engineering Mechanics* **23**, 208–218, 2008.

[172] M. C. Kennedy, Bayesian quadrature with non-normal approximating functions, *Statistics and Computing* **8**, 365–375, 1998.

[173] M. C. Kennedy and A. O'Hagan, Predicting the output from a complex computer code when fast approximations are available, *Biometrika* **87**, 1–13, 2000.

[174] M. C. Kennedy and A. O'Hagan, Bayesian calibration of computer models, *Journal of the Royal Statistical Society: Series B (Statistical Methodology)* **63**, 425–464, 2001.

[175] P. Kersaudy, B. Sudret, N. Varsier, O. Picon, and J. Wiart, A new surrogate modeling technique combining Kriging and polynomial chaos expansions – Application to uncertainty analysis in computational dosimetry, *Journal of Computational Physics* **286**, 103–117, 2015.

[176] A. Khintchine, Korrelationstheorie der stationären stochastischen Prozesse, *Mathematische Annalen* **109**, 604–615, 1934.

[177] G. S. Kimeldorf and G. Wahba, A correspondence between Bayesian estimation on stochastic processes and smoothing by splines, *The Annals of Mathematical Statistics*, 495–502, 1970.

[178] O. M. Knio and O. P. Le Maître, Uncertainty propagation in CFD using polynomial chaos decomposition, *Fluid Dynamics Research* **38**, 616–640, 2006.

[179] O. M. Knio, H. N. Najm, and R. G. Ghanem, A stochastic projection method for fluid flow: I basic formulation, *Journal of Computational Physics* **173**, 481–511, 2001.

[180] A. N. Kolmogorov, Grundbegriffe der Wahrscheinlichkeitstheorie, *Ergebnisse der Mathematik und ihrer Grenzgebiete* **2**, 1933.

[181] A. Kottas and A. E. Gelfand, Bayesian semiparametric median regression modeling, *Journal of the American Statistical Association* **96**, 1458–1468, 2001.

[182] P.-S. Koutsourelakis, A multi-resolution, non-parametric, Bayesian framework for identification of spatially-varying model parameters, *Journal of Computational Physics* **228**, 6184–6211, 2009.

[183] P.-S. Koutsourelakis, Accurate uncertainty quantification using inaccurate models, *SIAM Journal on Scientific Computing* **31**, 3274–3300, 2009.

[184] P.-S. Koutsourelakis, H. J. Pradlwarter, and G. I. Schuëller, Reliability of structures in high dimensions, part I: algorithms and applications, *Probabilistic Engineering Mechanics* **19**, 409–417, 2004.

[185] E. Kuhl and G. A. Holzapfel, A continuum model for remodeling in living structures, *Journal of Materials Science* **42**, 8811–8823, 2007.

[186] M. G. Larson and F. Bengzon, *The finite element method: theory, implementation, and applications*, Springer, 2013.

[187] E. Larsson, F. Granath, J. Swedenborg, and R. Hultgren, A population-based case-control study of the familial risk of abdominal aortic aneurysm, *Journal of Vascular Surgery* **49**, 47–51, 2009.

[188] L. Le Gratiet, Bayesian Analysis of Hierarchical Multifidelity Codes, *SIAM/ASA Journal on Uncertainty Quantification* **1**, 244–269, 2013.

[189] O. P. Le Maître and O. M. Knio, *Spectral methods for uncertainty quantification: with applications to computational fluid dynamics*, Springer, 2010.

[190] F. A. Lederle, G. R. Johnson, S. E. Wilson, E. P. Chute, R. J. Hye, M. S. Makaroun, G. W. Barone, D. Bandyk, G. L. Moneta, and R. G. Makhoul, The Aneurysm Detection and Management Study Screening Program: Validation Cohort and Final Results, *Archives of Internal Medicine* **160**, 1425–1430, 2000.

[191] F. A. Lederle, G. R. Johnson, and S. E. Wilson, Abdominal aortic aneurysm in women, *Journal of Vascular Surgery* **34**, 122–126, 2001.

[192] C. A. D. Leguy, E. M. H. Bosboom, A. S. Z. Belloum, A. P. G. Hoeks, and F. N. van de Vosse, Global sensitivity analysis of a wave propagation model for arm arteries, *Medical Engineering and Physics* **33**, 1008–1016, 2011.

[193] M. Lemaire, *Structural reliability*, Wiley, 2013.

[194] R. Li and R. G. Ghanem, Adaptive polynomial chaos expansions applied to statistics of extremes in nonlinear random vibration, *Probabilistic Engineering Mechanics* **13**, 125–136, 1998.

[195] J. S. Lindholt, E. W. Henneberg, H. Fasting, and S. Juul, Hospital based screening of 65-73 year old men for abdominal aortic aneurysms in the county of Viborg, Denmark., *Journal of Medical Screening* **3**, 43–46, 1996.

[196] M. Loève, *Fonctions aleatoires du second ordre*, supplement to P. Levy, Processus Stochastic at Mouvement Browien, Gauthier Villars, 1948.

[197] J. Lu, X. Zhou, and M. L. Raghavan, Inverse elastostatic stress analysis in pre-deformed biological structures: demonstration using abdominal aortic aneurysms, *Journal of Biomechanics* **40**, 693–696, 2007.

[198] B. Ma, J. Lu, R. E. Harbaugh, and M. L. Raghavan, Nonlinear Anisotropic Stress Analysis of Anatomically Realistic Cerebral Aneurysms, *Journal of Biomechanical Engineering* **129**, 88, 2007.

[199] D. J. C. MacKay, Bayesian interpolation, *Neural computation* **4**, 415–447, 1992.

[200] D. J. C. MacKay, Introduction to Gaussian processes, In C. M. Bishop (ed.), *Neural Networks and Machine Learning*, pages 133–166. Springer, 1998.

[201] D. J. C. MacKay, *Information theory, inference and learning algorithms*, Cambridge University Press, 2003.

[202] A. Maier, *Computational Modeling of Rupture Risk in Abdominal Aortic Aneurysms*, PhD thesis, Technische Universität München, 2012.

[203] A. Maier, M. W. Gee, C. Reeps, J. Pongratz, H. H. Eckstein, and W. A. Wall, A Comparison of Diameter, Wall Stress, and Rupture Potential Index for Abdominal Aortic Aneurysm Rupture Risk Prediction, *Annals of Biomedical Engineering* **38**, 3124–3134, 2010.

[204] A. Maier, M. Essler, M. W. Gee, H. H. Eckstein, W. A. Wall, and C. Reeps, Correlation of biomechanics to tissue reaction in aortic aneurysms assessed by finite elements and [18F]–fluorodeoxyglucose–PET/CT, *International Journal for Numerical Methods in Biomedical Engineering* **28**, 456–471, 2012.

[205] A. Majumdar, A. M. Alencar, S. V. Buldyrev, Z. Hantos, K. R. Lutchen, H. E. Stanley, and B. Suki, Relating airway diameter distributions to regular branching asymmetry in the lung, *Physical review letters* **95**, 168101, 2005.

[206] G. Marini, A. Maier, C. Reeps, H. H. Eckstein, W. A. Wall, and M. W. Gee, A continuum description of the damage process in the arterial wall of abdominal aortic aneurysms, *International Journal for Numerical Methods in Biomedical Engineering* **28**, 87–99, 2011.

[207] J. E. Marsden and T. J. R. Hughes, *Mathematical foundations of elasticity*, Dover, 1994.

[208] G. Martufi, E. S. Di Martino, C. Amon, S. Muluk, and E. A. Finol, Three-dimensional geometrical characterization of abdominal aortic aneurysms: image-based wall thickness distribution, *Journal of Biomechanical Engineering* **131**, 061015, 2009.

[209] B. Matérn, *Spatial Variation*, Lecture Notes in Statistics, Springer, 2nd Edition, 1986.

[210] G. Matheron, Principles of geostatistics, *Economic geology* **58**, 1246–1266, 1963.

[211] M. D. McKay, R. J. Beckman, and W. J. Conover, Comparison of three methods for selecting values of input variables in the analysis of output from a computer code, *Technometrics* **21**, 239–245, 1979.

[212] E. R. Melchers, *Structural Reliability Analysis and Prediction*, Wiley, 2nd Edition, 1999.

[213] M. Merkx, M. van't Veer, L. Speelman, M. Breeuwer, J. Buth, and F. N. van de Vosse, Importance of initial stress for abdominal aortic aneurysm wall motion: dynamic MRI validated finite element analysis, *Journal of Biomechanics* **42**, 2369–2373, 2009.

[214] N. Metropolis and S. Ulam, The monte carlo method, *Journal of the American Statistical Association* **44**, 335–341, 1949.

[215] N. Metropolis, A. W. Rosenbluth, M. N. Rosenbluth, A. H. Teller, and E. Teller, Equation of state calculations by fast computing machines, *The Journal of Chemical Physics* **21**, 1087–1092, 1953.

[216] K. Miller and J. Lu, On the prospect of patient-specific biomechanics without patient-specific properties of tissues, *Journal of the Mechanical Behavior of Biomedical Materials* **27**, 154–166, 2013.

[217] T. P. Minka, Expectation propagation for approximate Bayesian inference, In J. S. Breese and D. Koller (eds.), *Proceedings of the Seventeenth conference on Uncertainty in artificial intelligence*, pages 362–369. Morgan Kaufmann Publishers Inc., 2001.

[218] S. Mishra, C. Schwab, and J. Šukys, Multi-level Monte Carlo finite volume methods for nonlinear systems of conservation laws in multi-dimensions, *Journal of Computational Physics* **231**, 3365–3388, 2012.

[219] S. Mishra and C. Schwab, Sparse tensor multi-level Monte Carlo finite volume methods for hyperbolic conservation laws with random initial data, *Mathematics of Computation* **81**, 1979–2018, 2012.

[220] B. Möller and M. Beer, *Fuzzy randomness: uncertainty in civil engineering and computational mechanics*, Springer, 2004.

[221] F. Müller, D. W. Meyer, and P. Jenny, Solver-based vs. grid-based multilevel Monte Carlo for two phase flow and transport in random heterogeneous porous media, *Journal of Computational Physics* **268**, 39–50, 2014.

[222] M. Müller, Gefäßchirugie - arterielle Aneurysmen, In *Chirugie für Studium und Praxis*, pages 58–61, 2005.

[223] K. P. Murphy, *Machine learning: a probabilistic perspective*, MIT Press, 2012.

[224] A. Narayan, C. Gittelson, and D. Xiu, A stochastic collocation algorithm with multifidelity Models, *SIAM Journal on Scientific Computing* **36**, A495–A521, 2014.

[225] A. Nataf, Détermination des distributions de probabilités dont les marges sont données, *Comptes rendus de l'Academie des Sciences de l'Academie des Sciences* **255**, 42–43, 1962.

[226] R. M. Neal, Monte Carlo Implementation of Gaussian process models for Bayesian regression and classification, Technical Report 9702, Department of Statistics, University of Toronto, 1997.

[227] R. M. Neal, Regression and classification using Gaussian process priors, In J. M. Bernardo, J. O. Berger, A. P. Dawid, and A. Smith (eds.), *Bayesian statistics 6*, 1999.

[228] R. M. Neal, Annealed importance sampling, *Statistics and Computing* **11**, 125–139, 2001.

[229] G. F. Nieman, L. A. Gatto, and N. M. Habashi, Impact of mechanical ventilation on the pathophysiology of progressive acute lung injury, *Journal of Applied Physiology* **119**, 1245–1261, 2015.

[230] F. Nobile, R. Tempone, and C. G. Webster, A sparse grid stochastic collocation method for partial differential equations with random input data, *SIAM Journal on Numerical Analysis* **46**, 2309–2345, 2008.

[231] P. E. Norman, K. Jamrozik, M. Lawrence-Brown, and J. Dickinson, Western Australian randomized controlled trial of screening for abdominal aortic aneurysm, *British Journal of Surgery* **90**, 492–492, 2003.

[232] J. Oakley, *Bayesian Uncertainty Analysis for Complex Computer Codes*, PhD thesis, University of Sheffield, 1999.

[233] J. Oakley, Estimating percentiles of uncertain computer code outputs, *Journal of the Royal Statistical Society: Series C (Applied Statistics)* **53**, 83–93, 2004.

[234] J. Oakley and A. O'Hagan, Bayesian inference for the uncertainty distribution of computer model outputs, *Biometrika* **89**, 769–784, 2002.

[235] J. E. Oakley and A. O'Hagan, Probabilistic sensitivity analysis of complex models: a Bayesian approach, *Journal of the Royal Statistical Society: Series B (Statistical Methodology)* **66**, 751–769, 2004.

[236] R. W. Ogden, Large Deformation Isotropic Elasticity - On the Correlation of Theory and Experiment for Incompressible Rubberlike Solids, *Proceedings of the Royal Society of London A: Mathematical, Physical and Engineering Sciences* **326**, 565–584, 1972.

[237] R. W. Ogden, *Non-linear elastic deformations*, Dover, 1997.

[238] A. O'Hagan, Bayes–hermite quadrature, *Journal of statistical planning and inference* **29**, 245–260, 1991.

[239] A. O'Hagan and J. Kingman, Curve fitting and optimal design for prediction, *Journal of the Royal Statistical Society. Series B (Methodological)*, 1–42, 1978.

[240] A. O'Hagan and J. E. Oakley, Probability is perfect, but we can't elicit it perfectly, *Reliability Engineering & System Safety* **85**, 239–248, 2004.

[241] S. A. O'Leary, D. A. Healey, E. G. Kavanagh, M. T. Walsh, T. M. Mcgloughlin, and B. J. Doyle, The Biaxial Biomechanical Behavior of Abdominal Aortic Aneurysm Tissue, *Annals of Biomedical Engineering* **42**, 2440–2450, 2014.

[242] S. A. O'Leary, E. G. Kavanagh, P. A. Grace, T. M. Mcgloughlin, and B. J. Doyle, The biaxial mechanical behaviour of abdominal aortic aneurysm intraluminal thrombus: Classification of morphology and the determination of layer and region specific properties, *Journal of Biomechanics* **47**, 1430–1437, 2014.

[243] A. Olsson and G. E. Sandberg, Latin hypercube sampling for stochastic finite element analysis, *Journal of Engineering Mechanics* **128**, 121–125, 2002.

[244] H. Osnes and J. Sundnes, Uncertainty analysis of ventricular mechanics using the probabilistic collocation method, *IEEE Transactions on Biomedical Engineering* **59**, 2171–2179, 2012.

[245] I. Papaioannou and D. Straub, Reliability updating in geotechnical engineering including spatial variability of soil, *Computers and Geotechnics* **42**, 44–51, 2012.

[246] A. Papoulis and S. U. Pillai, *Probability, random variables, and stochastic processes* , McGraw-Hill, 2002.

[247] K. H. Parker, A brief history of arterial wave mechanics, *Medical & Biological Engineering & Computing* **47**, 111–118, 2009.

[248] D. Pati and D. B. Dunson, Bayesian nonparametric regression with varying residual density, *Annals of the Institute of Statistical Mathematics* **66**, 1–31, 2014.

[249] T. J. Pedley, R. C. Schroter, and M. F. Sudlow, The prediction of pressure drop and variation of resistance within the human bronchial airways, *Respiration physiology* **9**, 387–405, 1970.

[250] M. F. Pellissetti, G. I. Schuëller, H. J. Pradlwarter, A. Calvi, S. Fransen, and M. Klein, Reliability analysis of spacecraft structures under static and dynamic loading, *Computers & Structures* **84**, 1313–1325, 2006.

[251] E. Peña, B. Calvo, M. A. Martínez, and M. Doblaré, On finite-strain damage of viscoelastic-fibred materials. Application to soft biological tissues , *International Journal for Numerical Methods in Engineering* **74**, 1198–1218, 2008.

[252] J. M. C. Pereira, J. P. S. e. Moura, A. R. Ervilha, and J. C. F. Pereira, On the uncertainty quantification of blood flow viscosity models, *Chemical Engineering Science* **101**, 253–265, 2013.

[253] S. Polzer and T. C. Gasser, Biomechanical rupture risk assessment of abdominal aortic aneurysms based on a novel probabilistic rupture risk index, *Journal of The Royal Society Interface* **12**, 20150852–38, 2015.

[254] R. Popescu, G. Deodatis, and J. Prevost, Simulation of homogeneous non-Gaussian stochastic vector fields, *Probabilistic Engineering Mechanics* **13**, 1–13, 1998.

[255] A. Popp, *Mortar Methods for Computational Contact Mechanics and General Interface Problems*, PhD thesis, Technische Universität München, 2012.

[256] J. T. Powell, P. Worrell, S. T. R. MacSweeney, P. J. Franks, and R. M. Greenhalgh, Smoking as a risk factor for Abdominal Aortic Aneurysm, *Annals of the New York Academy of Sciences* **800**, 246–248, 1996.

[257] S. Pranesh and D. Ghosh, Faster computation of the Karhunen–Loève expansion using its domain independence property, *Computer Methods in Applied Mechanics and Engineering* **285**, 125–145, 2015.

[258] M. Prinssen, E. L. G. Verhoeven, J. Buth, P. W. M. Cuypers, M. R. H. M. van Sambeek, R. Balm, E. Buskens, D. E. Grobbee, and J. D. Blankensteijn, A randomized trial comparing conventional and endovascular repair of abdominal aortic aneurysms, *The New England journal of medicine* **351**, 1607–1618, 2004.

[259] A. Protti, M. Cressoni, A. Santini, T. Langer, C. Mietto, D. Febres, M. Chierichetti, S. Coppola, G. Conte, S. Gatti, O. Leopardi, S. Masson, L. Lombardi, M. Lazzerini, E. Rampoldi, P. Cadringher, and L. Gattinoni, Lung Stress and Strain during Mechanical Ventilation, *American Journal of Respiratory and Critical Care Medicine* **183**, 1354–1362, 2011.

[260] V. S. Pugachev, *Theory of Random Functions: And Its Application to Control Problems*, Pergamon Press, 1965.

[261] B. Puig, F. Poirion, and C. Soize, Non-Gaussian simulation using Hermite polynomial expansion: convergences and algorithms, *Probabilistic Engineering Mechanics*, 2002.

[262] P. Z. Qian and C. J. Wu, Bayesian hierarchical modeling for integrating low-accuracy and high-accuracy experiments, *Technometrics* **50**, 192–204, 2008.

[263] A. Quarteroni, R. Sacco, and F. Saleri, *Numerical mathematics*, Springer, 2010.

[264] R. Rackwitz, Reviewing probabilistic soils modelling, *Computers and Geotechnics* **26**, 199–223, 2000.

[265] M. Ragaller and T. Richter, Acute lung injury and acute respiratory distress syndrome, *Journal of Emergencies, Trauma and Shock* **3**, 43–51, 2010.

[266] M. L. Raghavan and D. A. Vorp, Toward a biomechanical tool to evaluate rupture potential of abdominal aortic aneurysm: identification of a finite strain constitutive model and evaluation of its applicability, *Journal of Biomechanics* **33**, 475–482, 2000.

[267] M. L. Raghavan, M. W. Webster, and D. A. Vorp, Ex vivo biomechanical behavior of abdominal aortic aneurysm: assessment using a new mathematical model, *Annals of Biomedical Engineering* **24**, 573–582, 1996.

[268] M. L. Raghavan, J. A. Kratzberg, E. Castro de Tolosa, M. M. Hanaoka, P. J. Walker, and E. S. Da Silva, Regional distribution of wall thickness and failure properties of human abdominal aortic aneurysm, *Journal of Biomechanics* **39**, 3010–3016, 2006.

[269] M. L. Raghavan, M. M. Hanaoka, J. A. Kratzberg, M. d. L. Higuchi, and E. S. Da Silva, Biomechanical failure properties and microstructural content of ruptured and unruptured abdominal aortic aneurysms, *Journal of Biomechanics* **44**, 2501–2507, 2011.

[270] E. Ramm, Strategies for Tracing the Nonlinear Response Near Limit Points, In *Nonlinear Finite Element Analysis in Structural Mechanics*, pages 63–89, Springer, 1981.

[271] C. E. Rasmussen and H. Nickisch, Gaussian Processes for Machine Learning (GPML) Toolbox, *The Journal of Machine Learning Research* **11**, 3011–3015, 2010.

[272] S. Rausch, C. Martin, P. B. Bornemann, S. Uhlig, and W. A. Wall, Material model of lung parenchyma based on living precision-cut lung slice testing, *Journal of the Mechanical Behavior of Biomedical Materials* **4**, 583–592, 2011.

[273] C. Reeps, M. W. Gee, A. Maier, M. Gurdan, H. H. Eckstein, and W. A. Wall, The impact of model assumptions on results of computational mechanics in abdominal aortic aneurysm, *Journal of Vascular Surgery* **51**, 679–688, 2010.

[274] C. Reeps, A. Maier, J. Pelisek, F. Härtl, V. Grabher-Meier, W. A. Wall, M. Essler, H. H. Eckstein, and M. W. Gee, Measuring and modeling patient-specific distributions of material properties in abdominal aortic aneurysm wall, *Biomechanics and Modeling in Mechanobiology* **12**, 1–17, 2012.

[275] C. Robert and G. Casella, *Monte Carlo statistical methods*, Springer, 2013.

[276] A. M. Robertson and P. N. Watton, Computational Fluid Dynamics in Aneurysm Research: Critical Reflections, Future Directions, *American Journal of Neuroradiology* **33**, 992–995, 2012.

[277] J. Rodríguez, G. Martufi, M. Doblaré, and E. A. Finol, The effect of material model formulation in the stress analysis of abdominal aortic aneurysms, *Annals of Biomedical Engineering* **37**, 2218–2221, 2009.

[278] J. F. Rodriguez, V. Alastrue, and M. Doblare, Finite element implementation of a stochastic three dimensional finite-strain damage model for fibrous soft tissue , *Computer Methods in Applied Mechanics and Engineering* **197**, 946–958, 2008.

[279] M. Rosenblatt, Remarks on a multivariate transformation, *The Annals of Mathematical Statistics*, 470–472, 1952.

[280] S. Ross, *A first course in probability*, Pearson, 2012.

[281] C. J. Roth, T. Becher, I. Frerichs, N. Weiler, and W. A. Wall, Coupling of EIT with a computational lung model for predicting patient-specific ventilatory responses, *Journal of Applied Physiology*, 2016. Submitted.

[282] C. J. Roth, M. Ismail, L. Yoshihara, and W. A. Wall, A comprehensive computational human lung model incorporating inter-acinar dependencies: Application to spontaneous breathing and mechanical ventilation, *International Journal for Numerical Methods in Biomedical Engineering*, 2016. Submitted.

[283] Y. Saad, *Iterative methods for sparse linear systems*, SIAM, 2003.

[284] J. Sacks, W. J. Welch, T. J. Mitchell, and H. P. Wynn, Design and analysis of computer experiments, *Statistical Science* **4**, 409–423, 1989.

[285] N. Sakalihasan, R. Limet, and O. D. Defawe, Abdominal aortic aneurysm, *The Lancet* **365**, 1577–1589, 2005.

[286] S. Sakamoto and R. G. Ghanem, Polynomial chaos decomposition for the simulation of non-Gaussian nonstationary stochastic processes, *Journal of Engineering Mechanics* **128**, 190–201, 2002.

[287] S. Sakamoto and R. G. Ghanem, Simulation of multi-dimensional non-Gaussian non-stationary random fields, *Probabilistic Engineering Mechanics* **17**, 167–176, 2002.

[288] A. Saltelli, M. Ratto, T. Andres, F. Campolongo, and J. Cariboni, *Global sensitivity analysis: the primer*, Wiley, 2008.

[289] S. Sankaran and A. L. Marsden, A stochastic collocation method for uncertainty quantification and propagation in cardiovascular simulations, *Journal of Biomechanical Engineering* **133**, 031001–031001–12, 2011.

[290] G. I. Schuëller, H. J. Pradlwarter, and P.-S. Koutsourelakis, A critical appraisal of reliability estimation procedures for high dimensions, *Probabilistic Engineering Mechanics* **19**, 463–474, 2004.

[291] C. A. Schulze-Bauer and G. A. Holzapfel, Determination of constitutive equations for human arteries from clinical data **36**, 165–169, 2003.

[292] S. Seyedsalehi, L. Zhang, J. Choi, and S. Baek, Prior distributions of material parameters for Bayesian calibration of growth and remodeling computational model of abdominal aortic wall, *Journal of Biomechanical Engineering* **137**, 101001, 2015.

[293] D. M. Sforza, C. M. Putman, and J. R. Cebral, Computational fluid dynamics in brain aneurysms, *International Journal for Numerical Methods in Biomedical Engineering* **28**, 801–808, 2011.

[294] G. Shafer, *A mathematical theory of evidence*, Princeton university press, 1976.

[295] Y. Shi and G. Deodatis, A novel approach for simulation of non-Gaussian fields: application in estimating wire strengths from experimental data, In *9th international conference on structural safety and reliability*, 2005.

[296] M. D. Shields and G. Deodatis, A simple and efficient methodology to approximate a general non-Gaussian stationary stochastic vector process by a translation process with applications in wind velocity simulation, *Probabilistic Engineering Mechanics* **31**, 19–29, 2013.

[297] M. D. Shields, G. Deodatis, and P. Bocchini, A simple and efficient methodology to approximate a general non-Gaussian stationary stochastic process by a translation process, *Probabilistic Engineering Mechanics* **26**, 511–519, 2011.

[298] M. D. Shields, K. Teferra, A. Hapij, and R. P. Daddazio, Refined stratified sampling for efficient Monte Carlo based uncertainty quantification, *arXiv.org preprint*, 2015. URL http://arxiv.org/abs/1505.02689v1.

[299] M. Shinozuka and G. Deodatis, Simulation of multi-dimensional Gaussian stochastic fields by spectral representation, *Applied Mechanics Reviews* **49**, 29–53, 1996.

[300] M. Shinozuka and C. M. Jan, Digital simulation of random processes and its applications, *Journal of Sound and Vibration* **25**, 111–128, 1972.

[301] M. Shinozuka and G. Deodatis, Simulation of stochastic processes by spectral representation, *Applied Mechanics Reviews* **44**, 191–204, 1991.

[302] J. Shum, E. S. DiMartino, and A. Goldhammer, Semiautomatic vessel wall detection and quantification of wall thickness in computed tomography images of human abdominal aortic aneurysms, *Medical physics* **37**, 638–648, 2010.

[303] J. C. Simo, On a fully three-dimensional finite-strain viscoelastic damage model: formulation and computational aspects, *Computer Methods in Applied Mechanics and Engineering* **60**, 153–173, 1987.

[304] J. C. Simo and R. L. Taylor, Quasi-incompressible finite elasticity in principal stretches. Continuum basis and numerical algorithms, *Computer Methods in Applied Mechanics and Engineering* **85**, 273–310, 1991.

[305] S. A. Smolyak, Quadrature and interpolation formulas for tensor products of certain classes of functions, *Dokl. Akad. Nauk SSSR* **4**, 123, 1963.

[306] I. M. Sobol, Global sensitivity indices for nonlinear mathematical models and their Monte Carlo estimates, *Mathematics and computers in simulation* **55**, 271–280, 2001.

[307] C. Soize and R. G. Ghanem, Physical systems with random uncertainties: chaos representations with arbitrary probability measure, *SIAM Journal on Scientific Computing* **26**, 395–410, 2004.

[308] T. T. Soong and M. Grigoriu, *Random vibration of mechanical and structural systems*, Prentice Hall, 1993.

[309] P. D. Spanos and B. A. Zeldin, Monte Carlo treatment of random fields: a broad perspective, *Applied Mechanics Reviews* **51**, 219–237, 1998.

[310] P. D. Spanos and R. G. Ghanem, Stochastic finite element expansion for random media, *Journal of Engineering Mechanics* **115**, 1035–1053, 1989.

[311] L. Speelman, E. M. H. Bosboom, G. W. H. Schurink, J. Buth, M. Breeuwer, M. J. Jacobs, and F. N. van de Vosse, Initial stress and nonlinear material behavior in patient-specific AAA wall stress analysis, *Journal of Biomechanics* **42**, 1713–1719, 2009.

[312] L. Speelman, A. Bohra, E. M. H. Bosboom, G. W. H. Schurink, F. N. van de Vosse, M. S. Makaroun, and D. A. Vorp, Effects of wall calcifications in patient-specific wall stress analyses of abdominal aortic aneurysms, *Journal of Biomechanical Engineering* **129**, 105–109, 2007.

[313] S. Standring, *Gray's Anatomy*, The Anatomical Basis of Clinical Practice, Elsevier, 41 Edition, 2015.

[314] G. Stefanou, The stochastic finite element method: past, present and future, *Computer Methods in Applied Mechanics and Engineering* **198**, 1031–1051, 2009.

[315] M. Stein, Large sample properties of simulations using Latin hypercube sampling, *Technometrics* **29**, 143–151, 1987.

[316] M. L. Stein, *Interpolation of spatial data: some theory for kriging*, Springer, 1999.

[317] C. B. Storlie and J. C. Helton, Multiple predictor smoothing methods for sensitivity analysis: Description of techniques, *Reliability Engineering & System Safety* **93**, 28–54, 2008.

[318] C. B. Storlie, L. P. Swiler, J. C. Helton, and C. J. Sallaberry, Implementation and evaluation of nonparametric regression procedures for sensitivity analysis of computationally demanding models, *Reliability Engineering & System Safety* **94**, 1735–1763, 2009.

[319] B. Sudret, *Uncertainty propagation and sensitivity analysis in mechanical models–Contributions to structural reliability and stochastic spectral methods*, PhD thesis, Université Blaise Pascal, 2007.

[320] B. Sudret and A. Der Kiureghian, Stochastic finite element methods and reliability: a state-of-the-art report, Technical report, Department of Civil and Environmental Engineering, University of California, 2000.

[321] M. A. Taddy and A. Kottas, A Bayesian Nonparametric Approach to Inference for Quantile Regression, *Journal of Business & Economic Statistics* **28**, 357–369, 2010.

[322] L. Tamellini, *Polynomial approximation of PDEs with stochastic coefficients*, PhD thesis, Politecnico di Milano, 2012.

[323] M. H. Tawhai, A. J. Pullan, and P. J. Hunter, Generation of an Anatomically Based Three-Dimensional Model of the Conducting Airways, *Annals of Biomedical Engineering* **28**, 793–802, 2000.

[324] C. A. Taylor, T. A. Fonte, and J. K. Min, Computational Fluid Dynamics Applied to Cardiac Computed Tomography for Noninvasive Quantification of Fractional Flow Reserve, *Journal of the American College of Cardiology* **61**, 2233–2241, 2013.

[325] J. Thubrikar, M. Labrosse, F. Robicsek, J. Al-Soudi, and B. Fowler, Mechanical properties of abdominal aortic aneurysm wall, *Journal of Medical Engineering & Technology* **25**, 133–142, 2001.

[326] M. E. Tipping, The Relevance Vector Machine, In S. A. Solla, T. K. Leen, and K. R. Müller (eds.), *Advances in Neural Information Processing Systems 12*, pages 652–658, 2000.

[327] M. E. Tipping, Sparse Bayesian learning and the relevance vector machine, *The Journal of Machine Learning Research* **1**, 211–244, 2001.

[328] M. Tonelli, N. Wiebe, B. Culleton, A. House, C. Rabbat, M. Fok, F. McAlister, and A. X. Garg, Chronic kidney disease and mortality risk: a systematic review, *Journal of the American Society of Nephrology* **17**, 2034–2047, 2006.

[329] J. Tong, T. Cohnert, P. Regitnig, and G. A. Holzapfel, Effects of Age on the Elastic Properties of the Intraluminal Thrombus and the Thrombus-covered Wall in Abdominal Aortic Aneurysms: Biaxial Extension Behaviour and Material Modelling, *European Journal of Vascular and Endovascular Surgery* **42**, 207–219, 2011.

[330] I. Trübswetter. Biaxiale Messung der mechanischen Eigenschaften von Schweineaorten. Master's thesis, Technische Universität München, 2011.

[331] K. Uhlig, J. S. Berns, B. Kestenbaum, R. Kumar, M. B. Leonard, K. J. Martin, S. M. Sprague, and S. Goldfarb, KDOQI US commentary on the 2009 KDIGO clinical practice guideline for the diagnosis, evaluation, and treatment of CKD–mineral and bone disorder (CKD-MBD), *American Journal of Kidney Diseases* **55**, 773–799, 2010.

[332] U. Uhlig and S. Uhlig, Ventilation-Induced Lung Injury, In *Comprehensive Physiology*, 2011.

[333] E. Ullmann and I. Papaioannou, Multilevel estimation of rare events, *SIAM/ASA Journal on Uncertainty Quantification* **3**, 922–953, 2015.

[334] S. R. Vallabhaneni, G. L. Gilling-Smith, T. V. How, S. D. Carter, J. A. Brennan, and P. L. Harris, Heterogeneity of tensile strength and matrix metalloproteinase activity in the wall of abdominal aortic aneurysms, *Journal of Endovascular Therapy* **11**, 494–502, 2004.

[335] F. N. van de Vosse and N. Stergiopulos, Pulse Wave Propagation in the Arterial Tree, *Annual Review of Fluid Mechanics* **43**, 467–499, 2011.

[336] C. Van Ertbruggen, C. Hirsch, and M. Paiva, Anatomically based three-dimensional model of airways to simulate flow and particle transport using computational fluid dynamics, *Journal of Applied Physiology* **98**, 970–980, 2005.

[337] J. P. Vande Geest, E. S. Di Martino, A. Bohra, M. S. Makaroun, and D. A. Vorp, A Biomechanics-Based Rupture Potential Index for Abdominal Aortic Aneurysm Risk Assessment: Demonstrative Application, *Annals of the New York Academy of Sciences* **1085**, 11–21, 2006.

[338] J. P. Vande Geest, M. S. Sacks, and D. A. Vorp, The effects of aneurysm on the biaxial mechanical behavior of human abdominal aorta, *Journal of Biomechanics* **39**, 1324–1334, 2006.

[339] J. P. Vande Geest, M. S. Sacks, and D. A. Vorp, A planar biaxial constitutive relation for the luminal layer of intra-luminal thrombus in abdominal aortic aneurysms, *Journal of Biomechanics* **39**, 2347–2354, 2006.

[340] J. P. Vande Geest, D. H. J. Wang, S. R. Wisniewski, M. S. Makaroun, and D. A. Vorp, Towards a noninvasive method for determination of patient-specific wall strength distribution in abdominal aortic aneurysms, *Annals of Biomedical Engineering* **34**, 1098–1106, 2006.

[341] E. Vanmarcke, *Random fields: analysis and synthesis*, World Scientific, 2010.

[342] J. Vappou, J. Luo, and E. E. Konofagou, Pulse wave imaging for noninvasive and quantitative measurement of arterial stiffness in vivo, *American Journal of Hypertension* **23**, 393–398, 2010.

[343] K. A. Vardulaki, N. M. Walker, E. Couto, N. E. Day, S. G. Thompson, H. A. Ashton, and R. A. P. Scott, Late results concerning feasibility and compliance from a randomized trial of ultrasonographic screening for abdominal aortic aneurysm, *British Journal of Surgery* **89**, 861–864, 2002.

[344] F. Viana and G. Venter, An algorithm for fast optimal Latin hypercube design of experiments, *International Journal for Numerical Methods in Engineering* **82**, 135–156, 2010.

[345] K. Y. Volokh, Comparison of biomechanical failure criteria for abdominal aortic aneurysm, *Journal of Biomechanics* **43**, 2032–2034, 2010.

[346] K. Y. Volokh, Modeling failure of soft anisotropic materials with application to arteries, *Journal of the Mechanical Behavior of Biomedical Materials* **4**, 1582–1594, 2011.

[347] K. Y. Volokh and D. A. Vorp, A model of growth and rupture of abdominal aortic aneurysm, *Journal of Biomechanics* **41**, 1015–1021, 2008.

[348] M. Volrechovsky, Simulation of simply cross correlated random fields by series expansion methods, *Structural Safety* **30**, 337–363, 2008.

[349] D. A. Vorp, M. L. Raghavan, and M. W. Webster, Mechanical wall stress in abdominal aortic aneurysm: Influence of diameter and asymmetry, *Journal of Vascular Surgery* **27**, 632–639, 1998.

[350] W. A. Wall and M. W. Gee, BACI: A parallel multiphysics simulation environment, Technical report, Institute for Computational Mechanics, Technische Universität München, 2016.

[351] L. S. Waltrup, F. Sobotka, and T. Kneib, Expectile and quantile regression—David and Goliath?, *Statistical Modelling* **15**, 433–456, 2015.

[352] C. Wang and R. M. Neal, Gaussian process regression with heteroscedastic or non-gaussian residuals, Technical report, University of Toronto, 2012.

[353] D. H. Wang, M. Makaroun, M. W. Webster, and D. A. Vorp, Mechanical properties and microstructure of intraluminal thrombus from abdominal aortic aneurysm, *Journal of Biomechanical Engineering* **123**, 536–539, 2001.

[354] E. R. Weibel, Geometric and Dimensional Airway Models of Conductive, Transitory and Respiratory Zones of the Human Lung, In *Morphometry of the Human Lung*, pages 136–142, 1963.

[355] H. Weisbecker, D. M. Pierce, and G. A. Holzapfel, A generalized prestressing algorithm for finite element simulations of preloaded geometries with application to the aorta, *International Journal for Numerical Methods in Biomedical Engineering* **30**, 857–872, 2014.

[356] S. Weisberg, *Applied linear regression*, John Wiley & Sons, 4 Edition, 2014.

[357] N. Wiener, Generalized harmonic analysis, *Acta mathematica* **55**, 117–258, 1930.

[358] N. Wiener, The homogeneous chaos, *American Journal of Mathematics*, 897–936, 1938.

[359] K. Willcox and J. Peraire, Balanced model reduction via the proper orthogonal decomposition, *AIAA Journal* **40**, 2323–2330, 2002.

[360] C. K. Williams and C. E. Rasmussen, Gaussian processes for regression, In S. D. Touretzky, M. C. Mozer, and M. E. Hasselmo (eds.), *Advances in Neural Information Processing Systems 8*. MIT, 1996.

[361] C. K. Williams and C. E. Rasmussen, *Gaussian processes for machine learning*, MIT Press, 2006.

[362] J. Witteveen and H. Bijl, Uncertainty Quantification in Fluid-Structure Interaction Simulations Using a Simplex Elements Stochastic Collocation Approach, In *19th AIAA Computational Fluid Dynamics*, pages 1–17. American Institute of Aeronautics and Astronautics, 2009.

[363] P. Wriggers, *Nonlinear finite element methods*, Springer, 2008.

[364] D. Xiu, *Numerical methods for stochastic computations: a spectral method approach*, Princeton University Press, 2010.

[365] D. Xiu and J. S. Hesthaven, High-order collocation methods for differential equations with random inputs, *SIAM Journal on Scientific Computing* **27**, 1118–1139, 2005.

[366] D. Xiu and G. E. Karniadakis, The Wiener–Askey polynomial chaos for stochastic differential equations, *SIAM Journal on Scientific Computing* **24**, 619–644, 2002.

[367] D. Xiu and S. J. Sherwin, Parametric uncertainty analysis of pulse wave propagation in a model of a human arterial network, *Journal of Computational Physics* **226**, 1385–1407, 2007.

[368] F. Yamazaki, Simulation of stochastic fields and its application to finite element analysis, Technical Report 87-04, Ohsaki Research Institute, 1987.

[369] F. Yamazaki and M. Shinozuka, Digital generation of non-Gaussian stochastic fields, *Journal of Engineering Mechanics* **114**, 1183–1197, 1988.

[370] F. Yamazaki and M. Shinozuka, Simulation of stochastic fields by statistical preconditioning, *Journal of Engineering Mechanics* **116**, 268–287, 1990.

[371] K. Yu and R. A. Moyeed, Bayesian quantile regression, *Statistics & Probability Letters* **54**, 437–447, 2001.

[372] A. R. Zankl, H. Schumacher, U. Krumsdorf, H. A. Katus, L. Jahn, and C. P. Tiefenbacher, Pathology, natural history and treatment of abdominal aortic aneurysms, *Clinical Research in Cardiology* **96**, 140–151, 2006.

[373] X. Zhu, A. Narayan, and D. Xiu, Computational Aspects of Stochastic Collocation with Multifidelity Models, *SIAM/ASA Journal on Uncertainty Quantification* **2**, 444–463, 2014.

[374] O. C. Zienkiewicz, R. L. Taylor, and J. C. Zhu, *The Finite Element Method: It's Basis and Fundamentals*, Butterworth-Heinemann, 7th Edition, 2013.